Electrochemical Promotion of Non-Noble Metal Catalysts for the Reverse Water Gas Shift Reaction

Ju Wang

Thesis submitted to the University of Ottawa
in partial Fulfillment of the requirements for the
Degree of Doctor of Philosophy

Department of Chemical and Biological Engineering
Faculty of Engineering
University of Ottawa

Abstract

The greenhouse gas carbon dioxide (CO_2) can be transformed into carbon monoxide (CO) via the reverse water gas shift (RWGS) reaction. This process not only mitigates CO_2 emissions but also recycles it into valuable chemicals, as CO is an essential precursor in hydrocarbon production through the Fischer-Tropsch process. Nanostructured metals immobilized on oxide supports serve as catalysts for this reaction, where the formation of metal-support interactions (MSI) influence both catalytic performance and thermal stability. Additionally, the catalytic activity can be regulated and modified through the electrochemical promotion of catalysis (EPOC), also known as non-Faradaic electrochemical modification of catalytic activity (NEMCA) by applying electrical potential or current across the catalyst deposited on solid electrolyte.

In pursuit of a cost-effective and high-performance EPOC system, copper (Cu) is investigated as a promising non-noble metal catalyst for the RWGS reaction due to its affordability, high activity, and selectivity. When deposited on yttria-stabilized zirconia (YSZ) solid electrolyte, the electrochemical polarization at +2V leads to the migration of oxygen ions (O^{2-}) toward Cu, inducing its partial oxidation from Cu^0 to Cu^{1+} and enhancing the reaction rate by 20%. Non-noble metal oxides such as cobalt oxide (Co_3O_4) and zinc oxide (ZnO) are explored as supports for Cu to prevent its deactivation due to oxidation and sintering at elevated temperatures. Co_3O_4, in particular, acts as an active phase and an oxygen reservoir in the Cu/Co_3O_4 co-catalyst. Under positive potential, O^{2-} transfer from Co_3O_4 to Cu decreases the reaction rate by 42%, while the reverse process at negative potential increases it by 16%. Additionally, studies on Cu/ZnO catalysts with Cu loadings between 5 to 60 wt.% confirm that ZnO effectively prevents Cu from sintering and complete oxidation, and the MSI between Cu and ZnO improves the catalytic rate by 75%. Under positive polarization at +400μA, all catalysts exhibit EPOC effects, with 10Cu/ZnO showing the largest increase of 14%. Density functional theory (DFT) modelling further investigates the migration of O^{2-} from ZnO to Cu and the subsequent formation of Cu_2O. A correlation

is established between the electrochemical active surface area (ECSA) and the magnitude of the EPOC effect, offering insights into the selection of suitable oxide supports for EPOC studies.

To expand the application of EPOC to reactions favorable at lower temperatures, a lithium-ion (Li^+) conductor, lithium lanthanum titanate (LLTO), is introduced as an alternative solid electrolyte because of its high ionic conductivity at reduced temperatures. For the first time, Li^+ is shown to act as a promoter of catalytic RWGS reaction and CO oxidation in EPOC experiments. Unique interactions between Li^+ and metal/metal oxide catalysts using platinum (Pt) and iron-oxide (FeO_x) are revealed, enabling EPOC to drive CO oxidation at temperatures as low as 150°C. The MSI between FeO_x and LLTO also enhances the RWGS catalytic rate, making it 3 times higher compared to FeO_x deposited on YSZ. This discovery opens new possibilities for practical EPOC applications in energy conversion processes.

Physicochemical characterizations, including scanning electron microscopy (SEM), transmission electron microscopy (TEM), scanning transmission electron microscopy (STEM), Brunauer-Emmett-Teller (BET) analysis, X-ray diffraction (XRD), and X-ray photoelectron spectroscopy (XPS), are conducted to analyze the morphology, size, elemental composition, specific surface area, crystallite structure, and oxidation state of the metal catalysts. Electrochemical characterization through cyclic voltammetry (CV) provides in-situ insights into the interactions between the metal catalysts and ionic species from the solid electrolyte.

Résumé

Le dioxyde de carbone (CO_2), un gaz à effet de serre, peut être transformé en monoxyde de carbone (CO) par la réaction de décalage inverse du gaz à l'eau (RWGS). Ce processus permet non seulement de réduire les émissions de CO_2, mais aussi de le recycler en produits chimiques de valeur, car le CO est un précurseur essentiel dans la production d'hydrocarbures via le procédé Fischer-Tropsch. Les métaux nanostructurés immobilisés sur des supports d'oxyde agissent comme catalyseurs pour cette réaction, où la formation d'interactions métal-support (IMS) influence à la fois la performance catalytique et la stabilité thermique. En outre, l'activité catalytique peut être régulée et modifiée grâce à la promotion électrochimique de la catalyse (EPOC), également connue sous le nom de modification électrochimique non faradaïque de l'activité catalytique (NEMCA), en appliquant un potentiel ou un courant électrique à travers le catalyseur déposé sur un électrolyte solide.

Dans la quête d'un système EPOC performant et économique, le cuivre (Cu) est étudié comme catalyseur non noble prometteur pour la réaction RWGS en raison de son faible coût, de sa grande activité et de sa sélectivité. Lorsqu'il est déposé sur un électrolyte solide de zircone stabilisée à l'yttrium (YSZ), la polarisation électrochimique à +2V entraîne la migration des ions oxygène (O^{2-}) vers le Cu, induisant son oxydation partielle de Cu^0 à Cu^{1+} et augmentant le taux de réaction de 20%. Des oxydes métalliques non nobles tels que l'oxyde de cobalt (Co_3O_4) et l'oxyde de zinc (ZnO) sont explorés comme supports pour le Cu afin de prévenir sa désactivation due à l'oxydation et au frittage à des températures élevées. Co_3O_4, en particulier, agit comme une phase active et un réservoir d'oxygène dans le co-catalyseur Cu/Co_3O_4. Sous un potentiel positif, le transfert d'O^{2-} de Co_3O_4 vers le Cu réduit le taux de réaction de 42%, tandis que le processus inverse sous potentiel négatif l'augmente de 16%. De plus, des études sur des catalyseurs Cu/ZnO avec des charges de Cu comprises entre 5 et 60% en poids confirment que le ZnO empêche efficacement le Cu de se fritté et de s'oxyder complètement, et que l'IMS entre Cu et

ZnO améliore le taux catalytique de 75%. Sous une polarisation positive à +400μA, tous les catalyseurs présentent des effets EPOC, le 10Cu/ZnO montrant la plus forte augmentation de 14%. La modélisation par la théorie de la fonctionnelle de densité (DFT) examine plus en détail la migration des ions O^{2-} du ZnO vers le Cu et la formation subséquente de Cu2O. Une corrélation est établie entre la surface active électrochimique (ECSA) et l'ampleur de l'effet EPOC, offrant des indications sur la sélection de supports d'oxyde appropriés pour les études EPOC.

Pour étendre l'application de l'EPOC à des réactions favorables à des températures plus basses, un conducteur d'ions lithium (Li^+), le titanate de lanthane et de lithium (LLTO), est introduit comme électrolyte solide alternatif en raison de sa haute conductivité ionique à des températures réduites. Pour la première fois, il est démontré que le Li^+ agit comme promoteur dans la réaction catalytique RWGS et l'oxydation du CO lors des expériences EPOC. Des interactions uniques entre Li^+ et des catalyseurs métal/oxyde de métal, tels que le platine (Pt) et l'oxyde de fer (FeO_x), sont révélées, permettant à l'EPOC d'activer l'oxydation du CO à des températures aussi basses que 150°C. L'IMS entre FeO_x et LLTO améliore également le taux catalytique de la réaction RWGS, le rendant trois fois plus élevé que celui obtenu avec FeO_x déposé sur YSZ. Cette découverte ouvre de nouvelles possibilités pour des applications pratiques de l'EPOC dans les processus de conversion énergétique.

Des caractérisations physicochimiques, incluant la microscopie électronique à balayage (SEM), la microscopie électronique en transmission (TEM), la microscopie électronique à transmission par balayage (STEM), l'analyse de Brunauer-Emmett-Teller (BET), la diffraction des rayons X (XRD), et la spectroscopie photoélectronique à rayons X (XPS), sont réalisées pour analyser la morphologie, la taille, la composition élémentaire, la surface spécifique, la structure cristalline, et l'état d'oxydation des catalyseurs métalliques. La caractérisation électrochimique par voltamétrie cyclique (CV) fournit des informations in situ sur les interactions entre les catalyseurs métalliques et les espèces ioniques issues de l'électrolyte solide.

Statement of Contributors of Collaborators and Co-Authorship

I hereby declare that I am the sole author of this thesis.

Chapter 1 and 2 were written by me with editorial comments by Prof. Elena Baranova.

Chapter 3 and 4 were written by me with editorial comments by Prof. Elena Baranova. The synthesis, catalytic setup, EPOC experiments were conducted by me. Catalyst characterization was performed by Dr. Martin Couillard at National Research Council of Canada (NRC).

Chapter 5 was done in collaboration with Dr. Mario G. Sandoval (co-authorship) and with editorial comments by his supervisor Prof. Alfredo Juan from Instituto de Física del Sur (IFISUR) in Universidad Nacional del Sur (UNS) in Bahía Blanca, Argentina and Prof. Elena Baranova. Catalytic setup and experimental work were done by me. Density functional theory (DFT) calculations were performed by Dr. Mario G. Sandoval with the assistance of Prof. Estela A. González and Prof. Paula V. Jasen at UNS. The DFT calculation was enabled in part by support from the Digital Research Alliance of Canada thanks to Prof. Arnaud Weck at University of Ottawa. Catalyst characterization was performed by Dr. Martin Couillard at NRC.

Chapter 6 was written by me with editorial comments by Prof. Elena Baranova. The catalytic setup and experimental work were conducted by me. The lithium lanthanum titanate (LLTO) was prepared by Ph.D. candidate, Shuo Yan. The iron-oxide (FeO_x) nanowires were synthesized by Dr. Christopher Panaritis. Catalyst characterization was performed by Kholoud Abousalem and Prof. Drew Higgins at McMaster University.

Chapter 7 was written by me with editorial comments by Prof. Elena Baranova.

Acknowledgments

I would like to express my deepest gratitude to Professor Elena Baranova for the important role she played in my academic career and for choosing me as a doctoral student in early 2020. Her mentorship has provided me with valuable opportunities to explore and develop innovative ideas and engage in meaningful collaborations. Under her guidance, my enthusiasm for scientific research was greatly enhanced, and my cooperation and resource integration abilities were also improved, which are all very important to my future development and life.

Thank you to Dr. Christopher Panaritis, who provided training when I first joined the research group. His expertise and approach to science greatly accelerated my acclimation to the new environment and enhanced my laboratory skills.

Thank you to Professor Mario G. Sandoval and Professor Alfredo Juan from Universidad Nacional del Sur (UNS) in Bahía Blanca, Argentina, for their instruction in density functional theory (DFT) calculations and for the opportunity to visit Argentina, an experience that enriched my academic and personal life.

Thank you to Dr. Martin Couillard, co-author of most of my publications. His expertise in creating high-quality STEM images of nanostructured catalysts was crucial for our publications.

Thank you to Professor Christopher Q. Lan and Professo Nicholas Burn at the University of Ottawa for invaluable guidance in both my academic journey and daily life. Serving as their teaching assistant for the past three years has been incredibly enriching.

Thank you to Professor F. Handan Tezel, Professor Jason Zhang, Professor Clémence Fauteux-Lefebvre from the University of Ottawa, and Professor Natalia Semagina from the University of Alberta for being my thesis evaluation committee.

A heartfelt thank you to all my past, present, and future lab colleagues and friends — Dr. Mohamed Houache, Dr. Emily Cossar, Dr. Hilal Al-Salih, Dr. Shuo Yan,

Dr. Arash Fella Jahromi, Dr. Ashwini Reddy Nallayagari, Dr. Najmeh Ahledel, Frédéric Murphy, Shadia Khan, Yawar Farhan, Giselle Granchelli, Pranita Chougule, Alexandra Baczynska, Mustapha Ezzeddine, and Karim Harb — for their kindness and support.

Special thanks to Facu, Mauro, and Julian at UNS who treated me like a family during my stay in Argentina. Immense gratitude to my friends in Canada — Zitong Xu, Zijian Long, Yu Shen, and Fang Li — who have been a constant source of companionship and support over the past four years.

I am eternally grateful to my grandmother, Yufen Cui, and my parents, Jingqi Liang and Chunguo Wang, for their unwavering love, guidance, and support throughout my life. Their encouragement has been the foundation of my achievements.

Lastly, but most importantly, I want to express my deepest appreciation to my wife, Hongying Zhou, for her endless love and steadfast support. Her patience and understanding have been crucial to my success, and this achievement is as much hers as it is mine. I am incredibly fortunate to have her by my side.

Table of Contents

Abstract ..... **II**

Résumé ..... **IV**

Statement of Contributors of Collaborators and Co-Authorship ..... **VI**

Acknowledgments ..... **VII**

Table of Contents ..... **IX**

List of Figures ..... **XIII**

Abbreviations ..... **XVI**

List of Symbols ..... **XVIII**

List of Greek Symbols ..... **XIX**

Chapter 1: Literature Review and Research Objectives **1**

1.1 Rationale of CO_2 Utilization **1**

1.2 CO_2 Hydrogenation **2**

1.2.1 Reverse water gas shift reaction **4**

1.2.2 Methanation **5**

1.2.3 Methanol synthesis **6**

1.3 Metal Catalysts **8**

1.3.1 Noble metals **8**

1.3.2 Non-noble metals **10**

1.3.3 Metal-support interaction **12**

1.4 Electrochemical Promotion of Catalysis **14**

1.4.1 EPOC for CO_2 hydrogenation **22**

1.4.2 EPOC for CO oxidation and hydrocarbon oxidation **26**

1.4.3 Permanent EPOC **28**

1.4.4 DFT study in EPOC **30**

1.5 Motivation and Research Objectives **31**

1.6 Thesis Structure **32**

References **35**

Chapter 2: Experiments and Characterizations **50**

2.1 Catalyst Synthesis **50**

2.2 Cell Preparation **50**

2.3 Experimental Setup **51**

2.4 Physicochemical Characterization **53**

2.5 Electrochemical Characterization 54

References 55

Chapter 3: Electrochemical Promotion of Cu Nanoparticles for the Reverse Water Gas Shift Reaction 56

3.1 Introduction 56

3.2 Experimental 57

3.2.1 Catalysts synthesis 57

3.2.2 Experimental setup 57

3.2.3 Characterizations 59

3.3 Results 59

3.3.1 Catalyst characterizations 59

3.3.2 Open-circuit catalytic activity of Cu/YSZ 63

3.3.3 Cyclic voltammetry of Cu/YSZ 65

3.3.4 Electrochemical promotion of catalysis 68

3.4 Conclusion 74

References 75

Appendix A: Supplementary Information for Chapter 3 79

Chapter 4: Electrochemical Promotion of Cu/Co_3O_4 for the Reverse Water Gas Shift Reaction 85

4.1 Introduction 85

4.2 Experimental 86

4.2.1 Catalysts synthesis 86

4.2.2 Experimental setup 87

4.2.3 Characterizations 88

4.3 Results 89

4.3.1 Catalyst characterizations 89

4.3.2 Catalytic RWGS reaction 94

4.3.3 Cyclic voltammetry 96

4.3.4 Electrochemical promotion of catalysis 98

4.3.5 Exchange current density evaluation 104

4.4 Conclusion 106

References 106

Appendix B: Supplementary Information for Chapter 4 111

Chapter 5: Experimental and DFT Study on Electrochemical Promotion of Cu/ZnO for the

Reverse Water Gas Shift Reaction **119**
5.1 Introduction **119**
5.2 Experimental and Computational Methodology **121**
5.2.1 Catalysts preparation **121**
5.2.2 Experimental setup **122**
5.2.3 Electrochemical measurements **122**
5.2.4 Physicochemical characterizations **123**
5.2.5 Computational methodology **124**
5.3 Results **127**
5.3.1 Physicochemical characterizations **127**
5.3.2 Open-circuit activities **131**
5.3.3 Electrochemical promotion of catalysis **132**
5.3.4 Density functional theory **134**
5.3.5 Electrochemical characterizations **138**
5.3.6 Electrochemical active surface area **140**
5.4 Conclusion **142**
References **143**
Appendix C: Supplementary Information for Chapter 5 ..... **148**
Chapter 6: Electrochemical Promotion of Catalysis by Lithium-Ion **161**
6.1 Introduction **161**
6.2 Experimental **163**
6.2.1 Preparation of catalyst and electrochemical cell **163**
6.2.2 Experimental setup **164**
6.2.3 Electrochemical measurements **164**
6.2.4 Physicochemical characterizations **165**
6.3 Results and Discussions **165**
6.3.1 Physicochemical characterizations **165**
6.3.2 Open-circuit activity **169**
6.3.3 EPOC for CO oxidation **170**
6.3.4 EPOC for RWGS **175**
6.3.5 Cyclic voltammetry **178**
6.4 Conclusion **180**
References **182**
Appendix D: Supplementary Information for Chapter 6 ..... **186**

Chapter 7: Conclusions and Recommendations.....204

7.1 Conclusions.....204

7.2 Recommendations.....206

7.3 Scholarly Contributions.....208

List of Figures

Figure 1-1. Reaction pathways of CO_2 hydrogenation to CO, CH_4, and CH_3OH. *(X) indicates adsorbed species. Reprinted with permission from [25]. Copyright ACS 2017. 4
Figure 1-2. Schematic representation of main metal-support interactions and five main phenomena. Reprinted with permission from [98]. Copyright Nature 2019.....13
Figure 1-3. (a) EPOC phenomenon of Pt deposited on YSZ for C_2H_4 oxidation under an application of +1 μA. Reprinted with permission from [116]. Copyright Springer 2001. (b) The schematic structure of the EPOC cell.....15
Figure 1-4. Schematic of metal electrode deposited on a Na^+ conductor (a) and on an O^{2-} conductor (b), showing the location of the effective neutral double layer created at the tpb. Reprinted with permission from [118]. Copyright Springer 2010. 16
Figure 1-5. Catalytic rate responses to step changes of various applied positive currents during C_3H_8 oxidation on Pt/YSZ. Reprinted with permission from [122]. Copyright Elsevier 2012.....18
Figure 1-6. Schematic of the unpromoted and promoted states of metal-supported catalysts: (a) classical promotion (promoter added during synthesis), (b) EPOC (polarization-controlled O^{2-} backspillover), and (c) MSI (self-driven O^{2-} backspillover). Reprinted with permission from [102]. Copyright ACS 2013.....19
Figure 1-7. Rules of electrochemical behavior: (R1) electrophobic, (R2) electrophilic, (R3) volcano, and (R4) inverted volcano. Reprinted with permission from [125]. Copyright Elsevier 2014. 20
Figure 1-8. EPOC for RWGS over (a) FeO_x nanowires. Reprinted with permission from [152]. Copyright Elsevier 2020. (b) Co NPs deposited on YSZ. Reprinted with permission from [153]. Copyright ACS 2020.....25
Figure 1-9. (a) Persistent p-EPOC effect over Pd/YSZ for CH_4 oxidation. Reprinted with permission from [161]. Copyright Springer 2008. (b) Long-term p-EPOC effect over Pt/YSZ for C_3H_8 oxidation. Reprinted with permission from [142]. Copyright Elsevier 2010.....29
Figure 2-1. Schematic structure of (a) electrodes deposited on the solid electrolyte, (b) EPOC cell in reactor, and (c) experimental set-up.....51
Figure 3-1. STEM image of (a) and (b) as-prepared Cu catalyst and (c) EELS mapping of (d) copper, (e) oxygen and (f) carbon from the orange square in (b), where red means Cu, green represents oxygen, and blue is carbon.....61
Figure 3-2. SEM images of (a) as-prepared Cu and (b) spent Cu. 62
Figure 3-3. High-resolution XPS spectra for Cu 2p of (a)colloidal, (b)as-prepared, and (c)spent samples.....63
Figure 3-4. Open-circuit CO production rate of Cu NPs deposited on YSZ. 65
Figure 3-5. Cyclic voltammetry of Cu/YSZ at 400°C (a) in Ar and CO_2:H_2 ratio of 1:1 and (b) in Ar with varying positive potential, 0, 0.5, 1 and 1.5 V. Effect of holding potential at (c) 1.5V and (d) -1.5V for 10 min at 400°C in Ar. 68
Figure 3-6. Transient response of reaction rates under the application of 2V and CO_2:H_2 ratio of 1:1 at (a) 340°C, (b) 360°C, (c) 400°C and (d) 450°C.....70
Figure 3-7. Transient response of reaction rates under the application of 2V at 400°C for CO_2:H_2 ratio of (a) $3CO_2$:$1H_2$, (b) $6CO_2$:$1H_2$, (c) $1CO_2$:$3H_2$ and (d) $1CO_2$:$6H_2$.....72
Figure 3-8. Effect of temperature and CO_2:H_2 ratio on (a) the enhancement ratio (ρ) and (b) the

Faradaic efficiency (Λ) under the application of 2V. 73
Figure 3-9. Effect of applied voltage and CO_2:H_2 ratio on (a) the enhancement ratio (ρ) and (b) the Faradaic efficiency (Λ) at 400℃. 74
Figure 4-1. HAADF-STEM image of (a) as-prepared 4wt.%Cu/Co_3O_4 and EELS mappings with corresponding elemental composition of (b) as-prepared and (c) spent 4wt.%Cu/Co_3O_4 catalyst. 90
Figure 4-2. SEM images of spent (a) Co_3O_4, (b) 1wt.%Cu/Co_3O_4, (c) 4wt.%Cu/Co_3O_4, and (d) 8wt.%Cu/Co_3O_4 deposited on YSZ on the scale of 100nm. 91
Figure 4-3. XRD patterns of (a) as-prepared and (b) spent 4wt.%Cu/Co_3O_4. 92
Figure 4-4. High-resolution XPS spectra for (a) Cu $2p_{3/2}$ and (b) Co $2p_{3/2}$. 93
Figure 4-5. Light-off curves of bare Co_3O_4, Cu/Co_3O_4, and free-standing Cu catalysts under (a) stoichiometric, (b) oxidizing, and (c) reducing conditions. 96
Figure 4-6. Cyclic voltammetry of (a) as-prepared and spent 4wt.%Cu/Co_3O_4, and as-prepared (b) bare Co_3O_4 and (c) free-standing Cu deposited on YSZ in Argon at 400℃, scan rate 20 mV s^{-1} 98
Figure 4-7. Summary of ρ and Λ values for 4wt.%Cu/Co_3O_4 under (a) stoichiometric, (b) oxidizing, and (c) reducing conditions at 400℃. 99
Figure 4-8. EPOC of 4wt.%Cu/Co_3O_4 at (a) +2V and (b) -1V under different CO_2:H_2 ratios at 400℃, (c) EPOC under stoichiometric conditions at various anodic potentials, and (d) Percentage (%) rate increase after polarization under various conditions at 400℃. 102
Figure 4-9. Summary of N_G (mol O^{2-} uptake) at 400℃ under different reaction conditions and applied potentials. 104
Figure 4-10. Relationship between open circuit catalytic reaction rate (r_0) and exchange current density (i_0) of Cu/Co_3O_4 catalysts under the stochiometric condition at 400℃. 105
Figure 5-1. (a) TEM image of spent 10CuZnO. (b) STEM image and corresponding EELS mapping of Cu and Zn in the orange area (the yellow area is for drift correction). 128
Figure 5-2. (a) XRD patterns and (b) high-resolution XPS spectra of Cu $2p_{3/2}$ and Cu LMM for as-prepared and spent 10CuZnO. High-resolution XPS spectra of (c) O 1s and (d) Zn 2p for as-prepared ZnO, 10CuZnO and 60CuZnO. 129
Figure 5-3. Light-off curves of (a) all Cu/ZnO catalysts under stoichiometric conditions and (b) 20CuZnO catalyst under all reaction conditions. 132
Figure 5-4. Transient responses of CO rates to applied constant current of 400 μA for all Cu/ZnO catalysts under stoichiometric conditions at 400℃. 134
Figure 5-5. Schematic view of (a) ZnO (101) surface after Cu adsorption, (b) Cu/ZnO (101) system after O^* adsorption, (c) Cu/ZnO (101) system after Cu adsorption and (d) 2Cu/ZnO (101) system after O^* adsorption. The green oxygen atom represents the O^*. 136
Figure 5-6. Energy vs Step curves of the O1 migration of the ZnO (101) surface after two Cu atoms adsorption. The pink atom indicates the migrating oxygen. The graphics inserts present the initial, transition and final configuration. 138
Figure 5-7. CVs at 400℃ in Argon for (a) 5-20CuZnO and (b) 20-60CuZnO; (c) Peak locations of AI, AII, CI and CII; (d) Effects of Cu loadings on RF and S_{BET}; Correlation between (e) Λ and RF, and (f) r_0 and S_{BET} of Cu/ZnO catalysts. 140
Figure 6-1. TEM image (a) and EELS mapping (b) of RWGS spent Fe/LLTO. 166
Figure 6-2. High-resolution XPS spectra of as-prepared, CO spent, and RWGS spent Pt-50/LLTO catalysts for (a) Li 1s & Pt 5p and (b) C 1s, as well as Fe/LLTO catalysts for (c) Li 1s & Fe 3p and (d) C 1s. 168

Figure 6-3. Open-circuit (a) RWGS activities and (b) CO conversions of Fe/LLTO and Pt/LLTO. 170
Figure 6-4. CO oxidation rate on FeOx under (a) +3 V and -0.5 V, (b) various positive voltages, and (c) different polarization time at -0.5 V. CO oxidation rate on (d) Pt-100 with positive polarization, and on Pt-50 with (e) positive and (f) negative polarization. 173
Figure 6-5. Transient responses of RWGS rate to negative polarization at 350℃ under (a) stoichiometric, (b) oxidizing and (c) reducing conditions. (d) Transient responses of RWGS rate to different negative polarization on Pt-50 at 400℃. 177
Figure 6-6. CVs of CO oxidation on (a) Fe/LLTO at 150℃ and (b) Pt-50/LLTO at 200℃. CVs of RWGS on Fe/LLTO at 350℃ under (c) oxidizing and (d) reducing conditions, and on Pt-50/LLTO at 400℃ under (e) oxidizing and (f) reducing conditions. 179

Abbreviations

BE	Binding Energy
BET	Brunauer–Emmett–Teller
CE	Counter Electrode
CV	Cyclic Voltammetry
DFT	Density Functional Theory
DOS	Density of States
ECSA	Electrochemical Active Surface Area
EDX/EDS	Energy Dispersive X-ray
EELS	Energy Electron Loss Spectrometry
EG	Ethylene Glycol
EPOC	Electrochemical Promotion of Catalysis
FT	Fischer-Tropsch
FWHM	Full-Width at Half Maximum
GGA	General Gradient Approximation
GHG	Greenhouse Gas
HAADF	High-Angle Annular Dark-Field
ICP-ES	Inductively-Coupled Plasma Emission Spectroscopy
LLTO	Lithium Lanthanum Titanium Oxide
LSV	Linear Sweep Voltammetry
MIEC	Mixed Ionic-Electronic Conducting
MSI	Metal-Support Interaction
NEMCA	Non-Faradaic Electrochemical Modification of Catalytic Activity

NP	Nanoparticle
PAW	Projector Augmented Wave
PBE	Perdew-Burke-Ernzerhof
p-EPOC	Permanent/Persistent EPOC
O.C.	Open-Circuit
RE	Reference Electrode
RF	Roughness Factor
RT	Room Temperature
RWGS	Reverse Water Gas Shift
SEI	Solid Electrolyte Interface
SEM	Scanning Electron Microscopy
SMSI	Strong Metal-Support Interaction
SSE	Solid-State Electrolyte
STEM	Scanning Transmission Electron Microscopy
TEM	Transmission Electron Microscopy
TMAOH	Tetramethylammonium Hydroxide
TPD	Three-Phase Boundary
TPR	Temperature-Programmed Reduction
VASP	Vienna Ab-initio Simulation Package
VB	Valence Band
WE	Working Electrode
XPS	X-Ray Photoelectron Spectroscopy
XRD	X-Ray Diffraction
YSZ	Yttria-Stabilized Zirconia

List of Symbols

C_{dl}	($\mu F\ cm^{-2}$)	Double layer capacitance
d	(nm)	Average particle size
E_a	($kJ\ mol^{-1}$)	Activation energy
F	($C\ mol^{-1}$)	Faradaic constant
I	(mA)	Current
i_0	($mA\ cm^{-2}$)	Exchange current density
n	(-)	Number of electrons transferred
N_G	(mol)	Uptake of reactive ionic species in moles
r	($mol\ s^{-1}\ g^{-1}$)	Closed-circuit catalytic rate
r_0	($mol\ s^{-1}\ g^{-1}$)	Open-circuit catalytic rate
S_{BET}	($m^2\ g^{-1}$)	Specific surface area
U_{WR}	(V)	Catalyst-working electrode potential

List of Greek Symbols

Λ	(-)	Apparent Faradaic efficiency
ρ	(-)	Rate enhancement ratio
τ	(s)	Time constant
Φ	(eV)	Work function

Chapter 1: Literature Review and Research Objectives

1.1 Rationale of CO_2 Utilization

Overuse of fossil fuels for power generation leads to huge amounts of greenhouse gases (GHG), including carbon dioxide (CO_2), methane (CH_4), nitrous oxide (N_2O), and ozone (O_3)[1], emitted into the atmosphere and causes severe climate change which has great influence on geography[2], energy use[3], agriculture[4], and human health[5]. CO_2, which makes up the most (two-thirds) of the total GHG emissions, has led to a significant global warming phenomenon in the last decades, radiating heat back to the Earth's surface and overall increasing global temperature[6]. The atmospheric CO_2 concentration has consequently risen from 280 ppm before the Industrial Revolution to 390 ppm in 2010[7]. In 2015, the Paris Climate Agreement was adopted globally to limit the rise in global temperatures to 1.5 °C by the end of the century through reduced CO_2 emissions[8]. However, as of July 2020, efforts seem inadequate with a record CO_2 concentration of 414 ppm[9]. Therefore, CO_2 is in urgent demand for removal to restrict its continuous negative impact on climates and environments.

There are three main strategies to address CO_2 emissions: reduction, sequestration, and utilization. The first strategy focuses on improving the energy efficiency of industrial processes and transitioning from fossil fuels to alternative energy sources such as hydrogen, batteries, wind, and solar power. Although renewable technologies are advancing, they currently cannot fully replace fossil fuel energy and are too dependent on weather, geographical location, and battery storage[10]. The second strategy involves developing technologies for capturing and storing CO_2. While this process is well-known, the challenge lies in securely storing the carbon in an inert location. A proposed solution is to store it in depleted fossil fuel reserves, but concerns still exist about the potential for earthquakes and other natural events to release the stored CO_2 into the atmosphere in high concentrations[11].

Thus, an ideal and safe approach for atmosphere decarbonization is through the CO_2 utilization, which not only reduces CO_2 emission but also recycles it into value-added chemicals in the form of synthetic fuels. Although CO_2 is recognized as a promising C_1 feedstock for the synthesis of organic compounds, materials, and carbohydrates because of its economic viability and safety[12], its application as a carbon source in both laboratories and industries remains minimal. The usage is restricted to the production of a limited range of products, such as urea and its derivatives, salicylic acid, and carbonates[13]. This is attributed to the thermodynamic stability of CO_2, necessitating the need for high-energy substances or electrochemical reduction processes to convert CO_2 into usable chemicals.

1.2 CO_2 Hydrogenation

Hydrogen (H_2), known for its high energy content, serves as an effective agent for CO_2 conversion[14], leading to the production of fuels and chemicals through CO_2 hydrogenation, where CO_2 is reacted with H_2. Given the increasing demand for fuels and the depletion of fossil fuel resources, alongside fluctuating fuel prices, there is an urgent need for alternative fuel sources. CO_2 hydrogenation products, including carbon monoxide (CO), methane (CH_4), methanol (CH_3OH), dimethyl ether (DME), and various hydrocarbons[15–18], present viable fuel options for a wide range of industrial processes and are conducive to easy storage and transport. Additionally, methanol and formic acid serve as essential feedstocks and intermediates in numerous chemical manufacturing processes[18,19]. Nonetheless, it is essential to address challenges arising from hydrogen production, storage, and transport. Potential sources for hydrogen, integral to CO_2 hydrogenation, may derive from the remaining fossil fuel reserves, predominantly natural gas, or from water splitting through electrolysis or other methods[20].

The end-products in CO_2 hydrogenation are selective by altering the reaction conditions like pressure, temperature, CO_2: H_2 ratio, and catalyst type[21]. The overall reaction for the synthesis of hydrocarbons can be represented by the Equation (1-1). It

should be noted that direct conversion of CO_2 into long-chain hydrocarbons of C_xH_y-C_xH_y (z=0) is difficult since multiple reactants and products exist simultaneously during the process, making it difficult to construct a catalyst that can build CH bonds with incoming CO_2 molecules, and is the least studied and characterized process[22].

$$xCO_2 + \left(2x - z + \frac{y}{2}\right) H_2 \rightarrow C_xH_yO_z + (2x - z)H_2O \quad (1\text{-}1)$$

However, C_1 products can be produced more easily. Normally, there are three typical reactions involved in CO_2 hydrogenation: Equation (1-2) is known as the reverse water gas shift (RWGS) reaction with CO as the main product, which is endothermic and thermodynamically favored at higher temperatures[22,23]. Equation (1-3) is methanation where CH_4 is produced and Equation (1-4) is the methanol synthesis, both of which are favored at lower temperatures due to the exothermic properties and accelerated at higher pressures affiliated to the decrease in the total moles of gas during the reactions[24].

$$CO_2 + H_2 \rightarrow CO + H_2O \ \Delta H = 42.1 \text{ kJ mol}^{-1} \quad (1\text{-}2)$$

$$CO_2 + 4H_2 \rightarrow CH_4 + 2H_2O \ \Delta H = -49.5 \text{ kJ mol}^{-1} \quad (1\text{-}3)$$

$$CO_2 + 3H_2 \rightarrow CH_3OH + H_2O \ \Delta H = -167 \text{ kJ mol}^{-1} \quad (1\text{-}4)$$

Because of the complexity of CO_2 hydrogenation and multiple competitive reactions happen at the same time, several chemicals are produced and the separation of these products can be very difficult and expensive. Therefore, understanding the reaction pathways of CO_2 hydrogenation is critical in practice. **Figure 1-1** shows an example of the reaction network, using the metal/oxide interface in determining the product selectivity to C_1 compounds: CO, CH_4, and CH_3OH. After the adsorption of CO_2 onto catalyst surface, the hydrogenation of $^*CO_2$ species mainly has three pathways: RWGS+CO-hydro, Direct C-O bond cleavage, and Formate. In RWGS+CO-hydro pathway, $^*CO_2$ turns into carboxyl ($^*HOCO$) intermediate firstly, which is then decomposed into $^*CO$ and $^*OH$. The $^*CO$ will partially desorb from the surface and release as CO gas, while $^*OH$ will interact with H^+ and form $^*H_2O$[25].

The $^{*}CO$ and $^{*}H_2O$ continue to be hydrogenated and produce CH_4/CH_3OH[26]. In Direct C-O bond cleavage pathway, the $^{*}CO_2$ species will dissociate into $^{*}CO$ and $^{*}O$ directly. The $^{*}CO$ is then further dissociated into $^{*}C$ and $^{*}O$ with the C-O bond broken and the resulting $^{*}C$ will be hydrogenated into CH_4 stepwise[27]. In Formate pathway, the $^{*}CO_2$ and H^{+} will form formate ($^{*}HCOO$) intermediate initially and then turn into $^{*}H_2COOH$, which is decomposed and produce CH_4/CH_3OH eventually[28].

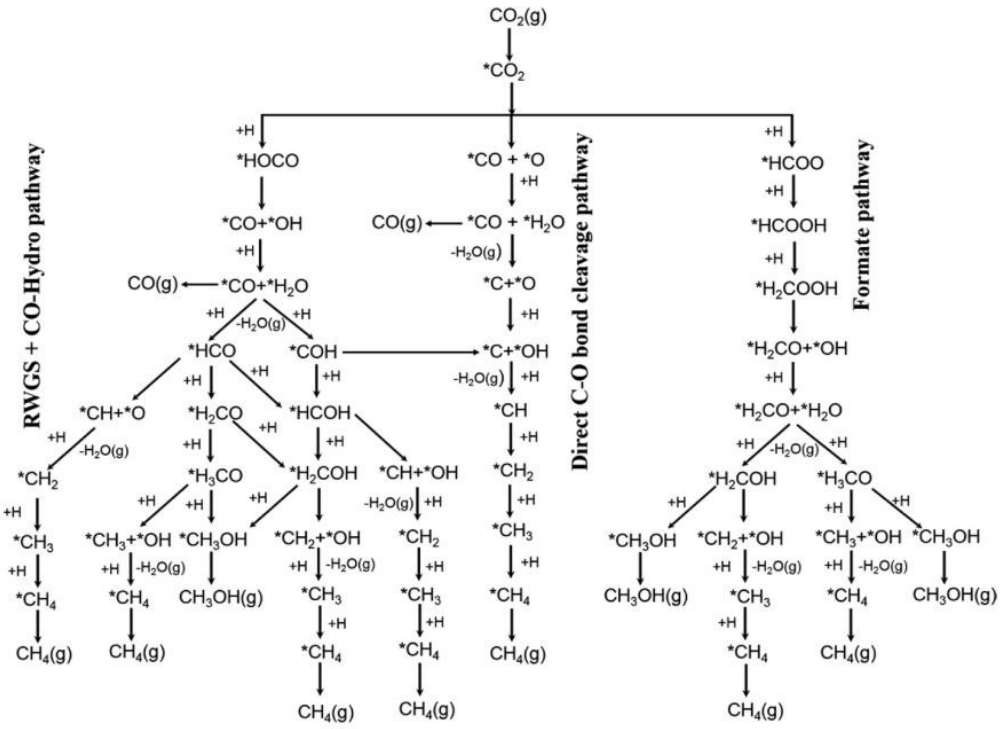

Figure 1-1. Reaction pathways of CO_2 hydrogenation to CO, CH_4, and CH_3OH. *(X) indicates adsorbed species. Reprinted with permission from [25]. Copyright ACS 2017.

1.2.1 Reverse water gas shift reaction

The RWGS process is gaining attention in industrial-scale production due to its role in generating CO, a crucial precursor for hydrocarbon synthesis through the Fischer-Tropsch (FT) process[29]. The FT process, described in Equation (1-5), is a well-known method developed during the industrial revolution to produce liquid fuels from syngas, a mixture of CO and H_2 typically derived from gasified coal or natural

gas[30]. However, the variation in the CO/H_2 ratio in syngas, depending on the sources used, often poses a challenge in obtaining a stable and significant amount of CO gas. Therefore, integrating RWGS with the FT process offers a feasible and effective method to produce methanol, formate acid, and alkanes from CO_2 and H_2 directly. In this approach, substantial amounts of CO are initially generated through RWGS with high selectivity, which are then further hydrogenated in the subsequent FT process. This combined process is also thermodynamically easier than RWGS because the overall process is exothermic and is very attractive[22]. More details about RWGS-FT will be discussed in Section 1.2.3.

$$nCO + (2n + 1)H_2 \rightarrow C_nH_{2n+2} + nH_2O \quad (1\text{-}5)$$

RWGS reaction can proceed via the *HOCO intermediate (**Figure 1-1**) or via the redox mechanism, where CO_2 oxidizes metal catalyst to generate CO and H_2 reduces metal catalyst back to form H_2O. Density functional theory (DFT) calculations show that CO_2 is activated and bound at the metal/oxide interface through a structure with the C atom of $^*CO_2$ bound to the metal site and one of the O atoms bound to the metal cations (M^+) of the oxide supports, like Al_2O_3, TiO_2, CeO_2, ZrO_2, In_2O_3, and ZnO, while the adsorption and dissociation of molecular H_2 preferably happens on the metal sites. The promotion in activity is determined by the adsorption strength with CO_2 at the metal/oxide interface and the binding capability of this interface for CO. The interface that adsorbs CO_2 strongly but binds CO weakly should be selective to RWGS reaction simply, because of facile dissociation of CO_2 and subsequent desorption of *CO. On the contrary, when *CO is strongly bound, its further hydrogenation or dissociation is more favorable than desorption. The reducibility of oxide support is also important since the presence of an O^{2-} vacancy provided additional sites for CO_2 adsorption.

1.2.2 Methanation

Methane is a notable fuel that can be utilized in both gaseous and liquid forms in internal combustion engines for the simultaneous generation of heat and energy[31].

Compared to other fossil fuels, the combustion of methane is relatively "cleaner" as it produces less CO_2[32]. The reaction for converting CO_2 to methane was discovered in 1902 by Paul Sabatier, a French chemist known for his work in catalytic hydrogenation processes[33]. Hence, CO_2 methanation is also referred to as the Sabatier reaction. From a thermodynamic standpoint, CO_2 methanation is more favorable at lower temperatures (< 400°C), often making it a competitive reaction with RWGS[34]. As the temperature rises, the RWGS reaction becomes more dominant, and the selectivity towards CH_4 decreases rapidly[33]. Although only low temperatures are required, the conversion of CO_2 to CH_4 still faces significant kinetic challenges due to the high thermostability of CO_2[35]. Therefore, the hydrogenation of CO_2 to methane requires the use of efficient catalysts to facilitate the reaction[36].

The reaction mechanism of CO_2 methanation appears to be difficult to establish. Normally, the CH_4 formation via CO_2 hydrogenation can occur in three possible pathways. In the direct C−O bond cleavage pathway, $^*CO_2$ dissociates into $^*O$ and $^*CO$, with the latter further dissociating into $^*C$ and subsequently being hydrogenated to CH_4[27]. Alternatively, $^*CO$ may be hydrogenated to $^*HCO$, which then dissociates to $^*CH$ and is further hydrogenated to CH_4[37]. In the RWGS+CO-hydro pathway, the C−O bond scission of $^*HCOH$, $^*H_2COH$ or $^*H_3CO$ results in the formation of CH_x species, which are then hydrogenated to form CH_4[38]. In the formate pathway, CH_4 formation happens via the C−O bond cleavage in H_2COH or H_3CO[39]. The main steps in CO_2 methanation closely resemble those in the formation of CH_3OH on a metal/oxide interface. The selectivity towards CH_4 or CH_3OH is likely influenced by the competition between the C−O bond scission in H_xCO species and their hydrogenation reactions. Therefore, to enhance the selectivity towards CH_4 rather than CH_3OH, the interfaces should be designed to strengthen the binding for H_xCO species, thereby promoting the C−O bond scission.

1.2.3 Methanol synthesis

Methanol is a clean, biodegradable, high-energy fuel that can also function as a starting material in chemical industry to produce a series of valuable

hydrocarbons[40,41]. Additionally, it is easier to store/transport as a hydrogen storage chemical and produces fewer carbon-containing side products[42]. Traditionally, methanol is produced on an industrial scale from syngas. However, the process often leads to the formation of numerous by-products due to the complex reactions and unstable composition of the syngas. Consequently, significant energy and costs are incurred in dealing with these by-products[43], which need to be separated from the methanol product before final use. Due to the integration of the RWGS and FT processes, CO_2 has emerged as an alternative feedstock for methanol synthesis, offering a practical approach[14]. By modifying the catalyst types and reaction conditions, excellent selectivity to CO via RWGS can be achieved. Subsequently, the produced CO, along with the feeding CO_2 and H_2, can be converted into methanol through the FT process with minimal by-products. Currently, this process achieves a methanol productivity of 75 Mt y^{-1}[22].

In **Figure 1-1**, it is illustrated that the production of CH_3OH involves various reaction intermediates and can proceed through multiple pathways. The preferred pathway is primarily determined by the catalyst's ability to bind with key reaction intermediates[25]. Therefore, identifying these active reaction intermediates is crucial for exploring the favorable routes. Two main reaction pathways have been proposed based on experimental and theoretical evidence[44]. The first pathway is the well-known RWGS+CO-hydro, while the second is the Formate pathway, which involves the C−O bond cleavage of the $*H_2COOH$ intermediate[25]. Among the materials studied, oxide-supported metals have shown promise as catalysts, as the metal/oxide interfaces have been found to play a critical role in controlling the activity and selectivity for CH_3OH synthesis[45,46]. In general, a catalyst that binds $^*CO$ strongly enough to facilitate its hydrogenation to formyl species ($^*HCO$), rather than allowing its desorption, is required in the RWGS+CO-hydro pathway. In contrast, for the Formate pathway, the binding of $^*HCOO$ should be adjusted to promote the hydrogenation of $^*CO_2$ to $^*HCOO$.

1.3 Metal Catalysts

Catalytic CO_2 hydrogenation processes generally occur on the metal catalyst surface, with the reaction bypassing the bulk of the material[47]. The use of nanostructured catalysts significantly increases the catalytic efficiency by maximizing the surface-to-volume ratio, ensuring that only the surface is active[48]. Moreover, nanostructured catalysts reduce the quantity of material needed while maintaining or even increasing the catalytic effectiveness. Typically, catalysts for CO_2 hydrogenation can be divided into homogeneous catalysts and heterogeneous catalysts, which have been explored to a great extent[47]. Homogeneous catalysts are characterized by their uniform active sites and excellent activity and selectivity[49]. However, they present challenges in terms of separation from the reaction mixture and reuse, which hinders their industrial applications and can lead to an increase in economic cost and environmental pollution in the case of metal-catalyzed synthesis[50]. In contrast, heterogeneous catalysts offer advantages in terms of ease of separation and recyclability, making them highly utilized in the field of hydrogenation[47]. A typical heterogeneous catalyst consists of metal/metal oxide immobilized on an oxide support.

1.3.1 Noble metals

For metal catalysts, there are normally two classifications based on their chemical properties and economic cost: noble metals and non-noble metals. Noble metals are regarded as metallic chemical elements that are generally resistant to oxidation and corrosion, including platinum (Pt), palladium (Pd), ruthenium (Ru), rhodium (Rh), iridium (Ir), and gold (Au)[51]. Moreover, given that precious metals and noble metals share many of the same elements, the terms are used interchangeably in most cases[52]. In CO_2 hydrogenation, Ru, Rh, and Pd are commonly used as the catalysts[53–55].

Ru is a Group VIII metal that shows excellent activity for CO_2 methanation despite using a low loading or at a low temperature. The ability of Ru to dissociate H_2 and bind CO positions it as the most active and stable material to produce CH_4[34]. It

was reported that Ru/Al_2O_3 achieved a CO_2 conversion of 85% at 375°C[56], while Ru/TiO_2 with exposed (001) facet exhibited a stronger CO_2 adsorption and led to a higher catalytic activity with a CO_2 conversion of 90% at 350°C[57], both of which showed excellent selectivity towards methanation rather than RWGS. Despite being a well-established process, recent efforts have been concentrated on exploring how alterations in the coordination of Ru on oxide surfaces can affect selectivity. A previous study on Ru/CeO_2 catalyst[58] demonstrated that redispersion of Ru occurred following treatment in an oxidizing atmosphere, resulting in the formation of single atoms at a low temperature of 210°C. These atoms remained isolated under reaction conditions due to their strong bond with the support. The redispersion altered the catalytic activity, shifting from a primarily methanation pathway to RWGS with a CO selectivity of approximately 90%. Another study on Ru/SiO_2 showed a 100% CO selectivity from 200 to 400°C without deactivation over a long time[59]. The catalyst configuration involved the encapsulation of Ru clusters into hollow SiO_2 shells, which prevented the sintering of Ru and avoided activity decreasing or preferential CH_4 formation.

Rh is also an active Group VIII metal for CO_2 hydrogenation due to its excellent ability to dissociate H_2 molecules. When supported on CeO_2, Rh/CeO_2 catalyst exhibited a high CO_2 conversion and CH_4 production with a low CO selectivity[60]. It was inferred that the CO species were strongly adsorbed on metallic Rh, which were further hydrogenated into CH_4 instead of being released as CO. However, when changing the support to TiO_2, RWGS reaction became the favored pathway and the isolated Rh near oxygen vacancy (O_V) was identified as the active site in Rh/TiO_2 catalyst[61]. The Rh-O_V sites favored a direct CO_2 dissociation into CO^* and O^* on the O_V. Concurrently, H_2 was adsorbed on the Rh and reacted with the O^* to form H_2O, while the CO^* was desorbed as CO.

Pd exhibits selectivity for both RWGS and methanation. Research on Pd/Al_2O_3 demonstrated that a catalyst with 5wt.% Pd and larger Pd particles featured a higher abundance of terrace sites[62]. This configuration facilitated the formation of

multi-bound CO^* and the adjacent binding of dissociated H, resulting in stronger CO interactions. These stable, multi-bound CO species acted as direct intermediates in the formation of CH_4. In contrast, 0.5wt.% Pd/Al_2O_3 catalyst, which had smaller Pd particles, was less effective at retaining CO^* formed from formate, thus showing higher selectivity towards CO production. Another study explored Pd/SiO_2 catalysts[63], which favored the production of both CO and CH_4. However, the introduction of a bimetallic $PdIn/SiO_2$ catalyst achieved an enhanced RWGS selectivity to 100%. In-situ spectroscopic analysis and density functional theory (DFT) calculations supported the findings that the preference for CO formation in the $PdIn/SiO_2$ system was due to the higher energy requirement for H_2 dissociation and the weaker adsorption of CO. These factors made the hydrogenation of CO to CH_4 less likely to occur.

1.3.2 Non-noble metals

In contrast to noble metals, non-noble metals like copper (Cu), iron (Fe), cobalt (Co), and nickel (Ni) are susceptible to oxidation but are more abundant on Earth, making them more economically viable as catalysts. When supported on oxides, these metals have been demonstrated to be effective in CO_2 hydrogenation, offering a cost-effective alternative for catalytic processes[64–66].

Cu is one of the most studied catalysts for the RWGS reaction because of its excellent selectivity, high activity and low price[67]. It has been demonstrated that the Cu catalyst is active in converting CO_2 into CO by following the redox mechanism during RWGS[68,69]. However, Cu is prone to sintering at high temperatures[70] and is easily oxidized into two main copper oxides: Cu_2O and CuO[71]. From temperature-programmed reduction (TPR) studies, the CuO_x are reduced in a temperature range of 200–500°C as $CuO \rightarrow Cu_2O \rightarrow Cu$[72]. This makes it easily deactivated when used as catalysts in RWGS, which is favored at high temperatures. Therefore, selecting suitable oxides is considered a practical method to improve its thermal stability and dispersion. In a previous study[73], Cu/Al_2O_3 catalyst was used in RWGS and the key intermediate was proposed to be the formate species from

association of H atoms and CO_2. At the same time, Cu_2O was also formed from the oxidation of Cu^0 by O^* due to CO_2 dissociation. Another study on Cu/ZrO_2[74] explained that the dissociation of CO_2 happened on Cu^0-ZrO_2 interface and was the rate determining step in RWGS. Moreover, research on Cu/CeO_2 catalyst unraveled that the existence of O_V in support oxide facilitated CO_2 adsorption and activation, which was derived from the Ce^{3+}-O_V-Cu^0 interface[75,76]. Cu/ZnO is a commonly used catalyst in methanol synthesis via Fischer-Tropsch process[77,78], where ZnO plays an important role in preventing sintering of Cu and removing catalyst poisons[79]. The Cu/ZnO interface was also reported as the critical factor in facilitating the CO_2 conversion process, where the initial step should primarily be the CO_2 dissociation and subsequent release of CO, referring to the RWGS pathway[80].

Fe, known for its abundance and cost-effectiveness, is commonly used as a catalyst in the Fischer-Tropsch process and the water-gas shift reaction[81]. Recent research, however, has shown that Fe-based catalysts also exhibit high efficiency and excellent selectivity for RWGS reaction[82,83]. According to DFT studies, Fe is noted for having a high CO_2 adsorption energy, resulting in CO_2 dissociation on the Fe surface into CO^* and O^*, where O^* diffuses into the bulk filling up an oxygen vacancy and is later reduced to form H_2O[84]. Investigations into Fe/Al_2O_3 catalyst demonstrated that RWGS over Fe catalyst followed redox mechanism, facilitated by the interactions with CO_2 and H_2[85]. Additional research on $Fe_2O_3/Ce_{0.5}Zr_{0.5}O_2$ revealed that the activity was attributed to the presence of various active states of Fe: Fe_2O_3, Fe_3O_4, FeO and Fe^0. These forms acted as oxygen storage and exchange reservoirs, cycling through redox reactions to facilitate catalytic processes[86]. Moreover, studies on CeO_2-supported Fe catalyst identified that the Fe phase could suppress the methanation reaction, which typically competed with RWGS at temperatures below 450°C, because FeO_x displayed a weak adsorption for CO, avoiding its further hydrogenation into CH_4[87].

Co is a promising transition metal for both CO_2 and CO hydrogenation. Similar to Fe, different CoO_x phases are formed during the reaction, some of which

are considered to be active for the RWGS[88]. Meanwhile, CO_2 dissociation follows a redox process, with the CoO_x is first reduced by H_2 and then re-oxidized by CO_2 to regain its lost oxygen, thereby producing CO. A previous study on Co/CeO_2 catalysts concluded that the reduction of Co^{3+} to Co^{2+} during RWGS resulted in the high catalytic activity[89]. Recent studies suggested that higher oxidation state of Co^{3+} was more active for the RWGS than Co^{2+} and Co^0[90]. Also, IR spectrometry confirmed a weaker adsorption of CO on the Co^{2+} phase as compared to the Co^{3+} phase[91]. Therefore, CO was desorbed easier from the surface, resulting in higher activity toward the RWGS. However, the presence of H_2 in the gas mixture led to a specific Co^{2+}/Co^{3+} ratio, which mainly depended on the reducibility of the support[92].

Ni is the most commonly used non-noble metal for CO_2 methanation. When supported on oxides like Al_2O_3[93], TiO_2[94], and MgO[95], Ni is maintained at a metallic state and achieves a CO_2 conversion of 80-90% and a CH_4 selectivity of 97-99%. However, the selectivity can be tuned by changing the valence state of Ni catalyst. This is attributed to the binding strength of the CO^* produced on the catalytic active sites and can be further correlated to the work function variation among the different NiO_x[96]. Specifically, the activation energy for further hydrogenation of CO^* to CH_4 increases as a function of the oxidation state of Ni, with NiO leading to a higher RWGS selectivity compared to Ni^0[97]. Like Cu, the main disadvantage of Ni is that it is prone to catalyst deactivation due to sintering of Ni particles, as evidenced in a study on Ni/Al_2O_3, and coke formation, as reported in work using Ni/TiO_2[34].

1.3.3 Metal-support interaction

The supports in heterogeneous catalysts not only enhance the dispersion of metal species but also prevent the sintering and aggregation of active phases. Additionally, some supports are not inert and their interactions with nanoparticles give rise to new interface phenomena, contributing additional active sites and inducing synergistic effects. Such metal-support interaction (MSI) may have a profound impact on the resulting catalytic performance of the metal catalysts[98].

Based on the chemical behavior, supports are divided into irreducible and

reducible oxides. Irreducible oxides, including SiO_2 and Al_2O_3, are difficult to lose O^{2-} due to the strong interaction with cations and are thereby considered to be inert as they only facilitate the dispersion of catalysts instead of participating in the reactions[99]. In contrast, oxides that function as O^{2-} promotors by exchanging O^{2-} with supported metals and show ionic conductivity are termed reducible oxides, including TiO_2, NiO, ZrO_2, and CeO_2[100]. Moreover, materials that exhibit both ionic and electrical conductivity are referred to as mixed ionic-electronic conductors (MIEC). These materials facilitate the migration of charged species (ions or electrons) internally, without the need for external electrical connections, making them highly useful as supports and solid-state electrolytes[101,102]. Examples of MIEC materials include samarium doped ceria (Sm-CeO_2 or SDC), beta-alumina (β''-Al_2O_3), and yttria-stabilized zirconia (YSZ). MSI plays an important role in modifying catalyst activities, making it one of the practical ways to optimize catalytic performance through various mechanisms[103]. Typical MSI phenomena involve charge transfer, interfacial perimeter, nanoparticle morphology, chemical composition, and strong metal-support interaction (SMSI). These phenomena are shown in **Figure 1-2** and are often entangled, with varying degrees of influence depending on the catalyst and reaction involved. Some may have a more pronounced effect than others.

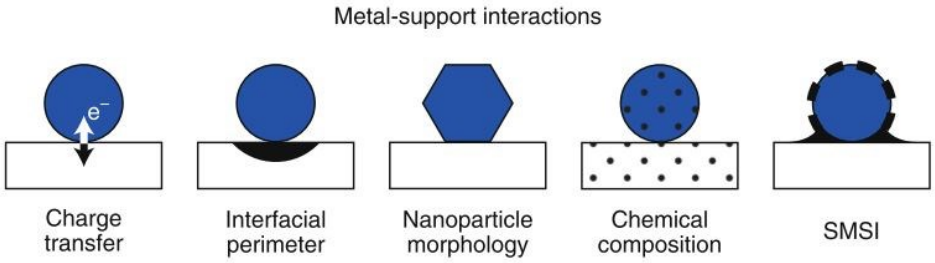

Figure 1-2. Schematic representation of main metal-support interactions and five main phenomena. Reprinted with permission from [98]. Copyright Nature 2019.

The interface between a metal nanoparticle (NP) and its support can lead to an electron rearrangement within both materials[104]. This redistribution of electrons, which usually impacts only a few atomic layers at the interface, may also result in

changes to the oxidation states of the metal atoms in the nanoparticle or the metal ions in the support[105]. Spillover can occur at the interfacial perimeter as well, starting with the activation of a reactant on one surface, typically the metal NP, which is then transferred to the other surface, such as the support[106,107]. Reverse spillover from the support to the metal NP is also possible. For instance, a previous study comparing the XPS spectra of Pt NPs on YSZ with that of Pt foil showed a significant shift in the Pt4f peak in Pt/YSZ (up to 0.9 eV) towards lower binding energy[108]. This shift indicated that charge transfer occurred from YSZ to Pt NPs, contributing to the observed MSI. The adhesion energy at the metal-support interface influences the morphology of the nanoparticles[109]. In general, supports with stronger adhesion result in particles with more faceted shapes. A solid-state reaction between the metal NPs and the support can lead to the formation of new phases, with species exchange occurring in both directions, often associated with a redox process involving oxidation or reduction at the interface[110]. However, the formation of inactive phases, such as mixed metal oxides, may happen and poison the active metal sites. Under high temperatures and reductive conditions, cations from the support can also migrate to the nanoparticle, facilitated by doping the support or using two-dimensional supports[111]. The strong metal-support interaction (SMSI) phenomenon refers to the coverage of metal NPs by suboxides from the support under reducing conditions[98,112]. This process is driven by the need to minimize the high surface energy of the metal NP through the mobility of suboxide species from the support. Reducible supports are essential for generating these suboxide species[113]. Although MSI can alter the properties and performance of catalysts through spontaneous charge redistribution and migration of promoting species[114], the unpredictability of these interactions poses challenges to precise measurement and control[102].

1.4 Electrochemical Promotion of Catalysis

Electrochemical promotion of catalysis (EPOC) or non-Faradaic electrochemical modification of catalytic activity (NEMCA) was first reported by

Stoukides and Vayenas at MIT in 1981[115]. It describes the phenomenon where a catalytic reaction rate alternation is observed upon an application of current or potential difference across the catalyst that is deposited on solid-state electrolyte supports and marks a significant advancement in the field of heterogeneous catalysts. **Figure 1-3a** shows an example of the EPOC phenomenon, where under an application of constant current at +1 μA, the reaction increases by 26 times without the need to alter other parameters[116]. **Figure 1-3b** shows a schematic structure of EPOC cell. The catalysts are deposited on one side of the solid-state electrolyte (SSE) and function as the working electrode (WE). On the other side of SSE, the counter electrode (CE) and reference electrode (RE) are prepared using gold. In this case, a current will flow between the WE and CE when applying a potential across the cell. The catalyst-WE potential with respect to RE is measured and represented as U_{WR} in EPOC studies[117].

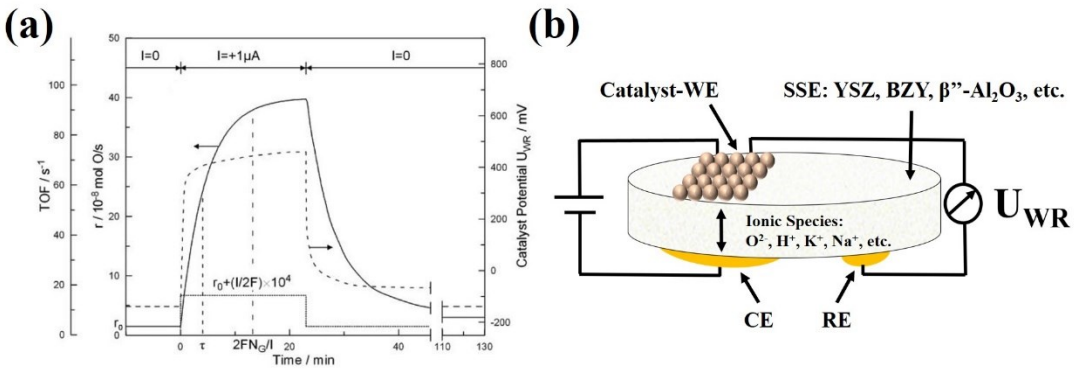

Figure 1-3. (a) EPOC phenomenon of Pt deposited on YSZ for C_2H_4 oxidation under an application of +1 μA. Reprinted with permission from [116]. Copyright Springer 2001. (b) The schematic structure of the EPOC cell.

The EPOC phenomenon is driven by the migration of promoting ionic species, which originate from the SSEs and vary depending on the types of the SSE. The normally used SSEs in EPOC include yttria-stabilized zirconia (YSZ, O^{2-} conductor), barium-doped zirconium (BZY, H^+ conductor), and β''-Al_2O_3 (K^+ or Na^+ conductor). Positive polarization ($U_{WR} > 0$), where a current flows from WE to CE, involves either the removal of electropositive ionic species (e.g. H^+, Na^+, and K^+) from the catalyst or

the supply of electronegative ionic species (e.g. O^{2-}) towards the catalyst[118], whereas the negative polarization ($U_{WR} < 0$) involves the reverse process. The spillover and backspillover of ionic species occurs at the catalyst-electrolyte-gas interface, also known as the three-phase boundary or tpb. These electrochemically created ionic species, accompanied by their compensating charges in the electrode, form an overall neutral double layer on the catalyst surface, as shown schematically in **Figure 1-4**. The presence of this effective double layer, whose density and field strength change with varying catalyst potential, affects the electronic properties (work function, Φ) of the catalyst surface and its chemisorptive properties subsequently, thus inducing pronounced and reversible alterations in catalytic rates and selectivity[102,119].

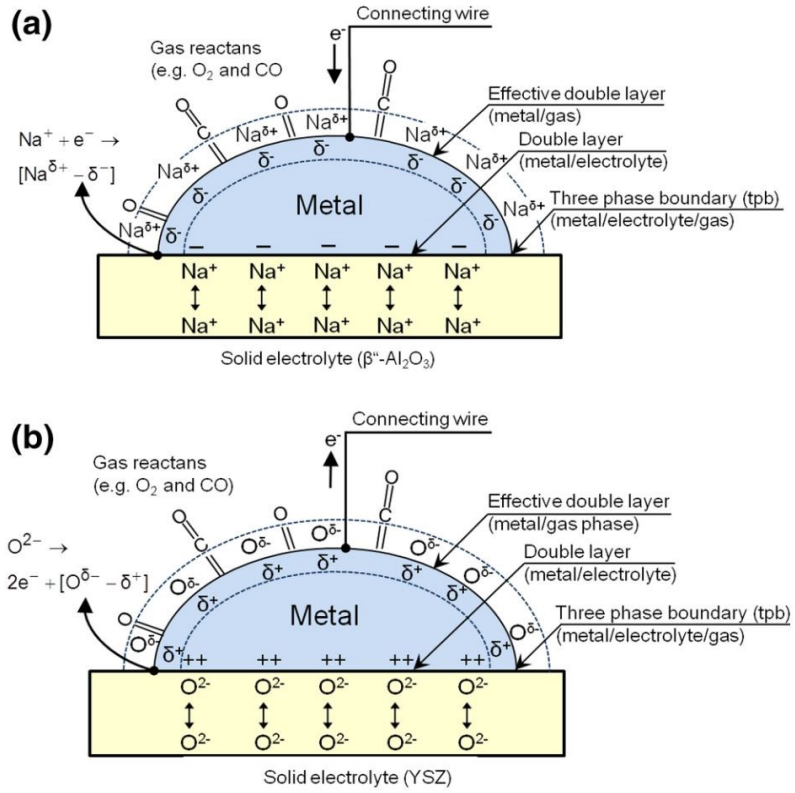

Figure 1-4. Schematic of metal electrode deposited on a Na^+ conductor (a) and on an O^{2-} conductor (b), showing the location of the effective neutral double layer created at the tpb. Reprinted with permission from [118]. Copyright Springer 2010.

The EPOC effect was characterized using the rate enhancement ratio (ρ) and

apparent Faradaic efficiency (Λ), which were calculated as Equation (1-6) and (1-7):

$$\rho = r/r_o \quad (1\text{-}6)$$

$$\Lambda = \frac{\Delta r}{I/nF} \quad (1\text{-}7)$$

Where r_0 is the open-circuit reaction rate and r is the steady-state rate after application of potential. Δr is the change in the reaction rate, I is the current response to the applied potential, n is the number of electrons transferred, and F is the Faradaic constant. The unit of r is mole per second per gram of metal catalyst (mol s^{-1} g^{-1}). The catalytic rate change is termed as EPOC effect when $|\Lambda| > 1$, which indicates a non-Faradaic enhancement[102,116] because the Δr is much higher than the migration rate of promoting ionic species (I/nF) at tpb upon polarization, meaning that each ion promoter supplied to the catalyst creates additional active sites and the Δr is not proportional to the applied polarization since it exceeds the steady-state rate increase expected from Faraday's law.

The functions of promoting ionic species in EPOC have been studied through direct observations via ex-situ XPS and in-situ cyclic voltammetry[120,121], or through indirect investigations via isotopic labeling studies[122,123]. For example, Tsampas et al.[122] conducted experiments to investigate the sacrificial promoter mechanism using Pt/YSZ for propane oxidation, aiming at in-situ distinguishing the O^{2-} derived from the SSE (promoting ionic oxygen) from those originating from the gas phase during EPOC. To achieve this goal, one compartment of the Pt/YSZ catalyst was exposed to propane and isotopic oxygen ($^{18}O_2$), while the other was supplied with air to replenish the electrolyte with standard oxygen ($^{16}O_2$). In this case, the reaction of promoting ionic species with propane would yield $C^{16}O_2$, whereas the combustion of propane with atmospheric oxygen would produce $C^{18}O_2$. EPOC effects under positive polarization, as shown in **Figure 1-5**, demonstrated that the oxidation of propane by gaseous oxygen was significantly enhanced by EPOC ($C^{18}O_2$ production) with the Λ observed up to 35. In contrast, the $C^{16}O_2$ production was only attributed to the Faradaic electrochemical oxidation of propane ($\Lambda \approx 1$). The formation of $C^{16}O^{18}O$

was attributed to surface oxygen exchange at tpb, which could also be electropromoted but to a lesser extent. These results indicated that the presence of promoting ionic species on the catalyst surface led to the generation of more reactive oxygen species, which either originated from the gas phase or transferred through the YSZ support, and was responsible for the non-Faradaic enhancement in the reaction rate.

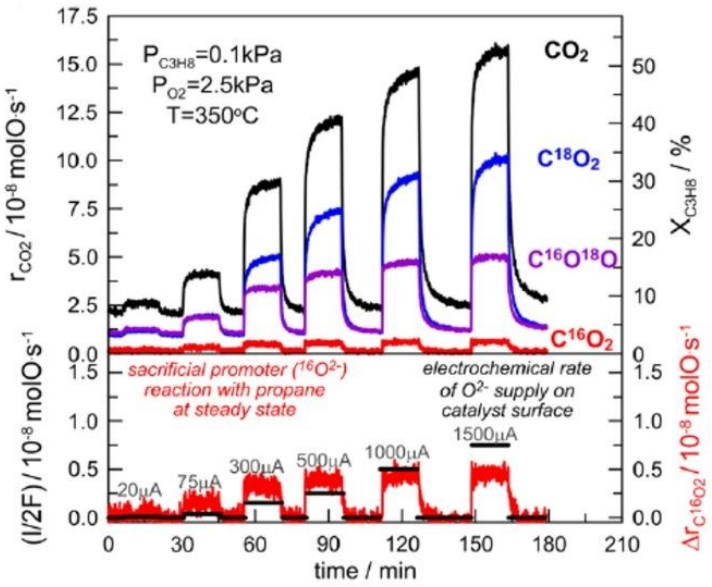

Figure 1-5. Catalytic rate responses to step changes of various applied positive currents during C_3H_8 oxidation on Pt/YSZ. Reprinted with permission from [122]. Copyright Elsevier 2012.

At a first glance, the phenomena of EPOC and MSI are similar because they both significantly influence the activity of metal/metal oxide catalysts due to the spillover and backspillover of promoting ionic species. However, these promotion phenomena could integrate three distinct mechanisms: classical promotion, where chemical species such as Na^+, K^+, Cl^-, etc., are added during synthesis; electrochemical promotion (EPOC); and self-driven spillover (MSI), as illustrated in **Figure 1-6**. The formation of the double layer at the metal/gas interface impacts the strength of chemisorptive bonds with reactants and intermediates, thereby affecting catalytic activity. As opposed to MSI, where promoters spontaneously migrate, a key

advantage of EPOC lies in the direct in-situ control of the promoter quantity on the catalyst surface. This control provides a method to modify catalytic rates in a predictable and manageable manner. As a result, EPOC is also referred to as an electrically controlled MSI[114] and MSI effect is also taken as a self-sustained electropromotion (SSEP)[124].

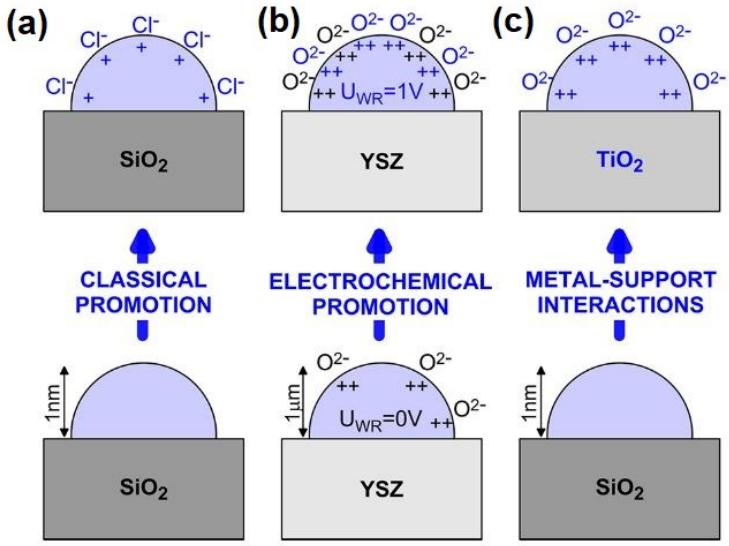

Figure 1-6. Schematic of the unpromoted and promoted states of metal-supported catalysts: (a) classical promotion (promoter added during synthesis), (b) EPOC (polarization-controlled O^{2-} backspillover), and (c) MSI (self-driven O^{2-} backspillover). Reprinted with permission from [102]. Copyright ACS 2013.

In 2001, a systematic and meticulous search of the electrochemical promotion literature[125] allowed Vayenas and coworkers to classify reactions into four types (electrophobic-, electrophilic-, volcano-, and inverted volcano-type reactions) based on the rate versus catalyst potential or work function behavior. This establishes simple and rigorous rules that offer a prediction of the electrochemical promotion behavior based on the reaction kinetics under unpromoted conditions or the chemisorptive bond strengths of the electron donor (D) and electron acceptor (A) reactants on the unpromoted catalyst. **Figure 1-7** summarizes the set of four electrochemical rules, which are discussed below:

Rule 1 (R1): The catalytic rate increases with potential, referred to as electrophobic behavior when it is positive order in the D species and zero or negative

order in the A species. Thus, species A is more strongly adsorbed on the surface than species D.

Rule 2 (R2): The catalytic rate decreases with potential, referred to as electrophilic behavior when the rate is positive order in A and zero or negative order in D. In this case, species D is more strongly adsorbed on the surface than species A.

Rule 3 (R3): The catalytic rate goes through a maximum, referred to as volcano-type behavior where the rate changes from a positive order in A and negative order in D to a negative order in A and a positive order in D. In this case, species A and D are strongly adsorbed on the surface.

Rule 4 (R4): The catalytic rate goes through a minimum, referred to as inverted volcano-type behavior when the kinetics are in positive order for A and D. In this case, species A and D are weakly adsorbed on the surface.

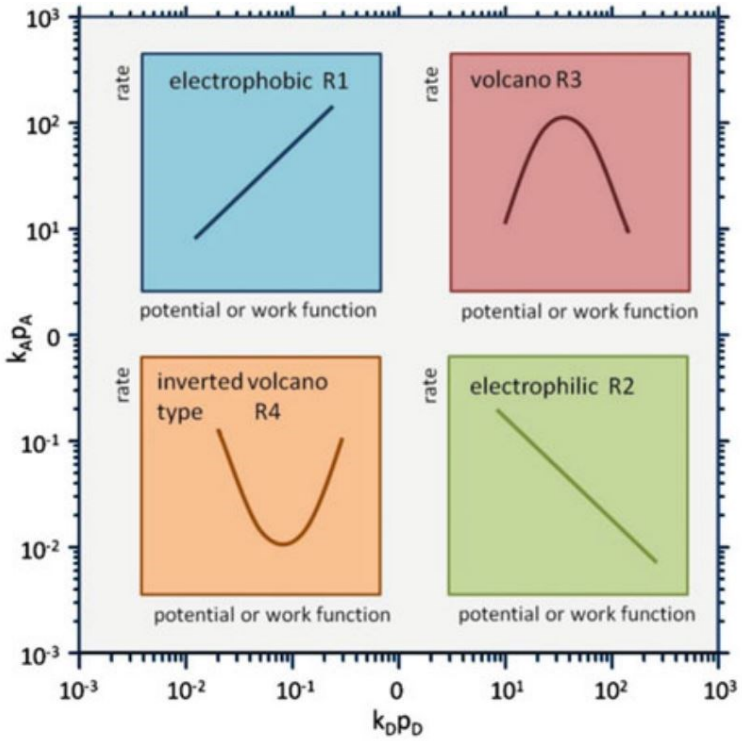

Figure 1-7. Rules of electrochemical behavior: (R1) electrophobic, (R2) electrophilic, (R3) volcano, and (R4) inverted volcano. Reprinted with permission from [125]. Copyright Elsevier 2014.

EPOC has been utilized in various reactions, such as CO_2 hydrogenation, CO oxidation, CH_4 oxidation, C_3H_8 oxidation, NO_x reduction, and H_2 production,

employing different catalytic systems. **Table 1-1** presents examples of EPOC studies for these reactions, highlighting the use of different ionic species as promoters. These studies involve transition metals like Fe, Co, Ni, Ru, Rh, Pd, Pt, and Ir, deposited on solid electrolytes such as YSZ, BZY, and β''-Al_2O_3, which can provide ionic species of O^{2-}, H^+, K^+, and Na^+. In EPOC, these four types of ionic species impact the catalytic reaction in distinct ways depending on the applied polarization, thus acting as promoters. The following sections will concentrate on EPOC studies related to CO_2 hydrogenation, specifically involving the RWGS reaction. Additionally, EPOC for oxidation reactions will be briefly discussed.

Table 1-1. Examples of EPOC studies for various reactions using different ionic species as the promoter.

Reaction	Catalyst	Solid Electrolyte	Ionic Species	Ref
CO_2 hydrogenation	FeO_x	YSZ	O^{2-}	[126]
CO_2 hydrogenation	CoO_x	YSZ	O^{2-}	[127]
CO_2 hydrogenation	NiO	YSZ	O^{2-}	[128]
CO_2 hydrogenation	Ru	YSZ	O^{2-}	[129]
CO_2 hydrogenation	Rh	YSZ	O^{2-}	[130]
CO_2 hydrogenation	Ru	BZY	H^+	[131]
CO_2 hydrogenation	CoO_x	BZY	H^+	[127]
CO_2 hydrogenation	Ru	β''-Al_2O_3	K^+	[132]
CO_2 hydrogenation	Pd	β''-Al_2O_3	Na^+	[133]
CO_2 hydrogenation	Pt	β''-Al_2O_3	Na^+	[134]
CO oxidation	Pt	β''-Al_2O_3	K^+	[135]
CO oxidation	Pt	β''-Al_2O_3	Na^+	[136]
CO oxidation	Pt	YSZ	O^{2-}	[137]
CH_4 oxidation	Pd	YSZ	O^{2-}	[138]
CH_4 oxidation	Pt	YSZ	O^{2-}	[139]
CH_4 oxidation	Rh	YSZ	O^{2-}	[140]
C_3H_8 oxidation	Ir	YSZ	O^{2-}	[141]
C_3H_8 oxidation	Ru	YSZ	O^{2-}	[141]
C_3H_8 oxidation	Pt	YSZ	O^{2-}	[142]
NO_x reduction	Pt	YSZ	O^{2-}	[143]
NO_x reduction	Rh	YSZ	O^{2-}	[144]
NO_x reduction	Pt	β''-Al_2O_3	K^+	[145]
H_2 production	Pt	β''-Al_2O_3	K^+	[146]
H_2 production	Pt	YSZ	O^{2-}	[147]

1.4.1 EPOC for CO_2 hydrogenation

Investigations on the EPOC for CO_2 hydrogenation have been conducted with various noble metal catalysts supported on different solid electrolytes. Bebelis et al.[133] first reported EPOC for RWGS over Pd/YSZ and Pd/Na-β″-Al_2O_3. CO formation rate was enhanced by approximately 6 times under either negative or positive polarization (inverted volcano behavior), due to the migration of ionic species towards or from the Pd catalyst. Negative polarization resulted in the decrease of the catalyst work function and favored the transfer of electrons from Pd to electron acceptor molecules like CO_2, which favored the adsorption of CO_2 and subsequent release of CO. Positive polarization resulted in increase of the Pd work function, thus increased the coverage of adsorbed H_2, which here behaved as an electron donor and favored the CO_2 hydrogenation.

Bebelis et al.[148] also reported EPOC for CO_2 hydrogenation over Rh/YSZ, which showed selectivity to both CO and CH_4. The CH_4 formation rate increased by 2.7 times under positive polarization (electrophobic behavior) while the CO formation rate increased by 1.7 times under negative polarization (electrophilic behavior). Hydrogen, demonstrating electron donor characteristics, exhibited increased interaction with the Rh surface under positive polarization, thereby preferentially facilitating the formation of rhodium carbonyl hydride species over rhodium carbonyl species. Consequently, this led to an enhanced rate of methanation and a reduced rate of CO production.

Ruiz et al.[134] studied EPOC of CO_2 hydrogenation over Pt/K-β″-Al_2O_3. The CH_4 production rate decreased (electrophobic behavior) and CO production rate increased (electrophilic behavior) under negative polarization at -1.5V, which was attributed to potassium ion (K^+) pumping to Pt catalyst. The K^+ migration led to a decrease of the catalyst work function, which favoured the transfer of electrons from Pt to electron acceptor molecules, like CO_2. This improved the dissociative adsorption of CO_2 and subsequent desorption of CO species, whereas H_2 dissociative adsorption and subsequent CH_4 formation were hindered accordingly.

Theleritis et al.[149] studied EPOC of CO_2 hydrogenation over Ru/YSZ, which showed that positive polarization resulted in increased methanation rate (electrophobic behavior) and decreased RWGS rate (electrophilic behavior). It was concluded that the formation of effective neutral double layer ($O^{\delta-}$ - $Ru^{\delta-}$) under positive polarization favoured the adsorption strength of H_2 due to the generation of OH bonds, which subsequently facilitated the hydrogenation of CO_2 into CH_4 and inhibited the production of CO.

Kalaitzidou et al.[132,150] and Makri et al.[151] compared the influence of different SSEs, including YSZ, BZY, and β″-Al_2O_3, on the EPOC effect of CO_2 hydrogenation over Ru catalyst. For YSZ and BZY, it exhibited similar results and summarized that positive polarization involved O^{2-} supply to, or H^+ removal from the Ru catalyst, leading to enhanced methanation and suppressed CO production. It also revealed that YSZ was regenerated by directly supplying the SSE with O^{2-} through the dissociation of CO_2, while BZY was regenerated by H^+ as a result of H_2 dissociation. On the contrary, for Na^+ and K^+ conducting SSEs, the EPOC for RWGS showed an electrophilic behavior, while the methanation rate exhibited a maximum with increasing the applied potential (volcano behavior). The addition of Na^+ and K^+ showed strengthening the CO_2 binding and in turn decreased the activation energy required to cleave an oxygen molecule. This resulted in decreasing the work function of Ru catalyst and thus improving the desorption of CO molecules. However, Na^+ and K^+ failed to be regenerated in-situ since they were added in the β''-Al_2O_3 initially. When the ions were consumed as sacrificial promoters over time, the electrochemical cell would short-circuit and promotion also ended.

For non-noble metal oxide catalysts, iron oxide (FeO_x), cobalt oxide (CoO_x), and nickel oxide (NiO) showed excellent selectivity towards RWGS, where no methane was produced in the temperature range of 200-400℃. The EPOC study over FeO_x catalyst deposited on YSZ was done by Panaritis et al.[152] and demonstrated that the RWGS rate was enhanced under both positive and negative polarization (inverted volcano behavior) by controlling the oxidation states of FeO_x nanowires,

which experienced redox processes during polarization. From open-circuit catalytic activity investigations, it revealed that the RWGS rates of FeO_x followed the sequence of Fe_3O_4 > FeO > Fe^0, while fully oxidized Fe_2O_3 and Fe_3C were found to inhibit the reaction. Therefore, the in-situ modification of Fe catalyst states resulted in changes in reaction rates. According to characterizations like XPS and cyclic voltammetry (CV), it was indicated that the electrochemical migration of oxygen ion (O^{2-}) conducted from the YSZ solid electrolyte was responsible for the oxidation state changes. This study also revealed significant rate increases upon both starting the polarization and interrupting the polarization, as shown in **Figure 1-8a**. The initial increase was affiliated with the carbon formed during reaction conditions and the second increase after polarization was associated with the reduction of oxygen reservoir of FeO_x formed during polarization. This was also the first time observing oxidation state changes of non-noble metal catalysts during EPOC and thereby offering novel insights into the EPOC mechanisms.

The EPOC study over CoO_x NPs deposited on YSZ was explored by Zagoraios et al.[153], which also revealed alterations in the oxidation states of CoO_x during polarization. Similarly, the reaction rate showed two increasing peaks upon and post polarization, as shown in **Figure 1-8b**, which dropped afterwards and became stable at suppressed state, as compared to the initial rate. The rate suppression under positive polarization (electrophilic behavior) was related to the O^{2-} supply and their interaction with the CoO_x catalyst surface. It was demonstrated that the initial state of Co^0 was oxidized into Co^{2+}, which was a more active phase for RWGS and led to the first peak. Continuing the polarization, the Co^{2+} state was further oxidized into Co_3O_4, which was less active and responsible for the later rate suppression. When polarization was stopped, the Co_3O_4 was reduced back to Co^0 stepwise and the reaction rate underwent reverse process, first increasing (to Co^{2+}) and then decreasing (to Co^0). Exploration of CoO_x NPs further indicated the electrochemical-induced redox processes of metal catalysts, which possessed multiple oxidation states and contributed differently to RWGS reaction.

EPOC study over NiO NPs deposited on YSZ was also done by Zagoraios et al.[128] and illustrated the redox transformation between Ni and NiO under polarization. The RWGS rate was promoted by 40% under positive polarization (electrophobic behavior), as NiO was electrochemically formed at tpb in this case. Therefore, EPOC provided a controllable way to modify reaction rate by in situ altering the oxidation states of transition metal catalysts.

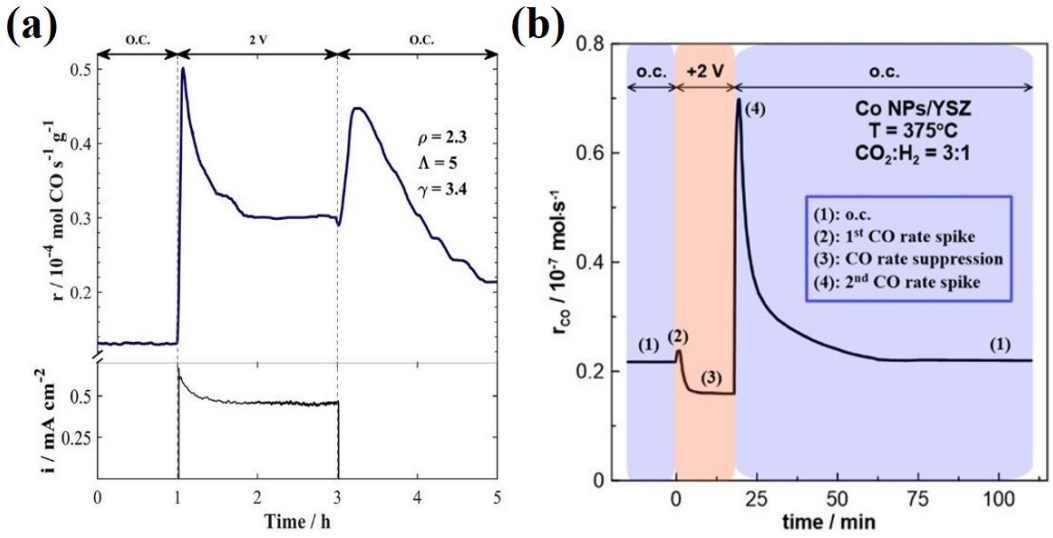

Figure 1-8. EPOC for RWGS over (a) FeO_x nanowires. Reprinted with permission from [152]. Copyright Elsevier 2020. (b) Co NPs deposited on YSZ. Reprinted with permission from [153]. Copyright ACS 2020.

To further modify electrocatalytic performance of metal catalysts, combining MSI with EPOC was also studied by supporting metals onto another metal oxide before being deposited on SSEs. In former research on EPOC over Ru and Ru/Co_3O_4 (deposited on BZY), Zagoraios et al.[154] revealed typical electrophobic behavior in methanation and electrophilic behavior in CO production. However, when further supporting Ru on Co_3O_4 (still deposited on BZY), the catalyst displayed a superior catalytic activity mostly due to spontaneous spillover of O^{2-} from Co_3O_4 to Ru, and the EPOC effect only happened to RWGS reaction rather than methanation, with the same behaviors as compared to Ru on its own. In another research, Panaritis et al.[155] studied EPOC over FeO_x supported on Co_3O_4 (deposited on YSZ), which displayed a high selectivity to CO (>99%). Unlike FeO_x on its own, under both positive and

negative polarization, the CO rate decreased (volcano behavior) by over 10% due to the in-situ change in the oxidation state of Co_3O_4 during polarization, thus affecting the MSI effect between FeO_x and Co_3O_4. These investigations provided innovative insights into EPOC mechanism over catalysts with multiple phases for CO_2 hydrogenation, where the interaction between metals and metal oxide supports played an important role and contributed to the alternations in EPOC behaviors.

1.4.2 EPOC for CO oxidation and hydrocarbon oxidation

EPOC has also been widely studied for CO oxidation and hydrocarbon (especially ethylene and methane) oxidation over noble metal catalysts to accelerate energy conversion. Yentekakis and Vayenas[156] revealed that the intrinsic rate of CO oxidation on polycrystalline Pt supported on YSZ was altered significantly by means of electrochemical O^{2-} pumping to or from the catalyst surface. The CO_2 production rate increased under positive polarization, while decreased under negative polarization (electrophilic behavior). Yentekakis et al.[136] also reported EPOC for CO oxidation over polycrystalline Pt films on Na-β''-Al_2O_3 and demonstrated that the use of the β''-Al_2O_3 enabled precise in situ control of Na^+ coverage on the Pt surface. Increasing Na^+ coverage under negative polarization caused 600% promotion in the CO_2 production rate (electrophilic behavior), which was due to enhanced oxygen chemisorption on the Pt surface. Similarly, Lucas-Consuegra et al.[135] studied the influence of K-β''-Al_2O_3 on EPOC effect over Pt and revealed electrophilic behavior for CO oxidation, where CO_2 rate increased by 11 times under negative polarization. This was due to the formation of potassium compounds on the Pt surface that enhanced the adsorption of O_2.

Comninellis et al.[157] first studied EPOC for ethylene oxidation over IrO_2/YSZ, which exhibited an increased reaction rate under positive polarization (electrophobic behavior) due to the supply of O^{2-} to catalyst from YSZ. Toghan et al.[158] used Pt/YSZ as the catalyst and also revealed an increase in ethylene oxidation rate under positive polarization (electrophobic behavior), which was due to the transition of Pt surface from an inactive carbon poisoned state to an active state.

Ibrahim et al.[159] studied the influence of Na^+ on Pt catalyst deposited on YSZ for ethylene oxidation, whose presence affected the EPOC behavior significantly. Under polarization, the reaction showed electrophilic behavior at low Na^+ coverage (0.11%), electrophobic behavior at high Na^+ coverage (65%), and volcano-type behavior at intermediate Na^+ coverage. This was because the increasing Na^+ coverage made its interaction with oxygen more significant and subsequently enhanced the reaction rate, changing electrophilic behavior gradually into electrophobic one. Hajar et al.[160] reported EPOC for ethylene oxidation over RuO_2/YSZ, which showed rate increase under both positive and negative polarization (inverted volcano behavior). Positive polarization increased the work function, leading to improved adsorption and facilitated cleavage of the C–C bond in ethylene. Conversely, negative polarization facilitated oxygen activation.

Roche et al.[161] studied EPOC for methane deep oxidation over Pd/YSZ and found that the catalytic activity could be in situ increased by applying a positive polarization (electrophobic behavior) thus supplying oxygen ions to the catalyst surface. The electrochemically migrated O^{2-} enhanced the thermal stability of the oxide and resulted in the transition between PdO and Pd phases under polarization. Similar studies and results were also performed and concluded by Matei et al. [162], Kalaitzidou et al.[163] and Hajar et al[164]. Moreover, Hajar et al.[165] synthesized and used bimetallic Ni_9Pd core-shell NPs as the catalyst for complete methane oxidation, which showed an improved open-circuit activity compared to bare Pd catalyst and an electrophobic EPOC behavior under polarization. It was demonstrated that electronic interaction between Pd and Ni was responsible for the modified electrocatalytic performance, providing a practical advancement of EPOC by lowering the noble metal content. Zagoraios et al.[138] introduced MSI by using Pd/Co_3O_4 catalyst (deposited on YSZ) in EPOC for methane oxidation. The CO_2 formation rate increased under positive polarization (electrophobic behavior) and the Pd/Co_3O_4 reached a faster promotional state, mainly due to the presence of Co_3O_4, which behaved as a “bridge” to allow for the O^{2-} promoter to reach the Pd NPs more

easily. Nakos et al.[140] used Rh/YSZ in EPOC for methane oxidation, whose catalytic rate was increased under positive polarization and decreased under negative polarization (electrophobic behavior). The enhanced CO_2 formation rate was attributed to the weakening of Rh–O bond strength, caused by the decrease of the coverage of oxygen of the catalytic surface because of the increase of the catalyst work function.

1.4.3 Permanent EPOC

"Permanent EPOC (p-EPOC)" effect was first discovered by Comninellis and co-workers[157], who studied the EPOC transient for C_2H_4 oxidation on IrO_2/YSZ. It was found that upon current interruption, neither the rate nor Φ returned to their initial open-circuit values, meaning a permanent rate enhancement accompanied by a permanent change in Φ. The remaining high activity was attributed to the formation of $IrO_{2+\delta}$ at the IrO_2/YSZ interface during current application, whose catalytic activity for ethylene combustion was thought to be higher than on IrO_2. Based on this, another study by Comninellis et al.[166] on Pt/YSZ catalysts provided strong support for a proposed hypothesis that p-EPOC was due to the storage of promoting $O^{\delta-}$ species at the catalyst-electrolyte interface during polarization.

Similar p-EPOC phenomena were also noticed by Stavrakakis and Poulidi[167] in studies for CO oxidation over Na-promoted Pt/YSZ. The storage of $O^{\delta-}$ promoting species at the catalyst-YSZ interface occurred under oxidizing conditions and resulted in formation of sodium oxides, which was responsible for the permanent enhanced reaction rate after polarization. Moreover, in EPOC studies for CH_4 oxidation, PdO layer formation at Pd/YSZ interface[161,163,168] and RhO layer formation at Rh/YSZ interface[140] under polarization were also confirmed and considered as the reason for p-EPOC effect. It was also found that the p-EPOC state ceased to exist a few hours after the polarization interruption, as shown in **Figure 1-9a**. This process occurred as a result of the depletion of all stored $O^{\delta-}$ species, leading to the restoration of the catalytic rate to its original level. Therefore, this phenomenon was more persistent than permanent.

However, research conducted by Souentie et al.[142] revealed that, C_3H_8 oxidation over thin sputtered Pt/YSZ showed long-term p-EPOC effect after polarization, as shown in **Figure 1-9b**. It was demonstrated that a thermodynamically stable PtO_x species was formed at the Pt/YSZ interface, which did not interact with the reactive gas mixture. In this case, the removal of p-EPOC was achievable only through the application of negative polarization, which led to the decomposition of the PtO_x species.

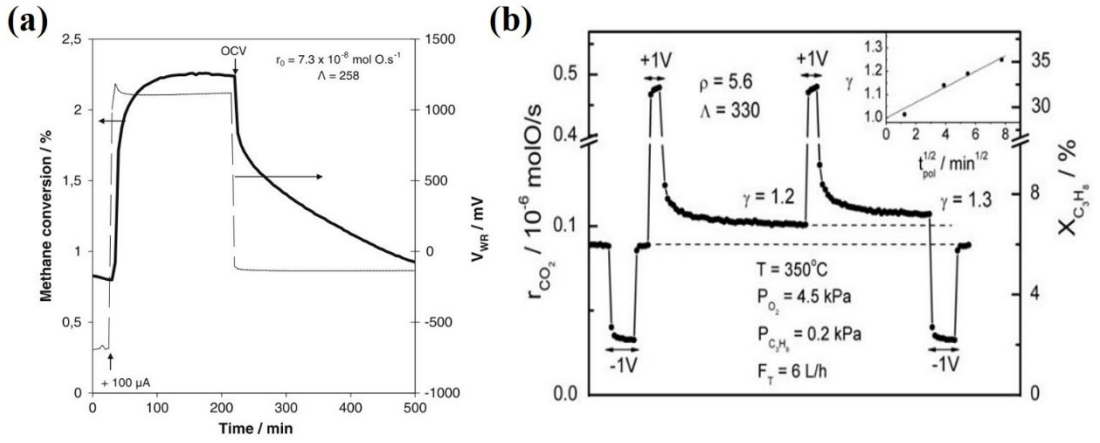

Figure 1-9. (a) Persistent p-EPOC effect over Pd/YSZ for CH_4 oxidation. Reprinted with permission from [161]. Copyright Springer 2008. (b) Long-term p-EPOC effect over Pt/YSZ for C_3H_8 oxidation. Reprinted with permission from [142]. Copyright Elsevier 2010.

The p-EPOC also occurred to FeO_x deposited on YSZ, as shown in **Figure 1-8a**. It was demonstrated due to oxygen promoter storage in the form of iron oxide during polarization. Upon current interruption, the stored O^{2-} became available as reaction promoters since the electrochemically formed iron oxide, which was induced by applied polarization, was no longer stable. This led to continuous promotion of the RWGS reaction until all the stored O^{2-} was depleted. The return of the promoted reaction rate to its initial open circuit conditions was dependent on the time of polarization. Considering its impact on improving catalytic performance, the p-EPOC was believed to be one of the most interesting and potentially important phenomena from a practical viewpoint aspect of electrochemical promotion.

1.4.4 DFT study in EPOC

Density Functional Theory (DFT) is a quantum mechanical approach used to understand and predict the electronic structure of atoms, molecules, and solids at the atomic and molecular levels. It provides a way to solve the Schrödinger equation approximately for complex systems with many electrons, which is otherwise intractable due to the electron-electron interaction term in the Hamiltonian. It originated from the work of Thomas and Fermi in the 1920s and was further developed by Hohenberg and Kohn in 1964, who proved that the ground-state properties of a many-electron system could be determined uniquely by its electron density. The use of approximations in DFT is necessary because the exact form of the exchange-correlation functional, which accounts for the complex interactions between electrons, is unknown. Two common approximations: Local Density Approximation (LDA) and the Generalized Gradient Approximation (GGA) have been extensively used in DFT studies. Despite the wide application of DFT in many other areas, it has been rarely studied in EPOC research.

For the first time, Hajar et al.[160] used DFT calculations to rationalize the experimental results for EPOC of ethylene oxidation on RuO_2 (110) surface, considering the influence of applied polarization. The experimental results showed reaction rate enhancements under both positive and negative polarization. From DFT results, C_2H_4 was revealed to preferably adsorbed on the O atoms and upon applying a positive polarization, the adsorption of C_2H_4 was favored (adsorption energy dropped from -3 eV to -4.75 eV) and the activation energy of the C–C bond dissociation was decreased (from -0.5 eV to -1 eV). Under negative polarization, however, the O_2 adsorption on the RuO_2 surface was favored (adsorption energy dropped from -1.5 eV to -3 eV) and the activation energy of the O–O dissociation was decreased accordingly (from -0.7 eV to -1 eV). As a result, the facilitation of the C–C bond dissociation under positive polarization and of the O–O bond dissociation under negative polarization explained the observed inverted volcano behavior.

Another research done by Panaritis et al.[129] utilized DFT model in EPOC

study of CO_2 hydrogenation over Ru/YSZ, where CH_4 production decreased and CO rate increased under negative polarization. DFT computations uncovered that electric field effects together with a change in surface electrochemical potential between intermediates were responsible for the contrasting influence of EPOC on the CH_4 and CO formation. Specifically, the influence of polarization on CO/CH_4 selectivity was illustrated by the branching from CO^* to CO and CHO^*. Under negative polarization, the preference for CO desorption increased due to destabilization of the CHO intermediate in this case, explaining the increase in CO production. On the contrary, positive polarization slightly favored the hydrogenation of CO^* into CHO^*, thus facilitating CH_4 production accordingly.

However, the mechanism of ion migration and its impact on the oxidation state changes of the supported metal catalysts remained unclear. Considering the rapid electrochemical reactions that happened on the catalyst surface in EPOC, DFT calculation is taken as a promising and alternative way to simulate and evaluate the transportation of ionic species from oxide supports toward metal catalysts.

1.5 Motivation and Research Objectives

Based on the literature review, it is found that EPOC for RWGS using noble metals like Pd, Ru, and Rh shows excellent catalytic performance but is high in cost. In contrast, non-noble metal oxide catalysts such as FeO_x, CoO_x, and NiO exhibit limited open-circuit activities and unstable EPOC effects. Additionally, current solid electrolytes like YSZ, BZY, and β''-Al_2O_3 have limited electrical and ionic conductivities at lower temperatures, restricting broader EPOC applications. Motivated by these research gaps, the overall objective of this research is to explore and study novel non-noble metal catalysts and solid electrolytes for the RWGS reaction using EPOC and MSI phenomena. For the first time, to study the Cu-based catalysts and their potential mechanisms in EPOC, and to study the effect of lithium ion (Li^+) promoter using lithium lanthanum titanate (LLTO) solid electrolyte on the catalytic activity and stability of metal oxide catalysts under MSI and EPOC

conditions.

The following objectives have been executed:

- Develop low cost, active, and stable Cu-based nanostructured catalysts.
- Determine the influence of the MSI effect and the EPOC phenomenon on the performance of Cu-based catalysts under reaction conditions.
- Understand EPOC mechanisms through comprehensive electrochemical and physicochemical characterizations.
- Use DFT to simulate the migration of ionic species and their impact on Cu-based catalysts under EPOC conditions.
- Establish the relationship between electrochemical active surface areas (ECSA) and EPOC magnitudes to inform future catalyst development.
- Implement LLTO as solid electrolyte and Li^+ as promoter for the RWGS reaction and CO oxidation, initiating its application in the EPOC field.
- Investigate the migration of Li^+ and its interactions with metal/metal oxide catalysts, and how these interactions influence catalytic reactions.

1.6 Thesis Structure

Based on the research objectives, this thesis is prepared in the following structure:

Chapter 1 discusses the literature review of the importance of utilizing CO_2, the CO_2 hydrogenation processes and mechanisms, catalysts including noble metals and non-noble metals to facilitate the reactions, MSI that involves spontaneous spillover of ions and promotion in catalytic performance, and EPOC phenomena that enable in situ control of ionic species and reaction rate with both noble metals and non-noble metals, as well as p-EPOC effect and theoretical DFT calculations.

Chapter 2 presents the methodologies used to synthesize nanostructured metal catalysts and assemble EPOC cells, along with a diagram of the experimental setup. It then describes the preparation steps for the experiments, including pre-treatment processes, catalytic reaction conditions, and electrochemical testings, which provide a

clear and fundamental overview. The chapter also includes a detailed explanation of the physicochemical and electrochemical characterizations conducted in this thesis.

Chapter 3 proposes to use Cu as the novel non-noble metal catalyst and explores the preparation of Cu NPs in the polyol synthesis method and its application in EPOC for RWGS. The EPOC mechanism was demonstrated to be the electrooxidation of Cu by O^{2-} from YSZ solid electrolyte. Due to the limited catalytic activity of Cu NPs and its drawbacks of being easily sintered and deactivated, it is necessary for the following study to employ the combination of Cu NPs and metal oxide supports to improve the catalyst morphology, properties, and EPOC phenomenon.

Chapter 4 studies the Cu/Co_3O_4 catalysts with different Cu loadings considering that Co_3O_4 is also a non-noble metal oxide with a huge oxygen storage capacity, which is considered beneficial for O^{2-} migration. Despite a huge change in EPOC behaviors due to interactions between Cu and Co_3O_4 and the improvement in the sintering of Cu NPs, the highly reactive Co_3O_4 shows to be unstable because of the existence of multiple oxidation states of cobalt, making the investigations on the interactions between Cu and Co_3O_4 complicated. This induces the need for using a simple, stable, and still non-noble metal oxide as the support for Cu NPs to study the influence of oxide support on the EPOC of Cu-based catalysts in the following study.

Chapter 5 starts with the synthesis of nanostructured ZnO and uses it as the support for Cu NPs with various loadings. The simple and stable structure of ZnO makes it a suitable support, which not only effectively prevents sintering and oxidation of Cu NPs, but also improves the catalytic activities by forming MSI. EPOC effects illustrate that the oxidation of metallic Cu into Cu_2O under polarization is responsible for rate enhancement. To provide insight into the origin of the O^{2-} migration, theoretical DFT calculations are performed and explain how the lattice O^{2-} in ZnO is driven to move towards Cu NPs under polarization and form Cu_2O. ECSA is also found to correlate with the EPOC effect, which is due to the oxygen vacancy of ZnO and betters the understanding of MSI influence on EPOC.

Chapter 6 innovatively uses LLTO as the solid electrolyte, aiming at using Li^+ as promoter and exploring EPOC over non-noble metal catalysts at low temperatures. FeO_x and Pt are used as comparative catalysts for both RWGS reaction and CO oxidation. The superior open-circuit activity of Fe/LLTO over Fe/YSZ is due to the MSI. The distinct EPOC behaviors in different systems reveal the unique interactions between migrated Li^+ and FeO_x. For the first time, Li^+ functions as promoter in EPOC and influences the catalytic reaction rates. This pioneering work demonstrates the promising potential of LLTO in EPOC studies, broadening its application in reactions that are favored at low temperatures.

In the end, the conclusions of this thesis work are summarized and recommendations for future development in EPOC studies are proposed, followed by contributions made to the EPOC research field in the past 4 years in the form of a list of publications and conference meetings.

The objectives of the research are achieved through the progression of Chapters 3-6, following the procedures: The open-circuit activities of synthesized nanostructured metal catalysts are studied first to illustrate the catalytic performance without polarization and under different reaction conditions, like temperatures and CO_2:H_2 ratios. The EPOC phenomenon is then employed by the application of constant potential or current and is measured according to the ρ and Λ. Physicochemical and electrochemical characterization techniques are also used to explain the mechanisms behind the phenomenon. All catalysts have been examined through HRTEM and STEM analysis to determine the catalyst structure and size in Chapters 3-6. SEM is used to determine the surface morphology of the catalyst in Chapters 3-6. EELS mapping is performed to identify and visualize the elemental compositions on the STEM images in Chapters 3-6. ICP-ES was used to determine the metal loadings of Cu NPs on the catalysts in Chapters 4 and 5. XRD was conducted to provide crystallite information on metal catalysts in Chapters 4-6. XPS spectra were collected to give insights into the oxidation states of the catalysts in Chapters 3-6. CVs are done to provide in situ information about the interactions

between migrated ionic species and metal catalysts and the changes in oxidation state within the potential window in Chapters 3-6. The appendices at the end of Chapters 3-6 include supplementary information to the main content of each chapter.

References

[1] A.E. Galashev, O.R. Rakhmanova, Emissivity of the main greenhouse gases, Russ. J. Phys. Chem. B. 7 (2013) 346–353. https://doi.org/10.1134/S1990793113030020.

[2] D. Castells-Quintana, M. del P. Lopez-Uribe, T.K.J. McDermott, Geography, institutions and development: a review of the long-run impacts of climate change, Clim. Dev. 9 (2017) 452–470. https://doi.org/10.1080/17565529.2016.1167665.

[3] D.H.W. Li, L. Yang, J.C. Lam, Impact of climate change on energy use in the built environment in different climate zones - A review, Energy. 42 (2012) 103–112. https://doi.org/10.1016/j.energy.2012.03.044.

[4] P.K. Thornton, P.J. Ericksen, M. Herrero, A.J. Challinor, Climate variability and vulnerability to climate change: A review, Glob. Chang. Biol. 20 (2014) 3313–3328. https://doi.org/10.1111/gcb.12581.

[5] H.L. Berry, T.D. Waite, K.B.G. Dear, A.G. Capon, V. Murray, The case for systems thinking about climate change and mental health, Nat. Clim. Chang. 8 (2018) 282–290. https://doi.org/10.1038/s41558-018-0102-4.

[6] Q. Zhu, Developments on CO2-utilization technologies, Clean Energy. 3 (2019) 85–100. https://doi.org/10.1093/ce/zkz008.

[7] S.N. Riduan, Y. Zhang, Recent developments in carbon dioxide utilization under mild conditions, Dalt. Trans. 39 (2010) 3347–3357. https://doi.org/10.1039/b920163g.

[8] J. Rogelj, M. Den Elzen, N. Höhne, T. Fransen, H. Fekete, H. Winkler, R. Schaeffer, F. Sha, K. Riahi, M. Meinshausen, Paris Agreement climate proposals need a boost to keep warming well below 2 °c, Nature. 534 (2016) 631–639. https://doi.org/10.1038/nature18307.

[9] L. Copolovici, A.C. Popitanu, D.M. Copolovici, Volatile organic compound emission and residual substances from plants in light of the globally increasing CO2 level, Curr. Opin. Environ. Sci. Heal. 19 (2021) 100216. https://doi.org/10.1016/j.coesh.2020.10.004.

[10] A. Rafiee, M. Panahi, K.R. Khalilpour, CO2 utilization through integration of post-combustion carbon capture process with Fischer-Tropsch gas-to-liquid (GTL) processes, J. CO2 Util. 18 (2017) 98–106. https://doi.org/10.1016/j.jcou.2017.01.016.

[11] S. Holloway, J.M. Pearce, V.L. Hards, T. Ohsumi, J. Gale, Natural emissions of CO2 from the geosphere and their bearing on the geological storage of carbon dioxide, Energy. 32 (2007) 1194–1201.

https://doi.org/10.1016/j.energy.2006.09.001.
[12] C. Song, Global challenges and strategies for control, conversion and utilization of CO2 for sustainable development involving energy, catalysis, adsorption and chemical processing, Catal. Today. 115 (2006) 2–32. https://doi.org/10.1016/j.cattod.2006.02.029.
[13] J. Ma, N. Sun, X. Zhang, N. Zhao, F. Xiao, W. Wei, Y. Sun, A short review of catalysis for CO2 conversion, Catal. Today. 148 (2009) 221–231. https://doi.org/10.1016/j.cattod.2009.08.015.
[14] W. Wang, S. Wang, X. Ma, J. Gong, Recent advances in catalytic hydrogenation of carbon dioxide, Chem. Soc. Rev. 40 (2011) 3703–3727. https://doi.org/10.1039/c1cs15008a.
[15] C.H. Huang, C.S. Tan, A review: CO2 utilization, Aerosol Air Qual. Res. 14 (2014) 480–499. https://doi.org/10.4209/aaqr.2013.10.0326.
[16] J. Zhang, Z. Li, Z. Zhang, K. Feng, B. Yan, Can thermocatalytic transformations of captured CO2 reduce CO2 emissions?, Appl. Energy. 281 (2021) 116076. https://doi.org/10.1016/j.apenergy.2020.116076.
[17] D.T. Whipple, P.J.A. Kenis, Prospects of CO2 utilization via direct heterogeneous electrochemical reduction, J. Phys. Chem. Lett. 1 (2010) 3451–3458. https://doi.org/10.1021/jz1012627.
[18] A. Álvarez, A. Bansode, A. Urakawa, A. V. Bavykina, T.A. Wezendonk, M. Makkee, J. Gascon, F. Kapteijn, Challenges in the Greener Production of Formates/Formic Acid, Methanol, and DME by Heterogeneously Catalyzed CO2 Hydrogenation Processes, Chem. Rev. 117 (2017) 9804–9838. https://doi.org/10.1021/acs.chemrev.6b00816.
[19] C.A. Cotton, N.J. Claassens, S. Benito-Vaquerizo, A. Bar-Even, Renewable methanol and formate as microbial feedstocks, Curr. Opin. Biotechnol. 62 (2020) 168–180. https://doi.org/10.1016/j.copbio.2019.10.002.
[20] G.A. Olah, G.K.S. Prakash, A. Goeppert, Anthropogenic chemical carbon cycle for a sustainable future, J. Am. Chem. Soc. 133 (2011) 12881–12898. https://doi.org/10.1021/ja202642y.
[21] A. V. Puga, On the nature of active phases and sites in CO and CO2 hydrogenation catalysts, Catal. Sci. Technol. 8 (2018) 5681–5707. https://doi.org/10.1039/c8cy01216d.
[22] M.D. Porosoff, B. Yan, J.G. Chen, Catalytic reduction of CO2 by H2 for synthesis of CO, methanol and hydrocarbons: Challenges and opportunities, Energy Environ. Sci. 9 (2016) 62–73. https://doi.org/10.1039/c5ee02657a.
[23] Y.A. Daza, J.N. Kuhn, CO2 conversion by reverse water gas shift catalysis: Comparison of catalysts, mechanisms and their consequences for CO2 conversion to liquid fuels, RSC Adv. 6 (2016) 49675–49691. https://doi.org/10.1039/c6ra05414e.
[24] L. Samiee, E. GhasemiKafrudi, Assessment of different kinetic models of carbon dioxide transformation to methanol via hydrogenation, over a Cu/ZnO/Al2O3 catalyst, React. Kinet. Mech. Catal. 133 (2021) 801–823. https://doi.org/10.1007/s11144-021-02045-1.

[25] S. Kattel, P. Liu, J.G. Chen, Tuning Selectivity of CO2 Hydrogenation Reactions at the Metal/Oxide Interface, J. Am. Chem. Soc. 139 (2017) 9739–9754. https://doi.org/10.1021/jacs.7b05362.
[26] E.L. Kunkes, F. Studt, F. Abild-Pedersen, R. Schlögl, M. Behrens, Hydrogenation of CO2 to methanol and CO on Cu/ZnO/Al2O3: Is there a common intermediate or not? This work is dedicated to the memory and achievements of Dr. Haldor Topsøe., J. Catal. 328 (2015) 43–48. https://doi.org/10.1016/j.jcat.2014.12.016.
[27] J. Ren, H. Guo, J. Yang, Z. Qin, J. Lin, Z. Li, Insights into the mechanisms of CO 2 methanation on Ni(111) surfaces by density functional theory, Appl. Surf. Sci. 351 (2015) 504–516. https://doi.org/10.1016/j.apsusc.2015.05.173.
[28] Y. Chen, S. Choi, L.T. Thompson, Low-temperature CO2 hydrogenation to liquid products via a heterogeneous cascade catalytic system, ACS Catal. 5 (2015) 1717–1725. https://doi.org/10.1021/cs501656x.
[29] D.U. Nielsen, X.M. Hu, K. Daasbjerg, T. Skrydstrup, Chemically and electrochemically catalysed conversion of CO2 to CO with follow-up utilization to value-added chemicals, Nat. Catal. 1 (2018) 244–254. https://doi.org/10.1038/s41929-018-0051-3.
[30] D. Sheldon, Methanol production - A technical history, Johnson Matthey Technol. Rev. 61 (2017) 172–182. https://doi.org/10.1595/205651317X695622.
[31] D. Zagoraios, C. Panaritis, A. Krassakopoulou, E.A. Baranova, A. Katsaounis, C.G. Vayenas, Electrochemical promotion of Ru nanoparticles deposited on a proton conductor electrolyte during CO2 hydrogenation, Appl. Catal. B Environ. 276 (2020) 119148. https://doi.org/10.1016/j.apcatb.2020.119148.
[32] C. Vogt, M. Monai, G.J. Kramer, B.M. Weckhuysen, The renaissance of the Sabatier reaction and its applications on Earth and in space, Nat. Catal. 2 (2019) 188–197. https://doi.org/10.1038/s41929-019-0244-4.
[33] C. Mebrahtu, F. Krebs, S. Abate, S. Perathoner, G. Centi, R. Palkovits, CO 2 Methanation: Principles and Challenges, 1st ed., Elsevier B.V., 2019. https://doi.org/10.1016/B978-0-444-64127-4.00005-7.
[34] W.K. Fan, M. Tahir, Recent trends in developments of active metals and heterogenous materials for catalytic CO2hydrogenation to renewable methane: A review, J. Environ. Chem. Eng. 9 (2021) 105460. https://doi.org/10.1016/j.jece.2021.105460.
[35] M. Younas, L. Loong Kong, M.J.K. Bashir, H. Nadeem, A. Shehzad, S. Sethupathi, Recent Advancements, Fundamental Challenges, and Opportunities in Catalytic Methanation of CO2, Energy and Fuels. 30 (2016) 8815–8831. https://doi.org/10.1021/acs.energyfuels.6b01723.
[36] J. Ashok, S. Pati, P. Hongmanorom, Z. Tianxi, C. Junmei, S. Kawi, A review of recent catalyst advances in CO2 methanation processes, Catal. Today. 356 (2020) 471–489. https://doi.org/10.1016/j.cattod.2020.07.023.
[37] S. Akamaru, T. Shimazaki, M. Kubo, T. Abe, Density functional theory analysis of methanation reaction of CO 2 on Ru nanoparticle supported on TiO2 (1 0 1), Appl. Catal. A Gen. 470 (2014) 405–411.

https://doi.org/10.1016/j.apcata.2013.11.016.
[38] S. Kattel, W. Yu, X. Yang, B. Yan, Y. Huang, W. Wan, P. Liu, J.G. Chen, CO2Hydrogenation over Oxide-Supported PtCo Catalysts: The Role of the Oxide Support in Determining the Product Selectivity, Angew. Chemie - Int. Ed. 55 (2016) 7968–7973. https://doi.org/10.1002/anie.201601661.
[39] S. Kattel, B. Yan, J.G. Chen, P. Liu, CO2 hydrogenation on Pt, Pt/SiO2 and Pt/TiO2: Importance of synergy between Pt and oxide support, J. Catal. 343 (2016) 115–126. https://doi.org/10.1016/j.jcat.2015.12.019.
[40] S. Ilias, A. Bhan, Mechanism of the catalytic conversion of methanol to hydrocarbons, ACS Catal. 3 (2013) 18–31. https://doi.org/10.1021/cs3006583.
[41] I. Yarulina, A.D. Chowdhury, F. Meirer, B.M. Weckhuysen, J. Gascon, Recent trends and fundamental insights in the methanol-to-hydrocarbons process, Nat. Catal. 1 (2018) 398–411. https://doi.org/10.1038/s41929-018-0078-5.
[42] S. Verhelst, J.W. Turner, L. Sileghem, J. Vancoillie, Methanol as a fuel for internal combustion engines, Prog. Energy Combust. Sci. 70 (2019) 43–88. https://doi.org/10.1016/j.pecs.2018.10.001.
[43] D.S. Marlin, E. Sarron, Ó. Sigurbjörnsson, Process Advantages of Direct CO2 to Methanol Synthesis, Front. Chem. 6 (2018) 1–8. https://doi.org/10.3389/fchem.2018.00446.
[44] S. Kattel, B. Yan, Y. Yang, J.G. Chen, P. Liu, Optimizing Binding Energies of Key Intermediates for CO2 Hydrogenation to Methanol over Oxide-Supported Copper, J. Am. Chem. Soc. 138 (2016) 12440–12450. https://doi.org/10.1021/jacs.6b05791.
[45] O. Martin, C. Mondelli, A. Cervellino, D. Ferri, D. Curulla-Ferré, J. Pérez-Ramírez, Operando Synchrotron X-ray Powder Diffraction and Modulated-Excitation Infrared Spectroscopy Elucidate the CO2Promotion on a Commercial Methanol Synthesis Catalyst, Angew. Chemie - Int. Ed. 55 (2016) 11031–11036. https://doi.org/10.1002/anie.201603204.
[46] O. Martin, A.J. Martín, C. Mondelli, S. Mitchell, T.F. Segawa, R. Hauert, C. Drouilly, D. Curulla-Ferré, J. Pérez-Ramírez, Indium oxide as a superior catalyst for methanol synthesis by CO2 hydrogenation, Angew. Chemie - Int. Ed. 55 (2016) 6261–6265. https://doi.org/10.1002/anie.201600943.
[47] Y. Ren, Y. Yang, M. Wei, Recent Advances on Heterogeneous Non-noble Metal Catalysts toward Selective Hydrogenation Reactions, ACS Catal. 13 (2023) 8902–8924. https://doi.org/10.1021/acscatal.3c01442.
[48] G. Centi, Catalysis from A to Z, Angew. Chemie Int. Ed. 47 (2008) 1547–1548. https://doi.org/10.1002/anie.200785548.
[49] M.J. Gilkey, B. Xu, Heterogeneous Catalytic Transfer Hydrogenation as an Effective Pathway in Biomass Upgrading, ACS Catal. 6 (2016) 1420–1436. https://doi.org/10.1021/acscatal.5b02171.
[50] M. Miceli, P. Frontera, A. Macario, A. Malara, Recovery/reuse of heterogeneous supported spent catalysts, Catalysts. 11 (2021). https://doi.org/10.3390/catal11050591.
[51] T.H. Yang, J. Ahn, S. Shi, P. Wang, R. Gao, D. Qin, Noble-Metal Nanoframes

and Their Catalytic Applications, Chem. Rev. 121 (2021) 796–833. https://doi.org/10.1021/acs.chemrev.0c00940.
[52] M. Grimwade, Introduction to precious metals : metallurgy for jewelers & silversmiths, (2009) 230.
[53] T. Inoue, T. Iizuka, Hydrogenation of carbon dioxide and carbon monoxide over supported platinum catalysts, J. Chem. Soc. Faraday Trans. I. 82 (1986) 1681–1686. https://doi.org/10.1039/F19868201681.
[54] S.S. Kim, H.H. Lee, S.C. Hong, A study on the effect of support's reducibility on the reverse water-gas shift reaction over Pt catalysts, Appl. Catal. A Gen. 423–424 (2012) 100–107. https://doi.org/10.1016/j.apcata.2012.02.021.
[55] D.J. Pettigrew, D.L. Trimm, N.W. Cant, The effects of rare earth oxides on the reverse water-gas shift reaction on palladium/alumina, Catal. Letters. 28 (1994) 313–319. https://doi.org/10.1007/BF00806061.
[56] A. Quindimil, U. De-La-Torre, B. Pereda-Ayo, A. Davó-Quiñonero, E. Bailón-García, D. Lozano-Castelló, J.A. González-Marcos, A. Bueno-López, J.R. González-Velasco, Effect of metal loading on the CO2 methanation: A comparison between alumina supported Ni and Ru catalysts, Catal. Today. 356 (2020) 419–432. https://doi.org/10.1016/j.cattod.2019.06.027.
[57] S. Chai, Y. Men, J. Wang, S. Liu, Q. Song, W. An, G. Kolb, Boosting CO2 methanation activity on Ru/TiO2 catalysts by exposing (001) facets of anatase TiO2, J. CO2 Util. 33 (2019) 242–252. https://doi.org/10.1016/j.jcou.2019.05.031.
[58] A. Aitbekova, L. Wu, C.J. Wrasman, A. Boubnov, A.S. Hoffman, E.D. Goodman, S.R. Bare, M. Cargnello, Low-Temperature Restructuring of CeO2-Supported Ru Nanoparticles Determines Selectivity in CO2 Catalytic Reduction, J. Am. Chem. Soc. 140 (2018) 13736–13745. https://doi.org/10.1021/jacs.8b07615.
[59] R. Tang, Z. Zhu, C. Li, M. Xiao, Z. Wu, D. Zhang, C. Zhang, Y. Xiao, M. Chu, A. Genest, G. Rupprechter, L. Zhang, X. Zhang, L. He, Ru-Catalyzed Reverse Water Gas Shift Reaction with Near-Unity Selectivity and Superior Stability, ACS Mater. Lett. 3 (2021) 1652–1659. https://doi.org/10.1021/acsmaterialslett.1c00523.
[60] N.M. Martin, F. Hemmingsson, A. Schaefer, M. Ek, L.R. Merte, U. Hejral, J. Gustafson, M. Skoglundh, A.C. Dippel, O. Gutowski, M. Bauer, P.A. Carlsson, Structure-function relationship for CO2 methanation over ceria supported Rh and Ni catalysts under atmospheric pressure conditions, Catal. Sci. Technol. 9 (2019) 1644–1653. https://doi.org/10.1039/c8cy02097c.
[61] J.C. Matsubu, V.N. Yang, P. Christopher, Isolated metal active site concentration and stability control catalytic CO2 reduction selectivity, J. Am. Chem. Soc. 137 (2015) 3076–3084. https://doi.org/10.1021/ja5128133.
[62] X. Wang, H. Shi, J.H. Kwak, J. Szanyi, Mechanism of CO2 Hydrogenation on Pd/Al2O3 Catalysts: Kinetics and Transient DRIFTS-MS Studies, ACS Catal. 5 (2015) 6337–6349. https://doi.org/10.1021/acscatal.5b01464.
[63] J. Ye, Q. Ge, C.J. Liu, Effect of PdIn bimetallic particle formation on CO2

reduction over the Pd-In/SiO2 catalyst, Chem. Eng. Sci. 135 (2015) 193–201. https://doi.org/10.1016/j.ces.2015.04.034.
[64] A. Wolf, A. Jess, C. Kern, Syngas Production via Reverse Water-Gas Shift Reaction over a Ni-Al2O3 Catalyst: Catalyst Stability, Reaction Kinetics, and Modeling, Chem. Eng. Technol. 39 (2016) 1040–1048. https://doi.org/10.1002/ceat.201500548.
[65] G.C. Wang, L. Jiang, X.Y. Pang, Z.S. Cai, Y.M. Pan, X.Z. Zhao, Y. Morikawa, J. Nakamura, A theoretical study of surface-structural sensitivity of the reverse water-gas shift reaction over Cu(hkl) surfaces, Surf. Sci. 543 (2003) 118–130. https://doi.org/10.1016/S0039-6028(03)00876-8.
[66] J.A. Loiland, M.J. Wulfers, N.S. Marinkovic, R.F. Lobo, Fe/γ-Al2O3 and Fe-K/γ-Al2O3 as reverse water-gas shift catalysts, Catal. Sci. Technol. 6 (2016) 5267–5279. https://doi.org/10.1039/c5cy02111a.
[67] D.L. Jurković, A. Pohar, V.D.B.C. Dasireddy, B. Likozar, Effect of Copper-based Catalyst Support on Reverse Water-Gas Shift Reaction (RWGS) Activity for CO2 Reduction, Chem. Eng. Technol. 40 (2017) 973–980. https://doi.org/10.1002/ceat.201600594.
[68] S.I. Fujita, M. Usui, N. Takezawa, Mechanism of the reverse water gas shift reaction over Cu/ZnO catalyst, J. Catal. 134 (1992) 220–225. https://doi.org/10.1016/0021-9517(92)90223-5.
[69] C.S. Chen, W.H. Cheng, Study on the mechanism of CO formation in reverse water gas shift reaction over Cu/SiO2 catalyst by pulse reaction, TPD and TPR, Catal. Letters. 83 (2002) 121–126. https://doi.org/10.1023/A:1021006718974.
[70] M. Konsolakis, M. Lykaki, S. Stefa, S.A.C. Carabineiro, G. Varvoutis, E. Papista, G.E. Marnellos, Co2 hydrogenation over nanoceria-supported transition metal catalysts: Role of ceria morphology (nanorods versus nanocubes) and active phase nature (co versus cu), Nanomaterials. 9 (2019) 1739. https://doi.org/10.3390/nano9121739.
[71] S.A. Patil, C.H. Ryu, H.S. Kim, Synthesis and Characterization of Copper Nanoparticles (Cu-Nps) using Rongalite as Reducing Agent and Photonic Sintering of Cu-Nps Ink for Printed Electronics, Int. J. Precis. Eng. Manuf. - Green Technol. 5 (2018) 239–245. https://doi.org/10.1007/s40684-018-0024-7.
[72] J. Pike, S.W. Chan, F. Zhang, X. Wang, J. Hanson, Formation of stable Cu2O from reduction of CuO nanoparticles, Appl. Catal. A Gen. 303 (2006) 273–277. https://doi.org/10.1016/j.apcata.2006.02.008.
[73] C.-S. Chen, W.-H. Cheng, S. Lin, Mechanism of CO Formation in Reverse Water – Gas Shift Reaction over Cu / Al2O3 Catalyst., Catal. Letters. 68 (2000) 45–48. https://link.springer.com/content/pdf/10.1023%2FA%3A1021006718974.pdf.
[74] E.L. Fornero, D.L. Chiavassa, A.L. Bonivardi, M.A. Baltanás, Transient analysis of the reverse water gas shift reaction on Cu/ZrO2 and Ga2O3/Cu/ZrO2 catalysts, J. CO2 Util. 22 (2017) 289–298. https://doi.org/10.1016/j.jcou.2017.06.002.
[75] Y. Zhang, L. Liang, Z. Chen, J. Wen, W. Zhong, S. Zou, M. Fu, L. Chen, D.

Ye, Highly efficient Cu/CeO2 -hollow nanospheres catalyst for the reverse water-gas shift reaction : Investigation on the role of oxygen vacancies through in situ UV-Raman and DRIFTS, Appl. Surf. Sci. 516 (2020) 146035. https://doi.org/10.1016/j.apsusc.2020.146035.

[76] G. Zhou, F. Xie, L. Deng, G. Zhang, Supported mesoporous Cu/CeO2-σ catalyst for CO2 reverse water-gas shift reaction to syngas, Int. J. Hydrogen Energy. 45 (2020) 11380–11393. https://doi.org/10.1016/j.ijhydene.2020.02.058.

[77] J. Sun, F. Liu, U. Salahuddin, M. Wu, C. Zhu, X. Lu, B. Zhang, B. Zhao, Z. Xie, Y. Ding, D. Li, C.Y. Nam, F.Y. Zhang, P.X. Gao, Optimization and understanding of ZnO nanoarray supported Cu-ZnO-Al2O3 catalyst for enhanced CO2 -methanol conversion at low temperature and pressure, Chem. Eng. J. 455 (2023) 140559. https://doi.org/10.1016/j.cej.2022.140559.

[78] Y. Li, H. Zhang, T. Chen, Y. Sun, F. Rosei, M. Yu, Dual-Interfacial Electrocatalyst Enriching Surface Bonded H for Energy-Efficient CO2-to-CH3OH Conversion, Adv. Funct. Mater. 2312970 (2023) 1–8. https://doi.org/10.1002/adfm.202312970.

[79] U.J. Etim, Y. Song, Z. Zhong, Improving the Cu/ZnO-Based Catalysts for Carbon Dioxide Hydrogenation to Methanol, and the Use of Methanol As a Renewable Energy Storage Media, Front. Earth Sci. 8 (2020) 1–26. https://doi.org/10.3389/fenrg.2020.545431.

[80] S.C. Qi, X.Y. Liu, R.R. Zhu, D.M. Xue, X.Q. Liu, L.B. Sun, Causation of catalytic activity of Cu-ZnO for CO2 hydrogenation to methanol, Chem. Eng. J. 430 (2022) 132784. https://doi.org/10.1016/j.cej.2021.132784.

[81] M. V Landau, N. Meiri, N. Utsis, R.V. Nehemya, M. Herskowitz, Conversion of CO2, CO, and H2 in CO2 Hydrogenation to Fungible Liquid Fuels on Fe-Based Catalysts, Ind. Eng. Chem. Res. 56 (2017) 13334–13355. https://doi.org/10.1021/acs.iecr.7b01817.

[82] D.H. Kim, S.W. Han, H.S. Yoon, Y.D. Kim, Journal of Industrial and Engineering Chemistry Reverse water gas shift reaction catalyzed by Fe nanoparticles with high catalytic activity and stability, J. Ind. Eng. Chem. 23 (2015) 67–71. https://doi.org/10.1016/j.jiec.2014.07.043.

[83] B. Dai, G. Zhou, S. Ge, H. Xie, Z. Jiao, G. Zhang, K. Xiong, CO2 Reverse Water-Gas Shift Reaction on Mesoporous M-CeO2 Catalysts, Can. J. Chem. Eng. 95 (2017) 634–642. https://doi.org/10.1002/cjce.22730.

[84] C. Liu, T.R. Cundari, A.K. Wilson, CO2 Reduction on Transition Metal (Fe, Co, Ni, and Cu) Surfaces: In Comparison with Homogeneous Catalysis, J. Phys. Chem. C. 116 (2012) 5681–5688.

[85] J.A. Loiland, M.J. Wulfers, N.S. Marinkovicb, R.F. Lobo, Fe/γ-Al2O3 and Fe–K/γ-Al2O3 as reverse water-gas shift catalysts, Catal. Sci. Technol. 6 (2016). https://doi.org/10.1039/c5cy02111a.

[86] M. Wenzel, N.V.R.A. Dharanipragada, V. V Galvita, H. Poelman, G.B. Marin, L. Rihko-struckmann, K. Sundmacher, CO production from CO2 via reverse water–gas shift reaction performed in a chemical looping mode : Kinetics on

modified iron oxide, Biochem. Pharmacol. 17 (2017) 60–68. https://doi.org/10.1016/j.jcou.2016.10.015.
[87] C. Panaritis, M. Edake, M. Couillard, R. Einakchi, E.A. Baranova, Insight towards the role of ceria-based supports for reverse water gas shift reaction over RuFe nanoparticles, J. CO2 Util. 26 (2018) 350–358. https://doi.org/10.1016/j.jcou.2018.05.024.
[88] A. V. Puga, On the nature of active phases and sites in CO and CO2 hydrogenation catalysts, Catal. Sci. Technol. 8 (2018) 5681. https://doi.org/10.1039/c8cy01216d.
[89] L. Wang, H. Liu, Y. Chen, S. Yang, Reverse water e gas shift reaction over co-precipitated Co-CeO2 catalysts : Effect of Co content on selectivity and carbon formation, Int. J. Hydrogen Energy. 42 (2016) 3682–3689. https://doi.org/10.1016/j.ijhydene.2016.07.048.
[90] C.H. Mejía, T.W. van Deelen, K.P. de Jong, Activity enhancement of cobalt catalysts by tuning metal-support interactions, Nat. Commun. 9 (2018) 4459. https://doi.org/10.1038/s41467-018-06903-w.
[91] G. Garbarino, T. Cavattoni, P. Riani, G. Busca, Support effects in metal catalysis : a study of the behavior of unsupported and silica-supported cobalt catalysts in the hydrogenation of CO2 at atmospheric pressure, Catal. Today. 345 (2020) 213–219. https://doi.org/10.1016/j.cattod.2019.10.016.
[92] A.R. Puigdollers, P. Schlexer, S. Tosoni, G. Pacchioni, Increasing Oxide Reducibility : The Role of Metal/Oxide Interfaces in the Formation of Oxygen Vacancies, ACS Catal. 7 (2017) 6493−6513. https://doi.org/10.1021/acscatal.7b01913.
[93] M.M. Jaffar, M.A. Nahil, P.T. Williams, Parametric Study of CO2 Methanation for Synthetic Natural Gas Production, Energy Technol. 7 (2019) 1–12. https://doi.org/10.1002/ente.201900795.
[94] P. Unwiset, K.C. Chanapattharapol, P. Kidkhunthod, Y. Poo-arporn, B. Ohtani, Catalytic activities of titania-supported nickel for carbon-dioxide methanation, Chem. Eng. Sci. 228 (2020) 115955. https://doi.org/10.1016/j.ces.2020.115955.
[95] A. Loder, M. Siebenhofer, S. Lux, The reaction kinetics of CO2 methanation on a bifunctional Ni/MgO catalyst, J. Ind. Eng. Chem. 85 (2020) 196–207. https://doi.org/10.1016/j.jiec.2020.02.001.
[96] M.T. Greiner, L. Chai, M.G. Helander, W.M. Tang, Z.H. Lu, Transition metal oxide work functions: The influence of cation oxidation state and oxygen vacancies, Adv. Funct. Mater. 22 (2012) 4557–4568. https://doi.org/10.1002/adfm.201200615.
[97] B. Zhao, B. Yan, Z. Jiang, S. Yao, Z. Liu, Q. Wu, R. Ran, S.D. Senanayake, D. Weng, J.G. Chen, High selectivity of CO2 hydrogenation to CO by controlling the valence state of nickel using perovskite, Chem. Commun. 54 (2018) 7354–7357. https://doi.org/10.1039/c8cc03829e.
[98] T.W. van Deelen, C. Hernández Mejía, K.P. de Jong, Control of metal-support interactions in heterogeneous catalysts to enhance activity and selectivity, Nat. Catal. 2 (2019) 955–970. https://doi.org/10.1038/s41929-019-0364-x.

[99] A.R. Puigdollers, P. Schlexer, S. Tosoni, G. Pacchioni, Increasing oxide reducibility: The role of metal/oxide interfaces in the formation of oxygen vacancies, ACS Catal. 7 (2017) 6493–6513. https://doi.org/10.1021/acscatal.7b01913.
[100] G.L. Haller, D.E. Resasco, Metal–Support Interaction: Group VIII Metals and Reducible Oxides, Adv. Catal. 36 (1989) 173–235. https://doi.org/10.1016/S0360-0564(08)60018-8.
[101] I. Riess, Mixed ionic-electronic conductors - Material properties and applications, Solid State Ionics. 157 (2003) 1–17. https://doi.org/10.1016/S0167-2738(02)00182-0.
[102] P. Vernoux, L. Lizarraga, M.N. Tsampas, F.M. Sapountzi, A. De Lucas-Consuegra, J.L. Valverde, S. Souentie, C.G. Vayenas, D. Tsiplakides, S. Balomenou, E.A. Baranova, Ionically conducting ceramics as active catalyst supports, Chem. Rev. 113 (2013) 8192–8260. https://doi.org/10.1021/cr4000336.
[103] T.W. Tom W.van Deelen, H. Mejía, Control of metal-support interactions in heterogeneous catalysts to enhance activity and selectivity, Nat. Catal. 2 (2019) 955–970. https://doi.org/10.1038/s41929-019-0364-x.
[104] G. Pacchioni, H.J. Freund, Controlling the charge state of supported nanoparticles in catalysis: lessons from model systems, Chem. Soc. Rev. 47 (2018) 8474–8502. https://doi.org/10.1039/c8cs00152a.
[105] M.S. Chen, D.W. Goodman, The structure of catalytically active gold on titania, Science (80-.). 306 (2004) 252–255. https://doi.org/10.1126/science.1102420.
[106] W.C. Conner, J.L. Falconer, Spillover in Heterogeneous Catalysis, Chem. Rev. 95 (1995) 759–788. https://doi.org/10.1021/cr00035a014.
[107] S. Takakusagi, K.I. Fukui, R. Tero, K. Asakura, Y. Iwasawa, First direct visualization of spillover species emitted from Pt nanoparticles, Langmuir. 26 (2010) 16392–16396. https://doi.org/10.1021/la102013a.
[108] S. Ntais, R.J. Isaifan, E.A. Baranova, An X-ray photoelectron spectroscopy study of platinum nanoparticles on yttria-stabilized zirconia ionic support: Insight into metal support interaction, Mater. Chem. Phys. 148 (2014) 673–679. https://doi.org/10.1016/j.matchemphys.2014.08.033.
[109] C.R. Henry, Morphology of supported nanoparticles, Prog. Surf. Sci. 80 (2005) 92–116. https://doi.org/10.1016/j.progsurf.2005.09.004.
[110] S. Penner, M. Armbrüster, Formation of intermetallic compounds by reactive metal-support interaction: A frequently encountered phenomenon in catalysis, ChemCatChem. 7 (2015) 374–392. https://doi.org/10.1002/cctc.201402635.
[111] S. Furukawa, T. Komatsu, Intermetallic Compounds: Promising Inorganic Materials for Well-Structured and Electronically Modified Reaction Environments for Efficient Catalysis, ACS Catal. 7 (2017) 735–765. https://doi.org/10.1021/acscatal.6b02603.
[112] Z. Luo, G. Zhao, H. Pan, W. Sun, Strong Metal–Support Interaction in Heterogeneous Catalysts, Adv. Energy Mater. 12 (2022) 1–15. https://doi.org/10.1002/aenm.202201395.

[113] C.J. Pan, M.C. Tsai, W.N. Su, J. Rick, N.G. Akalework, A.K. Agegnehu, S.Y. Cheng, B.J. Hwang, Tuning/exploiting Strong Metal-Support Interaction (SMSI) in Heterogeneous Catalysis, J. Taiwan Inst. Chem. Eng. 74 (2017) 154–186. https://doi.org/10.1016/j.jtice.2017.02.012.
[114] J. Nicole, C. Comninellis, D. Tsiplakides, C. Pliangos, X.E. Verykios, C.G. Vayenas, Electrochemical promotion and metal-support interactions, J. Catal. 204 (2001) 23–34. https://doi.org/10.1006/jcat.2001.3360.
[115] Michael Stoukides and Costas G. Vayenas, The effect of electrochemical oxygen pumping on the rate and selectivity of ethylene oxidation on polycrystalline silver, J. Catal. 70 (1981) 134–146. https://doi.org/10.1007/BF00770948.
[116] C.G. Vayenas, S. Bebelis, C. Pliangos, S. Brosda, D. Tsiplakides, Electrochemical Activation of Catalysis, Springer, 2001. https://doi.org/10.1007/b115566.
[117] P. Vernoux, C.G. Vayenas, Recent Advances in Electrochemical Promotion of Catalysis (Modern Aspects of Electrochemistry, 61), Springer, 2023. https://doi.org/10.1007/978-3-031-13893-5.
[118] A. Katsaounis, Recent developments and trends in the electrochemical promotion of catalysis (EPOC), J. Appl. Electrochem. 40 (2010) 885–902. https://doi.org/10.1007/s10800-009-9938-7.
[119] C.G. Vayenas, S. Brosda, C. Pliangos, The double-layer approach to promotion, electrocatalysis, electrochemical promotion, and metal-support interactions, J. Catal. 216 (2003) 487–504. https://doi.org/10.1016/S0021-9517(02)00127-6.
[120] C.G.Vayenas, R.M.Lambert, S.Ladas, S. Bebelis, S.Neophytides, M.S.Tikhov, N.C.Filkin, M.Makri, D.Tsiplakides, C. Cavalca, Direct STM, XPS and TPD observation of spillover phenomena over mm distances on metal catalyst films interfaced with solid electrolytes, Stud. Surf. Sci. Catal. 112 (1997) 39–47.
[121] X. Li, F. Gaillard, P. Vernoux, Investigations under real operating conditions of the electrochemical promotion by O2 temperature programmed desorption measurements, Top. Catal. 44 (2007) 391–398. https://doi.org/10.1007/s11244-006-0131-5.
[122] M.N. Tsampas, F.M. Sapountzi, A. Boréave, P. Vernoux, Isotopical labeling mechanistic studies of electrochemical promotion of propane combustion on Pt/YSZ, Electrochem. Commun. 26 (2013) 13–16. https://doi.org/10.1016/j.elecom.2012.09.043.
[123] D. Tsiplakides, S. Balomenou, A. Katsaounis, D. Archonta, C. Koutsodontis, C.G. Vayenas, Electrochemical promotion of catalysis: Mechanistic investigations and monolithic electropromoted reactors, Catal. Today. 100 (2005) 133–144. https://doi.org/10.1016/j.cattod.2004.12.015.
[124] C. Panaritis, S. Yan, M. Couillard, E.A. Baranova, Electrochemical study of the metal-support interaction between FeOx nanoparticles and cobalt oxide support for the reverse water gas shift reaction, J. CO2 Util. 56 (2021) 101824. https://doi.org/10.1016/j.jcou.2021.101824.
[125] C.G. Vayenas, S. Brosda, Electron Donation-Backdonation and the Rules of

Catalytic Promotion, Top. Catal. 57 (2014) 1287–1301. https://doi.org/10.1007/s11244-014-0294-4.
[126] C. Panaritis, J. Zgheib, S.A.H. Ebrahim, M. Couillard, E.A. Baranova, Electrochemical in-situ activation of Fe-oxide nanowires for the reverse water gas shift reaction, Appl. Catal. B Environ. 269 (2020) 118826. https://doi.org/10.1016/j.apcatb.2020.118826.
[127] D. Zagoraios, S. Tsatsos, S. Kennou, C.G. Vayenas, G. Kyriakou, A. Katsaounis, Tuning the RWGS Reaction via EPOC and in Situ Electro-oxidation of Cobalt Nanoparticles, ACS Catal. 10 (2020) 14916–14927. https://doi.org/10.1021/acscatal.0c04133.
[128] D. Zagoraios, N. Kokkinou, G. Kyriakou, A. Katsaounis, Electrochemical control of the RWGS reaction over Ni nanoparticles deposited on yttria stabilized zirconia, Catal. Sci. Technol. 12 (2022) 1869–1879. https://doi.org/10.1039/d1cy02140k.
[129] C. Panaritis, C. Michel, M. Couillard, E.A. Baranova, S.N. Steinmann, Elucidating the role of electrochemical polarization on the selectivity of the CO2 hydrogenation reaction over Ru, Electrochim. Acta. 350 (2020) 136405. https://doi.org/10.1016/j.electacta.2020.136405.
[130] N. Kokkinou, F. Xydas, S. Brosda, G. Kyriakou, A. Katsaounis, Electrochemical Promotion of CO2 Hydrogenation Using Rh Catalysts Supported on O2− Conducting Solid Electrolyte, Catalysts. 13 (2023). https://doi.org/10.3390/catal13061014.
[131] A. Kotsiras, I. Kalaitzidou, D. Grigoriou, A. Symillidis, M. Makri, A. Katsaounis, C.G. Vayenas, Electrochemical promotion of nanodispersed Ru-Co catalysts for the hydrogenation of CO2, Appl. Catal. B Environ. 232 (2018) 60–68. https://doi.org/10.1016/j.apcatb.2018.03.031.
[132] I. Kalaitzidou, M. Makri, D. Theleritis, A. Katsaounis, C.G. Vayenas, Comparative study of the electrochemical promotion of CO2 hydrogenation on Ru using Na+, K+, H+ and O2- conducting solid electrolytes, Surf. Sci. 646 (2016) 194–203. https://doi.org/10.1016/j.susc.2015.09.011.
[133] S. Bebelis, H. Karasali, C.G. Vayenas, Electrochemical promotion of the CO2 hydrogenation on Pd/YSZ and Pd/β″-Al2O3 catalyst-electrodes, Solid State Ionics. 179 (2008) 1391–1395. https://doi.org/10.1016/j.ssi.2008.02.043.
[134] E. Ruiz, D. Cillero, P.J. Martínez, Á. Morales, G.S. Vicente, G. De Diego, J.M. Sánchez, Bench scale study of electrochemically promoted catalytic CO2 hydrogenation to renewable fuels, Catal. Today. 210 (2013) 55–66. https://doi.org/10.1016/j.cattod.2012.10.025.
[135] A. de Lucas-Consuegra, F. Dorado, J.L. Valverde, R. Karoum, P. Vernoux, Electrochemical activation of Pt catalyst by potassium for low temperature CO deep oxidation, Catal. Commun. 9 (2008) 17–20. https://doi.org/10.1016/j.catcom.2007.04.038.
[136] I. V. Yentekakis, G. Moggridge, C.G. Vayenas, R.M. Lambert, In Situ controlled promotion of catalyst surfaces via NEMCA: The effect of Na on the Pt-catalyzed CO oxidation, J. Catal. 146 (1994) 292–305.

https://doi.org/10.1016/0021-9517(94)90033-7.
[137] L. Lizarraga, S. Souentie, L. Mazri, A. Billard, P. Vernoux, Investigation of the CO oxidation rate oscillations using electrochemical promotion of catalysis over sputtered-Pt films interfaced with YSZ, Electrochem. Commun. 12 (2010) 1310–1313. https://doi.org/10.1016/j.elecom.2010.07.007.
[138] D. Zagoraios, A. Athanasiadi, I. Kalaitzidou, S. Ntais, A. Katsaounis, A. Caravaca, P. Vernoux, C.G. Vayenas, Electrochemical promotion of methane oxidation over nanodispersed Pd/Co3O4 catalysts, Catal. Today. 355 (2020) 910–920. https://doi.org/10.1016/j.cattod.2019.02.030.
[139] P. Tsiakaras, C.G. Vayenas, Non-faradaic electrochemical modification of catalytic activity. VII. The case of methane oxidation on platinum, J. Catal. 140 (1993) 53–70. https://doi.org/10.1006/jcat.1993.1068.
[140] A. Nakos, S. Souentie, A. Katsaounis, Electrochemical promotion of methane oxidation on Rh/YSZ, Appl. Catal. B Environ. 101 (2010) 31–37. https://doi.org/10.1016/j.apcatb.2010.08.030.
[141] S. Peng-ont, S. Souentie, S. Assabumrungrat, P. Praserthdam, S. Brosda, C.G. Vayenas, Electrochemical promotion of propane oxidation over Pd, Ir, and Ru catalyst-electrodes deposited on YSZ, Ionics (Kiel). 19 (2013) 1705–1714. https://doi.org/10.1007/s11581-013-0931-0.
[142] S. Souentie, L. Lizarraga, E.I. Papaioannou, C.G. Vayenas, P. Vernoux, Permanent electrochemical promotion of C3H8 oxidation over thin sputtered Pt films, Electrochem. Commun. 12 (2010) 1133–1135. https://doi.org/10.1016/j.elecom.2010.06.002.
[143] A. Lintanf, E. Djurado, P. Vernoux, Pt/YSZ electrochemical catalysts prepared by electrostatic spray deposition for selective catalytic reduction of NO by C3H6, Solid State Ionics. 178 (2008) 1998–2008. https://doi.org/10.1016/j.ssi.2008.01.008.
[144] I. Constantinou, D. Archonta, S. Brosda, M. Lepage, Y. Sakamoto, C.G. Vayenas, Electrochemical promotion of NO reduction by C3H6 on Rh catalyst-electrode films supported on YSZ and on dispersed Rh/YSZ catalysts, J. Catal. 251 (2007) 400–409. https://doi.org/10.1016/j.jcat.2007.07.034.
[145] A. de Lucas-Consuegra, F. Dorado, C. Jiménez-Borja, A. Caravaca, P. Vernoux, J.L. Valverde, Use of potassium conductors in the electrochemical promotion of environmental catalysis, Catal. Today. 146 (2009) 293–298. https://doi.org/10.1016/j.cattod.2009.04.009.
[146] A. De Lucas-Consuegra, J. González-Cobos, Y. García-Rodríguez, A. Mosquera, J.L. Endrino, J.L. Valverde, Enhancing the catalytic activity and selectivity of the partial oxidation of methanol by electrochemical promotion, J. Catal. 293 (2012) 149–157. https://doi.org/10.1016/j.jcat.2012.06.016.
[147] S. Souentie, L. Lizarraga, A. Kambolis, M. Alves-Fortunato, J.L. Valverde, P. Vernoux, Electrochemical promotion of the water-gas shift reaction on Pt/YSZ, J. Catal. 283 (2011) 124–132. https://doi.org/10.1016/j.jcat.2011.07.009.
[148] S. Bebelis, H. Karasali, C.G. Vayenas, Electrochemical promotion of CO2 hydrogenation on Rh/YSZ electrodes, J. Appl. Electrochem. 38 (2008) 1127–

1133. https://doi.org/10.1007/s10800-008-9574-7.
[149] D. Theleritis, S. Souentie, A. Siokou, A. Katsaounis, C.G. Vayenas, Hydrogenation of CO 2 over Ru/YSZ electropromoted catalysts, ACS Catal. 2 (2012) 770–780. https://doi.org/10.1021/cs300072a.
[150] I. Kalaitzidou, A. Katsaounis, T. Norby, C.G. Vayenas, Electrochemical promotion of the hydrogenation of CO2 on Ru deposited on a BZY proton conductor, J. Catal. 331 (2015) 98–109. https://doi.org/10.1016/j.jcat.2015.08.023.
[151] M. Makri, A. Katsaounis, C.G. Vayenas, Electrochemical promotion of CO2 hydrogenation on Ru catalyst-electrodes supported on a K-β″-Al2O3 solid electrolyte, Electrochim. Acta. 179 (2015) 556–564. https://doi.org/10.1016/j.electacta.2015.03.144.
[152] C. Panaritis, J. Zgheib, S.A.H. Ebrahim, M. Couillard, E.A. Baranova, Electrochemical in-situ activation of Fe-oxide nanowires for the reverse water gas shift reaction, Appl. Catal. B Environ. 269 (2020) 118826. https://doi.org/10.1016/j.apcatb.2020.118826.
[153] D. Zagoraios, S. Tsatsos, S. Kennou, C.G. Vayenas, G. Kyriakou, A. Katsaounis, Tuning the RWGS Reaction via EPOC and in Situ Electro-oxidation of Cobalt Nanoparticles, ACS Catal. (2020) 14916–14927. https://doi.org/10.1021/acscatal.0c04133.
[154] D. Zagoraios, C. Panaritis, A. Krassakopoulou, E.A. Baranova, A. Katsaounis, C.G. Vayenas, Electrochemical promotion of Ru nanoparticles deposited on a proton conductor electrolyte during CO2 hydrogenation, Appl. Catal. B Environ. 276 (2020) 119148. https://doi.org/10.1016/j.apcatb.2020.119148.
[155] C. Panaritis, S. Yan, M. Couillard, E.A. Baranova, Electrochemical study of the metal-support interaction between FeOx nanoparticles and cobalt oxide support for the reverse water gas shift reaction, J. CO2 Util. 56 (2022) 101824. https://doi.org/10.1016/j.jcou.2021.101824.
[156] I. V. Yentekakis, C.G. Vayenas, The effect of electrochemical oxygen pumping on the steady-state and oscillatory behavior of CO oxidation on polycrystalline Pt, J. Catal. 111 (1988) 170–188. https://doi.org/10.1016/0021-9517(88)90075-9.
[157] D. Tsiplakides, J. Nicole, C.G. Vayenas, C. Comninellis, Work Function and Catalytic Activity Measurements of an IrO2 Film Deposited on YSZ Subjected to In Situ Electrochemical Promotion, J. Electrochem. Soc. 145 (1998) 905–908. https://doi.org/10.1149/1.1838365.
[158] A. Toghan, L.M. Rösken, R. Imbihl, The electrochemical promotion of ethylene oxidation at a pt/YSZ catalyst, ChemPhysChem. 11 (2010) 1452–1459. https://doi.org/10.1002/cphc.200900936.
[159] N. Ibrahim, D. Poulidi, I.S. Metcalfe, The role of sodium surface species on electrochemical promotion of catalysis in a Pt/YSZ system: The case of ethylene oxidation, J. Catal. 303 (2013) 100–109. https://doi.org/10.1016/j.jcat.2013.03.015.
[160] Y.M. Hajar, L. Treps, C. Michel, E.A. Baranova, S.N. Steinmann, Theoretical

insight into the origin of the electrochemical promotion of ethylene oxidation on ruthenium oxide, Catal. Sci. Technol. 9 (2019) 5915–5926. https://doi.org/10.1039/c9cy01421g.
[161] V. Roche, R. Karoum, A. Billard, R. Revel, P. Vernoux, Electrochemical promotion of deep oxidation of methane on Pd/YSZ, J. Appl. Electrochem. 38 (2008) 1111–1119. https://doi.org/10.1007/s10800-008-9569-4.
[162] F. Matei, C. Jiménez-Borja, J. Canales-Vázquez, S. Brosda, F. Dorado, J.L. Valverde, D. Ciuparu, Enhanced electropromotion of methane combustion on palladium catalysts deposited on highly porous supports, Appl. Catal. B Environ. 132–133 (2013) 80–89. https://doi.org/10.1016/j.apcatb.2012.11.011.
[163] F. Matei, D. Ciuparu, C. Jiménez-Borja, F. Dorado, J.L. Valverde, S. Brosda, Electrochemical promotion of methane oxidation on impregnated and sputtered Pd catalyst-electrodes deposited on YSZ, Appl. Catal. B Environ. 127 (2012) 18–27. https://doi.org/10.1016/j.apcatb.2012.07.035.
[164] Y.M. Hajar, B. Venkatesh, E.A. Baranova, Electrochemical promotion of nanostructured palladium catalyst for complete methane oxidation, Catalysts. 9 (2019). https://doi.org/10.3390/catal9010048.
[165] Y.M. Hajar, B. Venkatesh, M.S.E. Houache, H. Liu, R. Safari, S. Prabhudev, G.A. Botton, E.A. Baranova, Electrochemical promotion of Bi-metallic Ni9Pd core double-shell nanoparticles for complete methane oxidation, J. Catal. 374 (2019) 127–135. https://doi.org/10.1016/j.jcat.2019.04.026.
[166] C. Falgairette, A. Jaccoud, G. Fóti, C. Comninellis, The phenomenon of “permanent” electrochemical promotion of catalysis (P-EPOC), J. Appl. Electrochem. 38 (2008) 1075–1082. https://doi.org/10.1007/s10800-008-9554-y.
[167] E. Stavrakakis, D. Poulidi, Electrochemical Promotion of CO Oxidation on Na-Promoted Pt/YSZ: Interaction Between Multiple Promoting Species, Top. Catal. 61 (2018) 276–287. https://doi.org/10.1007/s11244-018-0896-3.
[168] C. Jiménez-Borja, S. Brosda, F. Matei, M. Makri, B. Delgado, F. Sapountzi, D. Ciuparu, F. Dorado, J.L. Valverde, C.G. Vayenas, Electrochemical promotion of methane oxidation on Pd catalyst-electrodes deposited on Y2O3-stabilized-ZrO2, Appl. Catal. B Environ. 128 (2012) 48–54. https://doi.org/10.1016/j.apcatb.2012.02.011.
[169] A. Lymperi, C. Chatzilias, F. Xydas, E. Martino, G. Kyriakou, A. Katsaounis, Electrochemical Promotion of CO2 Hydrogenation Using a Pt/YSZ Fuel Cell Type Reactor, Nanomaterials. 13 (2023) 1–16. https://doi.org/10.3390/nano13131930.
[170] C. Chatzilias, E. Martino, A. Katsaounis, C.G. Vayenas, Electrochemical promotion of CO2 hydrogenation in a monolithic electrochemically promoted reactor (MEPR), Appl. Catal. B Environ. 284 (2021) 119695. https://doi.org/10.1016/j.apcatb.2020.119695.
[171] M. Makri, A. Symillidis, D. Grigoriou, A. Katsaounis, C.G. Vayenas, Electrochemical Promotion of CO2 Reduction on a Dispersed Ru/YSZ Catalyst Supported on YSZ Solid Electrolyte, Mater. Today Proc. 5 (2018) 27617–

27625. https://doi.org/10.1016/j.matpr.2018.09.082.
[172] J. Díez-Ramírez, P. Sánchez, J.L. Valverde, F. Dorado, Electrochemical promotion and characterization of PdZn alloy catalysts with K and Na ionic conductors for pure gaseous CO2 hydrogenation, J. CO2 Util. 16 (2016) 375–383. https://doi.org/10.1016/j.jcou.2016.09.007.
[173] N. Gutiérrez-Guerra, J. González-Cobos, J.C. Serrano-Ruiz, J.L. Valverde, A. De Lucas-Consuegra, Electrochemical activation of Ni catalysts with potassium ionic conductors for CO2 hydrogenation, Top. Catal. 58 (2015) 1256–1269. https://doi.org/10.1007/s11244-015-0488-4.
[174] V. Jiménez, C. Jiménez-Borja, P. Sánchez, A. Romero, E.I. Papaioannou, D. Theleritis, S. Souentie, S. Brosda, J.L. Valverde, Electrochemical promotion of the co2 hydrogenation reaction on composite ni or ru impregnated carbon nanofiber catalyst-electrodes deposited on YSZ, Appl. Catal. B Environ. 107 (2011) 210–220. https://doi.org/10.1016/j.apcatb.2011.07.016.

Chapter 2: Experiments and Characterizations

2.1 Catalyst Synthesis

The nanostructured metal catalysts are prepared using the polyol synthesis method adapted from the previous study[1]. In short, metal salt is measured and dissolved in ethylene glycol (EG) (Fisher Chemical, Ottawa, Canada), and then tetramethylammonium hydroxide (TMAOH) (pentahydrate, Sigma-Aldrich, Oakville, Canada, 97+%) is added until pH reaches 12. The EG functions as both solvent and reducing agent, and the TMAOH is used to control the particle size and distribution[1]. The solution is stirred for 30 minutes at room temperature (RT) and then refluxed at temperatures ranging from 100-200℃. The resulting colloidal solution is cooled down to RT and stored for future use. The pH of the solution dropped from the initial value of 12 to 8, indicating the reduction of metal ions.

The supported metal catalysts are prepared by mixing metal colloidal solution with measured oxide support powders in deionized water (DI water, 18 MΩ cm) for 48 h for the desired metal loadings. For instance, 10 mL metal colloidal solution (1 mg mL^{-1}), corresponding to 10 mg metal catalysts, is mixed with 1000 mg of oxide support powders in DI water to have 1 weight percent (wt.%) metal/oxide support. The dispersed supported catalysts are then centrifuged and washed three times with DI water with supernatant discarded and precipitate collected, followed by drying in air at 60℃ for 24h. The final catalysts are in powder forms and stored for future tests.

2.2 Cell Preparation

YSZ (8 mol% Y_2O_3-ZrO_2, Tosoh) is used as the solid electrolyte in Chapters 3-5 in the form of a disc and is prepared as reported elsewhere [2]. The disc is 19 mm in diameter and 1 mm in thickness. Two electrodes, counter and reference electrodes, are deposited by painting with gold paste (Ted Pella Inc., Redding, USA) on one side of the disc and calcined in air at 600 ℃ for 1 h and then cooled to RT. The metal catalysts are then deposited on the other side of the disc as the working electrode in a tape mask mold (surface area of 1 cm^2) directly opposite to the counter electrode. The

metal colloidal solution is applied using a micropipette in steps of 10 µL per deposition with a drying step at 100℃ for 10 minutes in between each application. This is repeated until the target mass loading is achieved. The structure of electrodes deposited on the YSZ is shown in **Figure 2-1a**. Subsequently, the electrochemical cell is assembled in a single-chamber quartz reactor by pressing a gold mesh over the catalysts to guarantee the film conductivity, and a porous borosilicate fritted disc is placed over the gold mesh to fix the disc in the reactor in a sandwich-like structure. The working, counter, and reference electrodes are connected to the potentiostat-galvanostat (Arbin Instruments, MSTAT, USA) via three gold wires. The schematic structure of the electrochemical cell in the reactor is shown in **Figure 2-1b**.

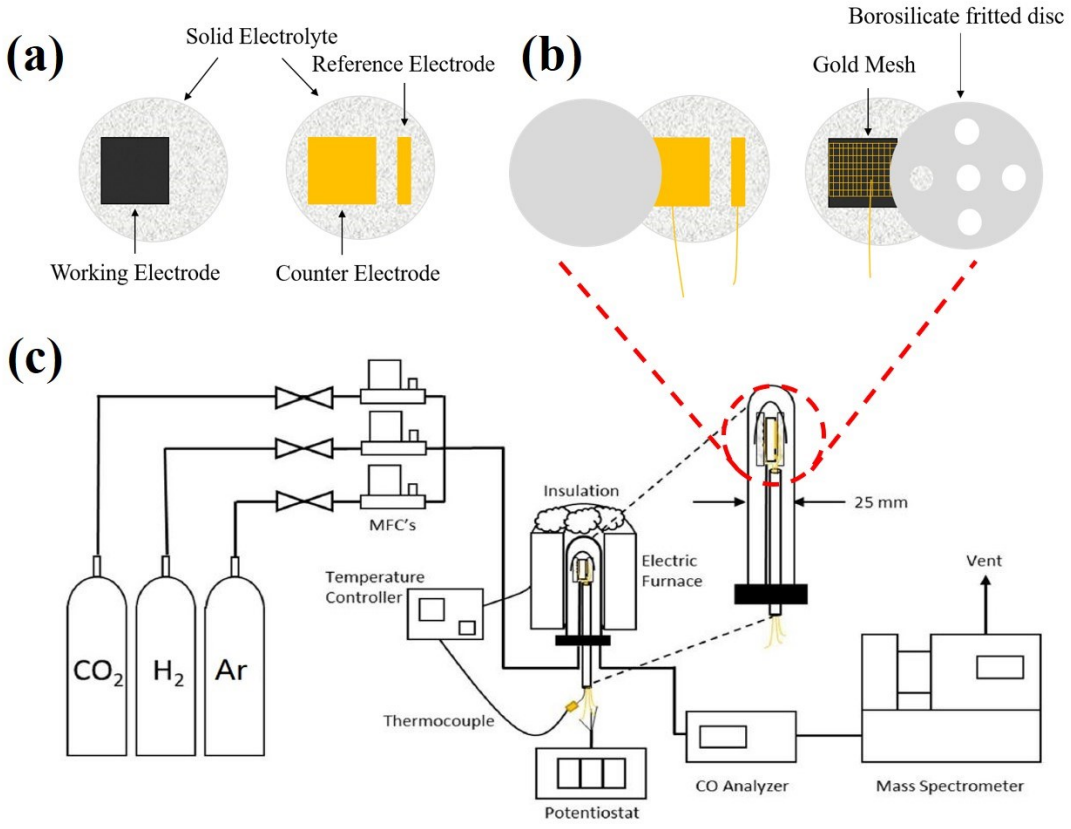

Figure 2-1. Schematic structure of (a) electrodes deposited on the solid electrolyte, (b) EPOC cell in reactor, and (c) experimental set-up.

2.3 Experimental Setup

The single-chamber quartz reactor is then placed in the catalytic system under ambient pressure and isothermal condition. The experimental set-up is displayed in

Figure 2-1c and consists of gas flow controllers, quartz reactor, gas analysis equipment, and a potentiostat-galvanostat. H_2 (Messer, 100 %), CO_2 (Messer, 99.99%), and Ar (Messer, 100 %) are fed to the reactor through three individual mass flow controllers (MFC, MKS Instruments). A non-dispersive infrared CO analyzer (Horiba VIA-510) and a quadrupole mass spectrometer (QMS, Ametek Proline DM 100) are connected to the reactor outlet to monitor the amount of produced CO in parts per million (ppm) and analyze the gas components with mass to charge ratios (m/z) of 44, 40, 28, and 2 corresponding to CO_2, Ar, CO, and H_2, respectively. This experimental set-up is applied for all studies in the following Chapters 3-6. Before any reactions, the catalysts deposited on solid electrolyte are pre-treated in air for 1 h at 350 ℃ to initially remove the EG and TMAOH, then in Ar for 1 h at 350℃ to get rid of air, and finally in H_2 (20% in Ar) for 2 h at 350℃ to reduce the metal catalysts back. For RWGS reaction, the gas ratio of CO_2:H_2 is modified to be 1:1, 3:1, 6:1, 1:3, and 1:6 under the protection of Ar by adjusting the flowrates of CO_2, H_2, and Ar, with the total flowrate of the inlet gas kept stable at 100mL min^{-1}. The experimental temperatures are controlled by the heating thermocouple.

The EPOC tests are carried out by applying constant voltages/currents across the working electrode and counter electrode. The magnitudes of EPOC effects are characterized by rate enhancement ratio (ρ) and apparent Faradaic efficiency (Λ), which are calculated by Eq. (2-1) and (2-2):

$$\rho = r/r_0 \tag{2-1}$$

$$|\Lambda| = \Delta r/(I/nF) \tag{2-2}$$

Where r_0 is the open-circuit CO production rate and r is the steady-state rate after application of voltage/current. Δr is the rate change upon polarization, I is the applied current or current response to the applied voltage, n is the number of electrons transferred (2 e^- for CO), and F is the Faradaic constant. The increase of catalytic rate is termed EPOC effect when $|\Lambda| > 1$, which indicates a non-Faradaic enhancement[3,4]. The unit of reaction rate r is calibrated from ppm (10^{-6}) into mole

CO per second per gram of catalyst (mol CO s^{-1} g^{-1}) by Eq. (2-3), where 24.465 L mol^{-1} is the molar volume at standard conditions:

$$\text{mol CO } s^{-1}g^{-1} = \frac{(\text{CO ppm} \times 10^{-6}) \times (100\text{mL/min}) \times (\text{min/60s})}{(24.465\text{L/mol}) \times (1000\text{mL/L}) \times (\text{g})} \quad (2\text{-}3)$$

This equation is applicable under the assumption that the reactor operates under differential conditions, where conversions are kept low. This minimizes the influence of mass transport limitations and allows the reaction to proceed at rates that are controlled by the intrinsic activity of the catalyst and the effects of electrochemical promotion, not by how quickly the reactants can reach the catalyst surface or how quickly the products can leave.

2.4 Physicochemical Characterization

The specimens used for physicochemical characterizations included both as-prepared and spent samples. The as-prepared catalyst samples are collected after pre-treatments but before engaging in reactions, showcasing the properties of the catalysts in their initial states. The spent catalyst samples are obtained directly after EPOC tests, providing insights into the properties of catalysts after the polarization.

Scanning Transmission Electron Microscopy (STEM), performed on an FEI Titan^3 80-300 microscope operated at 300 keV and equipped with a CEOS aberration corrector for the probe forming lens, is used on the analysis of catalyst samples to determine the particle size and shape. The samples are prepared by sonicating the catalyst powders in ethanol and are then one-drop deposited onto a lacey carbon support film (Ted Pella). The microscope is equipped with an EDAX Energy-dispersive X-ray (EDX) spectrometer, which is carried out to characterize the element composition. High-angle annular dark-field (HAADF) imaging is performed with a convergence semi-angle of 18 mrad and a collection semi-angle angle of 60 mrad to provide a contrast sensitive to the atomic number Z.

Scanning Electron Microscopy (SEM, JSM-7500F FESEM) is used to characterize the morphology of catalyst samples deposited on solid electrolytes.

Determination of the metal loadings on oxide supports are performed on triplicate samples by Inductively Coupled Plasma Optical Emission Spectroscopy (ICP-ES) (Agilent 8800).

X-ray Diffraction (XRD) patterns are measured over powder formed catalysts to investigate the crystalline structures by the Rigaku Ultima IV multipurpose diffractometer with a scanning rate of 1 degree (°) min^{-1} from 20 to 80 °2θ. The identification of peaks is accomplished by using the Powder Diffraction File (PDF) database.

X-Ray Photoelectron Spectroscopy (XPS, Kratos Axis Ultra XPS) equipped with a monochromated Al X-ray source is used to determine the oxidation states of catalyst samples. The colloidal samples are prepared by depositing colloid solution on a silicon wafer followed by drying at 200℃ for 1h under Argon, while the powder samples are mounted and attached to the coated aluminum platen using double-sided adhesive Cu tape. XPS analysis is conducted using an accelerating voltage of 15 kV and a current of 12 mA. The pressure in the chamber during analysis is 9.9 $x10^{-10}$ ± 0.4 $x10^{-10}$ torr. All XPS peaks are fitted using CasaXPS software with Shirley background corrections except those of colloidal Cu, which require a Tougaard background. A Gaussian-Lorentzian shape function is used for high resolution XPS spectra. High resolution analyses are calibrated to adventitious C 1s signal at 284.8 eV.

2.5 Electrochemical Characterization

Cyclic voltammetry (CV) tests are carried out under both inert conditions (in Ar) and reaction conditions by the potentiostat-galvanostat (Arbin Instruments, MSTAT). The voltage is set to sweep from a negative value to a positive one, followed by cycling back to the staring point with a scanning rate of 20 mV s^{-1}.

Linear sweep voltammetry (LSV) at scan rate of 20 mV s^{-1} is used to obtain Tafel plots. The exchange current density (i_0) is determined from the intercept at $U_{WR} = 0$ in Tafel plots (ln I vs. U_{WR}) based on the potentiostat-galvanostat data of current responses (I) to various applied potentials (U_{WR}).

The relative electrochemical active surface areas (ECSAs) are evaluated by the surface roughness factor (RF) values and are determined by measuring the double-layer capacitance (C_{dl}) of as-prepared catalysts. CVs are performed in a small potential window, where no faradaic reactions happen, with various scan rates (20 - 200 mV s^{-1}) under inert conditions. By plotting the charging current (I) vs. scan rate ($dV\,dt^{-1}$), the C_{dl} could be calculated from the slopes according to the Eq. (2-4)[5]:

$$I = dQ/dt = C_{dl}(dV/dt) \quad (2\text{-}4)$$

References

[1] E.A. Baranova, C. Bock, D. Ilin, D. Wang, B. MacDougall, Infrared spectroscopy on size-controlled synthesized Pt-based nano-catalysts, Surf. Sci. 600 (2006) 3502–3511. https://doi.org/10.1016/j.susc.2006.07.005.

[2] I.R. Gibson, G.P. Dransfield, J.T.S. Irvine, Sinterability of commercial 8 mol% yttria-stabilized zirconia powders and the effect of sintered density on the ionic conductivity, J. Mater. Sci. 33 (1998) 4297–4305. https://doi.org/10.1023/A:1004435504482.

[3] C.G. Vayenas, S. Bebelis, C. Pliangos, S. Brosda, D. Tsiplakides, Electrochemical Activation of Catalysis, Springer, 2001. https://doi.org/10.1007/b115566.

[4] P. Vernoux, L. Lizarraga, M.N. Tsampas, F.M. Sapountzi, A. De Lucas-Consuegra, J.L. Valverde, S. Souentie, C.G. Vayenas, D. Tsiplakides, S. Balomenou, E.A. Baranova, Ionically conducting ceramics as active catalyst supports, Chem. Rev. 113 (2013) 8192–8260. https://doi.org/10.1021/cr4000336.

[5] E. Cossar, M.S.E. Houache, Z. Zhang, E.A. Baranova, Comparison of electrochemical active surface area methods for various nickel nanostructures, J. Electroanal. Chem. 870 (2020) 114246. https://doi.org/10.1016/j.jelechem.2020.114246.

Chapter 3: Electrochemical Promotion of Cu Nanoparticles for the Reverse Water Gas Shift Reaction

Adapted from: ***J. Wang****, M. Couillard, E.A. Baranova, 2022, Catalysis Science & Technology.*

Abstract: The catalytic activity and EPOC effects of copper (Cu) nanoparticles (NPs), an inexpensive metal as an alternative to noble metals, are presented and show to be better than those of other non-noble metals, such as iron (Fe) and cobalt (Co). Through characterizations like SEM, STEM and XPS, the change from lower oxidized state to higher oxidized state of copper catalyst before and after reaction is confirmed, and Cu_2O and metallic copper are taken as the active states. It is found that the EPOC effects only occur under positive polarizations and vary significantly under different reaction conditions, indicating that the RWGS reaction over Cu NPs deposited on yttria-stabilized zirconia (YSZ) follows the redox mechanism. The best EPOC effect occurs under an application of +2V and CO_2:H_2 ratio of 1:1 at 400℃ with an enhancement ratio (ρ) of 1.2 and Faradaic efficiency (Λ) of 6.52.

3.1 Introduction

Copper (Cu) is one of the most studied catalysts for the RWGS reaction due to its excellent properties, high activity and low price[1]. Cu nanoparticles (NPs) are difficult to stabilize under ambient pressure due to their high reactivity and fast oxidation to two main copper oxides: Cu_2O (Cu(I)) and CuO (Cu(II))[2–4]. From temperature-programmed reduction (TPR) studies of CuO[5–7], the copper oxides are reduced in a temperature range of 200-500℃ as shown in Eq. (3-1):

$$CuO \rightarrow Cu_2O \rightarrow Cu \quad (3\text{-}1)$$

Most studies about CO_2 hydrogenation on copper-based catalysts focus on metal-support interaction (MSI) and no EPOC studies have ever been discussed. In a recent study[8], Cu/Al_2O_3 catalyst were used for RWGS and Cu_2O was reported as an

intermediate during CO production. In another study[9] of RWGS on Cu/ZrO_2, the dissociation of CO_2 adsorbed on Cu was confirmed. The importance of the interface for RWGS activity in Cu/ZnO catalytic system was also emphasized recently[10]. Similar to Fe and Co, it has been demonstrated that the Cu catalyst is active in converting CO_2 into CO by following the redox mechanism during RWGS[11,12].

In this study, the electrochemical promotion of Cu NPs of 20 nm average size deposited on YSZ was studied for the first time for RWGS reaction. Characterizations including cyclic voltammetry, SEM, STEM, and XPS were carried out to explore the morphology and oxidation state changes of Cu NPs before and after reactions. The open-circuit activities of RWGS over Cu NPs/YSZ were evaluated under the CO_2:H_2 ratio of 1:1, 3:1, 6:1, 1:3, and 1:6 in a temperature range of 250 - 450℃. The influence of polarization under different temperatures, CO_2:H_2 ratios, and applied potentials on the catalytic rate of RWGS reaction were investigated to illustrate the possible mechanism behind the phenomenon.

3.2 Experimental

3.2.1 Catalysts synthesis

The Cu NPs were synthesized using the polyol synthesis method mentioned in Chapter 2. Specifically, 0.0295g of copper (II) nitrate (hydrate, Alfa Aesar, 99.99%) was dissolved in 5 mL of ethylene glycol (EG) (Fisher Chemical), and then 5 mL of 0.25M tetramethylammonium hydroxide (TMAOH) (pentahydrate, Sigma-Aldrich, 97+%) was added. The solution was stirred for 30 minutes at room temperature (RT) and then refluxed at 190 ℃ for 30 minutes. The resulting colloidal solution was cooled down to RT with colour changed from blue to dark red. The pH of the solution dropped from the initial value of 12 to 8, indicating the reduction of copper (II) precursor.

3.2.2 Experimental setup

The electrochemical cell and experimental setup were prepared following the procedures detailed in Chapter 2. Counter and reference electrodes were painted on

one side of YSZ disc using gold paste and then calcined. The Cu NPs were deposited on the other side of the disc in a tape mask mold (surface area of 1 cm^2) directly opposite to the counter electrode. Cu NPs colloidal solution was applied using a micropipette in steps of 10μL per deposition with a drying step at 100℃ for 10 minutes in between every application. This was repeated until a metal mass loading of 0.5 mg cm^{-1} was achieved.

Subsequently, the electrochemical cell was assembled in a single-chamber quartz reactor in a sandwich-like structure using gold mesh and borosilicate fritted disc. The working, counter, and reference electrodes were connected to the potentiostat-galvanostat (Arbin Instruments, MSTAT) via three gold wires. The single-chamber quartz reactor was then placed in the catalytic system under ambient pressure and isothermal conditions. H_2 (Messer, 100 %), CO_2 (Messer, 99.99%), and Ar (Messer, 100 %) were fed to the reactor through three individual mass flow controllers (MFC, MKS Instruments). A non-dispersive infrared CO analyzer (Horiba VIA-510) was connected to the reactor outlet to monitor the amount of produced CO. Before any reactions, the Cu NPs were pre-treated as detailed in Chapter 2. The gas ratio of inlet CO_2:H_2 was modified to be 1:1, 3:1, 6:1, 1:3, and 1:6 under the protection of Ar with the total flowrate kept stable at 100mL min^{-1}. The temperature for the experiments ranged from 250℃ to 450℃ and was controlled by the heating thermocouple.

Cyclic voltammetry (CV) test for as-prepared catalyst after pre-treatment was carried out by the potentiostat-galvanostat (Arbin Instruments, MSTAT) under inert atmosphere (Argon) at 400℃. To illustrate the effect of positive potential on the oxidation states of the copper catalyst, the potential windows of the CV were set to begin from -1.5V to 1.5V, 1V, 0.5V, and 0V respectively, followed by cycling back to -1.5V with a scanning rate of 20mV s^{-1}. The effect of holding potential on the first cycle were demonstrated by holding potential at 1.5V and -1.5V for 10 min before starting the CV tests. CV test under stoichiometric condition (CO_2:H_2 =1:1) was also carried out at 400℃ to compare with inert condition and evaluate the difference of oxidation states before and after RWGS reaction.

Under experimental conditions, the EPOC effect was characterized using the rate enhancement ratio (ρ) and apparent Faradaic efficiency (Λ), which were calculated by Eq. (3-2) and (3-3):

$$\rho = r/r_0 \tag{3-2}$$

$$|\Lambda| = \Delta r/(I/nF) \tag{3-3}$$

Where r_0 is the open-circuit CO production rate and r is the steady-state CO production rate after application of potential. Δr is the change in CO production rate, I is the current response to the applied potential, n is the number of electrons transferred (2 e^- for CO), and F is the Faradaic constant. The unit of reaction rate r is mole CO per second per gram of catalyst (mol CO s^{-1} g^{-1}).

3.2.3 Characterizations

Scanning Transmission Electron Microscopy (STEM) was used on the analysis of as-prepared Cu catalyst to determine the particle size and morphology. The microscope is equipped with an Energy-dispersive X-ray (EDX) spectrometer, which was carried out to characterize the element composition. High-angle annular dark-field (HAADF) imaging was performed to provide a contrast sensitive to the atomic number Z. Scanning Electron Microscopy (SEM, JSM-7500F FESEM) was used to characterize the morphology alternation of as-prepared and spent Cu catalyst deposited on YSZ. X-Ray Photoelectron Spectroscopy (XPS, Kratos Axis Ultra XPS) was used for tests on colloidal, as-prepared and spent Cu catalyst to determine the oxidation states change before and after reactions. All XPS peaks were fitted using CasaXPS software with Gaussian-Lorentzian shape function and Shirley background corrections except those of colloidal Cu, which required a Tougaard background. High resolution analyses were calibrated to adventitious C 1s signal at 284.8 eV.

3.3 Results

3.3.1 Catalyst characterizations

Figure 3-1a and b shows the STEM images of as-prepared Cu catalyst after pre-

treatments and **Figure 3-1c, d, e and f** show corresponding EELS mapping of the orange square in **Figure 3-1b** (the yellow square is for drift correction) where red is Cu, green is oxygen and blue is carbon. From **Figure 3-1a**, the average particle size of as-prepared Cu catalyst showed to be 20nm with a core-shell structure. The brighter shell corresponds to more reduced copper than more oxidized core. The reduction could occur under the electron beam. **Figure A-1** shows the EDX spectrum of as-prepared catalyst where Cu was the only metal found with limited oxygen in Area 1 compared to the blank Area 2. The oxygen element came from the oxidation of Cu particle surface during storage since copper was easily oxidized even at room temperature[13], resulting in the core-shell structure, which was also illustrated in the Ref [14] where Cu_2O was formed as a shell on the surface of spherical Cu NPs. The oxygen element shown in EELS mapping was mostly from YSZ powders during sample preparation, whose position corresponded well to the smaller particles (d=10nm) presented in **Figure 3-1b** which showed no Cu content (red in EELS mapping), while the carbon was from the residual EG that was used for catalyst synthesis.

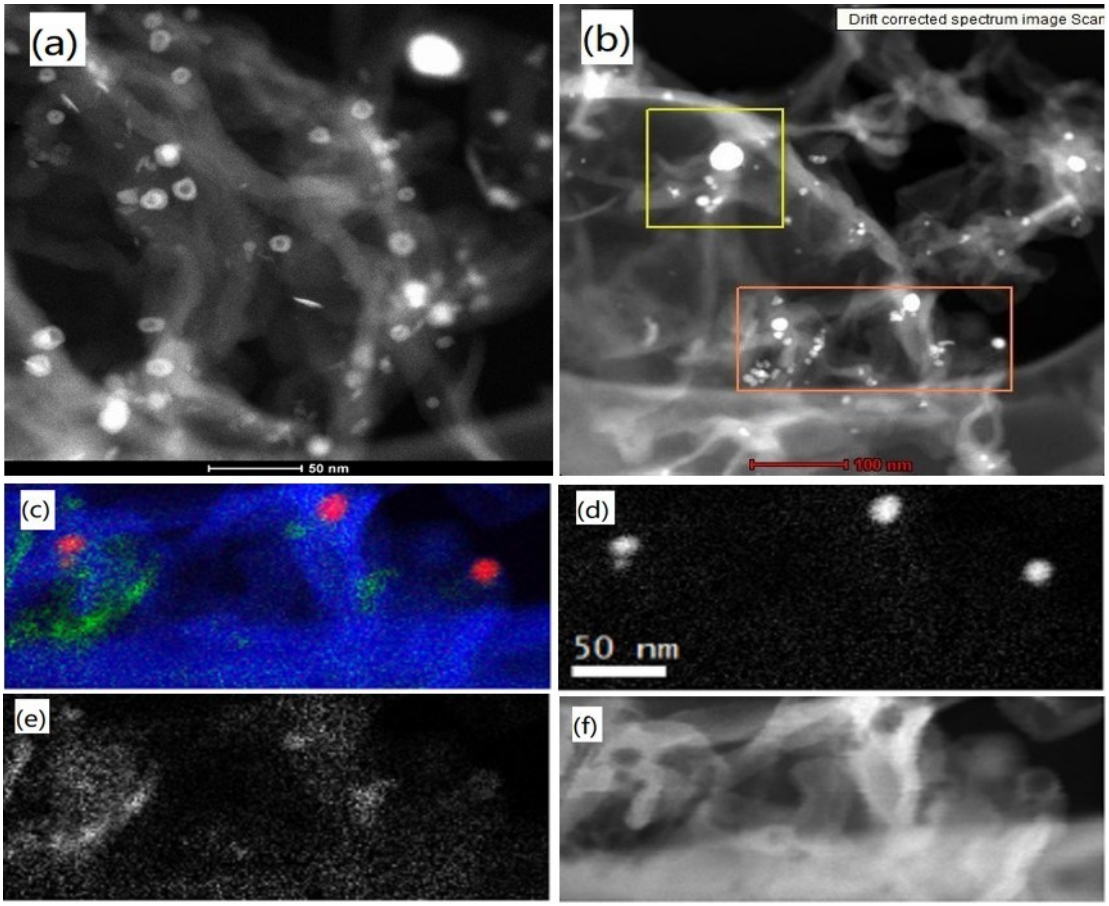

Figure 3-1. STEM image of (a) and (b) as-prepared Cu catalyst and (c) EELS mapping of (d) copper, (e) oxygen and (f) carbon from the orange square in (b), where red means Cu, green represents oxygen, and blue is carbon.

Figure 3-2a and b shows SEM images of as-prepared and spent Cu catalysts, respectively, deposited on YSZ (Cu/YSZ). After deposition and pre-treatment, Cu catalyst shows a porous structure with some large agglomerated Cu NPs of over 200nm in size with small white dots on the surface, which represented dispersed Cu NPs. The dispersed Cu NPs were 20-30nm in diameter, which agreed with the particle size of as-prepared Cu catalyst in STEM (**Figure 3-1a and d**). In the spent sample, i.e., catalyst that was used for RWGS under open circuit and EPOC experiments, Cu NPs in lower oxidized states were oxidized by O^{2-} under anodic polarization. This resulted in the formation of copper oxide NPs in the higher oxidation state that were prone to sintering and agglomeration at higher temperatures. As a result, the morphology of the catalyst film was changed with the absence of smaller Cu NPs and the presence of larger CuO_x particles.

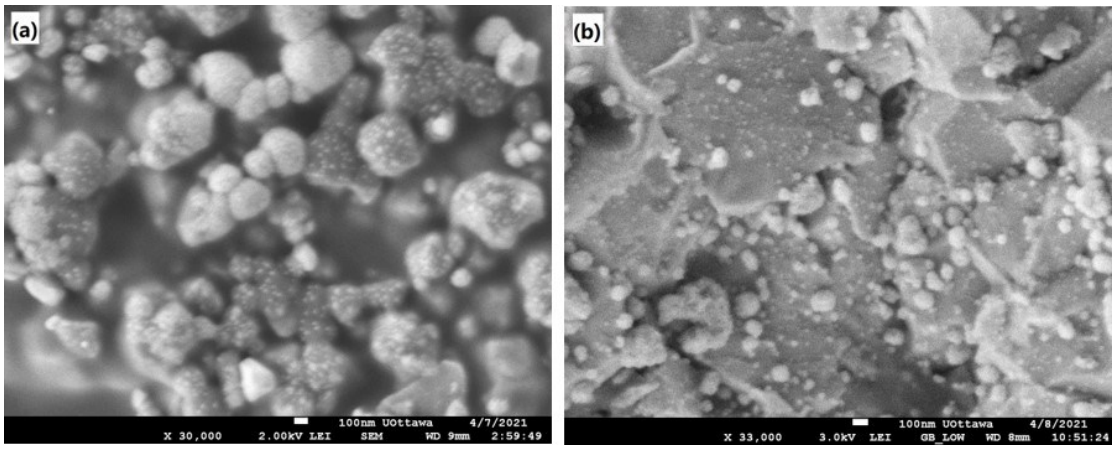

Figure 3-2. SEM images of (a) as-prepared Cu and (b) spent Cu.

Figure 3-3 shows the high resolution XPS spectra for Cu 2p of colloidal Cu NPs, as-prepared Cu/YSZ after pre-treatment, and spent Cu/YSZ sample, respectively. It was found that the Cu catalyst in the colloidal sample (**Figure 3-3a**) was mainly in copper oxide (CuO_x) state with limited amount of metallic copper (Cu(0)) and copper hydroxide since the catalyst was synthesized in EG solution open to air in the presence of TMAOH that could provide OH^- to form $Cu(OH)_2$. After the pre-treatment in H_2, the higher oxidized state of Cu(II) was expected to get reduced to metallic Cu^0, however metallic copper was unstable and easily oxidized even at RT[14]. As a result, most of copper was in Cu(I) state in the as-prepared sample (**Figure 3-3b**). The $Cu(OH)_2$ was also formed due to the reaction between CuO and H_2O, which was produced from CuO_x reduction during pre-treatment process.

However, the area percentage of Cu(I) was decreased from 74% to 41% with an increase in the area of Cu(II) from 7% to 36% after experiments (**Figure 3-3c**). This indicates the change in the oxidation state of Cu possibly due to O^{2-} supply under electrochemical anodic polarization, as will be discussed in the next section. The small peaks shown between Cu 2p1/2 and Cu 2p3/2 were the shake-up satellite structures of Cu(II) oxide, which are known to characterize the existence of CuO phase[15–17]. Therefore, the presence of these satellite structures in the colloidal and spent sample and their absence in the as-prepared sample further illustrated the reduction of CuO_x during pre-treatments and the oxidation state alternation after polarizations. The XPS species information associated to Cu 2p and C 1s averaged for

9 separate area scans is summarized in **Table A-1**. From **Table A-1**, the insignificant increase of C-C in the spent sample indicates that there is no carbon deposition on the surface of Cu, contrary to earlier observation of carbon deposition on FeO_x catalysts[18].

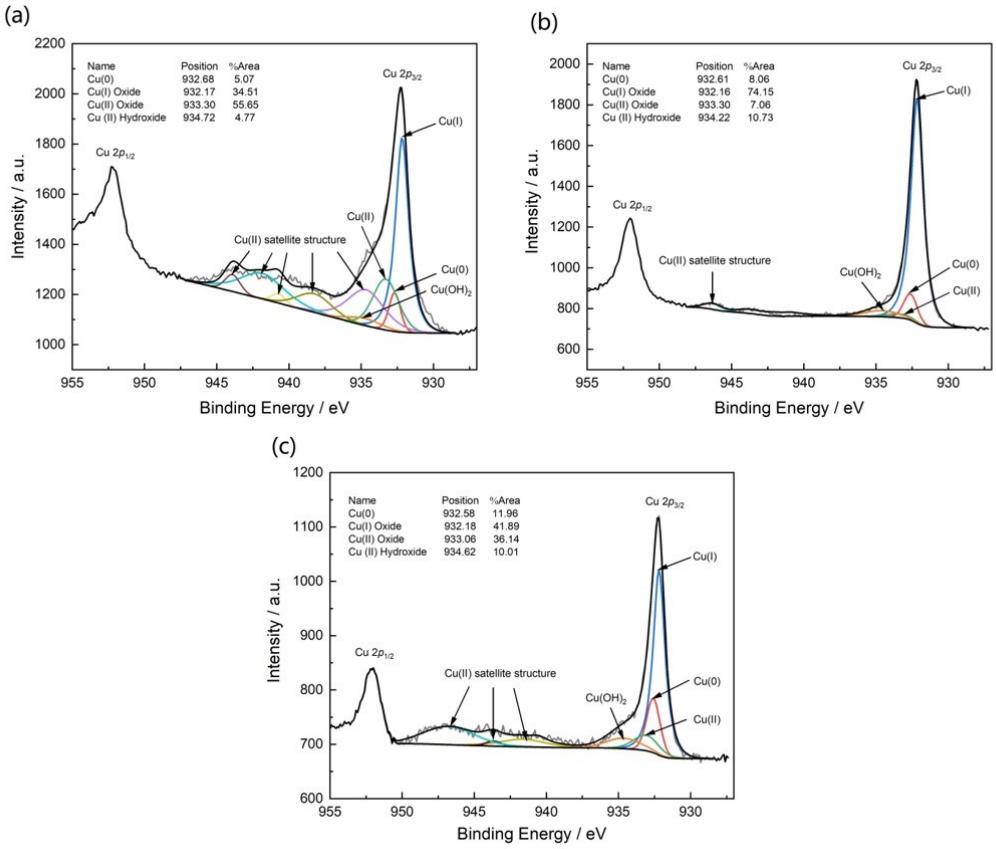

Figure 3-3. High-resolution XPS spectra for Cu 2p of (a)colloidal, (b)as-prepared, and (c)spent samples.

3.3.2 Open-circuit catalytic activity of Cu/YSZ

Before any experiments, the catalyst was left under reaction conditions for 5 h to ensure the stability of the CO production rate. The stable open-circuit catalytic reaction rates carried out on Cu NPs deposited on YSZ at various CO_2:H_2 ratios in a temperature range of 250℃ to 450℃ are shown in **Figure 3-4**, while the overall catalytic rates are summarized in **Figure A-3**, which shows 2 stable runs for each CO_2:H_2 ratios. Under all conditions, the RWGS reaction was dominant and CO was the main product. This demonstrated that the Cu catalyst deposited on YSZ favoured

the selectivity to CO, which was in agreement with a previous study on dispersed Cu catalyst[19]. The catalyst was activated above 300℃ and the catalytic rate increased with temperature in all cases. Under the same conditions, the open-circuit CO rate showed to be two times higher than those of recently reported FeO_x and CoO_x NPs on YSZ [18,20] but was still lower than that of ruthenium, a noble metal catalyst[21].

As reported before, under hydrogen, CuO starts reducing to Cu_2O at 200℃ and becomes metallic Cu at 350℃[5,6]. In this study, a reduction pre-treatment under 20% H_2 in Ar was carried out at 350℃ for 2 h, therefore, most of the catalyst was supposed to be metallic Cu (Cu^0) before RWGS reactions. The difference in CO rate at various CO_2:H_2 ratios indicated that the RWGS reaction over copper catalyst was following the redox mechanism. Under stoichiometric conditions, the CO_2 adsorbed on copper surface dissociates into *CO and *O, where the *CO desorbs from copper to form CO, and *O moves to the bulk copper filling up the oxygen vacancies, which reacts with H_2 to form H_2O[11,22]. Cu_2O plays an important role in RWGS reaction and works as an intermediate which enabled copper catalyst to participate in the reaction continuously[23,24].

Figure 3-4 shows that the CO production rate increases when the ratio is oxidizing conditions ($3CO_2$:$1H_2$) compared to stoichiometric conditions (CO_2:H_2=1:1). The enhancement indicated that excess of CO_2 led to oxidation of Cu^0 to Cu_2O, which could also adsorb CO_2 and be further oxidized to CuO with simultaneous CO production[25,26] according to Eq. (3-4) and (3-5):

$$2Cu + CO_2 \rightarrow Cu_2O + CO \quad (3\text{-}4)$$

$$Cu_2O + CO_2 \rightarrow 2CuO + CO \quad (3\text{-}5)$$

However, further increase in the CO_2:H_2 ratio to 6:1 did not lead to the rate enhancement. Under higher CO_2 concentration, CuO became the dominant state which lacked oxygen vacancies in crystal structures for *O and thereby prohibited the dissociation of CO_2 and release of CO. Under reducing conditions, the CO rate showed a limited increase when the ratio was CO_2:$3H_2$ compared to stoichiometric

conditions. This was likely due to the competitive reactions between the reduction of Cu_2O by hydrogen and the oxidation of Cu^0 by CO_2. The Cu_2O oxidized from Cu^0 was reduced back to Cu^0 by the existence of excessive hydrogen and thus the CO rate did not increase a lot compared to the CO_2:H_2 ratio of 1:1. When the CO_2:H_2 ratio decreased further to 1:6 , the CO rate was thermodynamically favoured over reduced Cu^0 catalyst[25,27–29]. CO_2 conversions are summarized in **Figure A-4**.

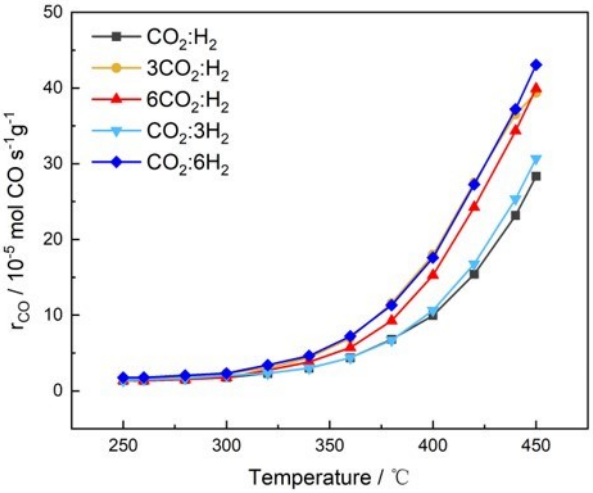

Figure 3-4. Open-circuit CO production rate of Cu NPs deposited on YSZ.

3.3.3 Cyclic voltammetry of Cu/YSZ

The CV tests were carried out under both inert atmosphere and reaction condition after pre-treatments to illustrate the change in the oxidation state and identify the active states of the copper catalyst. **Figure 3-5a** shows stable CV cycles of Cu/YSZ under both inert (in Argon) and reaction (CO_2:H_2 ratio of 1:1) conditions at 400℃ within a potential range of -1.5V to 1.5V. The complete CV cycles of both conditions were summarized in **Figure A-5** where the fifth cycles were taken as the stable ones. Under the inert condition, a small peak at ~ -0.25V (peak AI) is observed in the anodic scan corresponding to electrooxidation of Cu^0 to Cu_2O (Eq. (3-6)) by O^{2-} coming from YSZ[18,30]. In a small anodic peak at ~0.7V (peak AII) Cu_2O is further oxidized to CuO (Eq. (3-7)), following by oxygen evolution at higher potentials (Eq. (3-8)). In cathodic scan, two peaks are present at 0.5V (peak CI) and -0.5V (peak CII),

indicating the reduction of CuO to Cu_2O (Eq. (3-7)) and further reduction of Cu_2O to Cu^0 (Eq. (3-6)), respectively. Under the reaction condition, the current in anodic cycle was inferior to that under the inert condition with only one peak shown in cathodic cycle. This was due to the prohibition of oxidation of Cu^0 to CuO by the existence of H_2. As a result, only Cu_2O was formed during the process, which demonstrated the presence of Cu_2O as an intermediate [8] and also confirmed the stepwise oxidation of Cu.

$$Cu_2O + 2e^- \rightleftharpoons 2Cu + O^{2-}(YSZ) \quad (3\text{-}6)$$

$$2CuO + 2e^- \rightleftharpoons Cu_2O + O^{2-}\ (YSZ) \quad (3\text{-}7)$$

$$O^{2-}(YSZ) \rightarrow \frac{1}{2}O_2 + 2e^- \quad (3\text{-}8)$$

Figure 3-5b presents the CV cycles within various scanning ranges under Ar at 400°C. No current peak was found in cathodic cycle when the potential window was from -1.5V to 0V, while one peak appeared when the upper potential limit was increased from 0V to 0.5V, and two peaks were observed when further increased to 1V. This was due to the stepwise oxidation of Cu to Cu_2O and CuO. No copper oxide was formed within the potential range of -1.5V to 0V, while only Cu_2O was formed as an intermediate to CuO in anodic cycle in small amounts at 0.5V, and CuO began to form at potential above 1V, resulting in two reduction processes during cathodic cycle, which was in agreement with previous study[31]. The similarity of anodic current trends between various potential windows indicated a stable oxidation process, while the increase in cathodic current peak demonstrated that more CuO was formed under higher potential in anodic cycle. Moreover, the shift of cathodic peak potential to a more negative value under higher potential was on account of the larger amount of CuO formation which required more negative potential to reduce.

Figure 3-5c and d shows the effect of holding potential at 1.5V and -1.5V, respectively, for 10 min on the first cycles of CV. From **Figure 3-5c**, peak CI and CII shifted to larger potential values with higher cathodic currents after holding for 10 min, indicating that more CuO was formed during the holding time as a result of

spillover of O^{2-} to the catalyst, which was more easily reduced upon starting the CV. The negative potential of the CV was increased to -1.35V due to the depletion of O^{2-} in YSZ disk during positive polarization under Ar. Also, the peak current of AI was increased, indicating more Cu_2O formation (eq.3-5) than CuO (eq.3-6) on account of the depletion which led to less O^{2-} supply. In **Figure 3-5d**, the current peak AI increased significantly with a higher anodic current observed, while the current peaks CI and CII were decreased. The starting negative potential of the CV was increased from -1.5V to -1.2V during the holding time, possibly because O^{2-} was removed from the catalyst and penetrated deeply into YSZ bulk and occupied oxygen vacancies under negative polarization. The stored O^{2-} was then supplied to the catalyst rapidly and led to the oxidation of copper catalyst and the increase of peak AI and anodic current accordingly upon starting the CV. The decrease of cathodic current peaks was due to fewer copper oxides formation in anodic scan, which was because of the O^{2-} storage in YSZ bulk during the holding time. The effect of holding time further demonstrated the charging/discharging of O^{2-} between YSZ bulk and copper catalyst, which was also illustrated by a recent study about CV of FeO_x[18]. It was also confirmed that the oxidation and reduction processes could occur easily over the Cu/YSZ.

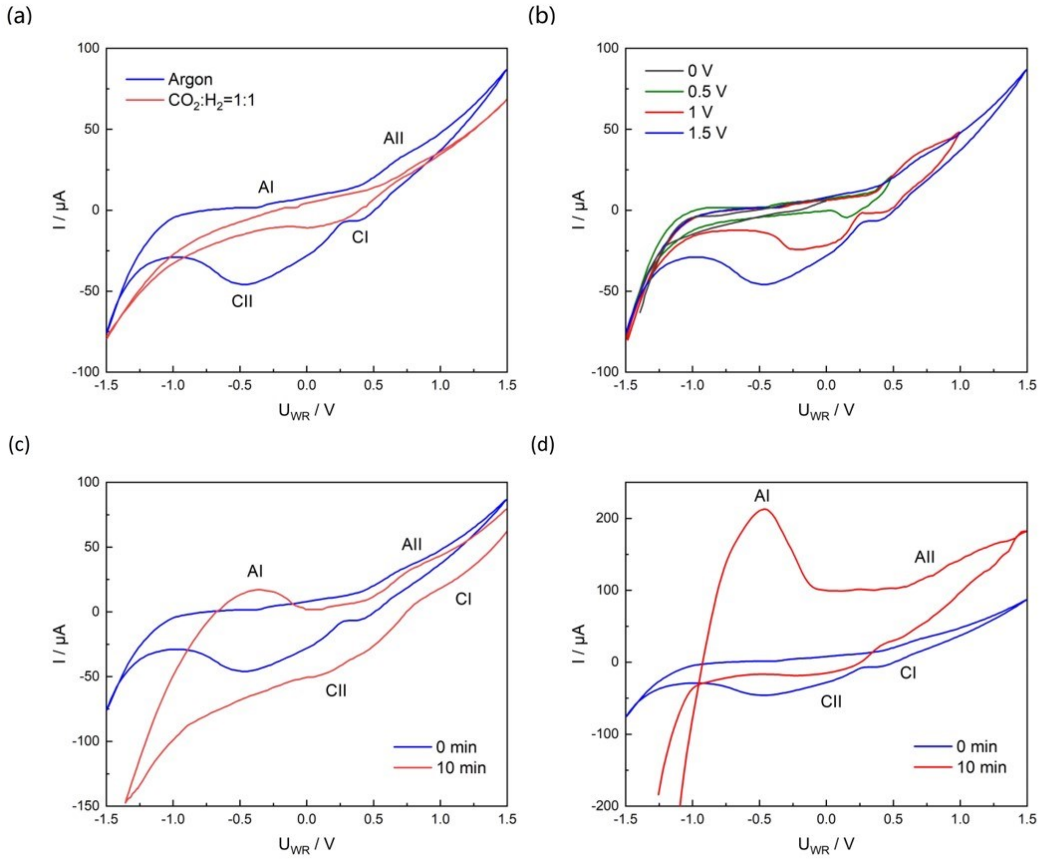

Figure 3-5. Cyclic voltammetry of Cu/YSZ at 400°C (a) in Ar and CO_2:H_2 ratio of 1:1 and (b) in Ar with varying positive potential, 0, 0.5, 1 and 1.5 V. Effect of holding potential at (c) 1.5V and (d) -1.5V for 10 min at 400°C in Ar.

3.3.4 Electrochemical promotion of catalysis

Figure 3-6 shows transient CO production rates and corresponding current response to an application of 2V under CO_2:H_2 ratio of 1:1 at different temperatures. Under all conditions, the reaction rate response was fast, where the rate increased upon the application of positive potential of 2V and rapidly reached the steady-state. When polarization was turned off, the rate quickly returned to its initial state. Before the steady-state, the CO production rate showed stepped growth and the corresponding currents showed a gradual increase upon application of potential, both indicating oxidation state changes of copper catalyst at the beginning of polarization. After the interruption of the potential, the continuous supply of O^{2-} species from YSZ was stopped and the oxidized Cu NPs were reduced under reaction conditions, leading

to a stepwise decline in CO production rate.

The electrochemical promotion of Cu NPs only occurred under anodic polarization at temperatures higher than 340℃ (**Figure 3-6a**) at which temperature a current of 80μA and a CO production rate enhancement of 10% were observed. By increasing the reaction temperature to 360℃ (**Figure 3-6b**) and 400℃ (**Figure 3-6c**), the CO reaction rates increased by 15% and 20% and the corresponding currents also increased to 125μA and 250μA, respectively. At the higher T = 450℃ (**Figure 3-6d**), a weaker enhancement (10%) with a higher current (700μA) compared to 400℃ was observed. The current response to applied potential increased with temperature due to the increased conductivity of YSZ and the reduced state of copper catalyst at high temperature. This was in good line with the TPR study where CuO was reduced to lower oxidation states by hydrogen[6].

Under the stoichiometric condition, a balance was achieved between oxidation of Cu^0 and reduction of copper oxides. After applying a positive potential across the cell, where the O^{2-} species coming from YSZ were supplied towards the catalyst surface through three-phase-boundary (tpb), higher oxidation states (Cu^+ and Cu^{2+}) of copper were formed and subsequently altered the CO production rates. At higher temperatures, an increasing amount of Cu^0 was formed, which provided more opportunities for reacting with O^{2-} species after a positive polarization, resulting in a higher ρ which reached the maximum at 400℃. However, since Cu NPs were easily sintered at high temperatures [25,32], the enhancement was inhibited at 450℃ as a result of the decrease in available active sites that enabled the formation of Cu_2O and CuO. The sintering of Cu NPs was also illustrated through SEM (**Figure 3-2b**). Under negative polarization, no promotion phenomenon was observed indicating an electrophobic EPOC for this type of catalyst[33].

The uptake of reactive oxygen in moles during polarizations, expressed as N_G (mol), was used to characterize the active metal catalyst surface area and estimated by Eq. (3-9):

$$N_G = \frac{I\tau}{2F} \tag{3-9}$$

where I was the current response, F was Faraday's constant, and τ represented the time required for catalytic rate to reach 63% of its promoted steady-state[34]. The N_G and ρ under stochiometric condition at various temperatures were summarized in **Table A-2**. From **Table A-2**, the N_G showed to increase with temperature until 440℃ (1.919×10^{-7} mol) and then decline at 450℃ (1.73×10^{-7} mol), suggesting the sintering of Cu NPs at high temperature which was in agreement with the SEM results.

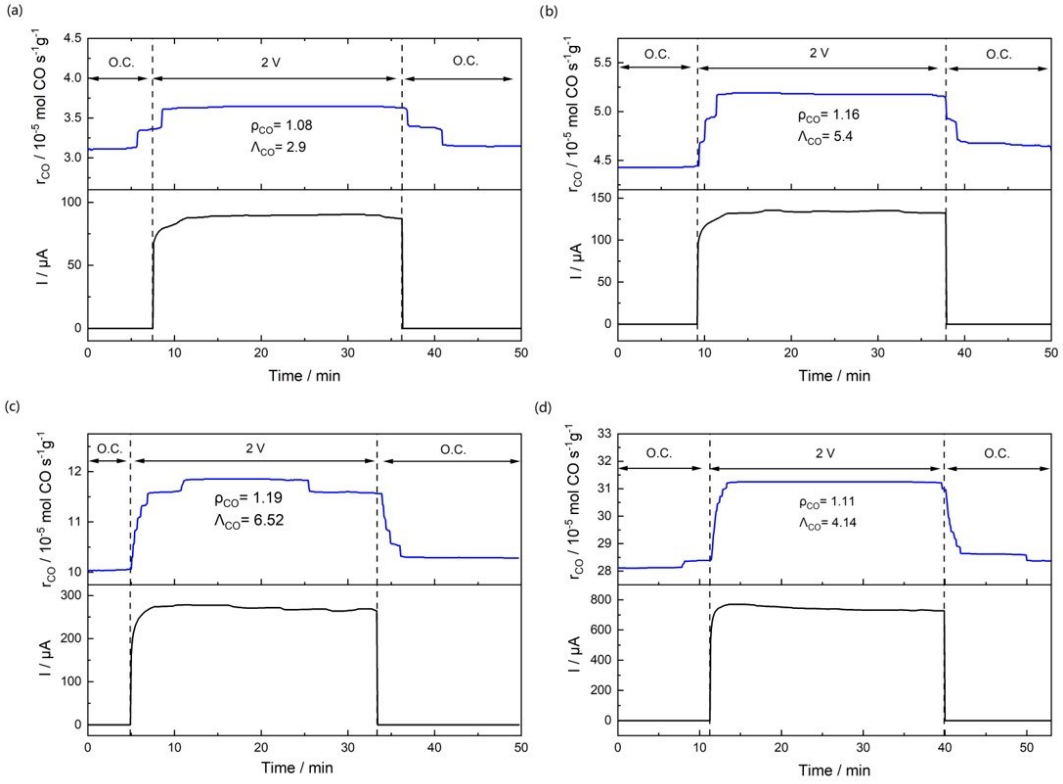

Figure 3-6. Transient response of reaction rates under the application of 2V and CO_2:H_2 ratio of 1:1 at (a) 340℃, (b) 360℃, (c) 400℃ and (d) 450℃.

Figure 3-7 shows transient rate and corresponding current response to an application of 2V at 400℃ under various CO_2:H_2 ratios. Upon polarization, the rate showed similar performance as in the case of CO_2:H_2 ratio of 1:1, increasing stepwise before reaching promoted stable states followed by decreasing to O.C. rates after interruption of potential. At CO_2:H_2 ratio of 3:1 (**Figure 3-7a**), the CO rate increased with ρ=1.17 which was inferior but still comparable to CO_2:H_2 ratio of 1:1 (**Figure 3-6c**) with ρ=1.19, and the rate enhancement performance was further decreased to ρ=1.14 when CO_2:H_2 ratio reached 6:1 (**Figure 3-7b**). However, the CO rate

enhancements under polarization showed prohibition at CO_2:H_2 ratio of 1:3 (**Figure 3-7c**) and 1:6 (**Figure 3-7d**) with ρ=1.11 and ρ=1.07, respectively. This phenomenon was due to the oxidation state alternation of the copper catalyst under different reaction conditions. Under oxidizing conditions ($3CO_2$:H_2 and $6CO_2$:H_2), Cu NPs were oxidized by excessive CO_2 and formed Cu_2O and CuO. At CO_2:H_2 ratio of 3:1 (**Figure 3-7a**), Cu_2O was still dominant which allowed the spillover of O^{2-} species towards catalyst from YSZ under polarization and enabled the dissociation of CO_2 into *O and *CO subsequently, resulting in a great enhancement in CO rate.

At CO_2:H_2 ratio of 6:1 (**Figure 3-7b**), however, the catalyst was fully oxidized and CuO was the dominant state which lacked sufficient oxygen vacancies for *O and thereby inhibited the dissociation of CO_2. After stopping the positive polarizations where Cu was oxidized by O^{2-}, the catalyst remained in the higher oxidation state (CuO) under oxidizing conditions due to the excess of CO_2. Copper oxide, CuO, is less active than Cu^0 and Cu_2O, therefore the open-circuit catalytic rates after polarizations were lower than the initial ones (**Figure 3-7a and b**). Under reducing conditions of CO_2:$3H_2$ (**Figure 3-7c**) and CO_2:$6H_2$ (**Figure 3-7d**), the catalyst was kept at reduced states. Although copper catalyst at lower oxidized states had sufficient oxygen vacancies, the existence of a high concentration of H_2 prohibited the formations of Cu_2O and/or CuO under polarization which were supposed to be the key processes in the electrochemical promotion of Cu NPs.

Also, from **Figure 3-7**, the corresponding currents under oxidizing conditions required a longer time to achieve steady states upon polarization, suggesting that fewer oxidation state changes of catalyst existed under highly reduced conditions. As a result, the enhancements of CO rate were limited and lower than other conditions under reducing circumstances. **Table A-3** summarizes the N_G and ρ at 400℃ under various CO_2:H_2 ratios. The N_G showed to decrease as the concentration of CO_2 increased, which was because of the formation of fully oxidized CuO. However, the N_G was still reduced by increasing the amount of H_2 since the O^{2-} coming from YSZ reacted with the excessive H_2, the uptake of O^{2-} by copper catalyst was thereby

prohibited. The comparison of N_G values between each CO_2:H_2 ratios was in agreement with the observed EPOC phenomenon (ρ), which further demonstrated the redox mechanism.

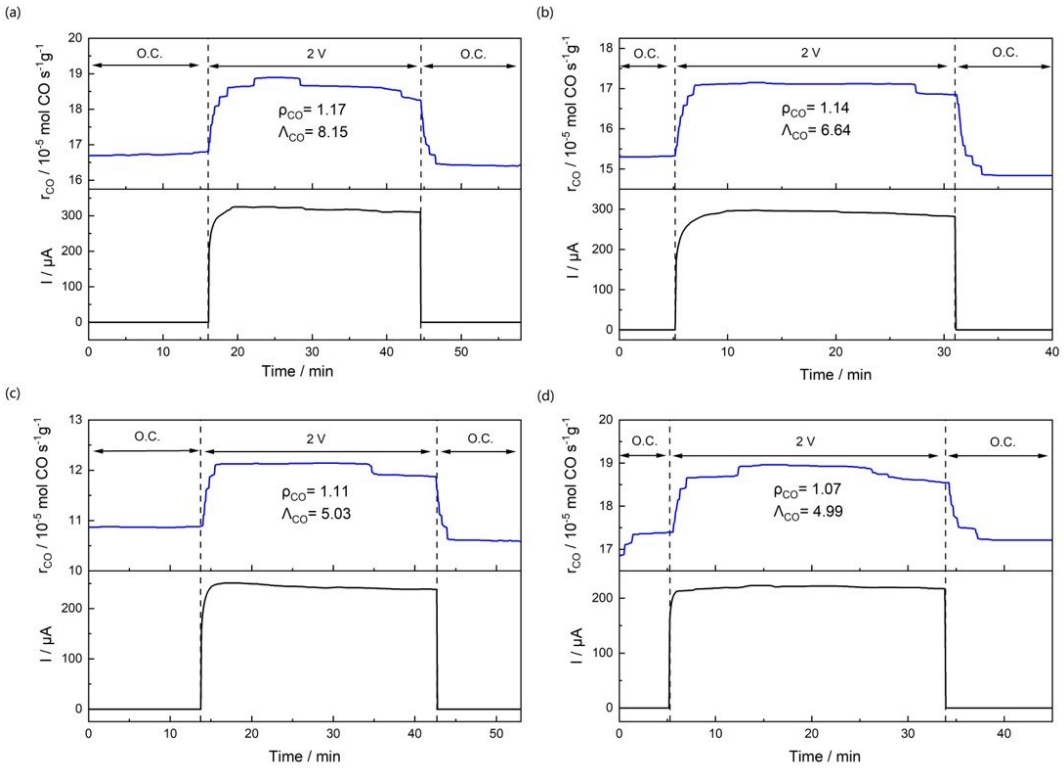

Figure 3-7. Transient response of reaction rates under the application of 2V at 400°C for CO_2:H_2 ratio of (a) $3CO_2$:$1H_2$, (b) $6CO_2$:$1H_2$, (c) $1CO_2$:$3H_2$ and (d) $1CO_2$:$6H_2$.

Figure 3-8a and b summarize the characteristics of ρ and Λ respectively, as functions of temperature and CO_2:H_2 ratio. Except for the CO_2:H_2 ratio of 1:6, under which condition ρ and Λ showed tendencies of going down with temperature, both ρ and Λ increased with temperature initially followed by a decline at higher temperature. This was because, Cu NPs were reduced to lower oxidized states with an increase of temperature under reaction conditions, which could be oxidized by O^{2-} species coming from YSZ after polarization. At temperatures higher than 400°C, Cu NPs started sintering and the promotion was inhibited as a result. From **Figure 3-8**, ρ and Λ reached the peaks at 400°C under stoichiometric and oxidizing conditions, whereas tended to maximize at lower temperatures under reducing conditions where the catalyst was easy to be reduced and thereby ρ and Λ could achieve the peaks more rapidly. The EPOC was prohibited at all temperatures under CO_2:H_2 ratio of 1:6 due

to the suppression of Cu_2O and CuO formations, which was discussed above. The stoichiometric condition showed the highest ρ, meaning that a good balance was achieved between the oxidation of Cu NPs by CO_2 and the reduction of Cu_2O and/or CuO by H_2, which maximized the possibility of oxidation state changes of copper catalyst. The CO_2:H_2 ratio of 3:1 had the highest Λ, which was due to the fact that the CO rate enhancement ratio was similar to that of the stoichiometric condition but the current response to the application of 2V was lower because of the inferior conductivity of copper oxides compared to metallic copper[35]. Further increasing the ratio to 6:1 led to a worse enhancement ratio with a similar current, as a result, the Faradaic efficiency was decreased by calculation.

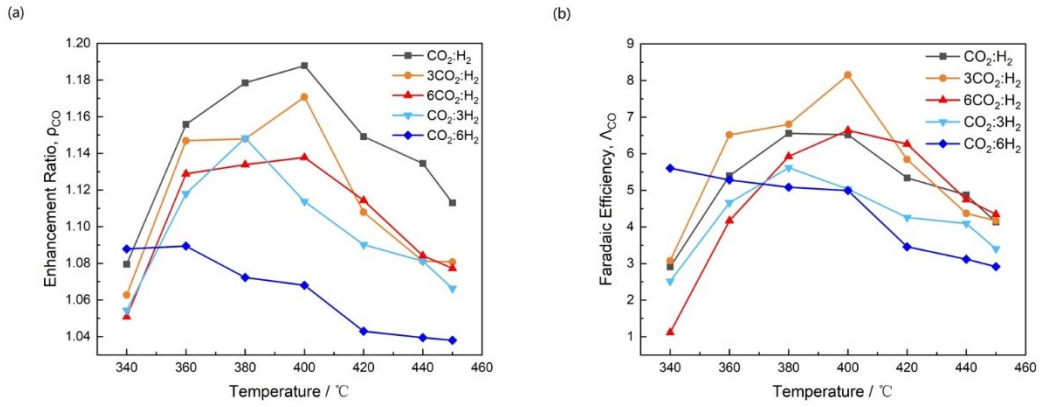

Figure 3-8. Effect of temperature and CO_2:H_2 ratio on (a) the enhancement ratio (ρ) and (b) the Faradaic efficiency (Λ) under the application of 2V.

The effects of applied potential and CO_2:H_2 ratio on ρ and Λ are presented in **Figure 3-9**. In all cases, no promotion occurred under negative polarization (-1V) because O^{2-} species were not supplied to the catalyst. ρ and Λ increased with the growth of positive potential until 2V was applied, and then began to decrease at 2.5V under stoichiometric and oxidizing conditions while kept increasing under reducing conditions. The transient response of CO production rates under various applied potentials and CO_2:H_2 ratios are summarized in **Figure A-6**. This phenomenon further demonstrated the oxidation state difference of copper catalyst under various conditions and the influence of this difference on the EPOC effect. Cu NPs were fully oxidized at 2.5V under oxidizing conditions, making fewer oxygen vacancies of the

catalyst compared to 2V and resulting in fewer CO_2 dissociation and lower values of ρ and Λ. Nevertheless, the catalyst was still at a lower oxidized state under reducing conditions, which meant Cu NPs at higher oxidized states could still be formed by reacting with O^{2-} species conducting from YSZ by increasing the potential from 2V to 2.5V, and ultimately enhanced the CO rate. The trend of CO_2:H_2 ratio effect on ρ and Λ in **Figure 3-9** was similar to that in **Figure 3-8** indicating the redox mechanism of EPOC was working for copper catalyst under particular conditions (temperature and applied potential).

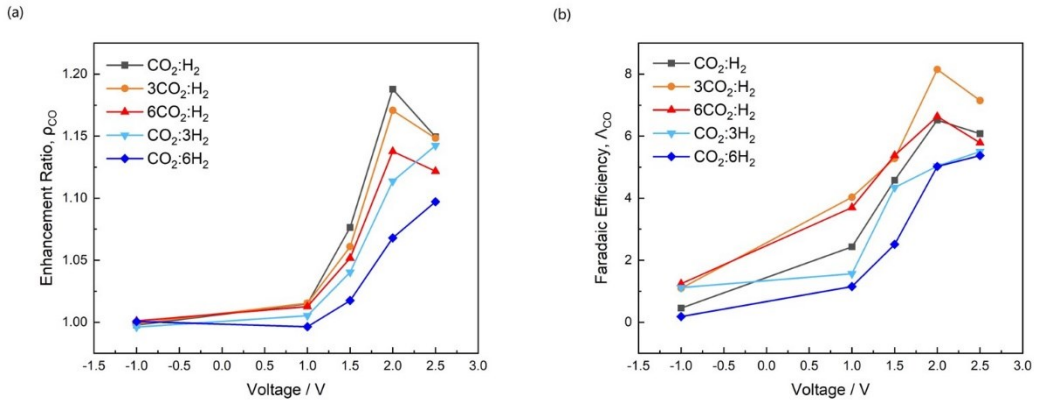

Figure 3-9. Effect of applied voltage and CO_2:H_2 ratio on (a) the enhancement ratio (ρ) and (b) the Faradaic efficiency (Λ) at 400℃.

3.4 Conclusion

In this study, the Cu NPs catalyst is shown to be a good alternative to other metals in the EPOC for the RWGS reaction. The best EPOC effect occurs with ρ=1.19 and Λ= 6.52 under a positive polarization of 2V at 400℃ and 1:1 CO_2:H_2 ratio. Through SEM, STEM, XPS, and CV characterizations, it is confirmed that the RWGS reaction over copper catalyst deposited on YSZ is following the redox mechanism, where the oxidation process of lower oxidized states to higher oxidized states of copper by direct supply of O^{2-} from YSZ under polarization is supposed to be the key process in the electrochemical promotion of Cu NPs. Under oxidizing conditions, the more active states of Cu^0 and Cu_2O are fully oxidized to the less active state of CuO and thereby suppresses the EPOC effect, while under reducing conditions, the limited

promotion is due to the prohibition of copper oxidation process. Our work on Cu/YSZ provides an opportunity of altering the RWGS reaction rates by in-situ controlling the oxidation states of a new copper nano-structured catalyst which is highly active and economic.

References

[1] D.L. Jurković, A. Pohar, V.D.B.C. Dasireddy, B. Likozar, Effect of Copper-based Catalyst Support on Reverse Water-Gas Shift Reaction (RWGS) Activity for CO2 Reduction, Chem. Eng. Technol. 40 (2017) 973–980. https://doi.org/10.1002/ceat.201600594.

[2] S.A. Patil, C.H. Ryu, H.S. Kim, Synthesis and Characterization of Copper Nanoparticles (Cu-Nps) using Rongalite as Reducing Agent and Photonic Sintering of Cu-Nps Ink for Printed Electronics, Int. J. Precis. Eng. Manuf. - Green Technol. 5 (2018) 239–245. https://doi.org/10.1007/s40684-018-0024-7.

[3] V.B. Nam, D. Lee, Copper nanowires and their applications for flexible, transparent conducting films: A review, Nanomaterials. 6 (2016) 47. https://doi.org/10.3390/nano6030047.

[4] P. Gurav, S.S. Naik, K. Ansari, S. Srinath, K.A. Kishore, Y.P. Setty, S. Sonawane, Stable colloidal copper nanoparticles for a nanofluid: Production and application, Colloids Surfaces A Physicochem. Eng. Asp. 441 (2014) 589–597. https://doi.org/10.1016/j.colsurfa.2013.10.026.

[5] J. Pike, S.W. Chan, F. Zhang, X. Wang, J. Hanson, Formation of stable Cu2O from reduction of CuO nanoparticles, Appl. Catal. A Gen. 303 (2006) 273–277. https://doi.org/10.1016/j.apcata.2006.02.008.

[6] J.Y. Kim, J.A. Rodriguez, J.C. Hanson, A.I. Frenkel, P.L. Lee, Reduction of CuO and Cu2O with H2: H embedding and kinetic effects in the formation of suboxides, J. Am. Chem. Soc. 125 (2003) 10684–10692. https://doi.org/10.1021/ja0301673.

[7] J.A. Rodriguez, J.Y. Kim, J.C. Hanson, M. Pérez, A.I. Frenkel, Reduction of CuO in H2: In situ time-resolved XRD studies, Catal. Letters. 85 (2003) 247–254. https://doi.org/10.1023/A:1022110200942.

[8] C.-S. Chen, W.-H. Cheng, S. Lin, Mechanism of CO Formation in Reverse Water – Gas Shift Reaction over Cu / Al2O3 Catalyst., Catal. Letters. 68 (2000) 45–48. https://link.springer.com/content/pdf/10.1023%2FA%3A1021006718974.pdf.

[9] E.L. Fornero, D.L. Chiavassa, A.L. Bonivardi, M.A. Baltanás, Transient analysis of the reverse water gas shift reaction on Cu/ZrO2 and Ga2O3/Cu/ZrO2 catalysts, J. CO2 Util. 22 (2017) 289–298. https://doi.org/10.1016/j.jcou.2017.06.002.

[10] C. Álvarez Galván, J. Schumann, M. Behrens, J.L.G. Fierro, R. Schlögl, E. Frei, Reverse water-gas shift reaction at the Cu/ZnO interface: Influence of the

Cu/Zn ratio on structure-activity correlations, Appl. Catal. B Environ. 195 (2016) 104–111. https://doi.org/10.1016/j.apcatb.2016.05.007.
[11] S.I. Fujita, M. Usui, N. Takezawa, Mechanism of the reverse water gas shift reaction over Cu/ZnO catalyst, J. Catal. 134 (1992) 220–225. https://doi.org/10.1016/0021-9517(92)90223-5.
[12] C.S. Chen, W.H. Cheng, Study on the mechanism of CO formation in reverse water gas shift reaction over Cu/SiO2 catalyst by pulse reaction, TPD and TPR, Catal. Letters. 83 (2002) 121–126. https://doi.org/10.1023/A:1021006718974.
[13] M.S. Usman, M.E. El Zowalaty, K. Shameli, N. Zainuddin, M. Salama, N.A. Ibrahim, Synthesis, characterization, and antimicrobial properties of copper nanoparticles, Int. J. Nanomedicine. 8 (2013) 4467–4479. https://doi.org/10.2147/IJN.S50837.
[14] J. Leitner, D. Sedmidubský, O. Jankovský, Thermodynamic modeling of copper nanoparticles oxidation, AIP Conf. Proc. 2170 (2019) 1–6. https://doi.org/10.1063/1.5132726.
[15] F.A. Akgul, G. Akgul, N. Yildirim, H.E. Unalan, R. Turan, Influence of thermal annealing on microstructural, morphological, optical properties and surface electronic structure of copper oxide thin films, Mater. Chem. Phys. 147 (2014) 987–995. https://doi.org/10.1016/j.matchemphys.2014.06.047.
[16] M. Swadźba-Kwaśny, L. Chancelier, S. Ng, H.G. Manyar, C. Hardacre, P. Nockemann, Facile in situ synthesis of nanofluids based on ionic liquids and copper oxide clusters and nanoparticles, Dalt. Trans. 41 (2012) 219–227. https://doi.org/10.1039/c1dt11578b.
[17] Y. Wang, Y. Lü, W. Zhan, Z. Xie, Q. Kuang, L. Zheng, Synthesis of porous Cu2O/CuO cages using Cu-based metal-organic frameworks as templates and their gas-sensing properties, J. Mater. Chem. A. 3 (2015) 12796–12803. https://doi.org/10.1039/c5ta01108f.
[18] C. Panaritis, J. Zgheib, S.A.H. Ebrahim, M. Couillard, E.A. Baranova, Electrochemical in-situ activation of Fe-oxide nanowires for the reverse water gas shift reaction, Appl. Catal. B Environ. 269 (2020) 118826. https://doi.org/10.1016/j.apcatb.2020.118826.
[19] Y. Liu, D. Liu, Study of bimetallic Cu-Ni/γ-Al2O3 catalysts for carbon dioxide hydrogenation, Int. J. Hydrogen Energy. 24 (1999) 351–354. https://doi.org/10.1016/S0360-3199(98)00038-X.
[20] D. Zagoraios, S. Tsatsos, S. Kennou, C.G. Vayenas, G. Kyriakou, A. Katsaounis, Tuning the RWGS Reaction via EPOC and in Situ Electro-oxidation of Cobalt Nanoparticles, ACS Catal. (2020) 14916–14927. https://doi.org/10.1021/acscatal.0c04133.
[21] D. Zagoraios, C. Panaritis, A. Krassakopoulou, E.A. Baranova, A. Katsaounis, C.G. Vayenas, Electrochemical promotion of Ru nanoparticles deposited on a proton conductor electrolyte during CO2 hydrogenation, Appl. Catal. B Environ. 276 (2020) 119148. https://doi.org/10.1016/j.apcatb.2020.119148.
[22] M.D. Porosoff, B. Yan, J.G. Chen, Catalytic reduction of CO2 by H2 for synthesis of CO, methanol and hydrocarbons: Challenges and opportunities,

Energy Environ. Sci. 9 (2016) 62–73. https://doi.org/10.1039/c5ee02657a.
[23] M. Hu, J. He, R. Guo, W. Yuan, W. Xi, J. Luo, Y. Ding, Visualizing oxidation of Cu nanoparticles at atomic resolution during the reverse water-gas shift reaction, Catal. Commun. 146 (2020) 106129. https://doi.org/10.1016/j.catcom.2020.106129.
[24] W. Wang, S. Wang, X. Ma, J. Gong, Recent advances in catalytic hydrogenation of carbon dioxide, Chem. Soc. Rev. 40 (2011) 3703–3727. https://doi.org/10.1039/c1cs15008a.
[25] M. Konsolakis, M. Lykaki, S. Stefa, S.A.C. Carabineiro, G. Varvoutis, E. Papista, G.E. Marnellos, Co2 hydrogenation over nanoceria-supported transition metal catalysts: Role of ceria morphology (nanorods versus nanocubes) and active phase nature (co versus cu), Nanomaterials. 9 (2019) 1739. https://doi.org/10.3390/nano9121739.
[26] W.N.R.W. Isahak, Z.A.C. Ramli, M.W. Ismail, K. Ismail, R.M. Yusop, M.W.M. Hisham, M.A. Yarmo, Adsorption-desorption of CO2 on different type of copper oxides surfaces: Physical and chemical attractions studies, J. CO2 Util. 2 (2013) 8–15. https://doi.org/10.1016/j.jcou.2013.06.002.
[27] J.A. Loiland, M.J. Wulfers, N.S. Marinkovic, R.F. Lobo, Fe/γ-Al2O3 and Fe-K/γ-Al2O3 as reverse water-gas shift catalysts, Catal. Sci. Technol. 6 (2016) 5267–5279. https://doi.org/10.1039/c5cy02111a.
[28] Y.A. Daza, J.N. Kuhn, CO2 conversion by reverse water gas shift catalysis: Comparison of catalysts, mechanisms and their consequences for CO2 conversion to liquid fuels, RSC Adv. 6 (2016) 49675–49691. https://doi.org/10.1039/c6ra05414e.
[29] L. Pastor-Pérez, F. Baibars, E. Le Sache, H. Arellano-García, S. Gu, T.R. Reina, CO2 valorisation via Reverse Water-Gas Shift reaction using advanced Cs doped Fe-Cu/Al2O3 catalysts, J. CO2 Util. 21 (2017) 423–428. https://doi.org/10.1016/j.jcou.2017.08.009.
[30] M. Fee, S. Ntais, A. Weck, E.A. Baranova, Electrochemical behavior of silver thin films interfaced with yttria-stabilized zirconia, J. Solid State Electrochem. 18 (2014) 2267–2277. https://doi.org/10.1007/s10008-014-2477-0.
[31] S.D. Giri, A. Sarkar, Electrochemical Study of Bulk and Monolayer Copper in Alkaline Solution, J. Electrochem. Soc. 163 (2016) H252–H259. https://doi.org/10.1149/2.0071605jes.
[32] C.S. Chen, W.H. Cheng, S.S. Lin, Enhanced activity and stability of a Cu/SiO2 catalyst for the reverse water gas shift reaction by an iron promoter, Chem. Commun. 1 (2001) 1770–1771. https://doi.org/10.1039/b104279n.
[33] S. Brosda, C.G. Vayenas, J. Wei, Rules of chemical promotion, Appl. Catal. B Environ. 68 (2006) 109–124. https://doi.org/10.1016/j.apcatb.2006.07.021.
[34] P. Vernoux, L. Lizarraga, M.N. Tsampas, F.M. Sapountzi, A. De Lucas-Consuegra, J.L. Valverde, S. Souentie, C.G. Vayenas, D. Tsiplakides, S. Balomenou, E.A. Baranova, Ionically conducting ceramics as active catalyst supports, Chem. Rev. 113 (2013) 8192–8260. https://doi.org/10.1021/cr4000336.

[35] A.A. Ogwu, Electrical resistivity of copper oxide thin films prepared by reactive magnetron sputtering, J. Achiev. Mater. Manuf. Eng. 24 (2007) 172–177. http://www.journalamme.org/papers_vol24_1/24121.pdf.

Appendix A: Supplementary Information for Chapter 3

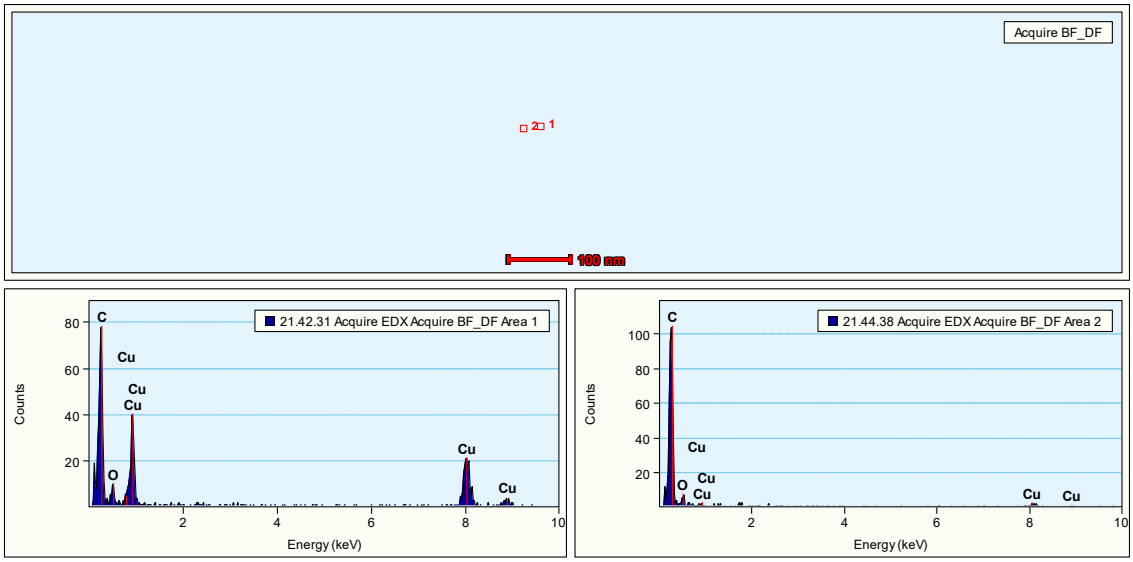

Figure A-1. EDX spectrum of as-prepared Cu catalyst.

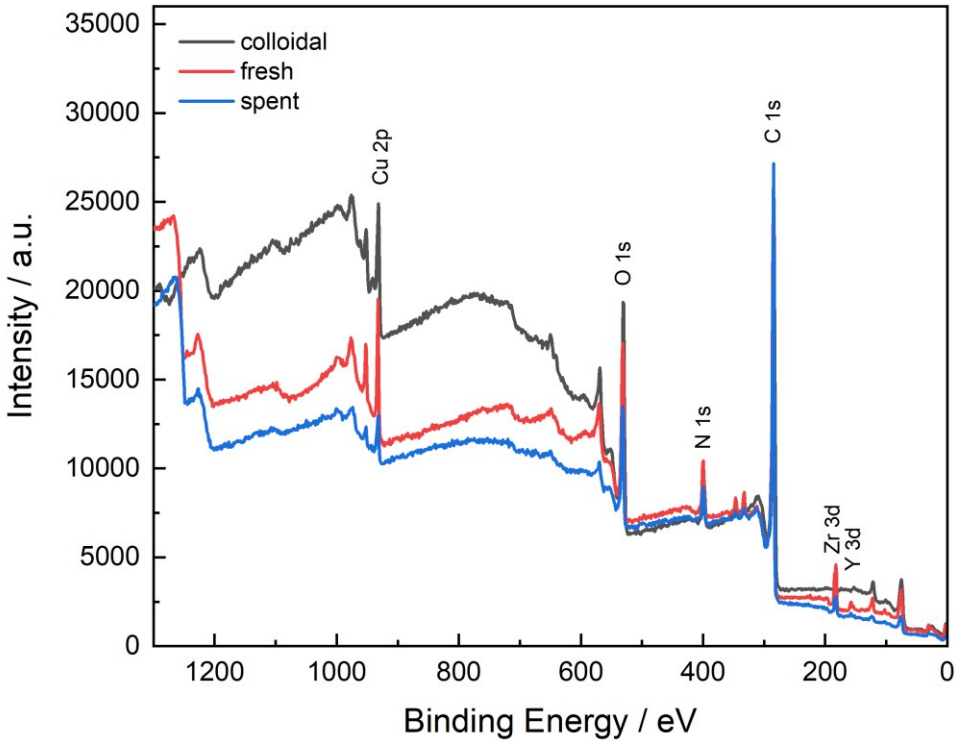

Figure A-2. Wide scan of XPS spectrum for colloidal, as-prepared, and spent samples.

Table A-1. XPS data of Cu 2p and C 1s for the colloidal, as-prepared, and spent samples.

		Position (eV)			FWHM			%Area		
		colloidal	as-prepared	spent	colloidal	as-prepared	spent	colloidal	as-prepared	spent
Cu2p	Cu(0)	932.68	932.61	932.58	0.94	1.10	1.10	5.07	8.06	11.96
	Cu(I) Oxide	932.17	932.16	932.18	1.09	1.01	0.97	34.51	74.15	41.89
	Cu(II) Oxide	933.30	933.30	933.06	2.08	2.06	2.06	55.65	7.06	36.14
	Cu(II) Hydroxide	934.72	934.62	934.62	2.84	2.84	2.84	4.77	10.73	10.01
C1s	C-C, C-H	284.83	284.80	284.80	1.40	1.20	1.15	67.44	77.90	84.60
	C-OH, C-O-C	286.62	286.62	286.63	1.60	1.57	1.17	21.05	15.51	8.95
	C=O	288.07	288.10	287.80	1.60	1.57	1.17	1.29	1.33	1.25
	O-C=O	288.73	288.82	288.93	1.60	1.60	1.50	5.62	4.06	3.98
	Carbonate	290.57	290.74	290.63	1.31	1.31	1.31	1.30	1.21	1.22
	Carbide	283.10			1.60			3.31		

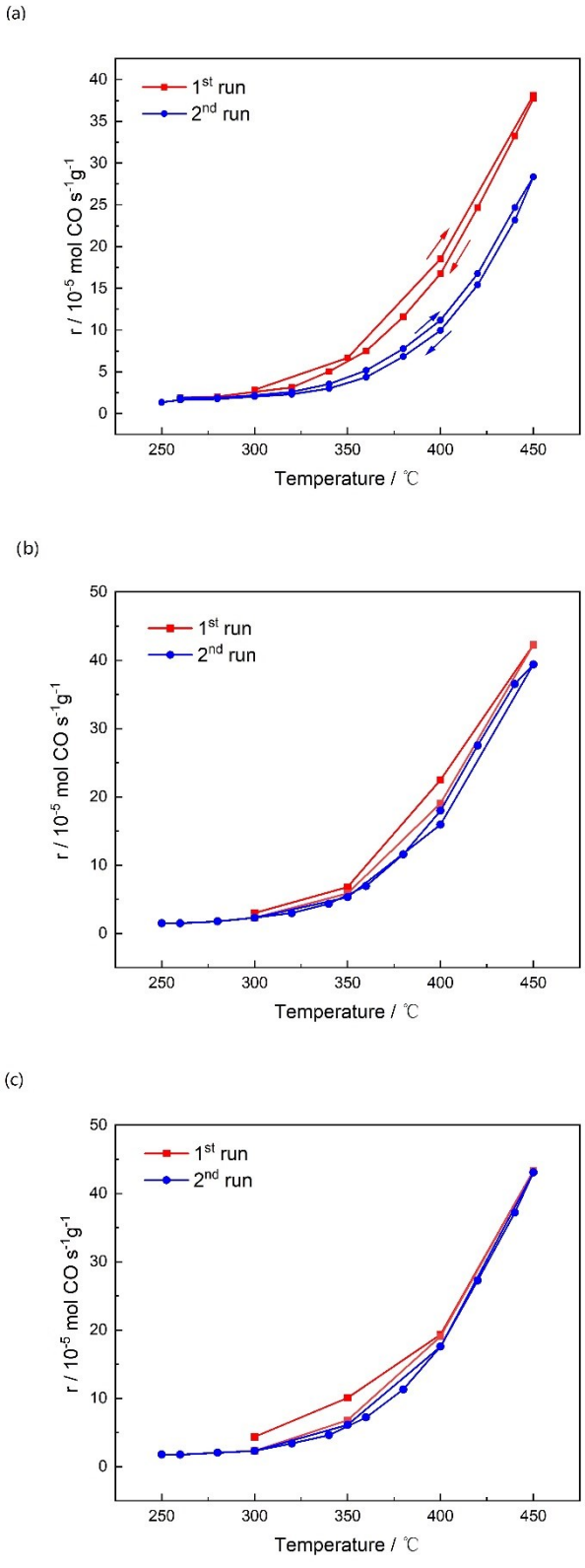

Figure A-3. Overall catalytic open-circuit CO production rate of Cu/YSZ under (a) CO_2:H_2 ratio of 1:1 (b) CO_2:H_2 ratio of 3:1 and (c) CO_2:H_2 ratio of 1:6.

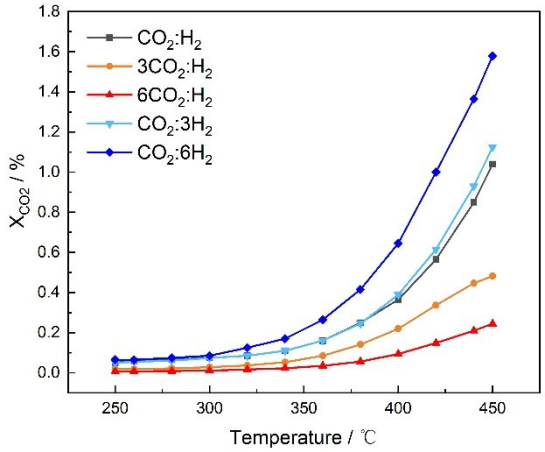

Figure A-4. Open-circuit CO_2 conversion rate of Cu/YSZ under different CO_2:H_2 ratios.

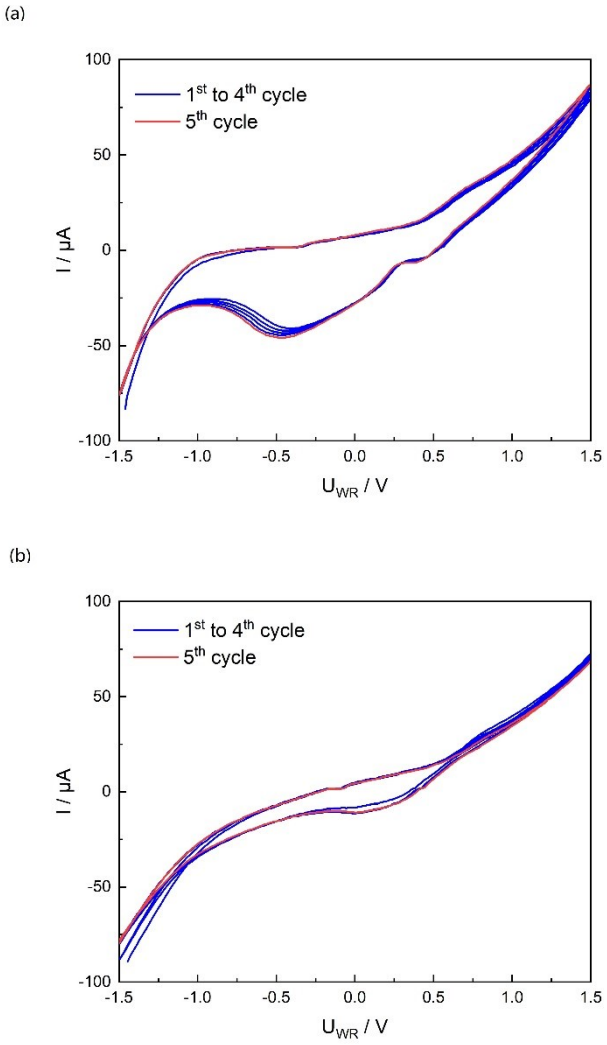

Figure A-5. Overall CV cycles of Cu/YSZ at 400℃ under (a) Argon and (b) CO_2:H_2 ratio of 1:1.

Table A-2. Summary of N_G and ρ under stochiometric condition at various temperatures.

Temperature (℃)	N_G (mol O uptake)	ρ
340℃	2.987×10^{-8}	1.08
360℃	3.813×10^{-8}	1.16
400℃	1.01×10^{-7}	1.19
440℃	1.919×10^{-7}	1.14
450℃	1.73×10^{-7}	1.11

Table A-3. Summary of N_G and ρ at 400℃ under various CO_2:H_2 ratios.

CO_2:H_2 ratio	N_G (mol O uptake)	ρ
$1CO_2$:$1H_2$	1.01×10^{-7}	1.19
$3CO_2$:$1H_2$	9.311×10^{-8}	1.17
$6CO_2$:$1H_2$	7.017×10^{-8}	1.14
CO_2:$3H_2$	6.934×10^{-8}	1.11
CO_2:$6H_2$	6.846×10^{-8}	1.07

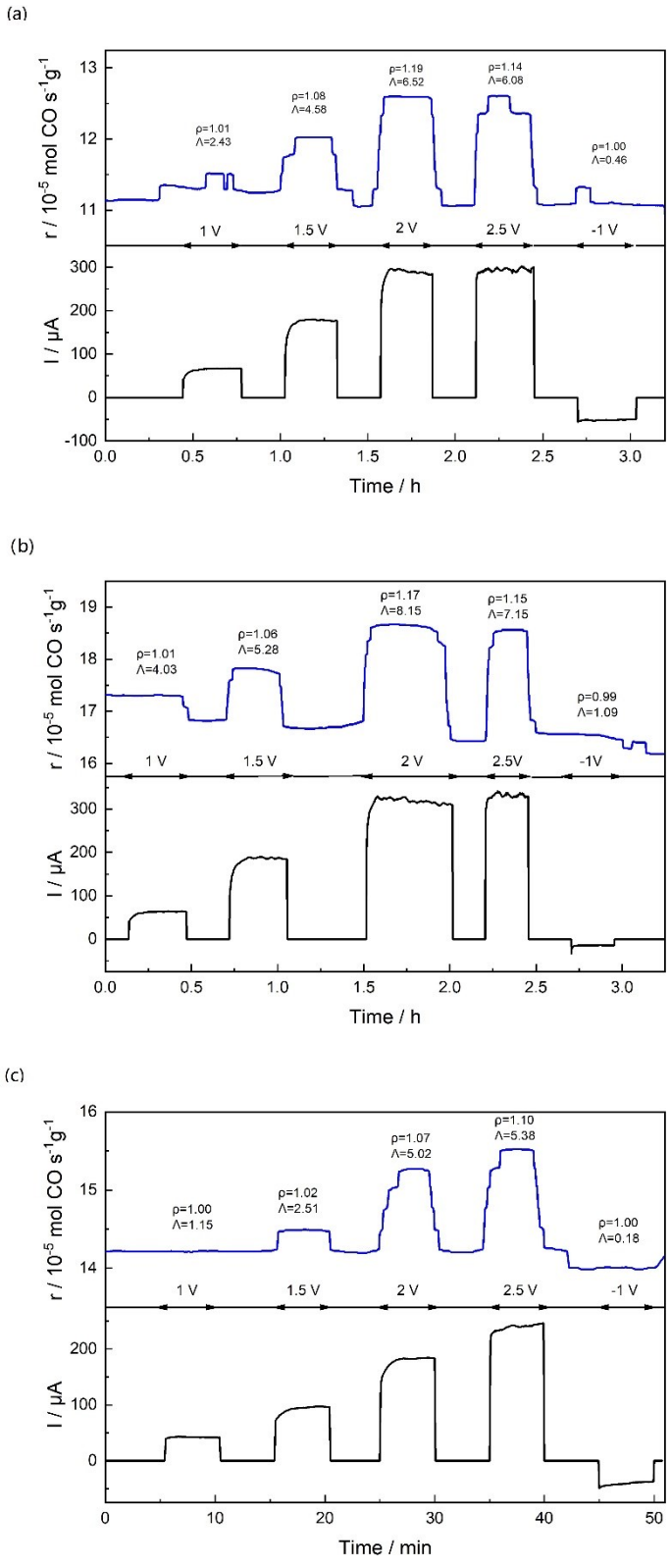

Figure A-6. Transient response of CO rate under various applied potential 1, 1.5, 2, 2.5, -1V at 400℃ under (a) CO_2:H_2 ratio of 1:1 (b) CO_2:H_2 ratio of 3:1 and (c) CO_2:H_2 ratio of 1:6.

Chapter 4: Electrochemical Promotion of Cu/Co_3O_4 for the Reverse Water Gas Shift Reaction

Adapted from: ***J. Wang****, M. Couillard, E.A. Baranova, 2023, ChemCatChem.*

Abstract: Copper-modified Co_3O_4 (Cu/Co_3O_4) catalysts were investigated for the reverse water gas shift (RWGS) reaction at 200-400°C under different CO_2:H_2 ratios. It was found that the electrocatalytic performance of Co_3O_4 was improved by loading 4 weight percent (wt.%) Cu nanoparticles (average size: 13 nm), which could be then used as an electrode in electrochemical promotion of catalysis (EPOC) studies. Under the applied voltages of +2 V and -1 V, the catalytic rates were suppressed and increased by about 40% and 14%, respectively. This was due to the changes in the active oxidation states of Cu and Co caused by O^{2-} migration under polarization, as confirmed by XPS, XRD, and cyclic voltammetry (CV). The study also revealed that the exchange current density (i_0) was counter-correlated with the open-circuit catalytic rate (r_0) and could serve as an informative tool for predicting the catalytic rate, which was demonstrated for the first time in the instance of RWGS reaction.

4.1 Introduction

Copper, a non-noble metal, shows great potential in catalyzing RWGS due to its high activity and low price[1,2]. Chapter 3 regarding Cu NPs deposited on YSZ (Cu/YSZ) illustrates the possibility of promoting RWGS catalytic rate by in-situ controlling the oxidation states of Cu NPs. However, catalyst deactivation remains a problem since copper is prone to oxidation[3] and sintering at high temperatures[4,5]. Therefore, selecting suitable oxides as supports for Cu NPs is considered a practical method to improve thermal stability and dispersion of Cu NPs[6]. Cobalt oxide (Co_3O_4) is a conductive metal oxide[7] and has a high oxygen storage-release capacity[7,8], which is considered beneficial for O^{2-} migration. Studies on Co_3O_4-based catalysts, including Ru/Co_3O_4 deposited on BZY[9] and Fe/Co_3O_4 deposited on

YSZ[10], have been investigated to further illustrate the interaction and O^{2-} migration between metal catalysts and oxide support during EPOC.

In the present study, we investigated commercial Co_3O_4 powder as a catalyst for RWGS in the temperature range of 200-400°C under stoichiometric (CO_2:H_2=1:1), oxidizing (CO_2:H_2=3:1) and reducing (CO_2:H_2=1:6) conditions. The powder was also modified by adding 1, 4 and 8 wt.% of Cu nanoparticles (NPs) with an average size of 13 nm. The open circuit catalytic rates (r_0) of bare and Cu-modified Co_3O_4 (Cu/Co_3O_4) catalysts were studied followed by detailed electrochemical characterizations using cyclic voltammetry (CV), linear sweep voltammetry (LSV), and chronoamperometry (CA). For the first time, the EPOC was demonstrated for Cu/Co_3O_4 catalysts to alter the catalytic performance of RWGS reaction. The exchange current density (i_0) was estimated for the first time as an informative tool to evaluate the electrocatalytic properties of Co_3O_4-based catalysts and predict the r_0. The crystalline structure, elemental composition, oxidation states and morphology of the catalysts were characterized using XRD, STEM, EELS, XPS and SEM.

4.2 Experimental

4.2.1 Catalysts synthesis

The Cu NPs were synthesized using the polyol method following the same procedures as reported in Chapter 3 and stored in colloidal solution (1 mg mL^{-1}). The Cu/Co_3O_4 catalysts were prepared by mixing Cu colloidal solution with commercially purchased Co_3O_4 (Cobalt (II, III) oxide nanopowder, Sigma-Aldrich, specific surface area of 40−70 m^2 g^{-1}) powders in deionized water (DI water, 18 MΩ cm) for 48 h for the desired Cu loadings of 1, 4, and 8wt.% on Co_3O_4. For instance, 10 mL of Cu colloidal solution, which corresponded to 10 mg of Cu NPs, was mixed with 1000 mg of Co_3O_4 powders in DI water to generate 1wt.%Cu/Co_3O_4. The dispersed Cu/Co_3O_4 catalysts were then centrifuged and washed three times with DI water at 6000 rpm with supernatant discarded and precipitate collected, followed by drying in air at 60°C

for 24h. The final catalysts after preparation were in powder forms and stored for future tests.

4.2.2 Experimental setup

The YSZ and gold electrodes were prepared as detailed in Chapter 2. For catalyst-working electrode, 0.1 g of the Cu/Co_3O_4 catalysts was dispersed in 10 mL of DI water under ultrasound. Then the catalyst ink was deposited on YSZ disks in the amount of 5 μL at a time over the masked area of 1 cm^2, opposite to the counter electrode, and left to dry in air at 100℃ in between each deposition until a mass loading of 0.5 mg cm^{-2} was achieved. The electrochemical cell was then placed in a single-chamber quartz reactor in a sandwich structure. H_2 (Messer, 100 %), CO_2 (Messer, 99.99%), and Ar (Messer, 100 %) were fed to the reactor via separate mass flow controllers (MFC, MKS Instruments), which were used to modify the inlet CO_2:H_2 ratios to be 1:1, 3:1, and 1:6 by adjusting the flowrates. The total volumetric flowrate was kept at 100 mL min^{-1}. Before any experiments, the catalysts were pre-treated using the same procedures in Chapter 2 and left under reaction conditions for 5h to ensure the steady state.

All electrochemical measurements were carried out using potentiostat–galvanostat (Arbin Instruments, MSTAT). Cyclic voltammetry (CV) was performed under inert condition (in Argon) at 400℃. The potential window was set to begin from -1.0 V to 1.5 V, followed by cycling back to -1.0 V with a scanning rate of 20 mV s^{-1}. The EPOC tests were carried out by applying a constant potential across the catalyst-working electrode and the counter electrode and were characterized by the rate enhancement ratio (ρ) in Eq. (4-1) and apparent Faradaic efficiency (Λ) in Eq. (4-2):

$$\rho = r/r_0 \tag{4-1}$$

$$|\Lambda| = \Delta r/(I/nF) \tag{4-2}$$

where r is the steady-state reaction rate after polarization, r_o is the open-circuit rate before polarization, I is the current response to the applied potential, F is the Faradaic

constant, and n is the number of electrons transferred, which is 2 in the case of RWGS reaction. The unit of reaction rate r is mole CO per second per gram of catalyst (mol CO s^{-1} g^{-1}).

Linear sweep voltammetry (LSV) at scan rate of 20 mV s^{-1} were used to obtain Tafel plots. The exchange current density (i_0) was determined from the intercept at U_{WR} = 0 in Tafel plots (ln I vs. U_{WR}) based on the potentiostat-galvanostat data of current responses (I) to various applied potentials (U_{WR}).

4.2.3 Characterizations

Scanning Transmission Electron Microscopy (STEM) was carried out on as-prepared and spent Cu/Co_3O_4 catalysts to determine the microstructure and particle size. High-angle annular dark-field (HAADF) imaging was conducted with a convergence semi-angle of 18 mrad and a collection semi-angle of 60 mrad to provide a contrast sensitive to the atomic number Z.

Scanning Electron Microscopy (SEM, JSM-7500F FESEM) was used to characterize the morphology of spent catalysts stayed on the YSZ surface.

X-ray Diffraction (XRD) patterns were measured over as-prepared and spent catalysts to investigate the crystalline structure changes by the Rigaku Ultima IV multipurpose diffractometer at a scanning rate of 1 degree (°) min^{-1} from 20 to 80 °2θ.

Determination of the metal composition of Cu/Co_3O_4 was performed on triplicate samples by Inductively Coupled Plasma Optical Emission Spectroscopy (ICP-ES) (Agilent 8800).

The X-ray photoelectron spectroscopy (XPS) spectra were measured on a Kratos AXIS Nova spectrometer equipped with an Al X-ray source to determine the oxidation states of Cu and Co. The data were collected using AlK_α radiation at 1486.69 eV (150 W, 10 mA). Binding energies were referred to the C 1s peak at 285 eV. All XPS peaks were fitted using CasaXPS software with Shirley background corrections and Gaussian-Lorentzian shape function for high resolution XPS spectra.

4.3 Results

4.3.1 Catalyst characterizations

The ICP-ES analysis confirmed consistency between the nominal and actual Cu loading amounts on Co_3O_4, which were 1, 4, and 8wt.% (± 0.3 – 0.5wt.%). **Figure 4-1** shows the STEM images of the as-prepared and spent 4wt.%Cu/Co_3O_4 with corresponding EELS mapping of Copper (Cu), Cobalt (Co), Oxygen (O), and Carbon (C) in the orange square (the yellow squares are for drift correction). From HAADF-STEM image in **Figure 4-1a**, Cu was found to be attached to the surface of Co_3O_4 structure in as-prepared sample. **Figure B-1** summarizes the size distribution of Cu NPs according to the TEM image, where the average particle size was found to be 13 ± 2 nm. Also, energy electron loss spectroscopy (EELS) mapping in **Figure 4-1b** showed that the location of O was in line with those of Cu and Co, confirming the high oxidation state of CuO_x and Co_3O_4. No carbon was found, suggesting complete removal of residual organics used for synthesis.

In spent sample (**Figure 4-1c**), Cu was still found on the surface of Co after all experimental tests with apparent agglomeration observed. Nevertheless, as opposed to the as-prepared catalyst, Co in spent catalyst showed fewer oxygen amounts since the areas of O and Co no longer fitted completely, while the position of O was still aligned to that of Cu. This indicated the reduction of Co_3O_4 under experimental conditions (reducing atmosphere and polarization) where O^{2-} was partially lost from CoO_x and supplied to Cu during catalytic experiments. Also, the appearance of carbon in EELS mapping revealed the occurrence of surface carbon deposition phenomenon in spent sample, which was derived from CO_2 under the reaction conditions.

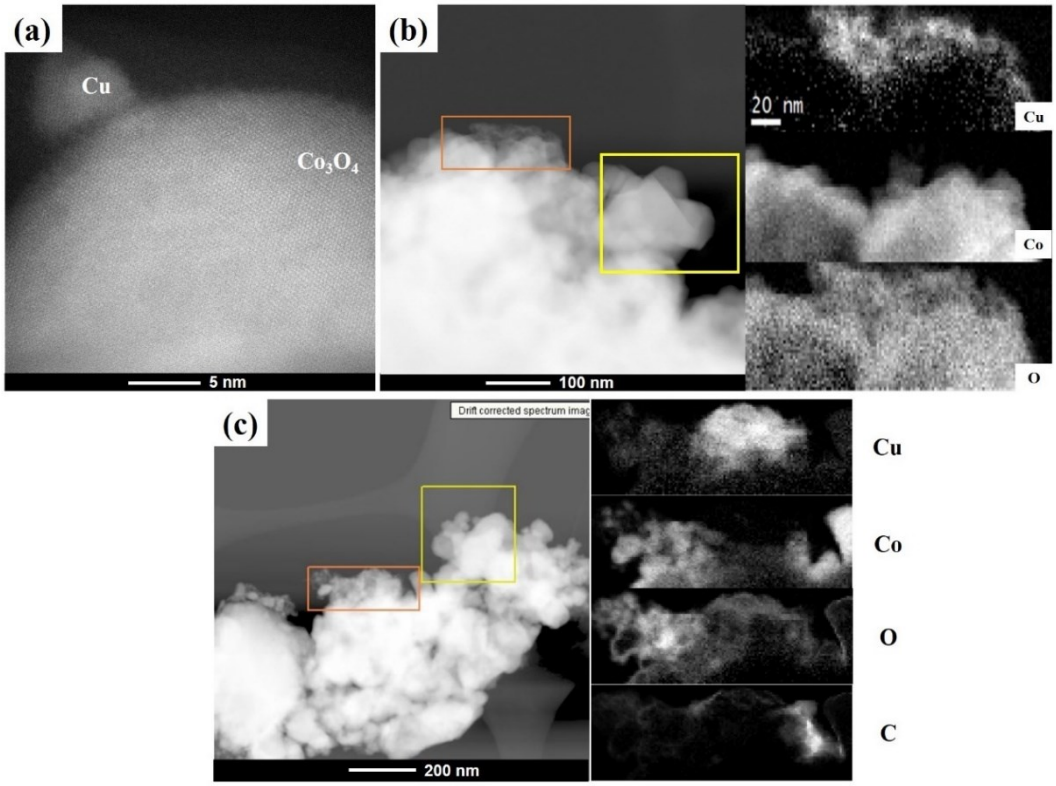

Figure 4-1. HAADF-STEM image of (a) as-prepared 4wt.%Cu/Co_3O_4 and EELS mappings with corresponding elemental composition of (b) as-prepared and (c) spent 4wt.%Cu/Co_3O_4 catalyst.

Figure 4-2 shows the SEM images of spent Cu/Co_3O_4 catalysts with various copper loading of 0, 1, 4, and 8wt.%. The bare Co_3O_4 showed a porous structure with a relatively smooth surface (**Figure 4-2a**), whereas as Cu loading on Co_3O_4 increased from 1 to 8wt.% (**Figure 4-2b, c, and d**), the structure became more rough and less porous with smaller particles observed on the surface that corresponded to Cu NPs. **Figure B-2** shows the SEM images on a larger scale (10μm) of the spent Cu/Co_3O_4 catalyst of 0, 1, 4 and 8wt.%Cu/Co_3O_4. The increased size of Cu NPs was due to the agglomeration that easily happened to Cu with high concentration, as shown in **Figure B-3a** where free-standing Cu NPs were found to be agglomerated. From **Figure B-3b**, free-standing Cu showed to be prone to sintering at high temperatures under reaction conditions, therefore, the increased amount of Cu on Co_3O_4 aggravated the occurrence of sintering phenomenon, which also resulted in the less porous structure. Additionally, **Figure B-4a** shows the fresh sample of 4wt.%Cu/Co_3O_4 that is collected after pre-treatments, where catalyst is well-dispersed compared to the

spent one (**Figure B-4b**), indicating that sintering occurs at temperatures higher than 350℃ under reaction conditions. According to the SEM results, the improvement in dispersion of Cu NPs and the prevention of heavy sintering were achieved by supporting on Co_3O_4.

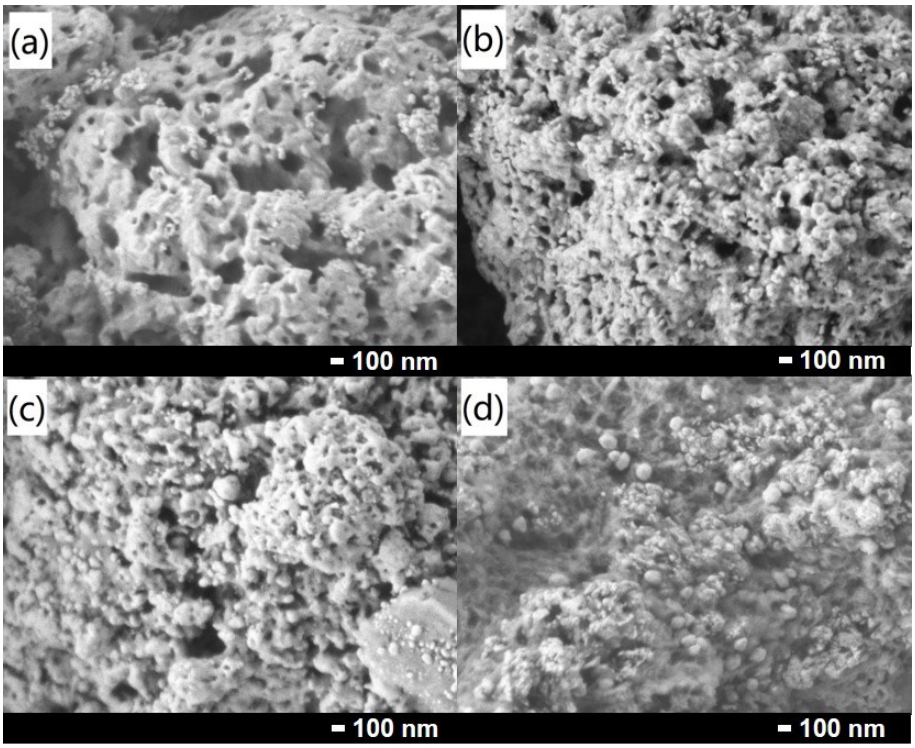

Figure 4-2. SEM images of spent (a) Co_3O_4, (b) 1wt.%Cu/Co_3O_4, (c) 4wt.%Cu/Co_3O_4, and (d) 8wt.%Cu/Co_3O_4 deposited on YSZ on the scale of 100nm.

Figure 4-3 shows XRD patterns of as-prepared and spent 4wt.%Cu/Co_3O_4 catalysts. Due to the small particle size and limited loading amount, Cu NPs were not detected in XRD. Also, no peaks associated with any impurities were observed. In **Figure 4-3a**, the as-prepared catalyst was mostly present in Co_3O_4, where the peaks were assigned to a pure Co_3O_4 phase[11–13]. The crystallite structure of the spent catalyst changed significantly with new diffraction peaks observed at 41, 47, and 76 °2θ, corresponding to metallic Co (100), (101), (110), respectively[14,15], while the peak at 44 °2θ indicated the dominant Co_3O_4 (404) phase. This confirms the change in the oxidation state of Co from higher one (Co_3O_4) to lower one CoO_x during the catalytic reaction under the reducing condition of RWGS and the applied polarization. The carbon deposition in spent sample was not detected in XRD due to

the amorphous structure of carbon and its small quantity on the surface as seen in STEM (**Figure 4-1b**). These results are different from a recent study on FeO_x/Co_3O_4 catalyst for RWGS where carbon nanotubes (CNTs) were formed on the surface and observed using the X-ray diffraction[10].

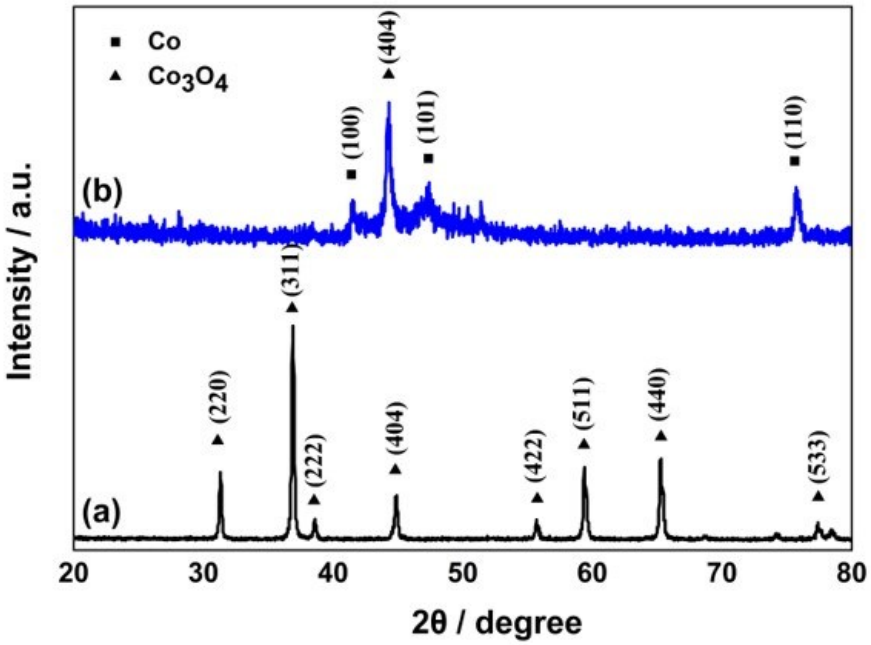

Figure 4-3. XRD patterns of (a) as-prepared and (b) spent 4wt.%Cu/Co_3O_4.

Figure 4-4 shows the XPS spectra of fresh and spent samples for Cu $2p_{3/2}$ and Co $2p_{3/2}$. The peaks at 932 and 934 eV in Cu $2p_{3/2}$ represent metallic copper/Cu_2O (Cu^0/Cu^{1+}) and CuO (Cu^{2+})[16], respectively. The peaks at 778, 779 and 781 eV in Co $2p_{3/2}$ are identified as metallic cobalt (Co^0), Co_3O_4 ($Co^{2+,3+}$) and CoO (Co^{2+})[17]. The species information is summarized in **Table B-1**. From **Figure 4-4a**, Cu was found to be mainly in reduced states in fresh sample where Cu^0/Cu^{1+} occupied 86% area and Cu^{2+} only had 14%. Nevertheless, Cu^{2+} increased to 86% and Cu^0/Cu^{1+} decreased to 14% in spent sample after polarization, indicating that Cu had changed into a more oxidized state. The satellite structures between 938 and 946 eV characterized the presence of the CuO phase[18].

From **Figure 4-4b**, Co^0 and $Co^{2+,3+}$ (Co_3O_4) were the main phases in fresh sample and owned 45% and 40% area, respectively, while Co^{2+} had 15%. After electrochemical experiments, the lower oxidized state of Co^0 was completely

transferred into higher ones in spent sample and Co^{2+} phase increased to 42% accordingly. The peaks over 784 eV were satellite structures of Co^{2+}[19]. The XPS results show that as expected some reduction of CuO_x and Co_3O_4 occurred during the pre-treatment in H_2, whereases the catalyst was mostly in oxidized state after the reaction under polarization. This agrees with STEM results and XRD patterns that showed higher oxidation states of both Cu and Co in the spent sample.

The significant changes in Cu oxidation states were possibly because of the O^{2-} storage-release ability of Co_3O_4, which was also confirmed by the existence of $Co^{2+,3+}$ (Co_3O_4) structure in both fresh and spent samples. The XPS spectra for O 1s is shown in **Figure B-5**, where the 528-530 eV is known as lattice O^{2-}, 531-532 eV is taken as defect O^{2-} and 533 eV represents water[20,21]. The O 1s spectra of fresh sample showed consistency with that of Co_3O_4 reported earlier[22], indicating that the large lattice/defect O^{2-} in Cu/Co_3O_4 catalyst was mainly provided by Co_3O_4 structure. Nevertheless, O^{2-} shifted to higher binding energies in spent sample, which was also in line with another study on Cu-Co oxide[20] and was due to the increased oxygen vacancies caused by partial substitution of Co^{2+} by Cu^{2+}[23] during the continuous O^{2-} cycling in EPOC. The presence of water in spent sample was a result of the RWGS reaction, as H_2O is one of the main products.

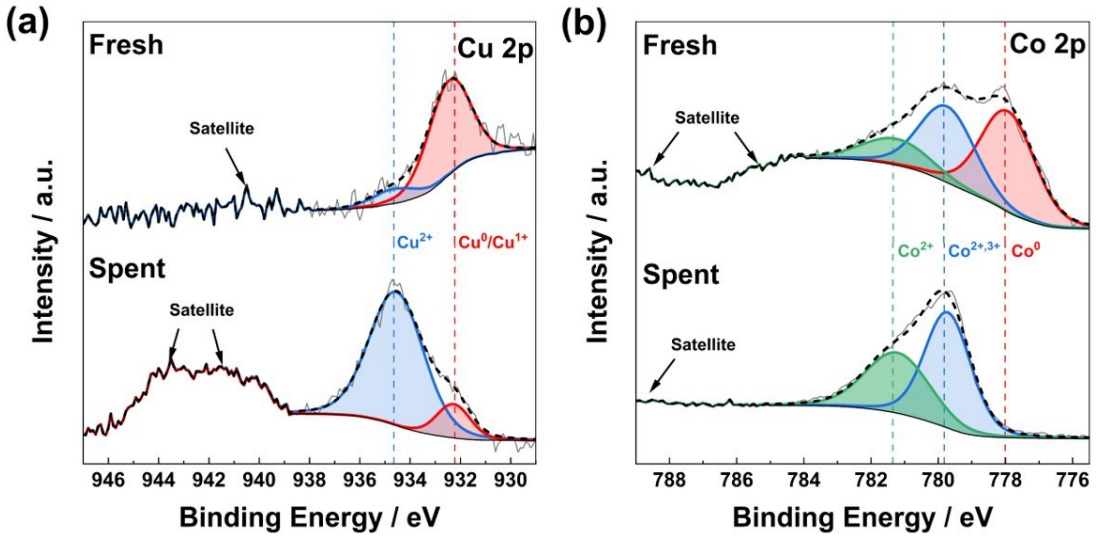

Figure 4-4. High-resolution XPS spectra for (a) Cu $2p_{3/2}$ and (b) Co $2p_{3/2}$.

4.3.2 Catalytic RWGS reaction

Figure 4-5a shows the light-off curves of bare Co_3O_4, Cu/Co_3O_4, and free-standing Cu catalysts deposited on YSZ under stoichiometric conditions (CO_2:H_2 = 1:1) after several runs until stable. The overall light-off curves of 4wt.%Cu/Co_3O_4 are summarized in **Figure B-6** as an example. Carbon monoxide was the only product for all catalysts, indicating 100% selectivity towards RWGS reaction. The reaction was activated above 250℃ for bare Co_3O_4 and Cu/Co_3O_4, while above 350℃ for the free-standing Cu. Bare Co_3O_4 was found to have the highest catalytic performance, which decreased with increasing the Cu loading from 1 to 8 wt.%. This was consistent with a recent study on the RWGS reaction of FeO_x/Co_3O_4[10], where bare Co_3O_4 also exhibited the highest activity under stoichiometric conditions, while the reaction rate slightly decreased when loaded with FeO_x.

The high open-circuit activity of Co_3O_4 for RWGS was attributed to its high surface area and porous structure as shown in **Figure 4-2a**, and due to its high reducibility affiliated to the oxidation states change between Co^{3+} and Co^{2+} under reaction conditions[24]. When Co_3O_4 was loaded with small amounts of Cu NPs, the decrease in the catalyst performance was attributed to the sintering of Cu and a charge transfer between Cu and Co_3O_4[25], where CoO_x provided oxygen to Cu and kept it in an oxidized station[10].

Both Cu and Co_3O_4 functioned as the active phase of catalyst by participating in the RWGS reaction and influenced each other. For instance, the stability and dispersion of Cu NPs after catalytic reactions were improved by supporting on Co_3O_4, as shown in SEM images, which prevented Cu from deactivation caused by agglomeration and sintering that easily happened at high temperatures[16]. Conversely, considering that Co_3O_4 acted as a semiconductor which only showed electrical conductivity above 350℃[9,26], it was necessary to modify Co_3O_4 by loading conductive Cu NPs to improve its conductivity and electrocatalytic properties before being used as an electrode in EPOC studies, which will be discussed later. Nevertheless, excessive loading amount of Cu on Co_3O_4 resulted in Cu sintering

(**Figure B-2b, c and d**) and formation of the less porous structures (**Figure 4-2b, c and d**), and the reaction rates were thereby decreased. As a result, 4wt.% was taken as the optimum Cu loading on Co_3O_4, which maintained a high activity and stability and could be promoted after polarization.

Figure 4-5b and c show that when increasing CO_2 or H_2 concentration, the open-circuit rates were both enhanced, while the rates in oxidizing conditions (**Figure 4-5b**) were slightly lower than in reducing conditions (**Figure 4-5c**). The superior RWGS reaction rates in reducing conditions were because of the increased oxygen vacancies under excess of H_2[6] where O^{2-} migration between metal and oxide was promoted and RWGS was thermodynamically favoured in H_2 rich atmosphere[27,28]. However, although high CO_2 concentration inhibited O^{2-} migration because catalysts were fully oxidized in this case, RWGS reaction rates over Cu/Co_3O_4 catalysts in oxidizing conditions were still comparable to those in reducing conditions. This was affiliated to the Co_3O_4 phase which was able to provide sufficient oxygen vacancies due to its porous structure and huge oxygen storage-release capacity.

The same phenomenon was also observed in a previous study, and it was demonstrated that the reaction was favored in CO_2 rich atmosphere over the Co_3O_4 based catalyst[10,17]. Blank tests were also performed over bare YSZ disk that was placed inside the reactor under all reaction conditions. It was found that YSZ was completely inert to RWGS reaction, confirming the catalytic activities of Cu/Co_3O_4 catalysts.

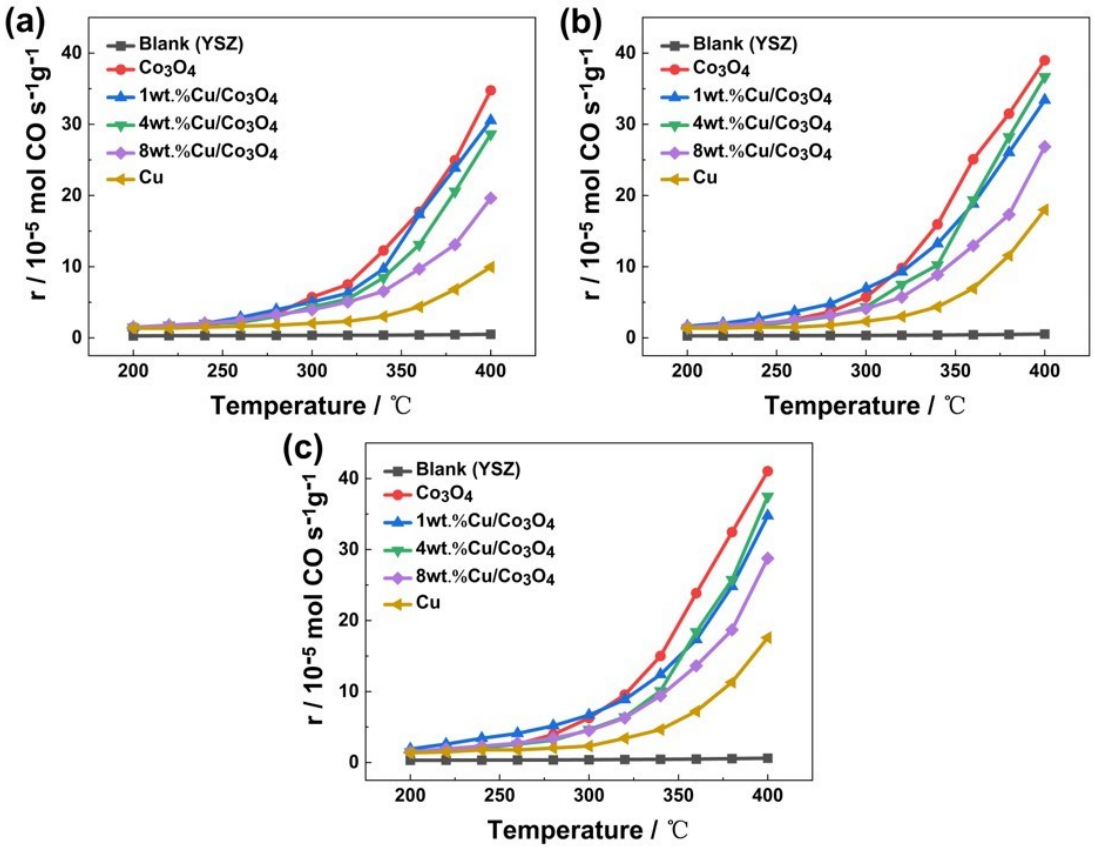

Figure 4-5. Light-off curves of bare Co_3O_4, Cu/Co_3O_4, and free-standing Cu catalysts under (a) stoichiometric, (b) oxidizing, and (c) reducing conditions.

4.3.3 Cyclic voltammetry

Cyclic voltammetry (CV) is commonly used to investigate the reduction and oxidation processes of a working electrode (WE) in electrochemical reactions[29–31]. In EPOC studies, the catalyst serves as a WE, where the charge transfer occurs at the three-phase boundary (tpb), between the solid electrolyte, the metal or metal oxide catalysts and the gas phase. Performing CV can provide a piece of in-situ information about the electrochemical processes at the tpb, backspillover phenomena, as well as redox properties and changes in the oxidation states of the catalysts before and after the reactions. Therefore, CV is widely applied in EPOC studies as an electrochemical characterization method[16,32,33].

Figure 4-6a shows the CV of the as-prepared and spent 4wt.%Cu/Co_3O_4 samples between -0.8 and 1.5 V under Argon at 400°C. The CV of as-prepared sample showed similar trend to that of bare Co_3O_4 deposited on YSZ, as shown in the **Figure 4-6b**.

Because the catalyst was kept at reduced state after pre-treatment, Cu was difficult to be reduced/oxidized due to the lack of O^{2-}, as a result, the Cu phase was inert and CoO_x showed its redox property in CV. In contrast, CV of spent sample changed significantly and showed two typical cathodic peaks, similar to that of as-prepared free-standing Cu deposited on YSZ, as shown in **Figure 4-6c**, which was consistent with the former study on Cu/YSZ[16]. During catalytic reactions, CuO phase that could store huge amounts of oxygen was formed by oxidizing Cu with O^{2-} supplied from YSZ and CoO_x under positive polarization. In this case, Co stayed at reduced state and CuO was dominant and exhibited the redox property. Upon starting the CV, CuO was formed in anodic cycle and was then reduced stepwise to Cu_2O (CI) and Cu^0 (CII) in cathodic cycle. Compared to **Figure 4-6c**, the positions of CI and CII in **Figure 4-6a** shifted to more positive values (from +0.6V and +0.3V to +0.7V and +0.5V, respectively) since more CuO was formed anodically in Cu/Co_3O_4 than in free-standing Cu due to the huge oxygen capacity of Co_3O_4, which enabled easier reduction processes. Therefore, the difference in CV shapes of as-prepared and spent 4wt.%Cu/Co_3O_4 further illuminated the oxidation state changes of Cu and Co_3O_4 during polarization.

The rapid increase of currents at higher potentials ($>$1.0 V) in CVs represented oxygen evolution reaction (OER), as shown in Eq. (4-3). However, it should be noted that the CVs were all tested under inert condition (in Argon), where OER would occur significantly and release O_2 at tpb when applying potentials higher than 1.0 V. Under reaction conditions with the presence of H_2, the released O_2 from YSZ was unable to oxidize the catalyst because it would react with H_2 to form H_2O, especially under reducing conditions (CO_2:H_2= 1:6), where the EPOC effects still occurred. Therefore, it meant that the oxidation state changes of Cu and Co_3O_4 were due to the O^{2-} migration during polarization instead of from the released O_2 during OER.

$$O^{2-}(\mathrm{YSZ}) \rightarrow \frac{1}{2}O_2 + 2e^- \qquad (4\text{-}3)$$

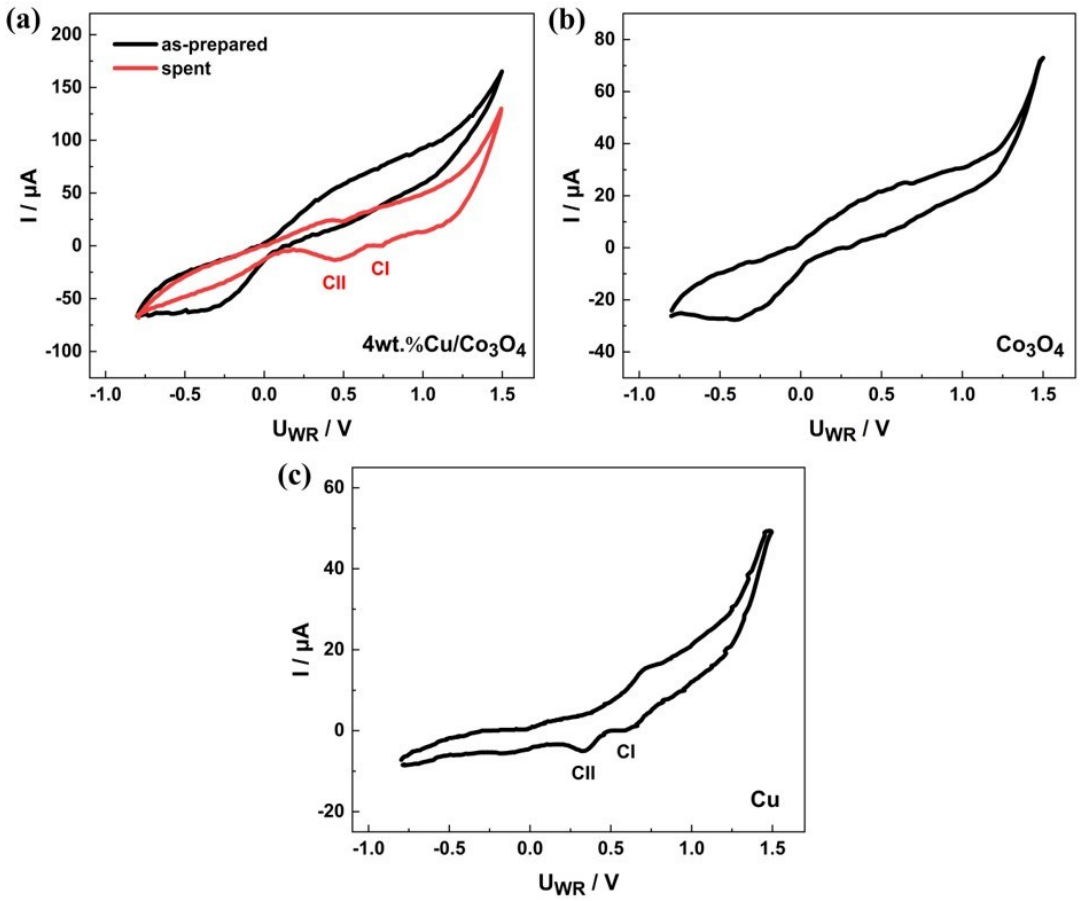

Figure 4-6. Cyclic voltammetry of (a) as-prepared and spent 4wt.%Cu/Co_3O_4, and as-prepared (b) bare Co_3O_4 and (c) free-standing Cu deposited on YSZ in Argon at 400°C, scan rate 20 mV s^{-1}.

4.3.4 Electrochemical promotion of catalysis

Electrochemical promotion of bare Co_3O_4 and Cu/Co_3O_4 were investigated using chronoamperometry (CA) under anodic and cathodic polarization. It was observed that the bare Co_3O_4 catalyst did not show any rate increase or decrease under polarization, which was attributed to its poor conductivity and electrocatalytic property. Among Cu modified Co_3O_4 catalysts, only 4wt.%Cu/Co_3O_4 showed the catalytic rate changes under applied polarization. In the former study of Cu/YSZ[16], the catalyst showed an electrophobic EPOC behaviour where the catalytic rates were promoted upon an application of +2V under all conditions, as summarized in **Figure B-7**. The best enhancement ratio (ρ) was 1.19 under stochiometric condition, which was slightly inhibited under oxidizing (ρ=1.17) condition due to the formation of less

active CuO by reacting with CO_2 and extremely prohibited under reducing (ρ=1.06) condition on account of the limited migration of O^{2-} towards Cu from YSZ caused by excessive H_2. However, when loading Cu NPs on Co_3O_4, the EPOC effects were completely different, where the catalytic rate was suppressed under positive polarization at +2V and enhanced under negative polarization at -1V. The overall transient responses of RWGS rate and current to applied potentials under all conditions are summarized in **Figure B-8**. The corresponding ρ and Faradaic efficiency (Λ) values at 400°C under polarization are summarized in **Figure 4-7** where the ρ values under all conditions show declined trends as increasing the applied potential, indicating an electrophilic property[26]. That was, the catalytic rate was suppressed more heavily at higher positive polarization and increased more apparently at higher negative polarization. The difference in RWGS rate response to positive/negative polarization suggested that the formation and decomposition of the active phase were reversed under the two conditions, due to the opposite O^{2-} migration directions.

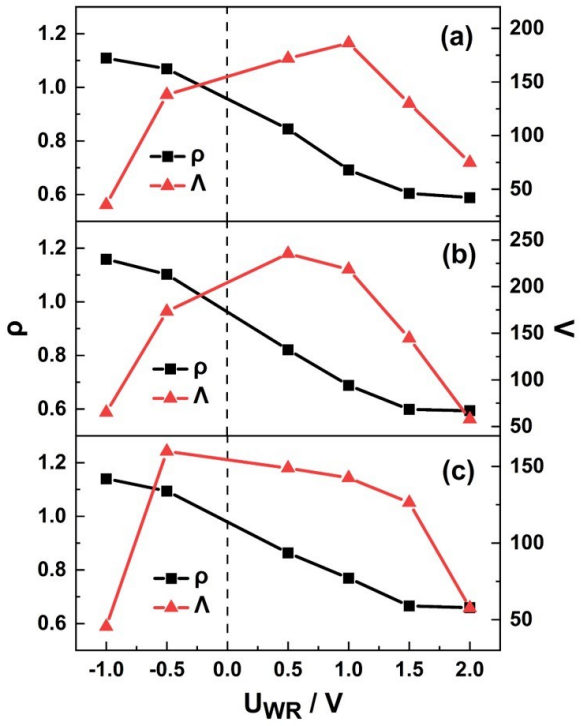

Figure 4-7. Summary of ρ and Λ values for 4wt.%Cu/Co_3O_4 under (a) stoichiometric, (b) oxidizing, and (c) reducing conditions at 400°C.

Figure 4-8a and b show the transient rate response of 4wt.%Cu/Co_3O_4 deposited on YSZ at 400°C under stoichiometric (CO_2:H_2=1:1), oxidizing (CO_2:H_2=3:1) and reducing (CO_2:H_2=1:6) conditions. In **Figure 4-8a**, under an application of +2V, the CO rate decreased gradually and reached a new steady state in 10 min. However, as opposed to free-standing Cu/YSZ, there was a sharp increase in the rate after interrupting the applied potential, followed by a slow and smooth decrease until returning to the initial state (the dashed lines represented the levels of open-circuit reaction rates). The suppression of reaction rate was the most pronounced in stoichiometric condition with ρ=0.58 and Λ=75, in comparison to the oxidizing (ρ=0.59 and Λ=58) and reducing conditions (ρ=0.66 and Λ=58). On the contrary, in **Figure 4-8b**, the CO rate increased upon an application of -1V and reached its steady state rapidly before returning to its initial state without any peaks when the polarization was stopped. In this case, the enhancement effect in CO rate was the least in stoichiometric condition with ρ=1.11 and Λ=35, and the most apparent in oxidizing condition with ρ=1.16 and Λ=65.

Since bare Co_3O_4 did not show any EPOC effects, the alternation in CO rate under polarization was due to the presence of Cu and its interaction with Co_3O_4. It was reported that when combining Cu with Co_3O_4, Cu^{2+} would substitute Co^{2+} in Co_3O_4 bulk[23], which created more oxygen vacancies by forming new bonding with Co^{3+}. As a result, Co_3O_4 functioned as an O^{2-} bridge between Cu and YSZ, where O^{2-} could be easily transferred through the oxygen vacancies during polarization.

This substitution phenomenon was effective up to a Cu loading of 4wt.%, above which the substitution was ineffective, resulting in more formation of CuO phase and influenced the synergistic effect[8]. Therefore, 8wt.%Cu/Co_3O_4 showed no traces of EPOC phenomenon due to the existence of CuO that had limited oxygen vacancies, without which O^{2-} was unable to be migrated between Cu and Co_3O_4 under polarization, thus making the catalyst less polarizable. The absence of EPOC effects over 1wt.%Cu/Co_3O_4 was because of the low conductivity of Co_3O_4 and low loading amount of Cu NPs, where the changes in oxidation state of Cu caused by O^{2-}

migration from Co_3O_4 under polarization was insignificant. This suggested that fewer catalyst was involved in the electrochemical oxidation/reduction processes, representing an inferior electrocatalytic property of the catalyst. In the case of 4wt.%Cu/Co_3O_4, the O^{2-} was supplied towards Cu from Co_3O_4 and YSZ electrolyte under positive polarization, forming a more oxidized state of CuO and more reduced state of Co, as also confirmed by the EELS mappings in **Figure 4-1** and XRD patterns in **Figure 4-3**. Since lower oxidation state of Co, e.g., metallic Co (Co^0) was less active than CoO_x in RWGS reaction[17,34] and CuO showed inferior activity than Cu_2O and Cu^0 due to its limited oxygen vacancies[16], the catalytic rate was thereby decreased.

The sharp increase upon depolarization was due to the oxygen storage phenomenon during positive polarization. Without the applied potential as the driven force, the stored oxygen functioned as promoting species to oxidize Co that was in lower oxidation state, as a result, more active phase of CoO_x was formed, leading to the instantaneous increase in reaction rate. The CoO_x was then reduced gradually by H_2 under reaction condition, which made the reaction rate decline slowly until it returned to the initial state. The storage of O^{2-} during polarization was confirmed by the influence of applied potential on the transient response of reaction rate, as shown in **Figure 4-8c**, with the percentage (%) rate increase during depolarization summarized in **Figure 4-8d** and calculated by Eq. (4-4)[17]:

$$\%\ \text{rate increase} = 100\% \times \left[\left(r_{peak} - r_0\right)/r_0\right] \quad (4\text{-}4)$$

where r_{peak} is the maximum value of rate peak and r_0 is the open-circuit rate. It can be seen that by increasing the applied potential, the % rate increase was also enhanced, representing more O^{2-} was stored and subsequently resulted in more formation of CoO_x that had higher activity. The lower values of % rate increase in oxidizing condition were due to the limited oxygen vacancies provided by highly oxidized catalysts induced by the positive polarization. Under reducing condition, the O^{2-} transfer was prohibited due to the huge amount of H_2, as a result, the suppression in

reaction rate under positive polarization and % rate increase during depolarization were inferior.

Conversely, O^{2-} was migrated in an opposite direction from supported Cu to Co_3O_4 and YSZ bulk under negative polarization, leading to an increase in the reaction rate. The rate peak after interrupting the application of -1V was absent because O^{2-} was not stored in this case, which further illustrated the oxygen storage phenomenon during positive polarization. In oxidizing condition, excessive CO_2 could constantly provide O^{2-} to the reduced states of Cu and Co under negative polarization, giving rise to continuous formation of higher oxidation state of CoO_x, and the enhancement ratio was thereby the highest. The migration of O^{2-} between Co_3O_4 and supported metal was also confirmed in a recent study on FeO_x/Co_3O_4[10].

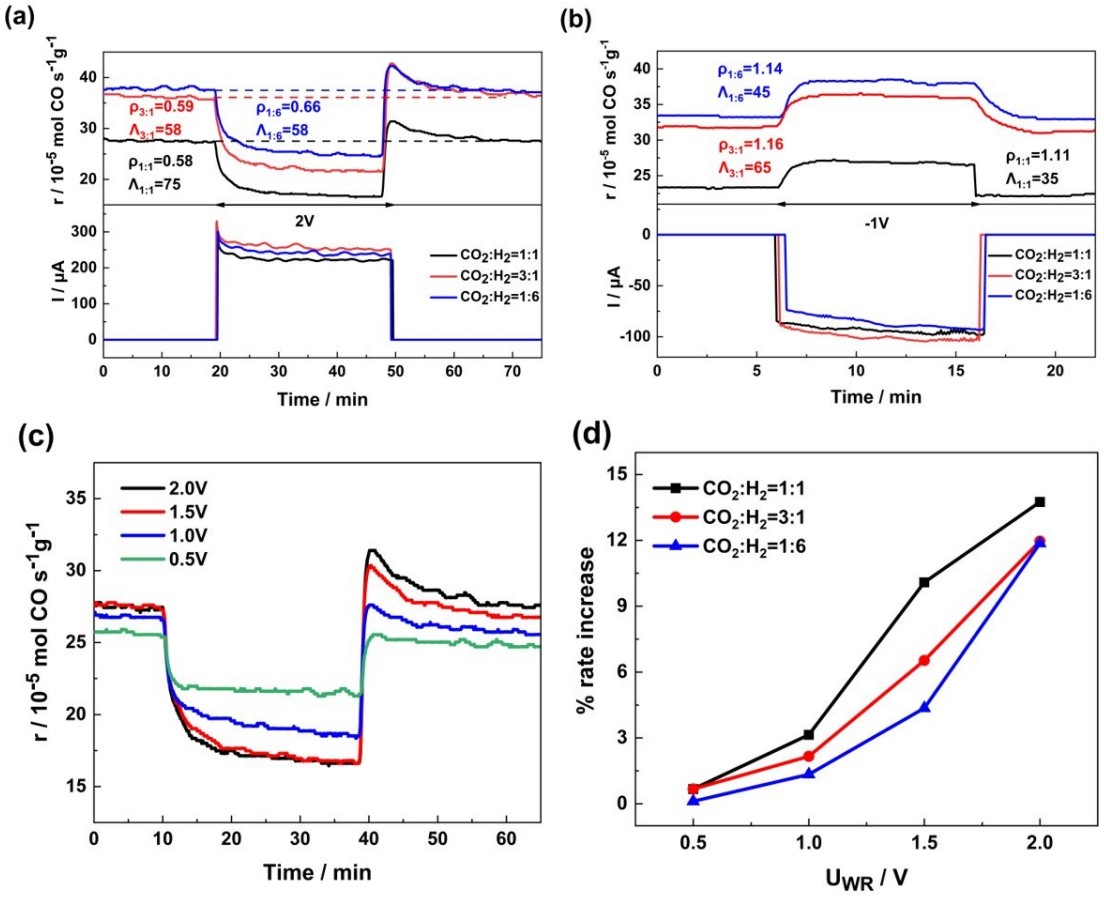

Figure 4-8. EPOC of 4wt.%Cu/Co_3O_4 at (a) +2V and (b) -1V under different CO_2:H_2 ratios at 400°C, (c) EPOC under stoichiometric conditions at various anodic potentials, and (d) Percentage (%) rate increase after polarization under various conditions at 400°C.

The uptake of reactive promoting species, O^{2-} in moles in this study, during EPOC was used to investigate the magnitude of oxygen migration. It was expressed as N_G (mol) and calculated by Eq. (4-5)[35]:

$$N_G = \frac{I\tau}{2F} \quad (4\text{-}5)$$

where I represented the current response, τ was the time required for catalytic rate to reach 63% of its suppressed/promoted steady-state, and F was Faraday's constant.

The N_G values under different conditions and applied potentials at 400℃ are summarized in **Figure 4-9**. Under positive polarization ($U_{WR} > 0$), the N_G was improved with an increase in the applied potential across the catalyst under all conditions, indicating that more O^{2-} was involved in the catalytic reactions by being supplied electrochemically towards catalyst from YSZ, in other words, more O^{2-} was stored during polarizations. This further provided evidence of the oxygen storage phenomenon, which was consistent with the results of % rate increase during depolarization as shown in **Figure 4-8d** that had a similar trend with **Figure 4-9**. The inferior N_G values in reducing condition was due to the high concentration of H_2 that inhibited the O^{2-} migration and in oxidizing condition was because of the highly oxidized catalysts, which provided fewer oxygen vacancies for O^{2-} transfer. Moreover, the N_G of 4wt.%Cu/Co_3O_4 under stoichiometric condition at +2V and 400℃ was 1.3×10^{-7} mol, 30% higher than that of free-standing Cu under the same condition, which was 1.0×10^{-7} mol[16]. The increased value of N_G was attributed to the existence of Co_3O_4, which had a huge oxygen capacity and could provide/receive O^{2-}.

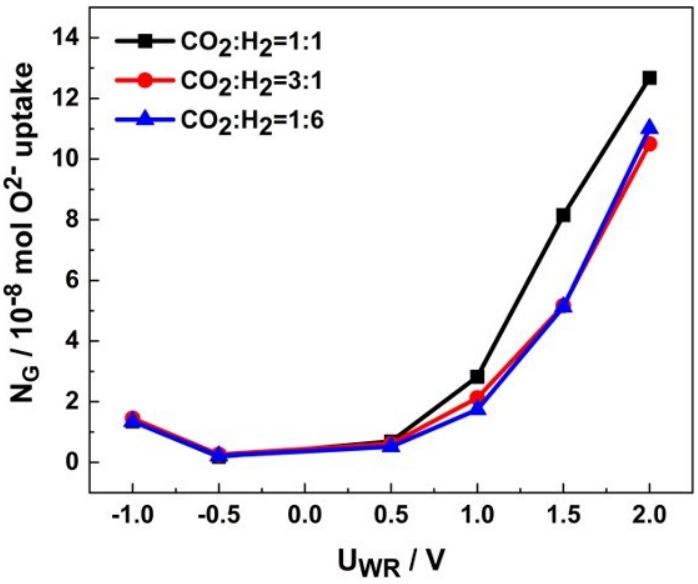

Figure 4-9. Summary of N_G (mol O^{2-} uptake) at 400℃ under different reaction conditions and applied potentials.

4.3.5 Exchange current density evaluation

The exchange current density (i_0) was used to express the electrocatalytic activity of the catalyst when the net current passing through the tpb was 0. The corresponding Tafel plots used to determine i_0 values of various Cu/Co_3O_4 catalysts are shown in **Figure B-9**. **Figure 4-10** summarizes the relationship between open-circuit catalytic rate (r_0) and i_0 for bare Co_3O_4, Cu/Co_3O_4, and free-standing Cu catalysts at 400℃ under stoichiometric condition. The results showed that catalyst with a lower value of i_0, which corresponded to a fewer loading amount of Cu, exhibited a higher reaction rate. The inversed relationship between r_0 and i_0 for Cu/Co_3O_4 was consistent with electrocatalytic studies on ethylene oxidation over IrO_x/CeO_2 and $IrOx/TiO_2$[36] as well as over Pt/CeO_2 and Ru/CeO_2[37]. Higher i_0 values represented that electrocatalytic reactions involving the participation of O^{2-} species in electrochemical reactions predominated, rather than catalytic reactions that did not consume catalyst during the process[38]. Therefore, the electrocatalytic property of catalyst was improved by adding and increasing the Cu loading on Co_3O_4, making the Cu/Co_3O_4 function more like an electrode that could take part in the electrochemical redox

reactions more readily. On the contrary, bare Co_3O_4 failed to function as the working electrode and display EPOC effect because of its poor conductivity and electrocatalytic property, although it showed the best catalytic activity.

Also, the i_0 was known to provide a measurement of non-polarizability of the catalyst[38,39] and predict the magnitude of Λ in EPOC[37], e.g., lower values of i_0 represented that the catalysts deposited on solid electrolytes were more polarizable, which were desirable to achieve higher Λ values. Taking free-standing Cu and 4wt.%Cu/Co_3O_4 that showed EPOC effects as the example, 4wt.%Cu/Co_3O_4 had a lower i_0 value of 1.4 μA cm^{-2} with a much higher Λ=75 compared to Cu whose i_0 was 2.8 μA cm^{-2} with Λ=6.54. This demonstrated that Cu/Co_3O_4 was more polarizable than free-standing Cu, which was affiliated to the huge oxygen capacity of Co_3O_4 that allowed for easier migration of O^{2-} at tpb under polarization. The relationships between r_0 and i_0 of Cu/Co_3O_4 under oxidizing and reducing conditions were shown in **Figure B-10**, both of which had similar trend with that under stoichiometric condition. The studies on i_0 revealed that the presence of Cu loading improved the electrocatalytic property of bare Co_3O_4 and enabled this Cu/Co_3O_4 catalyst to be utilized as the catalyst-working electrode in EPOC.

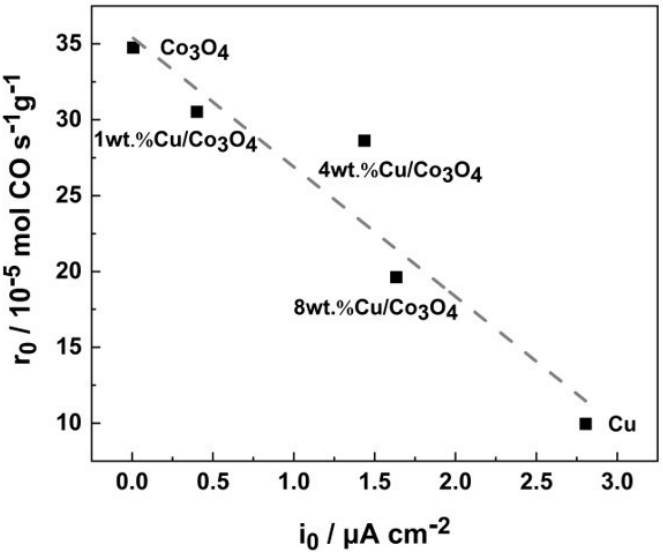

Figure 4-10. Relationship between open circuit catalytic reaction rate (r_0) and exchange current density (i_0) of Cu/Co_3O_4 catalysts under the stochiometric condition at 400°C.

4.4 Conclusion

In this study, Cu/Co_3O_4 catalysts with 1, 4 and 8wt.% of Cu NPs were shown to be highly active non-noble metal catalysts for the RWGS reaction in the temperature range of 200–400°C. Among all catalysts, only $4wt.\%Cu/Co_3O_4$ displayed electrophilic EPOC effects, where the reaction rate was promoted by 11-16% under negative polarization at -1V and suppressed by 34-42% under positive polarization at +2V. This was due to the formation and decomposition of active phases (Cu^0/Cu_2O and CoO_x) induced by O^{2-} migration under polarization. CV results also provided in situ information about the changes in the oxidation states of $4wt.\%Cu/Co_3O_4$ catalyst before and after reactions. Investigations of i_0 revealed an inverse relationship between r_0 and i_0, in agreement with EPOC theory. The counter-correlation between r_0 and i_0 also indicated that Cu NPs enhanced the electrocatalytic property of Co_3O_4 and allowed it to function as the catalyst-working electrode in EPOC. Therefore, our findings provide the opportunity to predict and alter the catalytic RWGS rate of $4wt.\%Cu/Co_3O_4$ catalyst under polarization.

References

[1] W. Wang, S. Wang, X. Ma, J. Gong, Recent advances in catalytic hydrogenation of carbon dioxide, Chem. Soc. Rev. 40 (2011) 3703–3727. https://doi.org/10.1039/c1cs15008a.

[2] G.C. Wang, J. Nakamura, Structure sensitivity for forward and reverse water-gas shift reactions on copper surfaces: A DFT study, J. Phys. Chem. Lett. 1 (2010) 3053–3057. https://doi.org/10.1021/jz101150w.

[3] P. Gurav, S.S. Naik, K. Ansari, S. Srinath, K.A. Kishore, Y.P. Setty, S. Sonawane, Stable colloidal copper nanoparticles for a nanofluid: Production and application, Colloids Surfaces A Physicochem. Eng. Asp. 441 (2014) 589–597. https://doi.org/10.1016/j.colsurfa.2013.10.026.

[4] C.S. Chen, W.H. Cheng, S.S. Lin, Enhanced activity and stability of a Cu/SiO2 catalyst for the reverse water gas shift reaction by an iron promoter, Chem. Commun. 1 (2001) 1770–1771. https://doi.org/10.1039/b104279n.

[5] M. Konsolakis, M. Lykaki, S. Stefa, S.A.C. Carabineiro, G. Varvoutis, E. Papista, G.E. Marnellos, Co2 hydrogenation over nanoceria-supported transition metal catalysts: Role of ceria morphology (nanorods versus nanocubes) and active phase nature (co versus cu), Nanomaterials. 9 (2019) 1739. https://doi.org/10.3390/nano9121739.

[6] X. Chen, Y. Chen, C. Song, P. Ji, N. Wang, W. Wang, L. Cui, Recent Advances in Supported Metal Catalysts and Oxide Catalysts for the Reverse Water-Gas Shift Reaction, Front. Chem. 8 (2020) 1–21. https://doi.org/10.3389/fchem.2020.00709.

[7] C. Schuschke, L. Fusek, V. Uvarov, M. Vorokhta, B. Šmíd, V. Johánek, Y. Lykhach, J. Libuda, J. Mysliveček, O. Brummel, Stability of the Pd/Co3O4(111) Model Catalysts in Oxidizing and Humid Environments, J. Phys. Chem. C. 125 (2021) 2907–2917. https://doi.org/10.1021/acs.jpcc.0c08915.

[8] S.A. Singh, S. Mukherjee, G. Madras, Role of CO2 methanation into the kinetics of preferential CO oxidation on Cu/Co3O4, Mol. Catal. 466 (2019) 167–180. https://doi.org/10.1016/j.mcat.2019.01.020.

[9] D. Zagoraios, C. Panaritis, A. Krassakopoulou, E.A. Baranova, A. Katsaounis, C.G. Vayenas, Electrochemical promotion of Ru nanoparticles deposited on a proton conductor electrolyte during CO2 hydrogenation, Appl. Catal. B Environ. 276 (2020) 119148. https://doi.org/10.1016/j.apcatb.2020.119148.

[10] C. Panaritis, S. Yan, M. Couillard, E.A. Baranova, Electrochemical study of the metal-support interaction between FeOx nanoparticles and cobalt oxide support for the reverse water gas shift reaction, J. CO2 Util. 56 (2021) 101824. https://doi.org/10.1016/j.jcou.2021.101824.

[11] M.Y. Nassar, T.Y. Mohamed, I.S. Ahmed, N.M. Mohamed, M. Khatab, Hydrothermally Synthesized Co3O4, α-Fe2O3, and CoFe2O4 Nanostructures: Efficient Nano-adsorbents for the Removal of Orange G Textile Dye from Aqueous Media, J. Inorg. Organomet. Polym. Mater. 27 (2017) 1526–1537. https://doi.org/10.1007/s10904-017-0613-x.

[12] J.-C. Mu, E.-Q. Wang, Y.-L. Zhang, L.-P. Zhang, Sandwich-Like Co 3 O 4 /Graphene Nanocomposites as Anode Material for Lithium Ion Batteries , J. Nanosci. Nanotechnol. 19 (2019) 7819–7825. https://doi.org/10.1166/jnn.2019.16744.

[13] D.D.M. Prabaharan, K. Sadaiyandi, M. Mahendran, S. Sagadevan, Precipitation method and characterization of cobalt oxide nanoparticles, Appl. Phys. A Mater. Sci. Process. 123 (2017) 1–6. https://doi.org/10.1007/s00339-017-0786-8.

[14] M. Manjunatha, G.S. Reddy, K.J. Mallikarjunaiah, R. Damle, K.P. Ramesh, Determination of Phase Composition of Cobalt Nanoparticles Using 59Co Internal Field Nuclear Magnetic Resonance, J. Supercond. Nov. Magn. 32 (2019) 3201–3209. https://doi.org/10.1007/s10948-019-5083-7.

[15] P. Patnaik, B.C. Tripathy, I.N. Bhattacharya, R.K. Paramguru, B.K. Mishra, Effect of Tetra Propyl Ammonium Bromide During Cobalt Electrodeposition from Acidic Sulfate Solutions, Metall. Mater. Trans. B Process Metall. Mater. Process. Sci. 46 (2015) 1252–1256. https://doi.org/10.1007/s11663-015-0301-6.

[16] J. Wang, M. Couillard, E.A. Baranova, Electrochemical promotion of copper nanoparticles for the reverse water gas shift reaction, Catal. Sci. Technol. 12 (2022) 1562–1573. https://doi.org/10.1039/d1cy02315b.

[17] D. Zagoraios, S. Tsatsos, S. Kennou, C.G. Vayenas, G. Kyriakou, A. Katsaounis, Tuning the RWGS Reaction via EPOC and in Situ Electro-oxidation of Cobalt Nanoparticles, ACS Catal. (2020) 14916–14927. https://doi.org/10.1021/acscatal.0c04133.
[18] L. Deng, Q. Su, Q. Ye, H. Wan, Y. He, X. Cui, Slag-based geopolymer microsphere-supported Cu: A low-cost and sustainable catalyst for CO2hydrogenation, Sustain. Energy Fuels. 6 (2022) 1436–1447. https://doi.org/10.1039/d2se00050d.
[19] S. Ghosh, G. Tudu, A. Mondal, S. Ganguli, H.R. Inta, V. Mahalingam, Inception of Co3O4as Microstructural Support to Promote Alkaline Oxygen Evolution Reaction for Co0.85Se/Co9Se8Network, Inorg. Chem. 59 (2020) 17326–17339. https://doi.org/10.1021/acs.inorgchem.0c02618.
[20] M.J. Jang, J. Yang, J. Lee, Y.S. Park, J. Jeong, S.M. Park, J.Y. Jeong, Y. Yin, M.H. Seo, S.M. Choi, K.H. Lee, Superior performance and stability of anion exchange membrane water electrolysis: PH-controlled copper cobalt oxide nanoparticles for the oxygen evolution reaction, J. Mater. Chem. A. 8 (2020) 4290–4299. https://doi.org/10.1039/c9ta13137j.
[21] S. Li, H. Wang, W. Li, X. Wu, W. Tang, Y. Chen, Effect of Cu substitution on promoted benzene oxidation over porous CuCo-based catalysts derived from layered double hydroxide with resistance of water vapor, Appl. Catal. B Environ. 166–167 (2015) 260–269. https://doi.org/10.1016/j.apcatb.2014.11.040.
[22] U. Baig, M.A. Dastageer, M.A. Gondal, Facile fabrication of super-wettable mesh membrane using locally-synthesized cobalt oxide nanoparticles and their application in efficient gravity driven oil/water separation, Colloids Surfaces A Physicochem. Eng. Asp. 660 (2023) 130793. https://doi.org/10.1016/j.colsurfa.2022.130793.
[23] M. Zhou, L. Cai, M. Bajdich, M. García-Melchor, H. Li, J. He, J. Wilcox, W. Wu, A. Vojvodic, X. Zheng, Enhancing Catalytic CO Oxidation over Co3O4 Nanowires by Substituting Co2+ with Cu2+, ACS Catal. 5 (2015) 4485–4491. https://doi.org/10.1021/acscatal.5b00488.
[24] O. Brummel, M. Bertram, C. Prössl, M. Ronovský, J. Knöppel, P. Matvija, L. Fusek, T. Skála, N. Tsud, M. Kastenmeier, V. Matolín, K.J.J. Mayrhofer, V. Johánek, J. Mysliveček, S. Cherevko, Y. Lykhach, J. Libuda, Cobalt oxide-supported pt electrocatalysts: Intimate correlation between particle size, electronic metal-support interaction and stability, J. Phys. Chem. Lett. 11 (2020) 8365–8371. https://doi.org/10.1021/acs.jpclett.0c02233.
[25] Y. Yamada, K. Yano, S. Fukuzumi, Catalytic application of shape-controlled Cu 2O particles protected by Co 3O 4 nanoparticles for hydrogen evolution from ammonia borane, Energy Environ. Sci. 5 (2012) 5356–5363. https://doi.org/10.1039/c1ee02639a.
[26] D. Zagoraios, A. Athanasiadi, I. Kalaitzidou, S. Ntais, A. Katsaounis, A. Caravaca, P. Vernoux, C.G. Vayenas, Electrochemical promotion of methane oxidation over nanodispersed Pd/Co3O4 catalysts, Catal. Today. 355 (2020)

910–920. https://doi.org/10.1016/j.cattod.2019.02.030.
[27] Y.A. Daza, J.N. Kuhn, CO2 conversion by reverse water gas shift catalysis: Comparison of catalysts, mechanisms and their consequences for CO2 conversion to liquid fuels, RSC Adv. 6 (2016) 49675–49691. https://doi.org/10.1039/c6ra05414e.
[28] L. Pastor-Pérez, F. Baibars, E. Le Sache, H. Arellano-García, S. Gu, T.R. Reina, CO2 valorisation via Reverse Water-Gas Shift reaction using advanced Cs doped Fe-Cu/Al2O3 catalysts, J. CO2 Util. 21 (2017) 423–428. https://doi.org/10.1016/j.jcou.2017.08.009.
[29] N. Elgrishi, K.J. Rountree, B.D. McCarthy, E.S. Rountree, T.T. Eisenhart, J.L. Dempsey, A Practical Beginner's Guide to Cyclic Voltammetry, J. Chem. Educ. 95 (2018) 197–206. https://doi.org/10.1021/acs.jchemed.7b00361.
[30] E.S. Rountree, B.D. McCarthy, T.T. Eisenhart, J.L. Dempsey, Evaluation of homogeneous electrocatalysts by cyclic voltammetry, Inorg. Chem. 53 (2014) 9983–10002. https://doi.org/10.1021/ic500658x.
[31] M. Fee, S. Ntais, A. Weck, E.A. Baranova, Electrochemical behavior of silver thin films interfaced with yttria-stabilized zirconia, J. Solid State Electrochem. 18 (2014) 2267–2277. https://doi.org/10.1007/s10008-014-2477-0.
[32] D. Zagoraios, N. Kokkinou, G. Kyriakou, A. Katsaounis, Electrochemical control of the RWGS reaction over Ni nanoparticles deposited on yttria stabilized zirconia, Catal. Sci. Technol. 12 (2022) 1869–1879. https://doi.org/10.1039/d1cy02140k.
[33] C. Panaritis, J. Zgheib, S.A.H. Ebrahim, M. Couillard, E.A. Baranova, Electrochemical in-situ activation of Fe-oxide nanowires for the reverse water gas shift reaction, Appl. Catal. B Environ. 269 (2020) 118826. https://doi.org/10.1016/j.apcatb.2020.118826.
[34] S.A. V Puga, A. V Puga, On the nature of active phases and sites in CO and CO2 hydrogenation catalysts, (2018). https://doi.org/10.1039/c8cy01216d.
[35] P. Vernoux, L. Lizarraga, M.N. Tsampas, F.M. Sapountzi, A. De Lucas-Consuegra, J.L. Valverde, S. Souentie, C.G. Vayenas, D. Tsiplakides, S. Balomenou, E.A. Baranova, Ionically conducting ceramics as active catalyst supports, Chem. Rev. 113 (2013) 8192–8260. https://doi.org/10.1021/cr4000336.
[36] Y. Hajar, H.A.E. Dole, M. Couillard, E.A. Baranova, Investigation of Heterogeneous Catalysts by an Electrochemical Method: Ceria and Titania-Supported Iridium Nanoparticles for Ethylene Oxidation, ECS Trans. 72 (2016) 161–172. https://doi.org/10.1149/07207.0161ecst.
[37] H.A.E. Dole, A.C.G.S.A. Costa, M. Couillard, E.A. Baranova, Quantifying metal support interaction in ceria-supported Pt, PtSn and Ru nanoparticles using electrochemical technique, J. Catal. 333 (2016) 40–50. https://doi.org/10.1016/j.jcat.2015.10.015.
[38] P. Vernoux, C.G. Vayenas, Recent Advances in Electrochemical Promotion of Catalysis (Modern Aspects of Electrochemistry, 61), Springer, 2023. https://doi.org/10.1007/978-3-031-13893-5.

[39] C.G. Vayenas, S. Ladas, S. Bebelis, I. V. Yentekakis, S. Neophytides, J. Yi, C. Karavasilis, C. Pliangos, Electrochemical promotion in catalysis: non-faradaic electrochemical modification of catalytic activity, Electrochim. Acta. 39 (1994) 1849–1855. https://doi.org/10.1016/0013-4686(94)85174-3.

Appendix B: Supplementary Information for Chapter 4

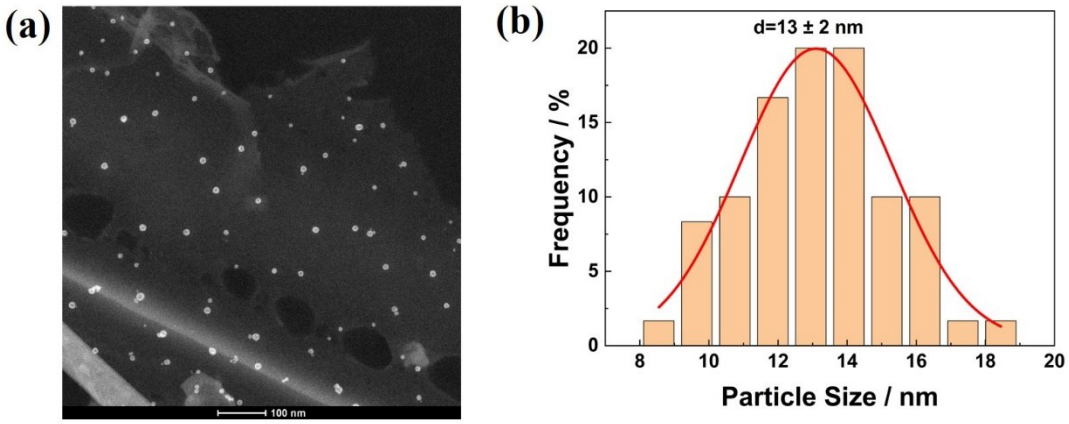

Figure B-1. (a) TEM image and (b) particle size distribution of copper nanoparticles.

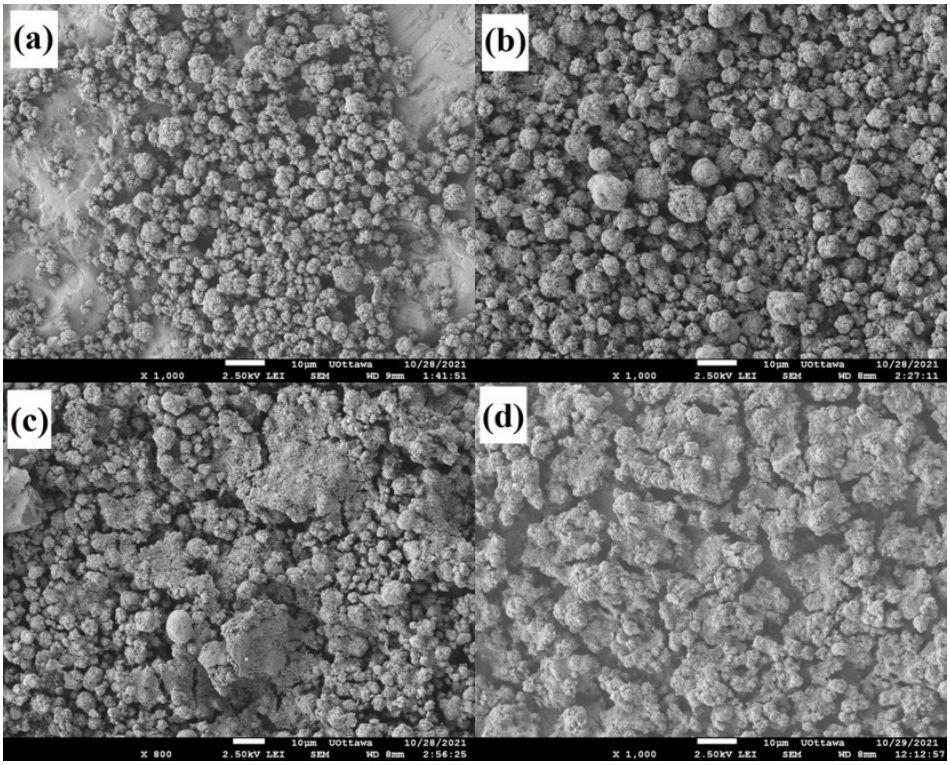

Figure B-2. SEM images (10µm) of spent (a) Co_3O_4, (b) 1wt.%Cu/Co_3O_4, (c) 4wt.%Cu/Co_3O_4, and (d) 8wt.%Cu/Co_3O_4 deposited on YSZ.

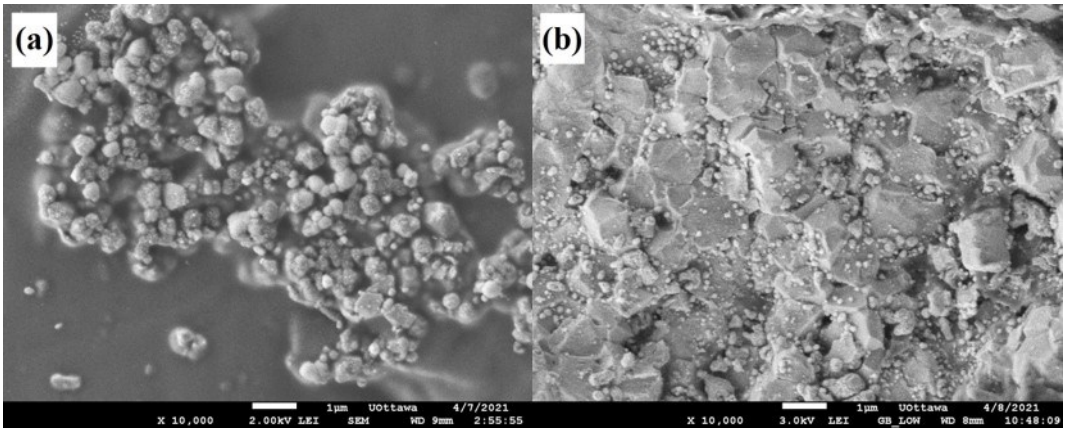

Figure B-3. SEM images (1µm) of (a) as-prepared and (b) spent free-standing Cu deposited on YSZ.

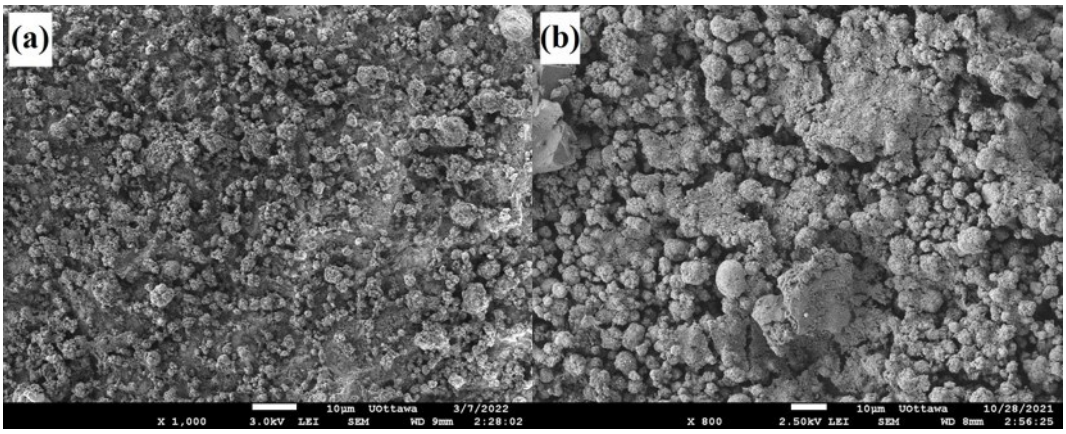

Figure B-4. SEM images (10µm) of (a) fresh and (b) spent 4wt.%Cu/Co_3O_4 deposited on YSZ.

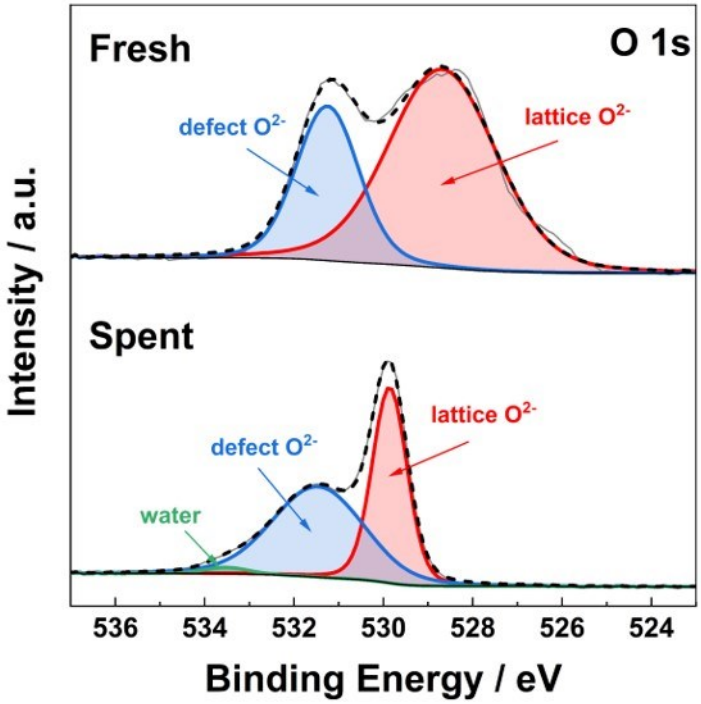

Figure B-5. High resolution XPS spectra for O 1s of fresh and spent 4wt.%Cu/Co_3O_4.

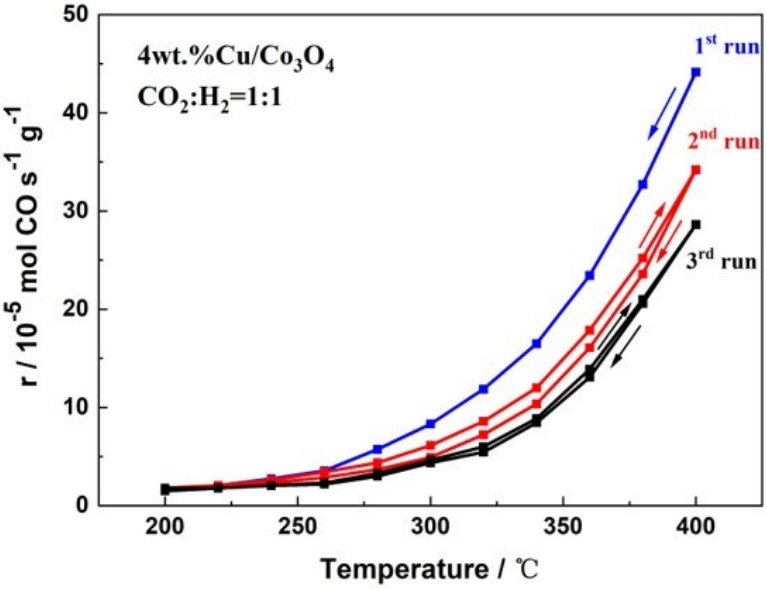

Figure B-6. Overall light-off curves of 4wt.%Cu/Co_3O_4 under the stoichiometric condition.

Table B-1. XPS data for Cu 2p, Co 2p and O 1s of fresh and spent samples.

		Position (eV)		FWHM		%Area	
		fresh	spent	fresh	spent	fresh	spent
Cu 2p	Cu^0/Cu^{1+}	932.3	932.3	1.93	1.57	85.72	13.54
	Cu^{2+}	934.6	934.4	2.14	2.54	14.28	86.46
Co 2p	Co^0	778.0	N/A	2.05	N/A	44.53	N/A
	Co^{2+}	781.5	781.2	2.86	2.24	15.62	42.01
	$Co^{2+,3+}$	779.8	779.7	2.39	1.62	39.85	57.99
O 1s	defect O^{2-}	531.2	531.5	1.65	2.40	31.15	53.84
	lattice O^{2-}	528.8	529.8	2.84	0.92	68.65	44.44
	H_2O	N/A	533.5	N/A	1.11	N/A	1.72

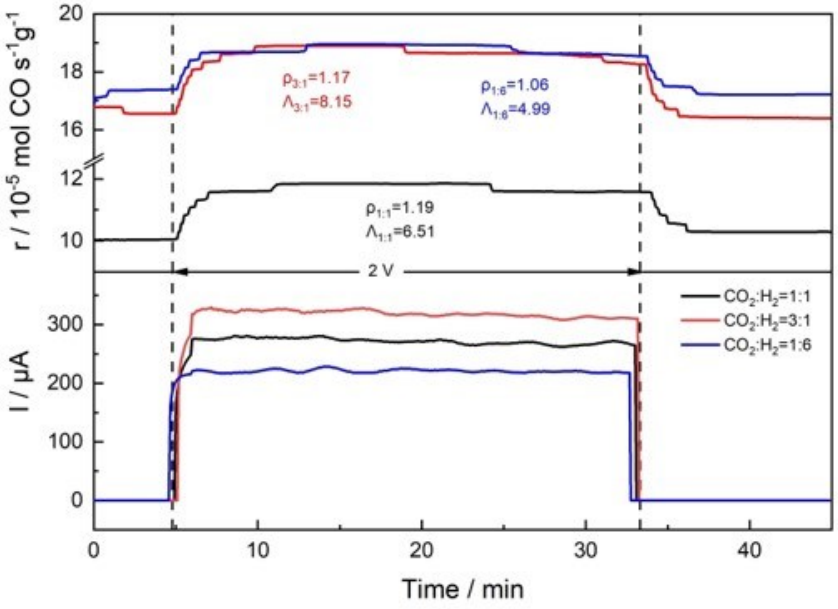

Figure B-7. EPOC effects of free-standing Cu/YSZ at 400℃ under various conditions.

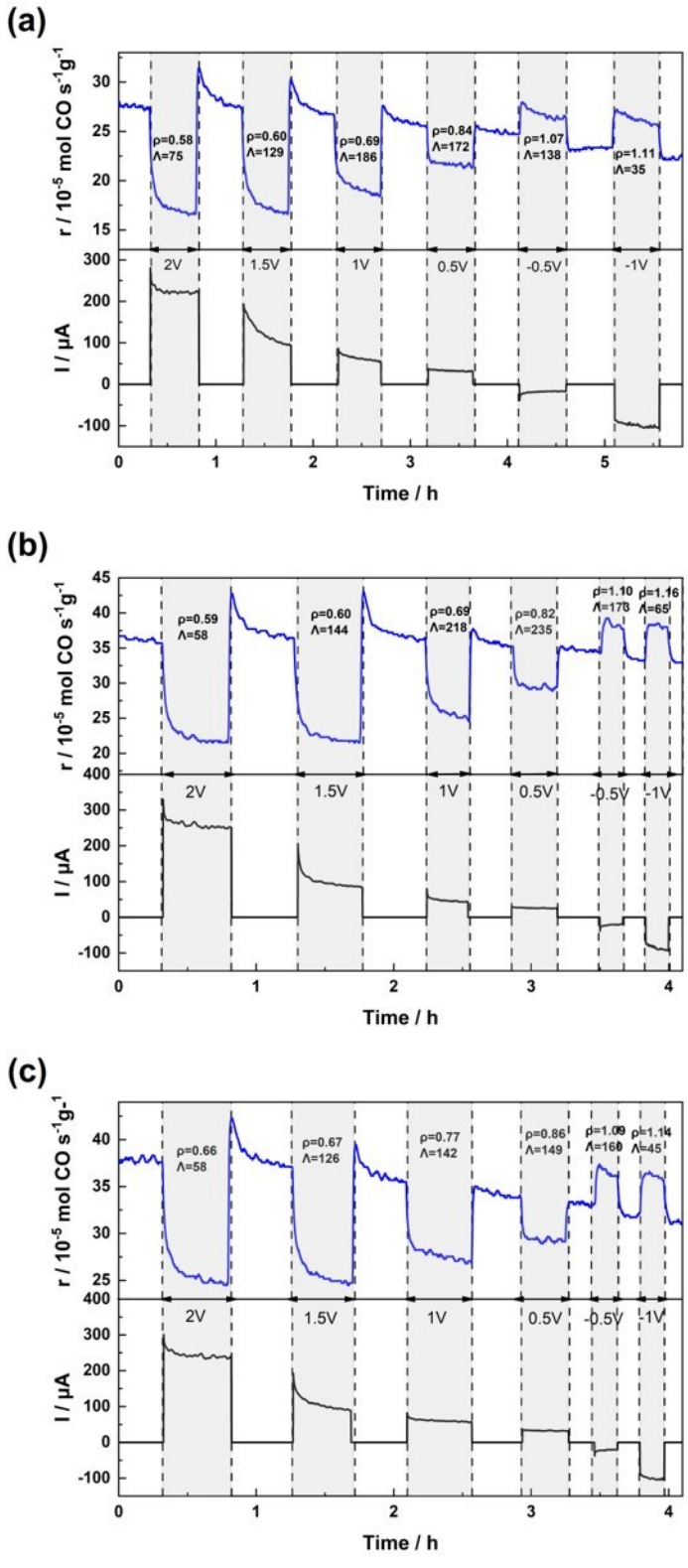

Figure B-8. Overall transient responses of reaction rate and current to applied potentials over 4wt.%Cu/Co_3O_4 at 400℃ under (a) stoichiometric, (b) oxidizing, and (c) reducing conditions.

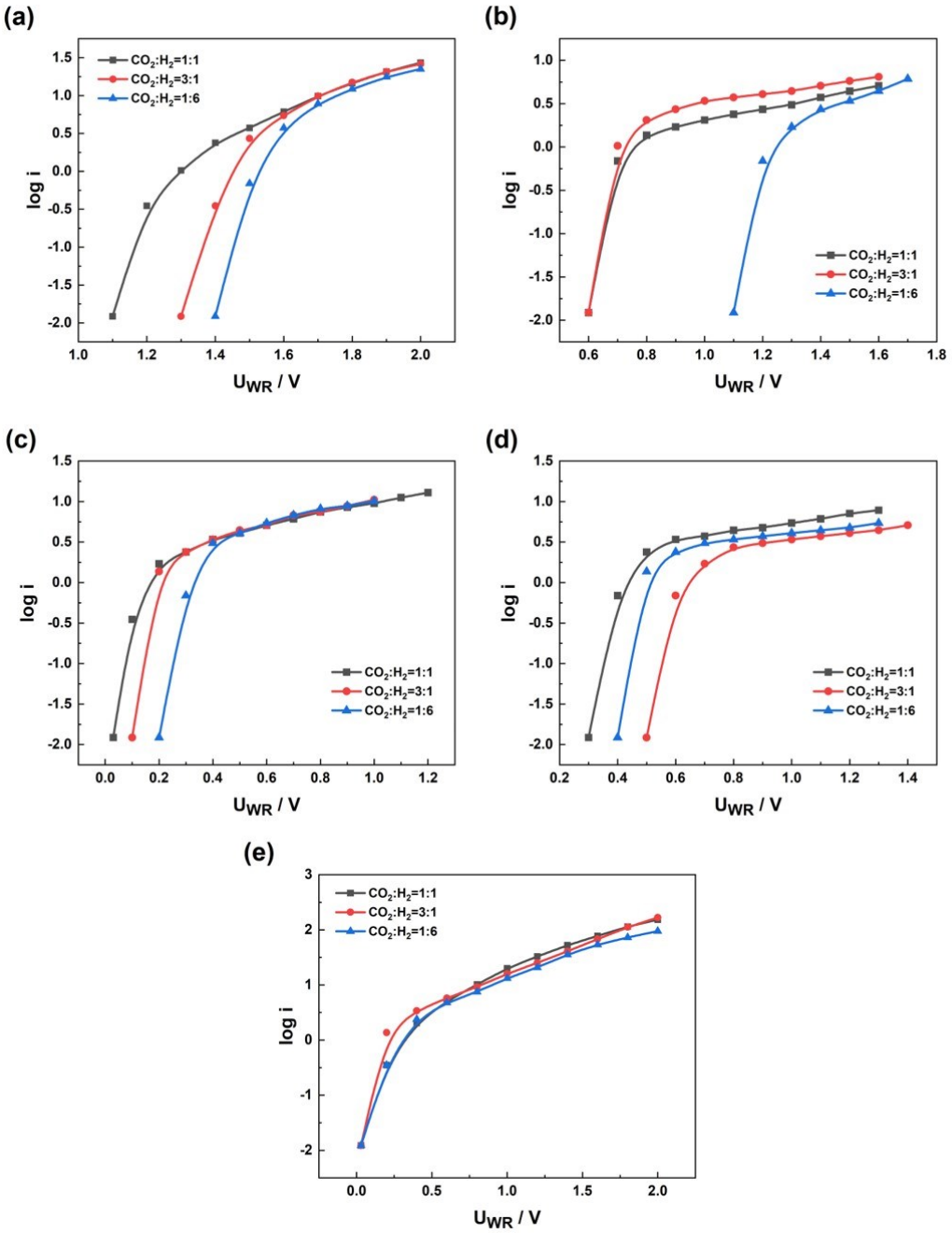

Figure B-9. Tafel plots of (a) bare Co_3O_4, (b) 1wt.%Cu/Co_3O_4, (c) 4wt.%Cu/Co_3O_4, (d)8wt.%Cu/Co_3O_4, and (e) free-standing Cu under all conditions at 400℃.

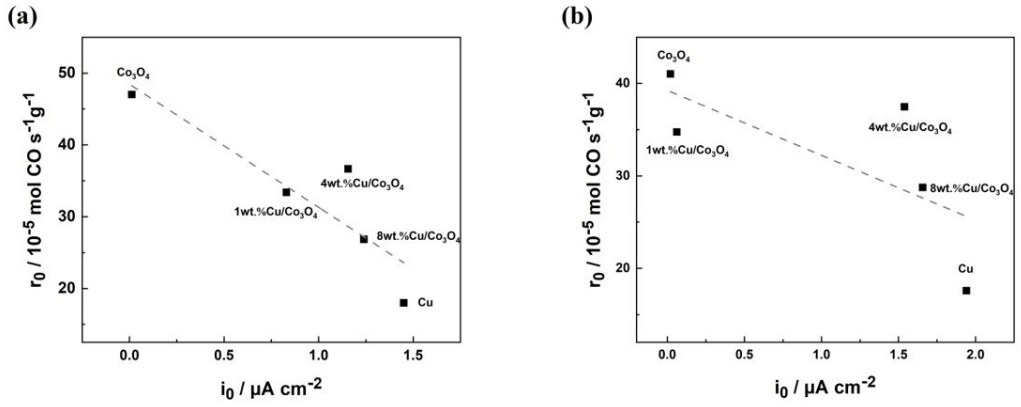

Figure B-10. Relationships between open circuit catalytic reaction rate (r_0) and exchange current density (i_0) of Cu/Co_3O_4 catalysts under (a) oxidizing and (b) reducing conditions.

Chapter 5: Experimental and DFT Study on Electrochemical Promotion of Cu/ZnO for the Reverse Water Gas Shift Reaction

Adapted from: ***J. Wang****, M. G. Sandoval, M. Couillard, E. A. González, P. V. Jasen, A. Juan, A. Weck, E. A. Baranova, 2024, ACS Sustainable Chemistry & Engineering.*

Abstract: This study investigates the use of electrochemical promotion of catalysis (EPOC) to in situ control the catalytic rate of reverse water gas shift (RWGS) reaction that recycles wasteful CO_2 into CO. Nanostructured Cu/ZnO catalysts with varying Cu loadings (5, 10, 20, 40, and 60 wt.%) are synthesized for RWGS. Compared to unsupported Cu nanoparticles and bare ZnO support, Cu/ZnO catalysts exhibit improved performance due to metal support interaction. 20 and 40 wt.% Cu/ZnO catalysts show the highest open-circuit catalytic rates (r_0) owing to larger specific surface areas (S_{BET} = ~38 m^2 g^{-1}). In EPOC experiments, the application of constant currents results in promoted reaction rates, with the highest enhancement ratio (ρ = 1.14) and apparent Faradaic efficiency (Λ = 3.16) observed for 10 wt.% Cu/ZnO. Density functional theory (DFT) computations and physicochemical characterizations support the lattice oxygen provision mechanism, where oxygen migrates from ZnO to Cu during polarization. This results in partial oxidation of Cu to Cu_2O and a subsequent increase in RWGS rate. A correlation between S_{BET} and r_0 and a positive relationship between the electrochemical surface area (ECSA) and Λ values in EPOC are identified, indicating that electrochemically active sites are important for catalyst activation under polarization.

5.1 Introduction

Although Cu/Co_3O_4 catalysts show good activities in Chapter 4, the existence of multiple oxidation states of Co makes the interaction between Cu and Co_3O_4 complicated and the sintering still occurs. To select a suitable support for Cu that prevents it from deactivation by forming MSI and to better the understanding of the

electrochemical interactions between Cu and oxide support, ZnO is chosen for its simple, stable structure, and affordability.

Density functional theory (DFT) is a powerful computational method to study the electronic structures of reactants, intermediates and products that interact with the catalyst surface during CO_2 hydrogenation processes[1], Research on DFT calculation of Cu surfaces[2] identified that the most critical step in RWGS was the dissociation of CO_2, which required a higher activation energy (1.51 eV) on Cu (111) surface compared to Cu (100) (1.26 eV) and Cu (110) (0.71 eV) surfaces. Consequently, the oxygen atom in CO_2 preferably bonded to Cu (110) rather than to Cu (111). In addition, DFT investigations on Cu_2O surface revealed that the existence of Cu_2O (110) further promoted the activation and subsequent reduction of CO_2[3]. Similarly, DFT studies on ZnO demonstrated the sensitivity of CO_2 adsorption to the oxide surface structure, highlighting that the binding strength of CO_2 was the highest on ZnO (101)[4]. DFT calculations also revealed that the oxygen vacancies within the ZnO structure played a crucial role in RWGS by increasing the charge density around the valence band maximum and enhancing the activation of CO_2[5]. Despite the widespread application of DFT in RWGS, it was rarely studied in the field of EPOC and the impact of O^{2-} migration on the oxidation state changes of the supported metal catalysts remained unclear. Considering the rapid electrochemical reactions that happened on the catalyst surface in EPOC, DFT calculation is taken as a promising and alternative way to simulate and evaluate the transportation of ionic species from oxide support towards metal catalyst.

In this study, we explored the EPOC using stable and active metal catalysts to emphasize the sustainability and innovation of our catalyst design, aiming to enhance the potential for energy-efficient and durable catalytic systems. A series of non-noble Cu/ZnO catalysts, with varying copper loadings on hexagonal-structured ZnO, were synthesized and deposited on YSZ for the RWGS reaction. These catalysts exhibited greater activity than previously studied Cu-based[6] and Fe-based catalysts[7] and demonstrated improved stability over Co-based catalysts[8], without surface sintering.

Moreover, unlike previous DFT studies on EPOC that focused on the potential changes on noble metal catalyst surfaces upon polarization, this work established a new DFT model. This model simulated the migration of O^{2-} towards Cu under polarization and demonstrated the redox processes occurring on the non-noble metal catalyst surface, leading to the electro-oxidation of Cu into Cu_2O. These findings were further validated through XPS and XRD characterizations. Additionally, this study innovatively used electrochemical active surface area (ECSA) to explain the magnitudes of EPOC effects, finding a positive correlation between them. This discovery offers valuable guidance and insights into developing sustainable and economical catalysts for future studies on EPOC for RWGS.

5.2 Experimental and Computational Methodology

5.2.1 Catalysts preparation

The nano-structured ZnO support was synthesized using the polyol method as mentioned in Chapter 2. Specifically, Zinc Acetate (dihydrate, Alfa Aesar, 97+%) was measured and dissolved in ethylene glycol (EG) (Fisher Chemical). Then, 0.25 M tetramethylammonium hydroxide (TMAOH) (pentahydrate, Sigma-Aldrich, 97+%) was added until the pH of the mixture reached 12. The final solution was stirred at room temperature (RT) for 30 minutes before starting the reflux with the temperature increased gradually from RT to 150°C. Once the colour changed from clear to turbid white, the solution was cooled down to RT while keep stirring throughout the period. The resulting colloidal solution was centrifuged at 6000 rpm, washed with deionized water (DI water, 18 MΩ cm), and dried in air at 60°C. The Cu NPs were synthesized following the same procedures as shown in Chapter 3 and were stored in colloidal solution (1 mg mL^{-1}).

The Cu/ZnO catalysts were prepared following the procedures in Chapter 2. Cu colloidal solution was mixed with the ZnO powders in DI water for 48 h for the desired metal loadings of Cu on ZnO. For example, mixing 5 mL of Cu colloidal solution with 50 mg of ZnO produced the catalyst with 10 weight percent (wt.%) Cu

on ZnO. The dispersed Cu/ZnO was then centrifuged and washed three times with DI water at 6000 rpm. The final catalysts were labelled as 5, 10, 20, 40, and 60CuZnO, where the number represented the wt.% of Cu NPs. The catalysts after centrifugation were dried in air at 60℃ for 24 h and stored in powder forms for future tests.

5.2.2 Experimental setup

YSZ, gold electrodes, and catalyst-working electrode were prepared following the same procedures as described in Chapter 4. The catalyst loading was 0.5 mg cm^{-2}. The electrochemical cell and reactor setup were assembled as mentioned in Chapter 2. H_2 (Messer, 100 %), CO_2 (Messer, 99.99%), and Argon (Ar, Messer, 100 %) were fed to the reactor through three individual mass flow controllers (MFC, MKS Instruments) and the CO_2:H_2 volumetric ratios were adjusted to be 1:1, 3:1, and 1:6 under the protection of Ar. CO analyzer was connected with gas outlet to monitor the amount of produced CO. Before starting the RWGS reaction, the catalysts were pre-treated following the procedures mentioned in Chapter 2. The catalysts were then left under stochiometric conditions (CO_2:H_2 =1:1) for 5 h to guarantee the steady state.

5.2.3 Electrochemical measurements

A potentiostat–galvanostat (Arbin Instruments, MSTAT) machine was used to conduct all electrochemical tests. The EPOC measurements were carried out by applying constant currents across the catalyst-working electrode and the counter electrode, and the effects were evaluated by the enhancement ratio (ρ) and apparent Faradaic efficiency (Λ) according to Eq. (5-1) and (5-2):

$$\rho = r/r_0 \tag{5-1}$$

$$|\Lambda| = (r - r_0)/(I/nF) \tag{5-2}$$

where r is the promoted reaction rate during polarization, r_0 is the open-circuit rate, I is the applied current, F is the Faradaic constant, and n is the number of electrons transferred, which is 2 in RWGS reaction.

Cyclic voltammetry (CV) was carried out over as-prepared samples right after pre-treatment. Before starting the CV, the atmosphere was changed into inert condition (in Argon) and the temperature was kept at 400℃. The potential window of CV was set to start from -0.8 V to 1.5 V, followed by cycling back to -0.8 V with a scanning rate of 20 mV s^{-1}.

The relative electrochemical active surface areas (ECSAs) of Cu/ZnO catalysts were evaluated by the surface roughness factor (RF) and were determined by measuring the double layer capacitance (C_{dl}) of as-prepared catalysts. CVs were performed in the potential window ranging from -0.25 V to 0.25 V, where no faradaic reactions happened, with various scan rates (20 - 200 mV s^{-1}) under inert conditions at 400℃. By plotting the charging current (I) vs. scan rate ($dV\ dt^{-1}$), the C_{dl} could be calculated from the slopes according to the Eq. (5-3)[9]:

$$I = dQ/dt = C_{dl}(dV/dt) \quad (5\text{-}3)$$

The resulting C_{dl} of all Cu/ZnO catalysts were then normalized to that of bare ZnO to obtain the RF, as shown in Eq. (5-4):

$$RF = C_{dl,CuZnO}/C_{dl,ZnO} \quad (5\text{-}4)$$

5.2.4 Physicochemical characterizations

Scanning Transmission Electron Microscopy (STEM) was used on spent 10CuZnO catalyst to determine the structure and particle size. High-angle annular dark-field (HAADF) imaging was performed to enhance contrast sensitivity to the atomic number Z. Scanning Electron Microscopy (SEM, JSM-7500F FESEM) was used to characterize the morphology of spent catalysts deposited on YSZ and Energy-dispersive X-ray spectrometer (EDS) connected to the microscope was carried out to characterize the elemental composition. X-ray Diffraction (XRD) patterns were measured over as-prepared and spent catalysts to investigate the crystalline structure changes before and after polarization by the Rigaku Ultima IV multipurpose diffractometer at a scan rate of 1 degree (°) min^{-1} from 20 to 80 °2θ. The crystallite

sizes of NPs, L, were estimated by using the major phase parameters according to Scherrer Equation (Eq. (5-5)) and the interplanar distances, d, were determined according to the Bragg Equation (Eq. (5-6))[10]:

$$L = K\lambda/FWHM \cdot \cos\theta \quad (5\text{-}5)$$

$$n\lambda = 2d \cdot \sin\theta \quad (5\text{-}6)$$

where FWHM is the full width at half maximum of the diffraction peak, θ is the diffraction angle, n=1, λ=0.15418 nm, and K=0.9.

The X-ray photoelectron spectroscopy (XPS) spectra were measured on as-prepared and spent samples using a Kratos AXIS Nova spectrometer equipped with an Al X-ray source to investigate the oxidation states of Cu and Zn. The XPS peaks were all fitted using the Shirley background corrections and the Gaussian-Lorentzian shape function in CasaXPS software with high resolution analyses calibrated to the C 1s signal at 284.8 eV. Brunauer-Emmett-Teller (BET) method was performed on as-prepared samples to determine the specific surface area (S_{BET}). The values were calculated from data points at relative pressures (p/p_0) between 0.05 and 0.30. The Cu loadings on ZnO in the as-prepared samples were confirmed through Inductively Coupled Plasma Emission Spectroscopy (ICP-ES, Agilent 8800).

5.2.5 Computational methodology

Spin-polarized (SP) Density Functional Theory (DFT) calculations, based on quantum mechanics, were performed using the Vienna Ab-initio Simulation Package code (VASP)[11]. The magnetic moments for both Zn- and O-atom were initialized at zero. The plane-wave basis set with a cut-off energy of 520 eV was used for the ZnO bulk and surface simulation. The general gradient approximation (GGA) parameterized by the Perdew-Burke-Ernzerhof functional (PBE) as an exchange–correlation term was considered[12]. The projector augmented wave (PAW) pseudo potential method for taking into account the electron–ion core interaction, was carried out[13]. For the long-range order phenomena, the Van der Waals interactions as implemented by the DFT-D3 correction method of Grimme et al. were used[14].

Because standard DFT fails to describe the localization in the Zn d orbitals, the Hubbard correction (DFT-U) enclosed by the Dudarev approximation was applied[15]. To obtain an electronic structure similar to the experimental one and avoid the energy fluctuations, an on-site Coulomb correction was also used for O 2p orbitals. Our computed values for effective U are 10 eV, 7.74 eV and 5.20 eV for Zn 3d-orbitals, O 2p-orbitals and Cu 3d-orbitals, respectively. These values are in good agreement with those reported in the literature[16,17]. All structures were optimized until the forces acting on each atom were smaller than 10^{-4} eV $Å^{-1}$ and the energy convergence was smaller than 10^{-2} meV. An automatically generated gamma-centered k-points mesh in the irreducible part of the Brillouin zone of 12 × 12 × 7 (bulk) and 7 × 7 × 1 (surface) k-point sampling grid was used for reciprocal space integration, following the Monkhorst-Pack scheme[18].

The bulk of wurtzite ZnO were simulated using the $p6\bar{3}mc$ space group.[19] The obtained lattice parameters of a = b = 3.166 Å, c/a = 1.611 Å (c = 5.102 Å) and α = β = 90°, γ = 60° are in good agreement with reported experimental[20] and theoretical[21] values. As shown in **Figure C-1**, the ZnO (101) low-index surface was modeled as a super-cell with five ZnO bilayers along the vacuum direction and 4 × 4 primitive cell on the in-plane direction. This ZnO plane was chosen based on experimental information in Section 5.3.1. The 15 Å vacuum layer on top (z-direction) was enough to prevent interactions between periodic images of the slabs. In the optimization of the surfaces, the three outmost layers on the top were relaxed, while the two bottom layers were frozen in the relaxed bulk positions.

The different high symmetrical adsorption sites that were considered to study the interaction of a Cu-atom with the surface are presented in **Figure C-1**. For a more realistic representation, a second Cu atom was adsorbed at the nearest and the most energetically favorable adsorption site. Then an O-atom was adsorbed along the high symmetrical adsorption sites surrounding the Cu-atom and the two Cu-atoms for both considered systems.

To assess the difficulty of vacancy formation, O and Zn vacancies were generated in the outmost layer by simply removing an atom. The specific atoms chosen for removal are also indicated in **Figure C-1**. In an effort to elucidate the potential mechanism of copper oxide formation during the electrooxidation process, the extraction of oxygen from the most stable O-vacancy locations was simulated by incrementally moving it in 0.1 Å steps upward on the ZnO surface with two adsorbed Cu-atoms.

The adsorption energies, represented as E_{ads} in eV, were computed as the difference between the total energy of the system after adsorption ($E_{adsorbate/substrate}$) and the energy of the isolated atom in a box ($E_{adsorbate}$) plus the energy of the clean surface ($E_{substrate}$). This calculation is expressed in Eq. (5-7):

$$\mathrm{E_{ads}} = \mathrm{E_{adsorbate/substrate}} - (\mathrm{E_{adsorbate}} + \mathrm{E_{substrate}}) \quad (5\text{-}7)$$

For the E_{ads}, a smaller value signifies a more favourable adsorption site and a positive value indicates an endothermic reaction, while a negative one suggests an exothermic process. In this case, the oxygen is considered as coming after the entire process of CO_2 electrochemical reduction to CO, where the final products are primarily CO(g) and O^*[5]. Then the $E_{adsorbate}$ is calculated from an atomic oxygen isolated in a box.

The energy barrier (E_{bar}), reaction energy (E_r), and reverse energy barrier (E_{rbar}) are calculated in Eq. (5-8)-(5-10):

$$\mathrm{E_{bar}} = \mathrm{E_{TS}} - \mathrm{E_{IS}} \quad (5\text{-}8)$$

$$\mathrm{E_{r}} = \mathrm{E_{FS}} - \mathrm{E_{IS}} \quad (5\text{-}9)$$

$$\mathrm{E_{rbar}} = \mathrm{E_{TS}} - \mathrm{E_{FS}} \quad (5\text{-}10)$$

where E_{IS}, E_{FS} and E_{TS} refer to the initial-, final- and transition-state energies. The vacancy formation energy (E_{vac}) is computed at zero kelvin in Eq. (5-11) (a lower value indicates a more energetically favorable condition):

$$\mathrm{E_{vac}} = \left(\mathrm{E_{ZnO(101)+vac}} + \mathrm{E_{vac-atom}}\right) - \mathrm{E_{ZnO(101)}} \quad (5\text{-}11)$$

where $E_{ZnO(101)+vac}$ is the total energy of the system in the presence of the defect, $E_{vac-atom}$ is the energy of the isolated atom deleted from the vacancy and $E_{ZnO(101)}$ is the total energy of the system without any vacancy[22].

5.3 Results

5.3.1 Physicochemical characterizations

The ICP-ES analysis confirmed the actual Cu loading amounts on ZnO (± 0.3 – 0.6 wt.%). **Figure 5-1a and b** show the TEM image and STEM image with corresponding EELS mapping (the orange area in **Figure 5-1b**) of spent 10CuZnO catalyst, respectively, where Cu was found on the surface of ZnO support. From the STEM image in **Figure C-2a**, the synthesized ZnO had a hexagonal structure with a diameter of 100 nm, while Cu on ZnO had a diameter of approximately 30 nm, which was consistent with the particle size of unsupported Cu NPs shown in **Figure C-2b**. Compared to unsupported Cu NPs, which were easily sintered and agglomerated after reactions (**Figure C-3**), the improvements in dispersion and thermal stability of Cu/ZnO were verified according to the SEM images of all spent Cu/ZnO catalysts on scale of 1 μm (**Figure C-4**), where no sintering was found. The EDS results from **Figure C-5** confirmed the existence of Cu and Zn without any other impurities (Zr was from YSZ).

The crystalline structure of 10CuZnO is shown in **Figure 5-1a**, where the lattice interplanar distance of the ZnO phase is measured to be 0.25 nm, which is referred to as ZnO (101)[23]. However, Cu showed two different lattice structures with interplanar distances of 0.21 nm and 0.3 nm, representing metallic Cu (111) and Cu_2O (110) phases[24,25], respectively. This indicated that the metallic Cu was partially oxidized during the electrocatalytic experiments, which was due to the polarization. This will be discussed later.

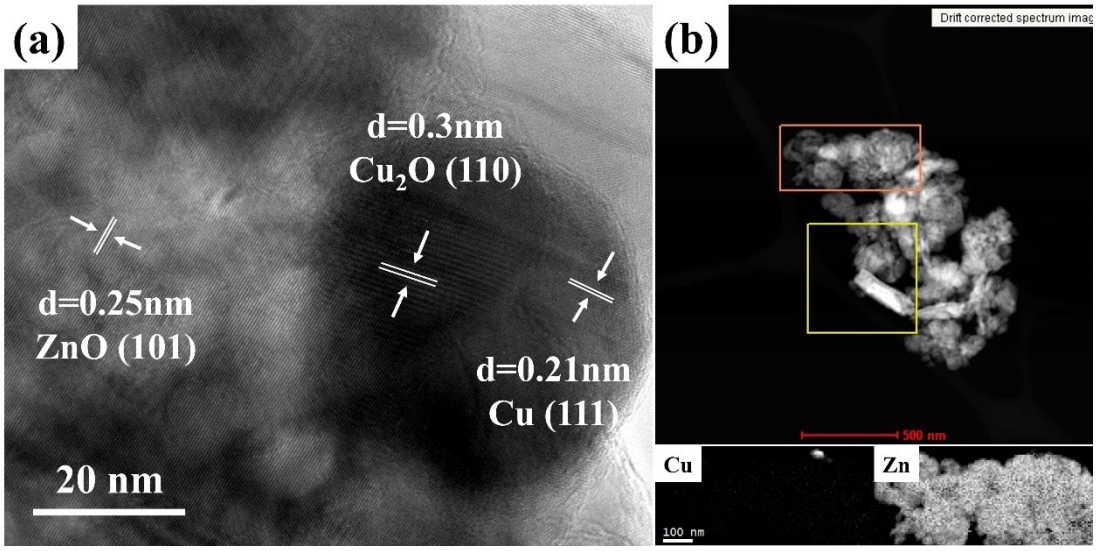

Figure 5-1. (a) TEM image of spent 10CuZnO. (b) STEM image and corresponding EELS mapping of Cu and Zn in the orange area (the yellow area is for drift correction).

Figure 5-2a shows the XRD patterns of as-prepared and spent 10CuZnO catalyst. The peak information of major phases in as-prepared and spent samples is summarized in **Table C-1**. The XRD patterns of bare ZnO and 60CuZnO are summarized in **Figure C-6**. It was found that ZnO (101), Cu (111) and Cu_2O (110) had the highest peak intensity in the phases of zinc oxide, metallic copper and copper oxide, respectively, and were taken as the major phases. For the synthesized ZnO support (**Figure C-6a**), the as-prepared sample exhibited several peaks within the diffraction range, illustrating the crystallinity of a hexagonal wurtzite-structured ZnO[26].

In the spent sample, ZnO showed the same peak locations with insignificant change in the crystallite size (from 25 nm to 26 nm), indicating its thermal stability. From **Figure 5-2a**, in addition to the peaks of ZnO, the as-prepared 10CuZnO sample showed three new peaks located at 43, 51, and 74 °2θ. These peaks represented Cu (111), (200) and (220)[27], respectively, and demonstrated that the Cu NPs existed in metallic state on the surface of ZnO. The Cu crystallite size was calculated to be 34.5 nm, fitting with the particle size observed in STEM. The stability of metallic Cu was

affiliated to the MSI effect between Cu and ZnO that prevented Cu NPs from oxidation. However, an additional peak at 30 °2θ appeared in the spent sample, which was known as the Cu_2O (110) phase[28], and the particle sizes of ZnO and Cu were both enlarged (**Table C-1**). The formation of Cu_2O agreed with STEM result. In terms of 60CuZnO (**Figure C-6b**), the larger Cu loading amount on ZnO yielded significantly higher peaks of metallic Cu, while the Cu_2O phase was still formed after catalytic experiments. Moreover, the interplanar distances of ZnO (101), Cu (111), and Cu_2O (110) at 36, 43, and 30 °2θ were calculated to be 0.248 nm, 0.209 nm, and 0.297 nm, respectively, all of which were in line with the STEM measurements in **Figure 5-1a**.

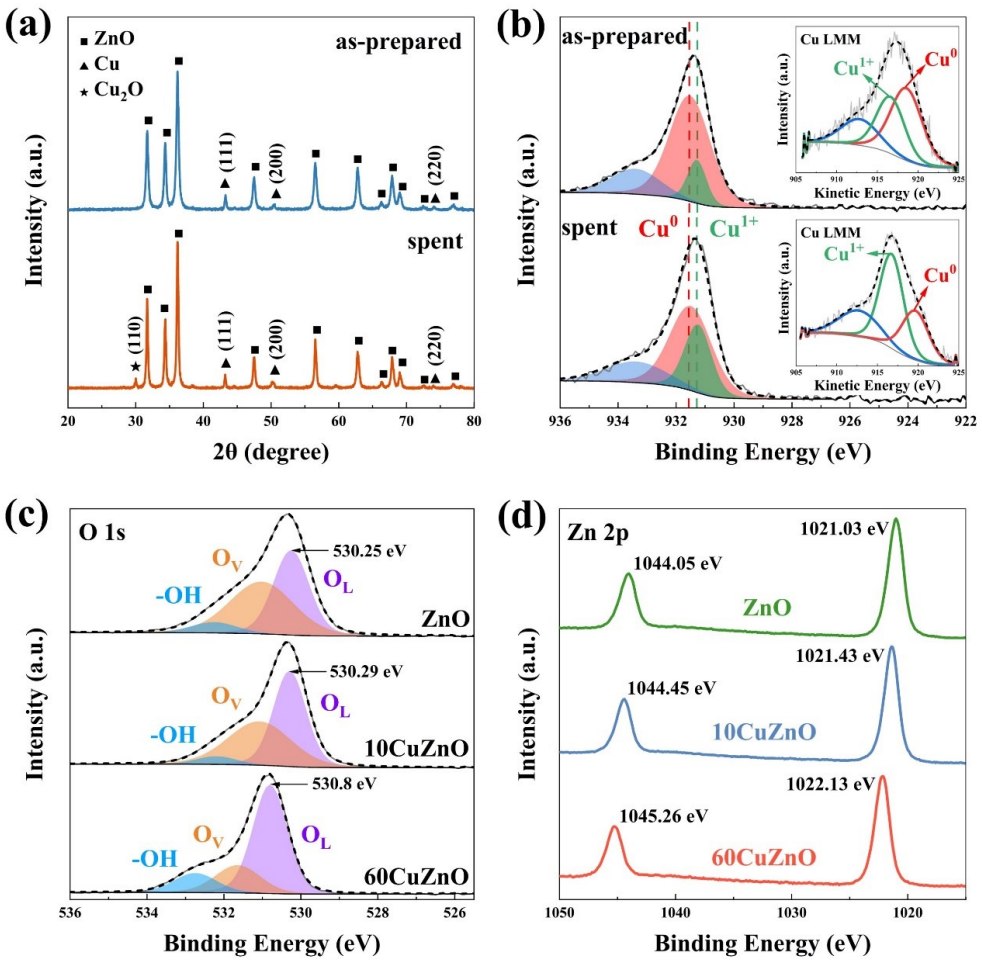

Figure 5-2. (a) XRD patterns and (b) high-resolution XPS spectra of Cu $2p_{3/2}$ and Cu LMM for as-prepared and spent 10CuZnO. High-resolution XPS spectra of (c) O 1s and (d) Zn 2p for as-prepared ZnO, 10CuZnO and 60CuZnO.

Figure 5-2b shows the XPS spectra of Cu $2p_{3/2}$ and Cu LMM for as-prepared and spent 10CuZnO. The peaks at 931.5, 931.2 and 933.4 eV represented metallic copper (Cu^0), Cu_2O (Cu^{1+}) and CuO (Cu^{2+})[6], respectively. The detailed Cu 2p species information is summarized in **Table C-2**. From **Figure 5-2b**, Cu in as-prepared sample was mainly in its reduced states, where Cu^0 and Cu^{1+} occupied 68% and 13% area, respectively, and Cu^{2+} had 19%. This confirmed the reduction of Cu after the pre-treatment in H_2. In spent sample, however, the Cu $2p_{3/2}$ slightly shifted to lower binding energy (dash line) with Cu^0 decreased to 53%, while Cu^{1+} increased to 28% and Cu^{2+} remained at 19%. This illustrated that Cu^0 was partially oxidized into Cu^{1+} by O^{2-} because of the applied currents. The oxidation state change was also confirmed by Cu LMM spectra, which showed a similar trend as Cu $2p_{3/2}$. This was consistent with XRD patterns showing only a tiny Cu_2O peak at 30 °2θ in the spent sample. The Cu^{2+} was formed during the storage as its content stayed constant and Cu was prone to oxidation even at RT[29]. Despite the formation of Cu^{2+}, the Cu^0 and Cu^{1+} were still the main phases after the reactions due to the protection of ZnO support.

The XPS spectra of O 1s for as-prepared ZnO, 10CuZnO and 60CuZnO are compared in **Figure 5-2c**, with lattice O^{2-} (O_L, represents Zn-O bonding) of ZnO found at 530 eV, defect O^{2-} (O_V, represents oxygen-deficient region) of ZnO observed at 531 eV, and adsorbed oxygen (-OH) located at 532 eV[30,31]. It was found that by increasing Cu content from 0 to 60 wt.%, the O_L increased from 44.19% to 64.23% and the O_V decreased from 48.58% to 21.47%. Moreover, the O_L peak position shifted from 530.25 eV to 530.8 eV. This illustrated that Cu/ZnO catalysts with a lower Cu/Zn ratio owned a higher amount of oxygen vacancies, which were provided by the ZnO phase.

Figure 5-2d exhibits the XPS spectra of Zn 2p with peaks near 1021 eV and 1044 eV referred to as Zn $2p_{3/2}$ and Zn $2p_{1/2}$, respectively. The peak shifts of Zn 2p towards higher binding energies further confirmed the decrease of oxygen vacancies in Cu/ZnO catalysts with increasing the Cu loading. The detailed XPS data of O 1s

and Zn 2p for as-prepared samples are included in **Table C-3** and the wide scan spectra are shown in **Figure C-7**.

5.3.2 Open-circuit activities

Figure 5-3a shows the open-circuit RWGS activities of Cu, ZnO and Cu/ZnO catalysts under stoichiometric conditions across the temperature range of 200 - 400℃. The catalytic rates under both oxidizing and reducing conditions are summarized in **Figure C-8**. The RWGS rates of 20CuZnO, which exhibits the best catalytic performance, under various conditions are shown in **Figure 5-3b**. Observations indicated a slightly elevated activity in oxidizing conditions compared to stoichiometric conditions, while the reaction was most favored under reducing conditions. This was because, more CO_2 was adsorbed and dissociated into CO on the surface of Cu[32] in oxidizing conditions, resulting in high CO production rates, while the RWGS was thermodynamically favored in H_2-rich atmosphere[33]. Considering the low carbon conversion in oxidizing condition and high H_2 consumption in reducing condition, the stoichiometric condition was chosen and studied in this work.

From catalytic investigations, both unsupported Cu NPs and the ZnO support were found to contribute to the RWGS rate, which were activated above 340℃. However, by loading small amounts of Cu NPs on ZnO, the Cu/ZnO catalysts showed apparent superior catalytic rates compared to bare Cu and ZnO and were activated above 280℃. This was due to the MSI effect that improved both thermal stability and dispersion of the nano-structured catalysts, which were also verified by the SEM images and crystallite size evaluation from XRD data. The catalytic rate was improved by adding more Cu NPs until a loading amount of 20 wt.%. Further increasing Cu to 40 wt.% only resulted in limited enhancement in reaction rate, which was then significantly inhibited when Cu reached 60 wt.%. According to the evaluation of S_{BET} as summarized in **Table 5-1**, it confirmed the increasing S_{BET} of 5-40CuZnO and the decrease in S_{BET} of 60CuZnO. This meant that the increasing catalytic activity was due to the enlarging geometric reaction sites. However, the

excessive existence of Cu NPs in 60CuZnO led to a decrease in the surface area and the reaction rate was inhibited as a result. This was attributed to Cu NPs that were prone to agglomeration at high temperatures[6,34], also confirmed in **Figure C-2**.

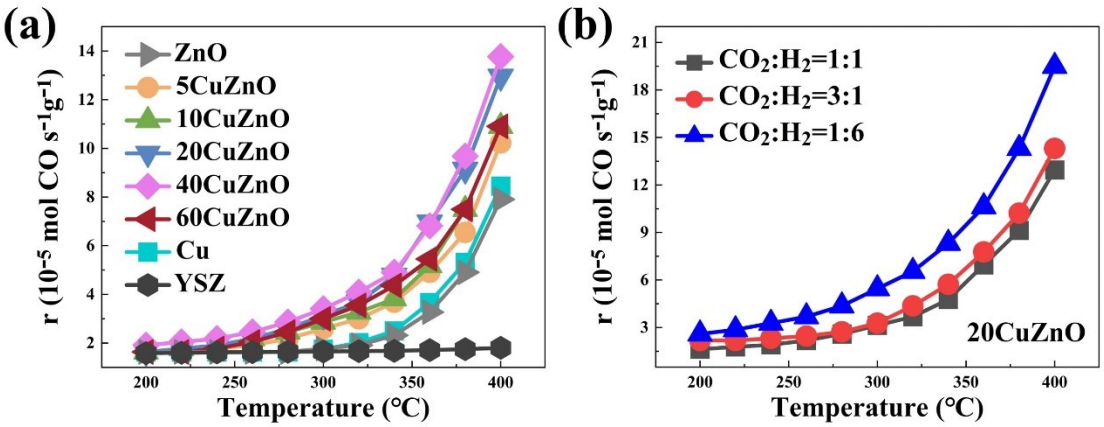

Figure 5-3. Light-off curves of (a) all Cu/ZnO catalysts under stoichiometric conditions and (b) 20CuZnO catalyst under all reaction conditions.

Table 5-1. Summary of parameters for Cu/ZnO catalysts at 400°C.

	ZnO	5CuZnO	10CuZnO	20CuZnO	40CuZnO	60CuZnO
r_0 ($\times 10^{-5}$ mol s^{-1} g^{-1})	7.90	10.2	10.9	12.9	13.7	10.9
S_{BET} (m^2 g^{-1})	10.47	23.64	30.11	36.77	39.24	25.86
ρ	1.06	1.13	1.14	1.08	1.06	1.05
Λ	2.45	3.15	3.16	2.57	2.04	1.76
RF	1.00	1.22	1.45	1.17	0.86	0.58

5.3.3 Electrochemical promotion of catalysis

Figure 5-4 shows the transient responses of RWGS rates to applied constant current of 400 μA over all Cu/ZnO catalysts. The overall catalytic rates under polarization are summarized in **Figure C-9**. All Cu/ZnO catalysts showed EPOC effects, where the catalytic reaction rates were promoted gradually upon starting the

polarization and achieved new steady-states soon. Once interrupting the applied currents, the promoted catalytic rates were decreased and returned to the open-circuit rates. The EPOC effects only occurred under positive polarization, indicative of an electrophobic behavior[35]. The ρ and Λ used to describe the magnitude of EPOC effects are summarized in **Table 5-1**.

It was found that 5CuZnO and 10CuZnO had the highest and similar ρ (~1.14) and Λ (~3.16), while further increasing Cu loading on ZnO led to declines in the values. 40CuZnO and 60CuZnO exhibited restricted EPOC effects with ρ to be 1.06 and 1.05 and Λ to be 2.04 and 1.76, respectively. Moreover, the open-circuit activities of 40CuZnO and 60CuZnO continuously decreased, particularly after polarization. These were attributed to the agglomeration of the huge amounts of Cu NPs on ZnO. When applying positive polarization across the catalysts, the O^{2-} in ZnO bulk were supplied towards Cu NPs thorough the oxygen vacancies. As a result, the metallic Cu was partially oxidized into Cu_2O and the catalytic rate was enhanced accordingly as Cu_2O was a more active phase which could adsorb CO_2 with simultaneous CO production[6]. Moreover, DFT calculations also supported that CO_2 was less likely to bond with Cu (111)[1], which was the primary phase of the Cu NPs in this study, but was more likely to interact with Cu_2O (110)[3], the newly identified Cu phase after polarization as per the STEM and XRD results. When the polarization was stopped, the continuous supplement of O^{2-} was also interrupted. The formed Cu_2O was reduced back to metallic Cu by H_2 and the catalytic activities returned to the initial states.

However, ZnO also showed an electrophobic EPOC behavior, demonstrating the existence of oxygen vacancies within the structure that enabled the migration of O^{2-} from ZnO bulk to ZnO surface, which contributed to the enhanced rate. This property was important as it ensured that ZnO served as an appropriate substrate for Cu in EPOC by providing sufficient O^{2-} through abundant oxygen vacancies under polarization. After loading Cu NPs, the MSI effect between Cu and ZnO contributed to the improvements in EPOC effects since the active phases of reduced states of Cu were maintained and protected by the ZnO phase. When the Cu loadings reached 20

wt.%, less oxygen vacancies were available due to the fewer amounts of ZnO and agglomeration of Cu NPs. The EPOC effects were thereby inferior to those of 5CuZnO and 10CuZnO which were enriched with ZnO phase. Also, from **Figure C-9**, applying currents of 300 μA and 200 μA resulted in worse EPOC effects. This was associated with less O^{2-} supplement at weaker applied currents.

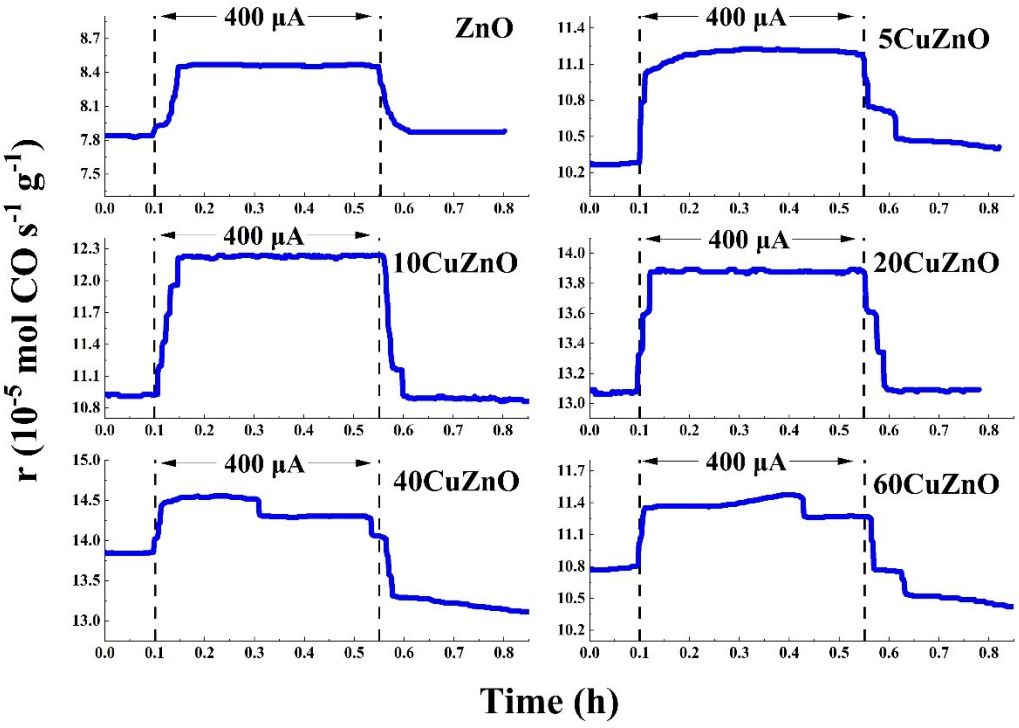

Figure 5-4. Transient responses of CO rates to applied constant current of 400 μA for all Cu/ZnO catalysts under stoichiometric conditions at 400°C.

5.3.4 Density functional theory

To clarify the source of oxygen in Cu_2O formed during EPOC tests and explore the potential lattice oxygen provision mechanism in the ZnO structure, DFT calculations were performed as a theoretical study. The electronic density of states (DOS) curves of bulk ZnO shown in **Figure C-10** serve as validation for the calculations. The symmetry observed in both spin-up and spin-down contributions indicated a zero magnetic moment. From **Figure C-10a**, the Fermi level was close to the valence band (VB), indicative of a type p semiconductor behaviour with a band

gap energy (E_g) of 3.2 eV, closely aligning with the experimental values and consistent with reported theoretical results[36]. From **Figure C-10b**, the projected DOS curves revealed three regions within the valence band: a deep segment (between -15 and -20 eV) primarily composed of O-2s states, a middle region (between -5 and -10 eV) dominated by Zn-3d and O-2p states, and a shallow portion (between -5 eV and E_F) mainly derived from O-2p states. Notably, a Zn-3d peak was observed around 8.7 eV, and the O-2p width was approximately 5 eV. These findings were in good agreement with experimental band compositions, Zn d peak and O p bandwidth values[37,38].

The calculations carried out on the ZnO (101) surface models described above attempted to evaluate the preference for oxygen supply during electrooxidation. Two potential alternatives were taken into account. The first alternative involved the supply of oxygen from the gas phase (O^*), while the second considered the migration of lattice oxygen from the ZnO phase ($O_{migrated}$), originating from a layer beneath the exposed surface. **Figure 5-5** shows the schematic views of the Cu/ZnO (101) surfaces under different conditions. The adsorption energies of Cu and O^* on different sites and the bond distances for the most stable configurations are summarized in **Table C-4 and C-5**, respectively.

Initially, the adsorption of Cu on ZnO was identified as a favorable process, exhibiting an adsorption energy of -5.90 eV. Cu was adsorbed on a B1 site, resulting in a final Cu_1-O_1 bond length of 1.82 Å, closely resembling the distance observed in Cu_2O surface oxide reported in the literature[39]. Meanwhile, the Zn_1-O_1 bond length was elongated by approximately 0.11 Å with respect to the bare surface (**Figure 5-5a** and **Table C-5**). Upon considering O^*, our results showed that the most stable site was on the Cu atom at a Cu_1-O^* distance of 2.80Å (**Figure 5-5b**) with an adsorption energy of -0.63 eV, indicating a favourable process. In this case, the Zn-O distances in the support remained unaltered. After the adsorption of the second Cu atom, the Cu_1-Cu_2 distance measured 2.59 Å (**Figure 5-5c**). The adsorption energy of the second Cu was -4.11 eV at a T1 site, resulting in final Cu_1-$O_{1(support)}$ and Cu_2-$O_{1(support)}$ distances

of 1.86 Å and 1.93 Å, respectively (**Figure 5-5c**). Meanwhile, the Zn_1-O_1 distance elongated to 2.06 Å (compared to a distance of 1.82 Å in bare support). In this system, the O^* was adsorbed in a bridge configuration on the Cu dimer at a Cu-O^* distance of 3.48 Å, with an adsorption energy of -0.28 eV (**Figure 5-5d**). All these results indicated that Cu preferred adsorption sites close to surface $O_{(support)}$, and gas-phase O^* exhibited a tendency to localize near a single Cu species with a more favourable O^* adsorption energy (-0.68 eV) rather than near a Cu dimer with a less favourable O^* adsorption energy (-0.28 eV). This simulated behavior explained that the presence of Cu_2O instead of CuO in spent sample as shown in STEM (**Figure 5-1a**) and XRD (**Figure 5-2a**) after electrocatalytic experiments implied that the oxidation of Cu was less likely attributed to CO_2 in the gas phase. Moreover, the support experienced only minimal distortion in their lattice distances throughout this adsorption process, which were less than 4% in the case of a Cu dimer.

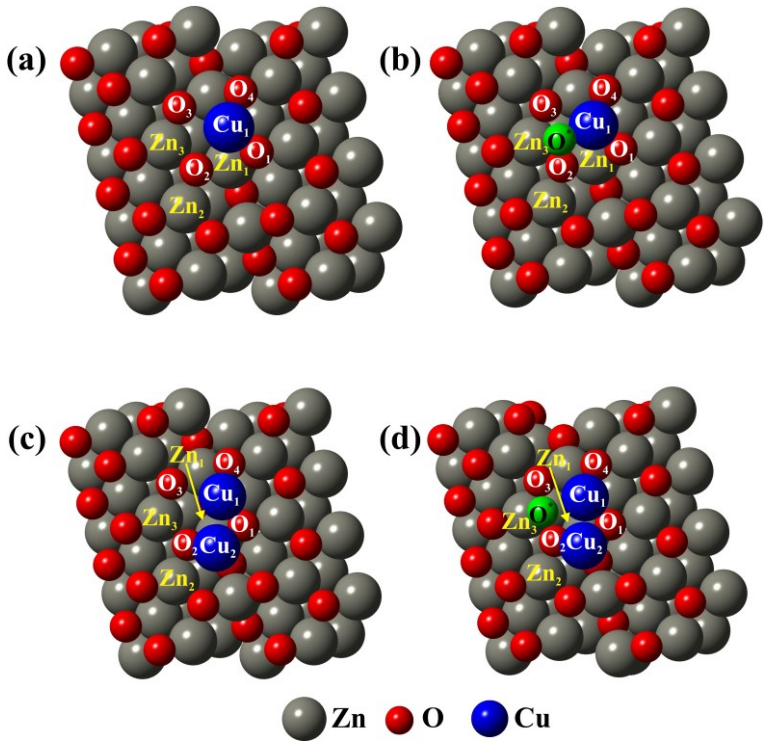

Figure 5-5. Schematic view of (a) ZnO (101) surface after Cu adsorption, (b) Cu/ZnO (101) system after O^* adsorption, (c) Cu/ZnO (101) system after Cu adsorption and (d) 2Cu/ZnO (101) system after O^* adsorption. The green oxygen atom represents the O^*.

To investigate the migration of oxygen from the support to a position between the Cu-Cu bridge, we first determined the O vacancy formation energy and Zn vacancy formation energy, resulting in values of 3.59 eV (V_{O1}) or 2.70 eV (V_{O2}) and 7.15 eV (V_{Zn1}) or 7.35 eV (V_{Zn2}). Subsequently, we displaced the O_1 lattice oxygen upwards until the Cu-O distance reached approximately 1.80 Å, similar to the metal-oxide distance in a Cu_2O surface.

The energy vs. step curve in **Figure 5-6** illustrated that the more favorable process involved the use of lattice oxygen from ZnO for the formation of a Cu_2O surface species. The lattice oxygen migration exhibited a small activation energy of approximately 0.25 eV, and the system stabilized with a favorable energy difference of about 0.385 eV compared to the initial location in the ZnO lattice. Moreover, the final Cu-$O_{migrated}$ distance (1.80 Å) due to ZnO lattice oxygen migration was found significantly shorter than the Cu-O^* distances (2.80 Å for a single Cu or 3.48 Å for a Cu dimmer) due to O^* adsorption in the gas phase. The most energetically favorable configuration entailed Cu_1-Cu_2, Cu_1-O_1 and Zn_1-O_1 distances of approximately 2.50 Å, 1.80 Å and 4.04 Å, respectively.

Furthermore, given that the XRD patterns of the as-prepared samples showed no observation of Cu_2O peak and an E_{bar} of 0.25 eV was required, the spontaneous process of O migration from ZnO to Cu in MSI did not occur herein. Instead, energy input from the outside was necessary to initiate migration, which could be attributed to the applied currents/potentials. Once O reached the Cu phase, the formation of Cu_2O was favored with an energy drop of 0.535 eV. The regeneration of ZnO lattice oxygen could be achieved by O^* from the CO_2 dissociation, mediated by the energy of electrooxidation. All these results supported the idea of lattice oxygen provision in a Mars Van Krevelen mechanism and indicated that the origin of O in Cu_2O was from ZnO, which could only happen under polarization.

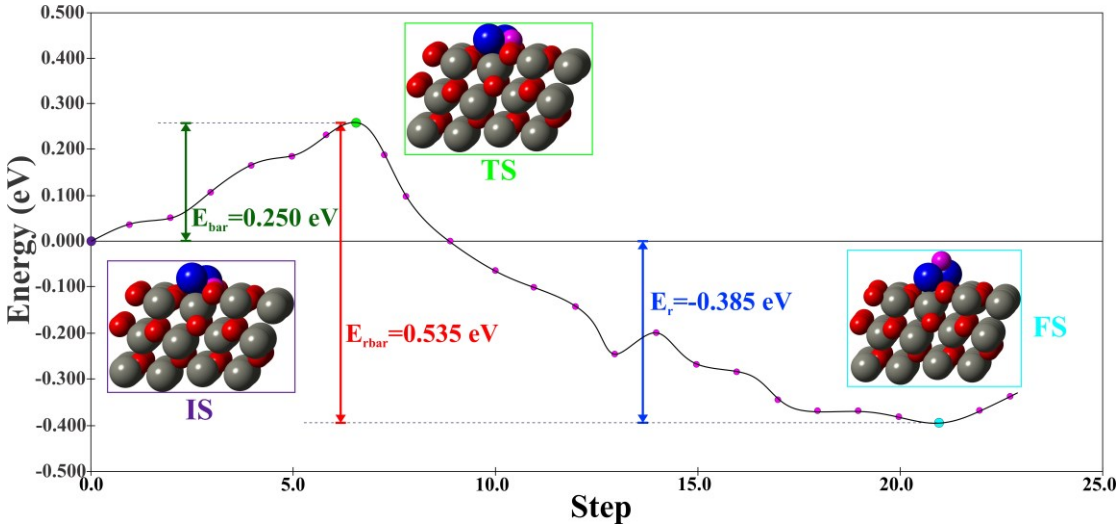

Figure 5-6. Energy vs Step curves of the O1 migration of the ZnO (101) surface after two Cu atoms adsorption. The pink atom indicates the migrating oxygen. The graphics inserts present the initial, transition and final configuration.

5.3.5 Electrochemical characterizations

CV is commonly applied to the catalyst-working electrode to investigate the redox properties of materials and provide in-situ information about the electrochemical processes and changes in the oxidation states, and thus is widely used in EPOC studies as an electrochemical characterization method[6,7,31]. **Figure 5-7a and b** show the CVs of as-prepared Cu/ZnO catalysts deposited on YSZ in Argon at 400°C. The CVs cycled from -0.8 V to 1.5 V and then back to -0.8 V at a scan rate of 20 mV s^{-1}, where the anodic cycle involved electro-oxidation and the cathodic cycle involved electro-reduction. The fifth cycle of each CV curves was chosen as the stable one. The CVs of bare ZnO support and free-standing Cu are shown in **Figure C-11**.

ZnO showed no anodic peaks but one cathodic peak (~ -0.3 V), whose shape was similar to ZnO film reported elsewhere[40]. This meant the synthesized ZnO could only be electro-reduced in cathodic cycle, indicating its fully oxidized state and confirming the existence of oxygen vacancies that allowed migrations of O^{2-}. However, the free-standing Cu showed one anodic peak AI (~ 0.6 V), representing partial oxidation of Cu to Cu_2O, and two cathodic peaks CI (~ 0.6 V) and CII (~ 0.3 V), representing stepwise reduction of CuO to Cu_2O and then to metallic Cu[6]. The

sharp increase in anodic currents after 1 V represented oxygen evolution reaction (OER) at tpb[7]. When supporting Cu NPs on ZnO, the CVs of Cu/ZnO catalysts were similar to that of free-standing Cu rather than bare ZnO. This was attributed to the Cu that functioned as an active phase in Cu/ZnO and could be easily electro-oxidized/reduced by O^{2-}. However, the apparent differences in shapes indicated distinct electrochemical properties. From **Figure 5-7a and b**, in addition to peak AI, a new anodic peak AII (~ 0.9 V) appeared in 5-40CuZnO, which was absent in 60CuZnO. The peak AII represented the oxidation of Cu_2O to CuO and was visible when Cu was not the main phase. In 5-40CuZnO, small amounts of Cu NPs on ZnO were fully oxidized, resulting in two anodic peaks. Nevertheless, Cu in 60CuZnO was partially oxidized to Cu_2O due to its huge content, and only the peak AI was shown accordingly.

Figure 5-7c summarizes the peak locations of AI, AII, CI and CII. It was found that the two anodic peaks shifted to more negative potentials initially and then returned to more positive potentials as increasing the Cu loading, while the two cathodic peaks exhibited exactly the opposite phenomenon. This further confirmed that 10CuZnO, which showed the most negative anodic peak positions and the most positive cathodic peak positions, was the easiest catalyst for electro-oxidation/reduction, indicative of its highest ability to be polarizable. On the contrary, 20-60CuZnO were more challenging to be electro-oxidized/reduced and thus less polarizable.

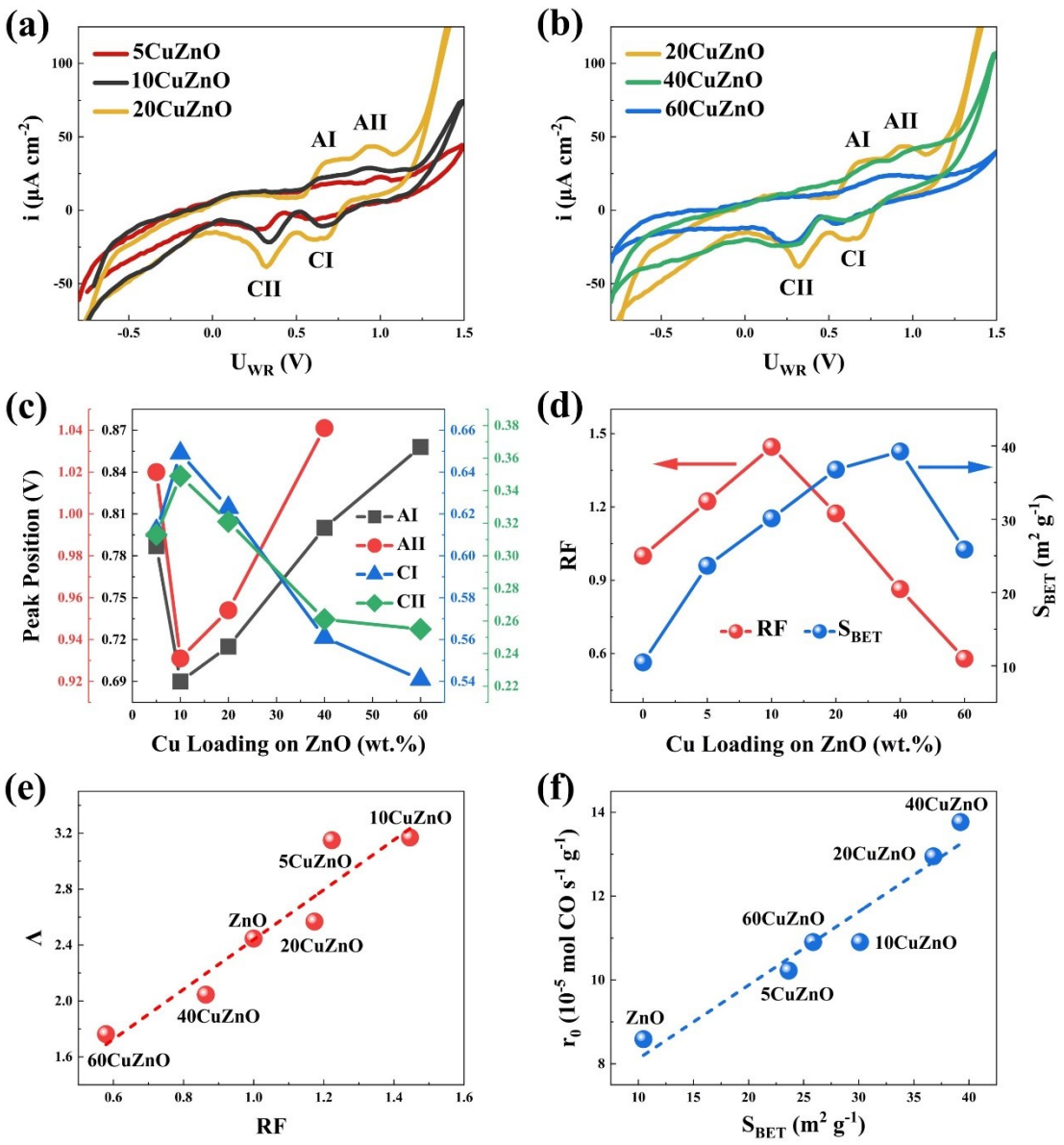

Figure 5-7. CVs at 400°C in Argon for (a) 5-20CuZnO and (b) 20-60CuZnO; (c) Peak locations of AI, AII, CI and CII; (d) Effects of Cu loadings on RF and S_{BET}; Correlation between (e) Λ and RF, and (f) r_0 and S_{BET} of Cu/ZnO catalysts.

5.3.6 Electrochemical active surface area

The ECSA is commonly used to estimate the activities of electrocatalysts and larger ECSAs represent more electrochemical active reaction sites[41]. Therefore, it is possible to perform ECSA evaluations in EPOC studies that involve the electrochemical migration of ions through the active sites and find out the origin of ECSA and a relationship between the significance of ECSA and EPOC effects.

However, the ECSA is mostly obtained by dividing the C_{dl} of the catalysts by a specific capacitance (C_s) which describes the capacitance of an ideal catalyst surface in liquid phase[9]. To apply the ECSA in EPOC with solid-gas phases and avoid using C_s, the RF is proposed to characterize the relative ECSA of the catalysts[42]. In this case, the C_{dl} of modified catalysts (Cu/ZnO) are normalized against that of unmodified catalyst (bare ZnO) to establish the RF[43,44], as C_{dl} reliably indicates ECSA due to their consistent positive relationship[45,46]. Since an effective double-layer is also formed during polarization in EPOC, the C_{dl} evaluation is considered appliable in this work.

The CVs of Cu/ZnO catalysts at various scan rates are shown in **Figure C-12a**, where no peaks were found within the range, meaning no Faradaic reactions happened. By increasing the scan rate from 20 mV s^{-1} to 200 mV s^{-1}, the current densities were increased accordingly. The slope obtained from the plot of current density vs. scan rate represented the C_{dl} value. The corresponding plots and C_{dl} values of all Cu/ZnO catalysts are summarized in **Figure C-12b.** The resulting RF values of Cu/ZnO catalysts are concluded in **Table 5-1** with RF of ZnO to be 1. The influences of Cu loadings on RF and S_{BET} of all Cu/ZnO catalysts are shown in **Figure 5-7d**. It was found that 5CuZnO and 10CuZnO had RF values of 1.22 and 1.45, respectively, both larger than ZnO. When further increasing the Cu loading, however, the RF began to decline and reached the bottom value of 0.58 for 60CuZnO. This indicated that the ECSA of Cu/ZnO was improved initially and then deteriorated drastically with an increase in the Cu content. It should also be noted that, although 10CuZnO exhibited the largest RF values, 20-40CuZnO showed the highest S_{BET} values. The inconsistency demonstrated that the specific surface area was different from electrochemical active surface area, which was more suitable for estimating electrochemical reactions.

Figure 5-7e and f show the correlation between Λ and RF, as well as r_0 and S_{BET} of Cu/ZnO catalysts, respectively. As a comparison, the relationship between r_0 and RF, as well as Λ and S_{BET} are shown in **Figure C-13**. **Figure 5-7e** elucidated a clear

positive correlation between Λ and RF, while r_0 showed no correlation with RF (**Figure C-13a**). In contrast, **Figure 5-7f** revealed a pronounced positive correlation between r_0 and S_{BET}, whereas Λ exhibited no relationship with S_{BET} (**Figure C-13b**). The consistency between Λ and RF demonstrated that larger ECSAs contributed to stronger EPOC effects under the same polarization. In EPOC, the induced change in the catalytic rate (= r - r_0) exceeded the electrocatalytic rate (= I/nF) expected by Faraday's law[35], which was equal to the transport rate of the promoting species (O^{2-} in this study). This indicated each O^{2-} supplied to the catalyst created additional active sites[47], whose magnitude was characterized by Λ.

Consequently, it could be concluded that larger ECSAs promoted the formation of additional active sites, thereby benefiting the EPOC effects. Moreover, according to the XPS results, the origin of ECSA was possibly the oxygen vacancies provided by ZnO. That was, 5-10CuZnO catalysts enriched with ZnO phase had more oxygen vacancies, enabling easier O^{2-} transport via larger ECSAs during polarization and formation of more active sites subsequently. On the contrary, the ECSAs of 20-60CuZnO catalysts were decreased due to the lack of ZnO phase and poor EPOC effects were shown accordingly. This also agreed with the results from **Figure 5-7c** and indicated that the polarizability of Cu/ZnO catalyst was related to ECSA and thus to oxygen vacancies. The correlation between r_0 and S_{BET} was also uncovered in Section 5.3.2 regarding open-circuit activity.

5.4 Conclusion

In this study, Cu/ZnO catalysts showed improved activities for RWGS reaction, attributed to both the MSI effect and the enlarged specific surface area. The most active 20-40CuZnO catalysts demonstrated S_{BET} achieving 38 m^2 g^{-1}. Upon applying constant positive currents to the catalyst-WE, both ZnO and Cu/ZnO catalysts displayed an increase in the catalytic rate, which returned to its initial value after the current interruption. The electrochemical promotion was most pronounced in the 10CuZnO catalyst, characterized by the highest ρ of 1.14 and Λ of 3.16.

Physicochemical characterizations including STEM, XRD, and XPS revealed the formation of Cu_2O (110) during polarization, which was considered responsible for the observed rate enhancement. To validate the source of oxygen in Cu_2O, DFT calculation was employed, shedding light on the potential mechanism. The results supported the idea of lattice oxygen migration from bulk ZnO to the Cu surface, influenced by polarization. CV as an electrochemical characterization method reflected distinct electrochemical properties for each Cu/ZnO catalyst, with 10CuZnO exhibiting the best polarizability. The relative ECSA, determined from CVs and characterized by RF, also attained the highest value of 1.45 in 10CuZnO. The consistency between RF and Λ indicated that Cu/ZnO catalysts enriched with ZnO phase possessed more oxygen vacancies, thereby guaranteeing larger ECSAs. This feature was conducive to achieving a stronger EPOC effect by promoting O^{2-} migration. These results suggest that the development of multi-phase catalyst-WE in future EPOC research should focus on creating MSI involving highly active metals and non-noble metal oxide supports that are chemically stable, ionically conductive, and rich in oxygen vacancies.

References

[1] E. Pahija, C. Panaritis, S. Gusarov, J. Shadbahr, F. Bensebaa, G. Patience, D.C. Boffito, Experimental and Computational Synergistic Design of Cu and Fe Catalysts for the Reverse Water-Gas Shift: A Review, ACS Catal. (2022) 6887–6905. https://doi.org/10.1021/acscatal.2c01099.

[2] G.C. Wang, J. Nakamura, Structure sensitivity for forward and reverse water-gas shift reactions on copper surfaces: A DFT study, J. Phys. Chem. Lett. 1 (2010) 3053–3057. https://doi.org/10.1021/jz101150w.

[3] H. Chen, T. Fan, Y. Ji, CO2 Reduction Mechanism on the Cu2O(110) Surface: A First-Principles Study, ChemPhysChem. (2023). https://doi.org/10.1002/cphc.202300047.

[4] Q.L. Tang, Q.H. Luo, Adsorption of CO2 at ZnO: A surface structure effect from DFT+ U Calculations, J. Phys. Chem. C. 117 (2013) 22954–22966. https://doi.org/10.1021/jp407970a.

[5] Z. Geng, X. Kong, W. Chen, H. Su, Y. Liu, F. Cai, G. Wang, J. Zeng, Oxygen Vacancies in ZnO Nanosheets Enhance CO2 Electrochemical Reduction to CO, Angew. Chemie - Int. Ed. 57 (2018) 6054–6059. https://doi.org/10.1002/anie.201711255.

[6] J. Wang, M. Couillard, E.A. Baranova, Electrochemical promotion of copper nanoparticles for the reverse water gas shift reaction, Catal. Sci. Technol. 12 (2022) 1562–1573. https://doi.org/10.1039/d1cy02315b.
[7] C. Panaritis, J. Zgheib, S.A.H. Ebrahim, M. Couillard, E.A. Baranova, Electrochemical in-situ activation of Fe-oxide nanowires for the reverse water gas shift reaction, Appl. Catal. B Environ. 269 (2020) 118826. https://doi.org/10.1016/j.apcatb.2020.118826.
[8] D. Zagoraios, S. Tsatsos, S. Kennou, C.G. Vayenas, G. Kyriakou, A. Katsaounis, Tuning the RWGS Reaction via EPOC and in Situ Electro-oxidation of Cobalt Nanoparticles, ACS Catal. (2020) 14916–14927. https://doi.org/10.1021/acscatal.0c04133.
[9] E. Cossar, M.S.E. Houache, Z. Zhang, E.A. Baranova, Comparison of electrochemical active surface area methods for various nickel nanostructures, J. Electroanal. Chem. 870 (2020) 114246. https://doi.org/10.1016/j.jelechem.2020.114246.
[10] H. Khan, A.S. Yerramilli, A. D'Oliveira, T.L. Alford, D.C. Boffito, G.S. Patience, Experimental methods in chemical engineering: X-ray diffraction spectroscopy—XRD, Can. J. Chem. Eng. 98 (2020) 1255–1266. https://doi.org/10.1002/cjce.23747.
[11] G. Kresse, D. Joubert, From ultrasoft pseudopotentials to the projector augmented-wave method, Phys. Rev. B - Condens. Matter Mater. Phys. 59 (1999) 1758–1775. https://doi.org/10.1103/PhysRevB.59.1758.
[12] J.P. Perdew, K. Burke, M. Ernzerhof, Generalized gradient approximation made simple, Phys. Rev. Lett. 77 (1996) 3865–3868. https://doi.org/10.1103/PhysRevLett.77.3865.
[13] P.E. Blöchl, Projector augmented-wave method, Phys. Rev. B. 50 (1994) 17953–17979. https://doi.org/10.1103/PhysRevB.50.17953.
[14] S. Grimme, J. Antony, S. Ehrlich, H. Krieg, A consistent and accurate ab initio parametrization of density functional dispersion correction (DFT-D) for the 94 elements H-Pu, J. Chem. Phys. 132 (2010). https://doi.org/10.1063/1.3382344.
[15] B. Himmetoglu, A. Floris, S. De Gironcoli, M. Cococcioni, Hubbard-corrected DFT energy functionals: The LDA+U description of correlated systems, Int. J. Quantum Chem. 114 (2014) 14–49. https://doi.org/10.1002/qua.24521.
[16] K. Harun, N.A. Salleh, B. Deghfel, M.K. Yaakob, A.A. Mohamad, DFT + U calculations for electronic, structural, and optical properties of ZnO wurtzite structure: A review, Results Phys. 16 (2020) 102829. https://doi.org/10.1016/j.rinp.2019.102829.
[17] E. Benrezgua, A. Zoukel, B. Deghfel, A. Boukhari, R. Amari, S. Kheawhom, A.A. Mohamad, A review on DFT + U scheme for structural, electronic, optical and magnetic properties of copper doped ZnO wurtzite structure, Mater. Today Commun. 31 (2022) 103306. https://doi.org/10.1016/j.mtcomm.2022.103306.
[18] H.J. Monkhorst, J.D. Pack, Special points for Brillouin-zone integrations, Phys. Rev. B. 16 (1977) 1748–1749. https://doi.org/10.1103/PhysRevB.16.1748.

[19] K. Harun, N.A. Salleh, B. Deghfel, M.K. Yaakob, A.A. Mohamad, DFT + U calculations for electronic, structural, and optical properties of ZnO wurtzite structure: A review, Results Phys. 16 (2020) 102829. https://doi.org/10.1016/j.rinp.2019.102829.
[20] H. Karzel, W. Potzel, M. Köfferlein, W. Schiessl, M. Steiner, U. Hiller, G. Kalvius, D. Mitchell, T. Das, Lattice dynamics and hyperfine interactions in ZnO and ZnSe at high external pressures, Phys. Rev. B. 53 (1996) 11425–11438. https://doi.org/10.1103/PhysRevB.53.11425.
[21] E. Irandegani, R. Maezono, M. Abbasnejad, Electronic and magnetic properties of pure and Cu doped non-polar ZnO (10 1 ¯ 0) surfaces, J. Appl. Phys. 132 (2022) 0–8. https://doi.org/10.1063/5.0106799.
[22] R. Yang, Y. Du, Adsorption and dissociation of a single water molecule on graphene-like ZnO monolayer with oxygen vacancies: a first-principles study, Phys. Scr. 98 (2023). https://doi.org/10.1088/1402-4896/acba59.
[23] M. de M. Machado, B.M. Savi, M.B. Perucchi, A. Benedetti, L.F.S. Oliveira, A.M. Bernardin, Effect of Temperature, Precursor Type and Dripping Time on the Crystallite Size of Nano ZnO Obtained by One-Pot Synthesis: 2 k Full Factorial Design Analysis , J. Nanosci. Nanotechnol. 18 (2017) 4409–4412. https://doi.org/10.1166/jnn.2018.15043.
[24] G. Zhang, Z.J. Zhao, D. Cheng, H. Li, J. Yu, Q. Wang, H. Gao, J. Guo, H. Wang, G.A. Ozin, T. Wang, J. Gong, Efficient CO2 electroreduction on facet-selective copper films with high conversion rate, Nat. Commun. 12 (2021) 1–11. https://doi.org/10.1038/s41467-021-26053-w.
[25] B. Ma, C. Kong, J. Lv, X. Zhang, S. Yang, T. Yang, Z. Yang, Cu–Cu2O Heterogeneous Architecture for the Enhanced CO Catalytic Oxidation, Adv. Mater. Interfaces. 7 (2020) 1–8. https://doi.org/10.1002/admi.201901643.
[26] J. Wen, C. Huang, Y. Sun, L. Liang, Y. Zhang, Y. Zhang, M. Fu, J. Wu, L. Chen, D. Ye, The study of reverse water gas shift reaction activity over different interfaces: The design of cu-plate zno model catalysts, Catalysts. 10 (2020). https://doi.org/10.3390/catal10050533.
[27] T. Ahmad, Ascorbic acid assisted synthesis, characterization and catalytic application of copper nanoparticles, Mater. Sci. Eng. Int. J. 2 (2018). https://doi.org/10.15406/mseij.2018.02.00040.
[28] K.K. Markose, M. Shaji, S. Bhatia, P.R. Nair, K.J. Saji, A. Antony, M.K. Jayaraj, Novel Boron-Doped p-Type Cu2O Thin Films as a Hole-Selective Contact in c-Si Solar Cells, ACS Appl. Mater. Interfaces. 12 (2020) 12972–12981. https://doi.org/10.1021/acsami.9b22581.
[29] Y.X. Li, J.X. Shen, S.S. Peng, J.K. Zhang, J. Wu, X.Q. Liu, L.B. Sun, Enhancing oxidation resistance of Cu(I) by tailoring microenvironment in zeolites for efficient adsorptive desulfurization, Nat. Commun. 11 (2020) 1–9. https://doi.org/10.1038/s41467-020-17042-6.
[30] M.P.L. Kang, M.J. Kolb, F. Calle-Vallejo, B.S. Yeo, The Role of Undercoordinated Sites on Zinc Electrodes for CO2 Reduction to CO, Adv. Funct. Mater. 32 (2022) 1–9. https://doi.org/10.1002/adfm.202111597.

[31] J. Wang, M. Couillard, E.A. Baranova, Insight into Electrochemical Promotion of Cu/Co3O4 Catalysts for the Reverse Water Gas Shift Reaction, ChemCatChem. (2023). https://doi.org/10.1002/cctc.202201514.
[32] M.D. Higham, M.G. Quesne, C.R.A. Catlow, Mechanism of CO2conversion to methanol over Cu(110) and Cu(100) surfaces, Dalt. Trans. 49 (2020) 8478–8497. https://doi.org/10.1039/d0dt00754d.
[33] L. Wang, H. Wang, H. Huang, T. Yun, C. Song, C. Shi, Transition Metal Carbides: Emerging CO2 Hydrogenation Catalysts, from Recent Advance to Future Exploration, Adv. Funct. Mater. 2309850 (2023). https://doi.org/10.1002/adfm.202309850.
[34] M. Konsolakis, M. Lykaki, S. Stefa, S.A.C. Carabineiro, G. Varvoutis, E. Papista, G.E. Marnellos, Co2 hydrogenation over nanoceria-supported transition metal catalysts: Role of ceria morphology (nanorods versus nanocubes) and active phase nature (co versus cu), Nanomaterials. 9 (2019) 1739. https://doi.org/10.3390/nano9121739.
[35] P. Vernoux, C.G. Vayenas, Recent Advances in Electrochemical Promotion of Catalysis (Modern Aspects of Electrochemistry, 61), Springer, 2023. https://doi.org/10.1007/978-3-031-13893-5.
[36] A. Sedky, A.M. Ali, H.H. Somaily, H. Algarni, Electrical, photoluminescence and optical investigation of ZnO nanoparticles sintered at different temperatures, Opt. Quantum Electron. 53 (2021) 1–21. https://doi.org/10.1007/s11082-021-02849-4.
[37] X. Ma, Y. Wu, Y. Lv, Y. Zhu, Correlation effects on lattice relaxation and electronic structure of zno within the GGA+ U formalism, J. Phys. Chem. C. 117 (2013) 26029–26039. https://doi.org/10.1021/jp407281x.
[38] H. Ahmoum, G. Li, M. Boughrara, R. Gebauer, M.S. Su'ait, K. Tanji, M. Kerouad, Q. Wang, Oxygen vacancy suppress room temperature ferromagnetism of p-type Cu doped ZnO: Synthesis and density functional theory, Micro and Nanostructures. 167 (2022) 207291. https://doi.org/10.1016/j.micrna.2022.207291.
[39] Z. Zhang, J. Zhang, A.P. Jia, J.Q. Lu, W. Huang, Morphology-Dependent CO Reduction Kinetics and Surface Copper Species Evolution of Cu2O Nanocrystals, J. Phys. Chem. C. 124 (2020) 21568–21576. https://doi.org/10.1021/acs.jpcc.0c06425.
[40] A. Maikap, K. Mukherjee, B. Mondal, N. Mandal, Zinc oxide thin film based nonenzymatic electrochemical sensor for the detection of trace level catechol, RSC Adv. 6 (2016) 64611–64616. https://doi.org/10.1039/c6ra09598d.
[41] J. Xu, Z. Zhao, W. Wei, G. Chang, Z. Xie, W. Guo, D. Liu, D. Qu, H. Tang, J. Li, Tuning the Intrinsic Activity and Electrochemical Surface Area of MoS2 via Tiny Zn Doping: Toward an Efficient Hydrogen Evolution Reaction (HER) Catalyst, Chem. - A Eur. J. 27 (2021) 15992–15999. https://doi.org/10.1002/chem.202102803.
[42] H.F. Wang, C. Tang, B. Wang, B.Q. Li, X. Cui, Q. Zhang, Defect-rich carbon fiber electrocatalysts with porous graphene skin for flexible solid-state zinc–air

batteries, Energy Storage Mater. 15 (2018) 124–130. https://doi.org/10.1016/j.ensm.2018.03.022.
[43] R. Martínez-Hincapié, J. Wegner, M.U. Anwar, A. Raza-Khan, S. Franzka, S. Kleszczynski, V. Čolić, The Determination of the Electrochemically Active Surface Area and its Effects on the Electrocatalytic Properties of Structured Nickel Electrodes Produced by Additive Manufacturing, Electrochim. Acta. 476 (2023) 143663. https://doi.org/10.1016/j.electacta.2023.143663.
[44] E.L. Clark, S. Ringe, M. Tang, A. Walton, C. Hahn, T.F. Jaramillo, K. Chan, A.T. Bell, Influence of Atomic Surface Structure on the Activity of Ag for the Electrochemical Reduction of CO 2 to CO, ACS Catal. 9 (2019) 4006–4014. https://doi.org/10.1021/acscatal.9b00260.
[45] W.J. Teh, M.J. Kolb, F. Calle-Vallejo, B.S. Yeo, Enhanced Charge Transfer Kinetics for the Electroreduction of Carbon Dioxide on Silver Electrodes Functionalized with Cationic Surfactants, Adv. Funct. Mater. 33 (2023) 1–8. https://doi.org/10.1002/adfm.202210617.
[46] K. Tang, C. Yuan, Y. Xiong, H. Hu, M. Wu, Inverse-opal-structured hybrids of N, S-codoped-carbon-confined Co9S8 nanoparticles as bifunctional oxygen electrocatalyst for on-chip all-solid-state rechargeable Zn-air batteries, Appl. Catal. B Environ. 260 (2020) 118209. https://doi.org/10.1016/j.apcatb.2019.118209.
[47] C.G. Vayenas, S. Bebelis, C. Pliangos, S. Brosda, D. Tsiplakides, Electrochemical Activation of Catalysis, Springer, 2001. https://doi.org/10.1007/b115566.

Appendix C: Supplementary Information for Chapter 5

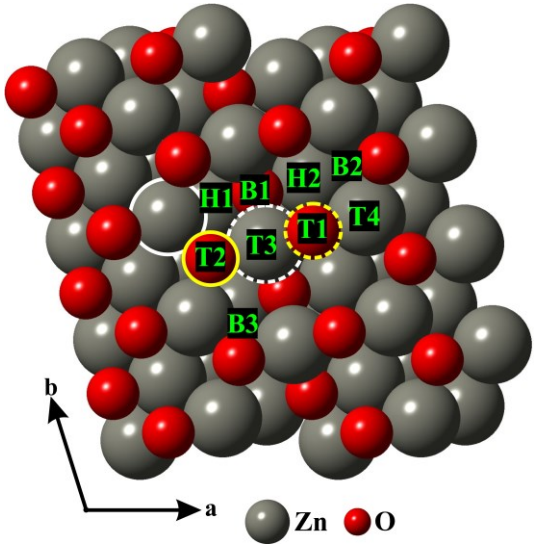

Figure C-1. Schematic view of high symmetrical possible adsorption sites on the ZnO (101) surface. The B1, B2, and B3 indicate the Zn-Zn bridge sites with different chemical environments. The H1 and H2 represent the hollow sites. The T1 and T2 labels show the Top sites on the O atoms, while the T3 and T4 are the Top sites on Zn atoms. The Zn and O highlighted atoms are those chosen to generate the different types of vacancies. The white and yellow full (V_{Zn1} or V_{O1}) and dotted (V_{Zn2} or V_{O2}) lines correspond to Zn and O vacancies.

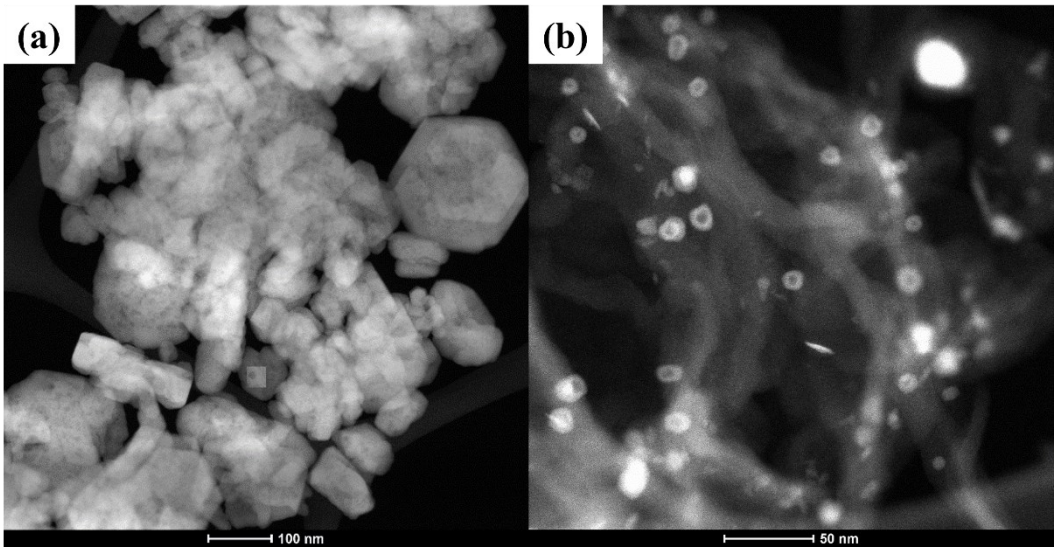

Figure C-2. HAADF-STEM image of (a) bare ZnO and (b) unsupported Cu NPs.

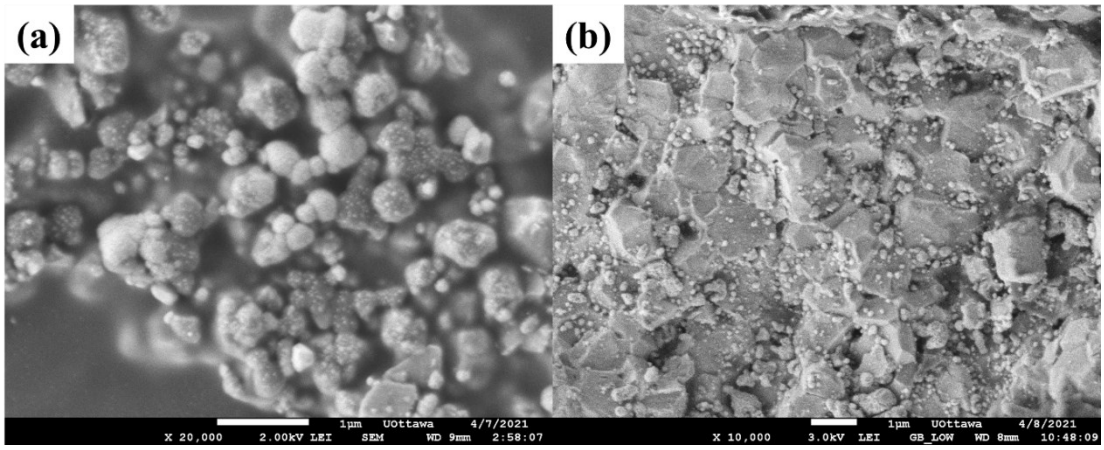

Figure C-3. SEM images of (a) as-prepared and (b) spent unsupported Cu NPs deposited on YSZ on scale of 1 µm.

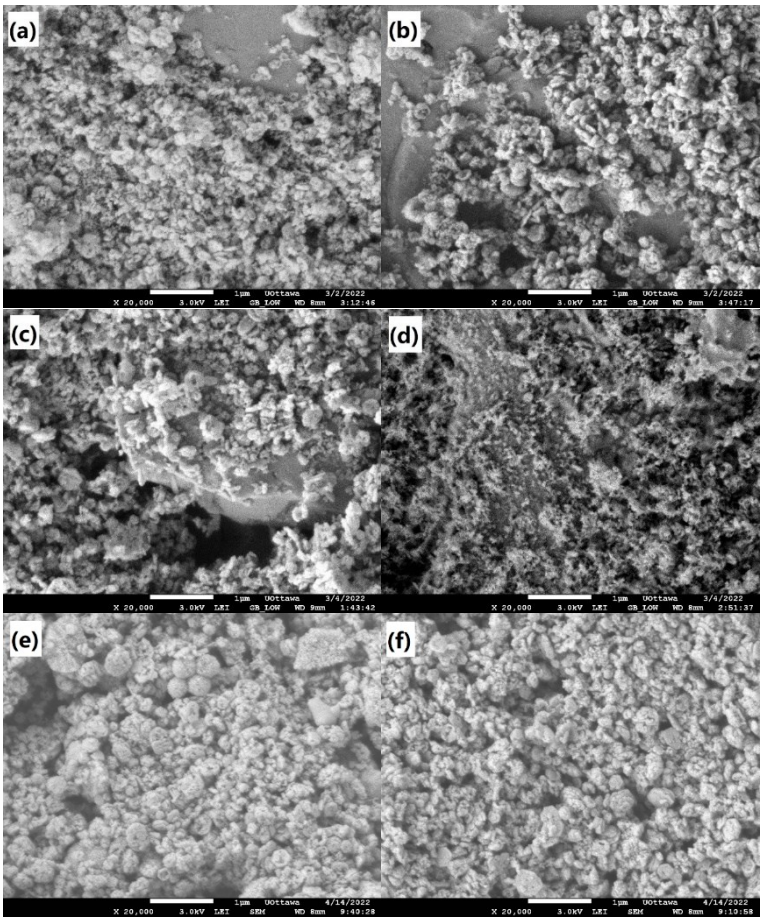

Figure C-4. SEM images of spent (a) ZnO, and (b) 5wt.%, (c) 10wt.%, (d) 20wt.%, (e) 40wt.%, and (f) 60wt.%Cu supported on ZnO on the scale of 1 µm.

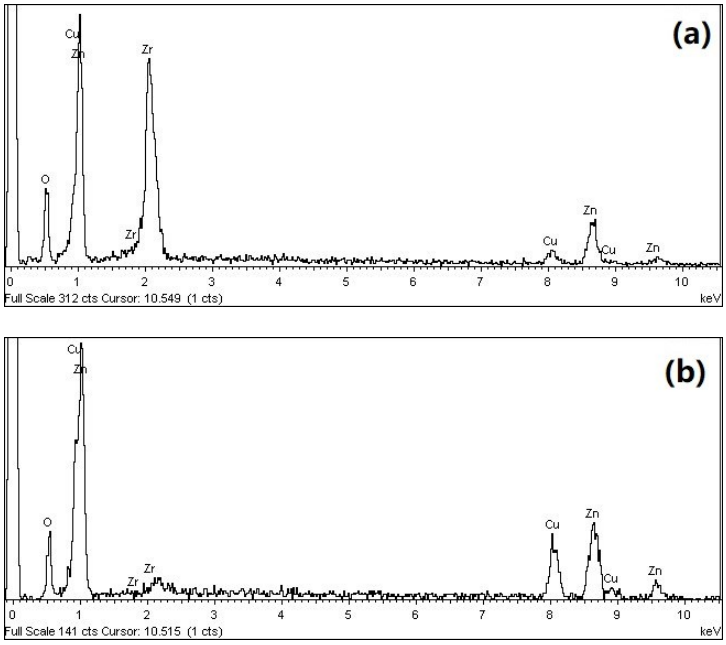

Figure C-5. EDS spectrums of (a) 10CuZnO and (b) 60CuZnO.

Table C-1. Summary of major peak positions and corresponding interplanar distances (d), full width at half maximum (FWHM) and crystallite sizes (L). n=1, λ=0.15418 nm, K=0.9.

ZnO									
	as-prepared					spent			
	2θ	d (nm)	FWHM (rad)	size (nm)		2θ	d (nm)	FWHM (rad)	size (nm)
ZnO (101)	36.16	0.248	0.00577703	25.26718	ZnO (101)	36.18	0.248	0.00551524	26.46807
Cu (111)	N/A	N/A	N/A	N/A	Cu (111)	N/A	N/A	N/A	N/A
Cu_2O (110)	N/A	N/A	N/A	N/A	Cu_2O (110)	N/A	N/A	N/A	N/A
10CuZnO									
	as-prepared					spent			
	2θ	d (nm)	FWHM (rad)	size (nm)		2θ	d (nm)	FWHM (rad)	size (nm)
ZnO (101)	36.18	0.248	0.00678933	21.50106	ZnO (101)	36.18	0.248	0.00532325	27.42266
Cu (111)	43.28	0.209	0.00432841	34.48922	Cu (111)	43.22	0.209	0.00376991	39.59052
Cu_2O (110)	N/A	N/A	N/A	N/A	Cu_2O (110)	30.02	0.297	0.00371755	38.64475
60CuZnO									
	as-prepared					spent			
	2θ	d (nm)	FWHM (rad)	size (nm)		2θ	d (nm)	FWHM (rad)	size (nm)
ZnO (101)	36.18	0.248	0.0056025	26.0558	ZnO (101)	36.16	0.248	0.00574213	25.42077
Cu (111)	43.22	0.209	0.00446804	33.4045	Cu (111)	43.22	0.209	0.00401425	37.18066
Cu_2O (110)	N/A	N/A	N/A	N/A	Cu_2O (110)	29.98	0.297	0.00438077	32.79108

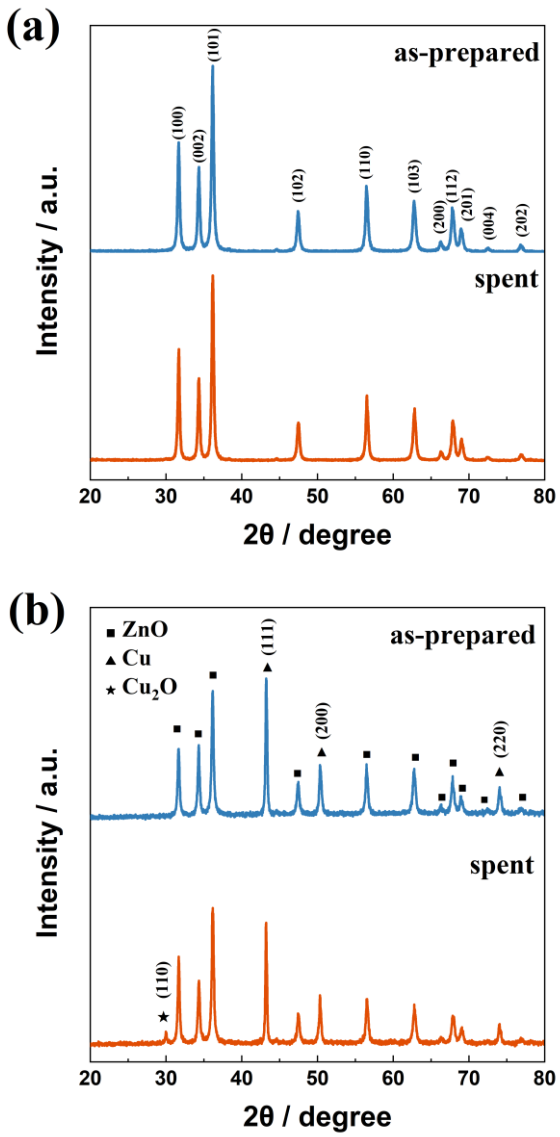

Figure C-6. XRD patterns of as-prepared and spent (a) bare ZnO and (b) 60CuZnO.

Table C-2. XPS data of Cu 2p for as-prepared and spent 10CuZnO.

Element	Composition	Position (eV)		FWHM		%Area	
		as-prepared	spent	as-prepared	spent	as-prepared	spent
Cu $2p_{1/2}$	N/A	951.3	951.3	N/A	N/A	N/A	N/A
Cu $2p_{3/2}$	Cu^0	931.5	931.5	1.60	1.68	67.62	53.26
	Cu^{1+}	931.3	931.2	0.78	1.09	12.93	27.54
	Cu^{2+}	933.5	933.4	2.01	2.49	19.45	19.20

Table C-3. XPS data of Zn 2p and O1s for as-prepared ZnO, 10CuZnO and 60CuZnO.

Catalyst	Element	Composition	Position (eV)	FWHM	%Area
ZnO	O 1s	O_L	530.25	1.103	44.19
		O_V	531.02	1.969	48.58
		-OH	532.26	1.41	7.23
	Zn 2p	$Zn\ 2p_{1/2}$	1044.05	N/A	N/A
		$Zn\ 2p_{3/2}$	1021.03	N/A	N/A
10CuZnO	O 1s	O_L	530.29	1.007	50.29
		O_V	531.08	1.942	44.43
		-OH	532.19	1.242	5.28
	Zn 2p	$Zn\ 2p_{1/2}$	1044.45	N/A	N/A
		$Zn\ 2p_{3/2}$	1021.43	N/A	N/A
60CuZnO	O 1s	O_L	530.8	1.063	64.23
		O_V	531.64	1.394	21.47
		-OH	532.74	1.318	14.3
	Zn 2p	$Zn\ 2p_{1/2}$	1045.26	N/A	N/A
		$Zn\ 2p_{3/2}$	1022.13	N/A	N/A

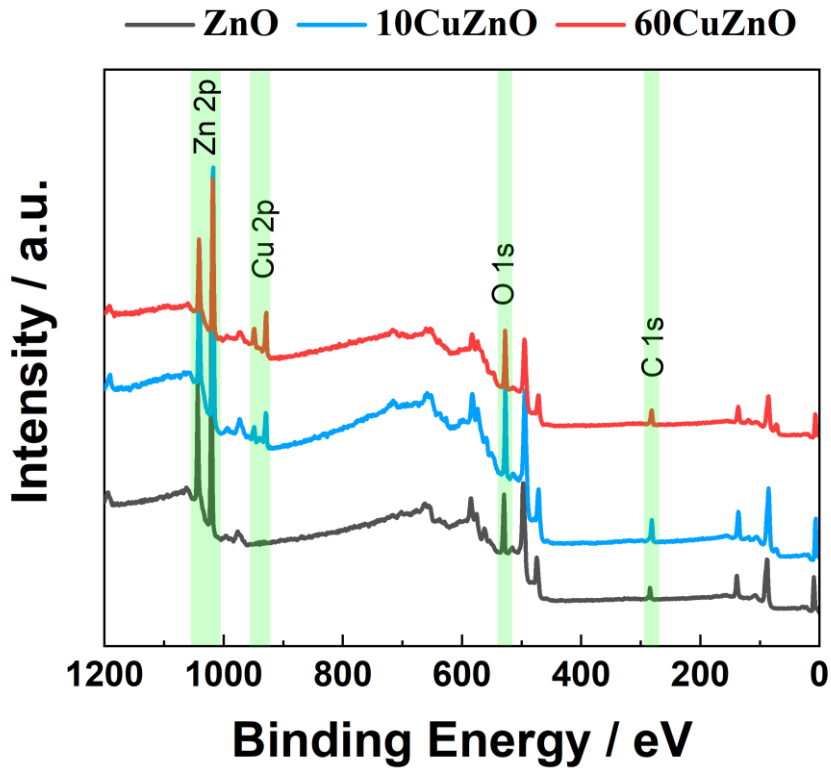

Figure C-7. Wide scan XPS spectra of as-prepared ZnO, 10CuZnO and 60CuZnO.

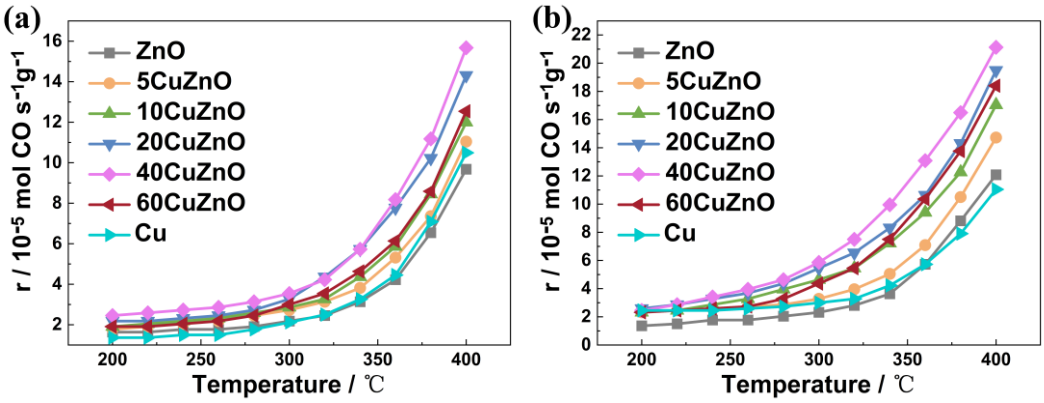

Figure C-8. Light-off curves for all Cu/ZnO catalysts under (a) oxidizing and (b) reducing conditions.

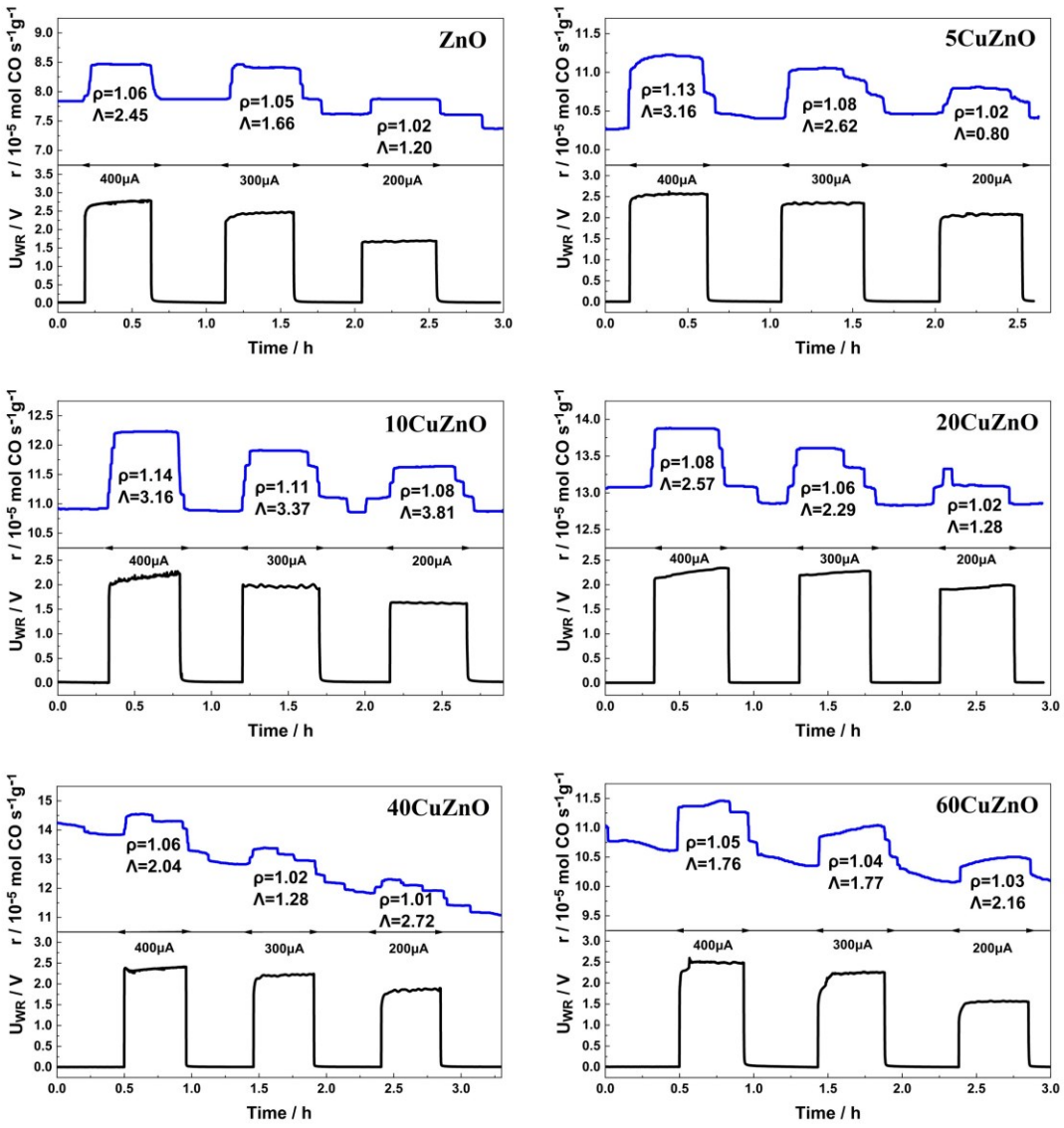

Figure C-9. Overall transient responses of CO rates to applied constant currents for all Cu/ZnO catalysts under stoichiometric conditions at 400°C.

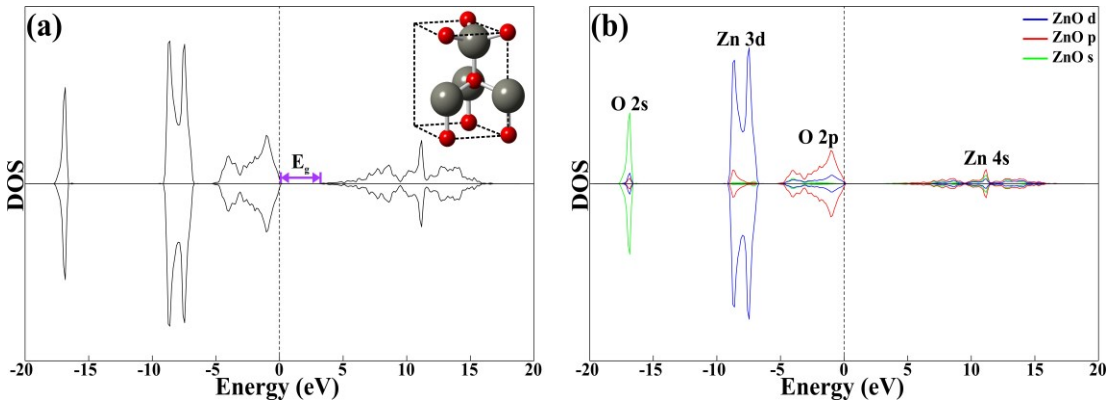

Figure C-10. Total (a) and projected (b) DOS curves of wurtzite ZnO bulk. The Fermi level is the dotted line at zero. The insert represents the wurtzite ZnO unit cell, where the grey and red spheres are the Zn and O atoms, respectively.

Table C-4. The adsorption sites and energies of adsorbed Cu- and O-atom on ZnO (101) surface.

Adsorption site/ Atom	E_{ads} (eV)	
	Cu	O*
B1	-5.90	-
B2	-3.52	-
B3	-3.55	-
H1	-4.10	-0.63
H2	-0.72	-0.50
T1	-4.01	-0.49
T2	-3.53	-0.36
T3	-4.87	-0.57
T4	-3.90	-0.58
Top Cu	-	-0.54

Table C-5. Bond distances for the most stable configurations.

	Distances (Å)				
System	ZnO(101)	Cu/ZnO(101)	Cu/ZnO(101) + O^*	2Cu/ZnO(101)	2Cu/ZnO(101) + O^*
Bond type					
O_1 - Zn_1	1.82	1.93	1.92	2.06	1.99
O_2 - Zn_1	1.84	1.87	1.87	1.96	1.98
O_2 - Zn_2	1.85	1.87	1.87	1.98	1.99
Cu_1 - O_1	-	1.82	1.83	1.86	1.92
Cu_1 - O_4	-	1.82	1.83	1.79	1.83
O^* - Cu_1	-	-	2.80	-	3.49
O^* - Cu_2	-	-	-	-	3.48
O^* - Zn_1	-	-	4.53	-	5.28
O^* - Zn_2	-	-	3.70	-	4.06
Cu_2 - Cu_1	-	-	-	2.59	2.45
Cu_2 - O_1	-	-	-	1.93	1.94
Cu_2 - O_2	-	-	-	1.93	1.95
Cu_2 - Zn_1	-	-	-	2.48	2.53

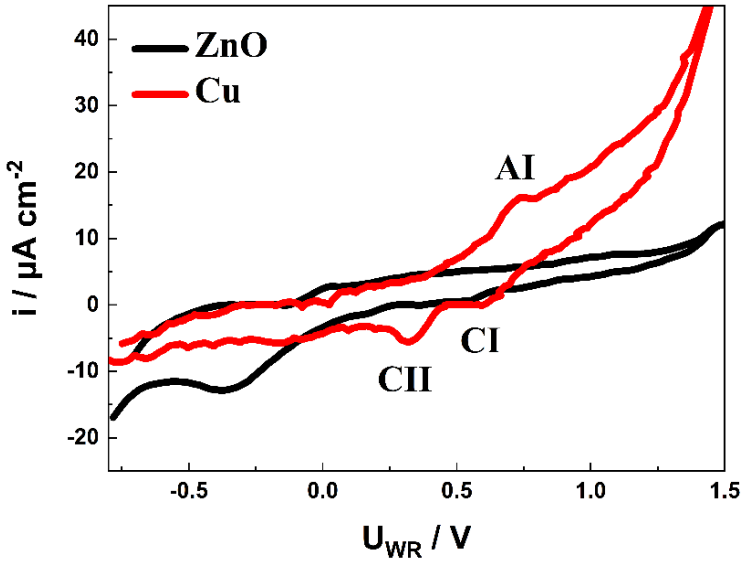

Figure C-11. CVs at 400°C in Argon from -0.8 V to 1.5 V at a scan rate of 20 mV s^{-1} for unsupported Cu NPs and bare ZnO.

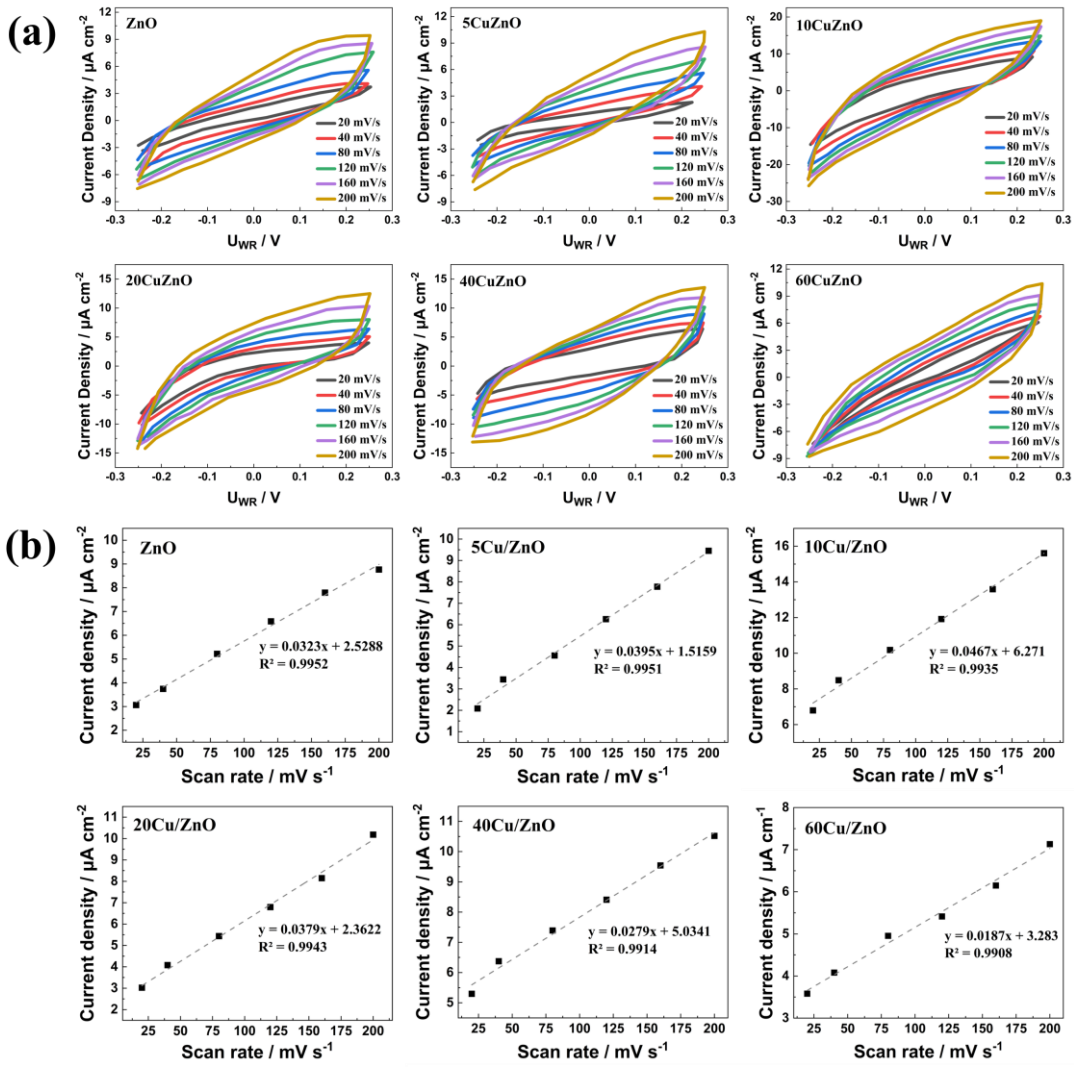

Figure C-12. CVs at various scan rates (a) and corresponding plots of current densities vs. scan rates (b) of all Cu/ZnO catalysts for C_{dl} evaluation.

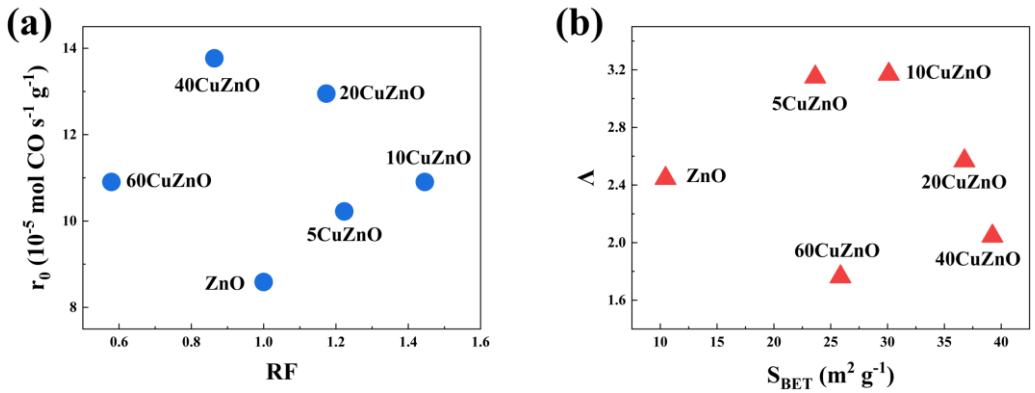

Figure C-13. Relationships between (a) r_0 and RF, and (b) Λ and S_{BET} of Cu/ZnO catalysts.

Chapter 6: Electrochemical Promotion of Catalysis by Lithium-Ion

Adapted from: ***J. Wang****, S. Yan, K. E. Salem, C. Panaritis, M. S. E. Houache, Y. Abu-lebdeh, D. Higgins, E. A. Baranova, 2024, ACS Catalysis (under review).*

Abstract: This research explores the application of lithium lanthanum titanate (LLTO) as the solid electrolyte in EPOC for both CO oxidation and reverse water gas shift (RWGS) reaction due to its lithium ion (Li^+) conductivity. Iron-oxide (FeO_x) nanowires and Platinum (Pt) film are used as catalysts and deposited on LLTO. The applied polarization introduced EPOC effects, where Li^+ is found to migrate and interact with metal catalysts under polarization according to physicochemical characterizations like STEM, XRD and XPS. The difference in EPOC behaviors indicates distinct interactions, where FeO_x reacts with Li^+ as FeO_x is prone to redox processes, while Pt does not exhibit similar interactions owing to its chemical stability. Cyclic voltammetry (CV) provides in situ insights into the electrochemical reactions and confirms that the interaction between metal/metal oxide and migrated Li^+ plays a critical role in exhibiting EPOC effects.

6.1 Introduction

EPOC has been widely utilized in the field of energy conversion processes with various catalytic systems[1]. In these studies, metal catalysts are typically deposited on YSZ and β''-Al_2O_3. However, a significant challenge arises from the limited electrical and ionic conductivities of these materials at reduced temperatures. This restricts the broader application of EPOC, especially impacting its efficiency in reactions requiring lower operational temperatures. Consequently, exploring solid electrolytes that are capable of maintaining high electrical and ionic conductivity at lower temperatures is necessary. Lithium lanthanum titanate (LLTO), chemically denoted as $LiLaTiO_3$ and part of the perovskite family, is known for its excellent electrochemical properties and advantageous application as solid electrolyte in

lithium-ion (Li^+) batteries[2]. Its unique crystal structure allows for significant ionic mobility, making it particularly effective in conducting Li^+, with the ionic conductivity ranging from 10^{-3} to 10^{-7} S cm^{-1} at room temperature[3]. Additionally, LLTO exhibits significant electrical conductivity, crucial for minimizing interface resistance and enhancing charge transfer efficiency between the electrolyte and electrodes[4]. This, combined with its chemical stability at elevated temperatures[5], positions LLTO as a promising solid electrolyte candidate in EPOC studies considering its ability to facilitate efficient ion transport and maintain structural integrity under operational conditions.

In this study, LLTO is utilized as the solid electrolyte in EPOC, representing a significant innovation in this area by employing Li^+ as the promoting ionic species for the first time. To broaden the scope of the investigation, both CO oxidation and RWGS reaction are selected as the target conversion reactions. CO oxidation is an ideal model for surface science studies due to its simplicity[6], while RWGS is regarded as a practical and promising CO_2 hydrogenation process as it is often combined with the Fischer-Tropsch (FT) process to produce a wide range of liquid hydrocarbons and chemicals[7]. Iron oxide (FeO_x) is chosen as one of the catalysts because it is a non-noble metal oxide susceptible to changes in oxidation state and demonstrates activity in both reactions. In contrast, the noble metal Pt is used for comparison with FeO_x, as it is chemically stable and resistant to oxidation[8].

The EPOC experiments are conducted on Fe/LLTO and Pt/LLTO systems for both reactions under applications of various constant voltages/currents and reaction conditions. Distinct observed EPOC behaviors are elucidated through proposed mechanisms involving the electrochemical interactions between the metal/metal oxide catalysts and Li^+ from LLTO. Cyclic voltammetry is employed as electrochemical characterizations to provide in situ insights into these interactions. Additional physicochemical characterizations, including STEM, SEM, XRD, and XPS are utilized to confirm the catalyst morphology, changes in metal oxidation states, and Li^+ migration under polarization. This research highlights the potential of LLTO in EPOC

and lays a foundational work for future studies in this field.

6.2 Experimental

6.2.1 Preparation of catalyst and electrochemical cell

The FeO_x nanowires were prepared by the polyol synthesis method, following the procedures as mentioned in Chapter 2. Typically, iron precursor (iron (III) nitrate ($Fe(NO_3)_3$) was dissolved in ethylene glycol (EG, Fisher Chemical). Then 0.12 M tetramethylammonium hydroxide (TMAOH, pentahydrate, 97+%, Sigma-Aldrich) solution was added to increase the pH to 12. The mixture, exhibiting a turbid yellow colour, underwent stirring at room temperature (RT) for a duration of 30 minutes. Following this, the mixture was heated up to 160 °C from RT under reflux conditions, after which it was allowed to cool down to RT. The resulting FeO_x nanowires were stored in colloidal solution with a concentration of 2 mg mL^{-1}.

In this study, the LLTO was utilized as the solid electrolyte, which was prepared as described elsewhere[10] and shaped into a disc with dimensions of 13 mm in diameter and 1 mm in thickness. Two electrodes, made of gold, were applied on one side of the disc using gold paste (Ted Pella, 16022) following the same procedures as described in Chapter 2.

In the process of fabricating the catalyst-working electrode, the FeO_x nanowires were applied using a wet deposition method as mentioned in Chapter 2, with the final loading to be 0.3 mg cm^{-2}. The Pt film was prepared using the physical vapor deposition (PVD) method via electron beam evaporation, where metallic Pt was deposited onto the LLTO surface, opposite the CE. The thickness of the Pt film was adjusted by varying the evaporation time, with Pt-100 denoting a thickness of 100 nm and Pt-50 a thickness of 50 nm. Subsequently, the catalyst-WE was covered with a gold mesh to ensure electrical conductivity and a porous fritted disc made of borosilicate was used to secure the electrochemical cell in a sandwich-like configuration.

6.2.2 Experimental setup

The assembled electrochemical cell and reactor setup are as shown in Chapter 2. Gas inputs for RWGS, including hydrogen (H_2, Messer, 99%), carbon dioxide (CO_2, Messer, 99%), and argon (Ar, Messer, 100%), were supplied to the reactor through separate mass flow controllers (MFC, MKS Instruments). The CO_2:H_2 inlet ratios were adjusted to 1:1, 3:1, and 1:6 by modulating the flowrates, while maintaining a total flow rate of 100 mL min^{-1}. As for CO oxidation, carbon monoxide (CO, Messer, 10% in Ar), oxygen (O_2, Messer, 99%), and argon (Ar, Messer, 100%) were fed to the reactor. The effluent gas composition was analyzed using CO analyzer and CO_2 analyzer, respectively. The deposited catalysts underwent a pre-treatment in the reactor prior to experimental runs, as detailed in Chapter 2.

6.2.3 Electrochemical measurements

Electrochemical measurements were conducted using a potentiostat-galvanostat (Arbin Instruments, MSTAT). The EPOC tests were carried out by applying constant currents or voltages across the catalyst-WE and CE and were characterized by the rate enhancement ratio (ρ) and apparent Faradaic efficiency (Λ) from Eq. (6-1) and (6-2), respectively:

$$\rho = r/r_0 \tag{6-1}$$

$$|\Lambda| = (r - r_0)/(I/nF) \tag{6-2}$$

where r refers to the rate observed after applying polarization, r_0 represents the open-circuit rate before polarization, I is the applied current or current response to the applied voltage, F is the Faradaic constant, and n is the number of electrons transferred, which is 2 for both RWGS reaction and CO oxidation. The unit of the reaction rate is expressed as moles of product gas per second per gram of catalyst, denoted as (mol s^{-1} g^{-1}).

Cyclic voltammetry (CV) was performed under reaction conditions using the potentiostat-galvanostat (Arbin Instruments, MSTAT) with a scan rate of 10 mV s^{-1}.

6.2.4 Physicochemical characterizations

Physicochemical characterizations of the catalysts were conducted using both as-prepared samples collected subsequent to pre-treatment and spent samples obtained after all electrocatalytic experiments. The sample was labeled as 'RWGS spent' after RWGS reaction and 'CO spent' after CO oxidation.

Scanning Transmission Electron Microscopy (STEM) was used to perform the structural and elemental analysis of the as-prepared and spent samples. Scanning Electron Microscopy (SEM, JSM-7500F FESEM) was employed to assess the morphology of the as-prepared and spent samples deposited on LLTO. Additionally, an Energy-dispersive X-ray spectrometer (EDS) integrated with the microscope was utilized to characterize the elemental compositions of the catalysts. X-ray Diffraction (XRD) analysis was carried out on both as-prepared and spent catalyst samples to evaluate changes in the crystalline structure. The identification of peaks was accomplished by using the Powder Diffraction File (PDF) database. X-ray photoelectron spectroscopy (XPS) spectra were measured on a Kratos AXIS Nova spectrometer equipped with an Al X-ray source to determine the oxidation state and to identify the presence of Li. High resolution spectra for Fe 2p, O 1s, C 1s, Pt 4f and Li 1s were recorded in the appropriate regions with the binding energies referred to the C1s peak at 284.8 eV. The XPS peaks were fitted using Shirley background corrections and the Gaussian-Lorentzian shape function in CasaXPS software.

6.3 Results and Discussions

6.3.1 Physicochemical characterizations

Figure 6-1a and b display the TEM image and EELS mapping of the RWGS spent Fe catalyst, illustrating microstructure of the material and distribution of elements where Fe is shown in blue, O in green, and C in red. From **Figure 6-1a**, a layer was found on the catalyst surface, which was amorphous and approximately 5 nm in thickness, as detailed in **Figure D-1**. The EELS mapping shown in **Figure 6-1b** highlighted the O area positioned outside the Fe region, creating a core-shell structure

of Fe(core)-O(shell). Moreover, the C map was divided into two distinct regions. One region, where C overlapped with Fe but not with O, suggested the formation of iron carbide (Fe_3C). The other region showed C attached to the O layer but not overlapping with Fe, indicating the likely formation of lithium carbonate (Li_2CO_3). This was consistent with the amorphous layer observed in **Figure 6-1a** and aligned with previous findings of Li_2CO_3 coated FeO_x catalysts[12]. The presence of Li_2CO_3 will be further verified by subsequent XPS analyses.

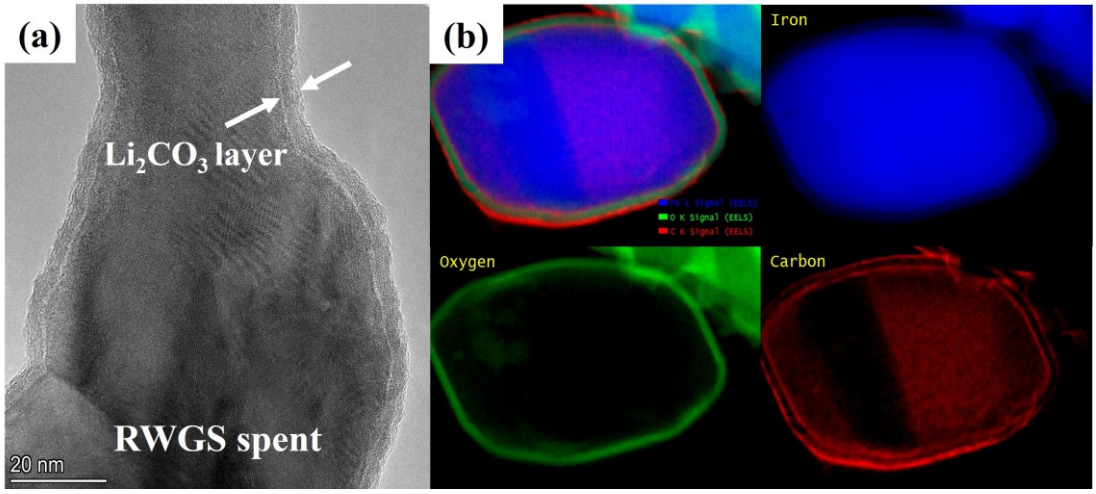

Figure 6-1. TEM image (a) and EELS mapping (b) of RWGS spent Fe/LLTO.

Figure D-2 shows the SEM images and corresponding EDS spectrums of as-prepared, CO spent, and RWGS spent Fe catalyst samples. The as-prepared sample was characterized by the unique nanowire structure of FeO_x catalyst. However, the CO spent and RWGS spent samples showed that the original morphology transformed significantly to a porous structure. The pores were irregularly shaped and distributed throughout the material, indicating a breakdown of the initial nanowire architecture. The change in the structure was possibly attributed to the reactions occurring at the catalyst surface, leading to material degradation and restructuring. The elemental composition analysis using EDS identified the presence of C, O, Li, and La without any other impurities.

Figure 6-2 shows the high-resolution XPS spectra of as-prepared, CO spent, and RWGS spent Pt-50/LLTO and Fe/LLTO samples for Li 1s and C 1s. The detailed XPS species information is summarized in **Table D-1**. The wide scans of Pt-50/LLTO and

Fe/LLTO samples are shown in **Figure D-3**. The high-resolution XPS spectra for Pt 4f, Fe 2p, and O1s are included in **Figure D-4**. **Figure 6-2a**, focusing on Li 1s & Pt 5p in Pt-50/LLTO, shows a broad peak at 51 eV identified as Pt $5p_{3/2}$, and a peak at 55 eV corresponding to Li_2CO_3[13,14]. It was found that Li_2CO_3 peak appeared only in the spent samples, indicative of the Li^+ migration due to polarization.

The formation of Li_2CO_3 was further confirmed through C 1s spectra shown in **Figure 6-2b**, where the carbonate peak located at 290 eV[13] was also exclusive to spent samples. A comparison between the two spent sample types revealed that the area percentage of Li_2CO_3 was greater in RWGS spent samples (16.48%) than in CO spent samples (6.86%), which will be elaborated on later regarding its decomposition in O_2-rich environments. The Pt 4f spectra in **Figure D-4a** indicates that the Pt remains at its metallic state (Pt^0)[15] and is chemically stable throughout the reactions without oxidation state changes. The O 1s spectra in **Figure D-4b** shows that the dominant oxygen species is C-O/C=O[16], affiliated to CO/CO_2 adsorption on the Pt surface.

As for the Fe/LLTO samples, the peaks at 53.5, 56.3, and 58.5 eV in **Figure 6-2c** regarding Li 1s & Fe 3p are identified as Fe^0, Fe^{2+} and Fe^{3+}, respectively[17]. The apparent presence of Fe^0 in as-prepared sample indicated a reduced state of Fe catalyst attributed to pre-treatments, although the main phase was Fe^{2+} due to sample oxidation when exposed to air during storage. Similarly, in CO and RWGS spent samples, the appearance of the Li_2CO_3 peak at 55 eV suggested Li^+ migration, consistent with HRTEM images showing Li_2CO_3 layer formation on the Fe surface. The absence of Fe^0 in CO spent sample indicated a complete oxidation, whereas its persistence in RWGS spent sample indicated a more reduced state.

Li_2CO_3 layer formation was further supported by the carbonate peak in C 1s spectra shown in **Figure 6-2d**, present only in spent samples. Moreover, the area of the C-C peak in the RWGS spent sample (55.6%) was significantly higher than in the other two (20.28% in as-prepared and 31.34% in CO spent), suggesting carbon deposition in the form of Fe_3C during the RWGS reaction, as corroborated by XRD

results in Appendix D. **Figure D-4c** demonstrates similar trends in Fe 2p as in Fe 3p. As opposed to metallic Pt film in Pt/LLTO, the O 1s spectra of Fe/LLTO in **Figure D-4d** also revealed the existence of lattice oxygen (O_L) at 529.8 eV and defect oxygen (O_V) at 530.7 eV[18] in addition to C-O/C=O peak. The O_V was found more prominent in as-prepared sample due to its reduced state. The significant increase in O_L and decrease in O_V in CO spent sample reflected complete oxidation of the iron catalyst, while similar levels of these species in RWGS spent sample suggested an intermediate oxidation state. Details on XRD patterns are discussed in Appendix D.

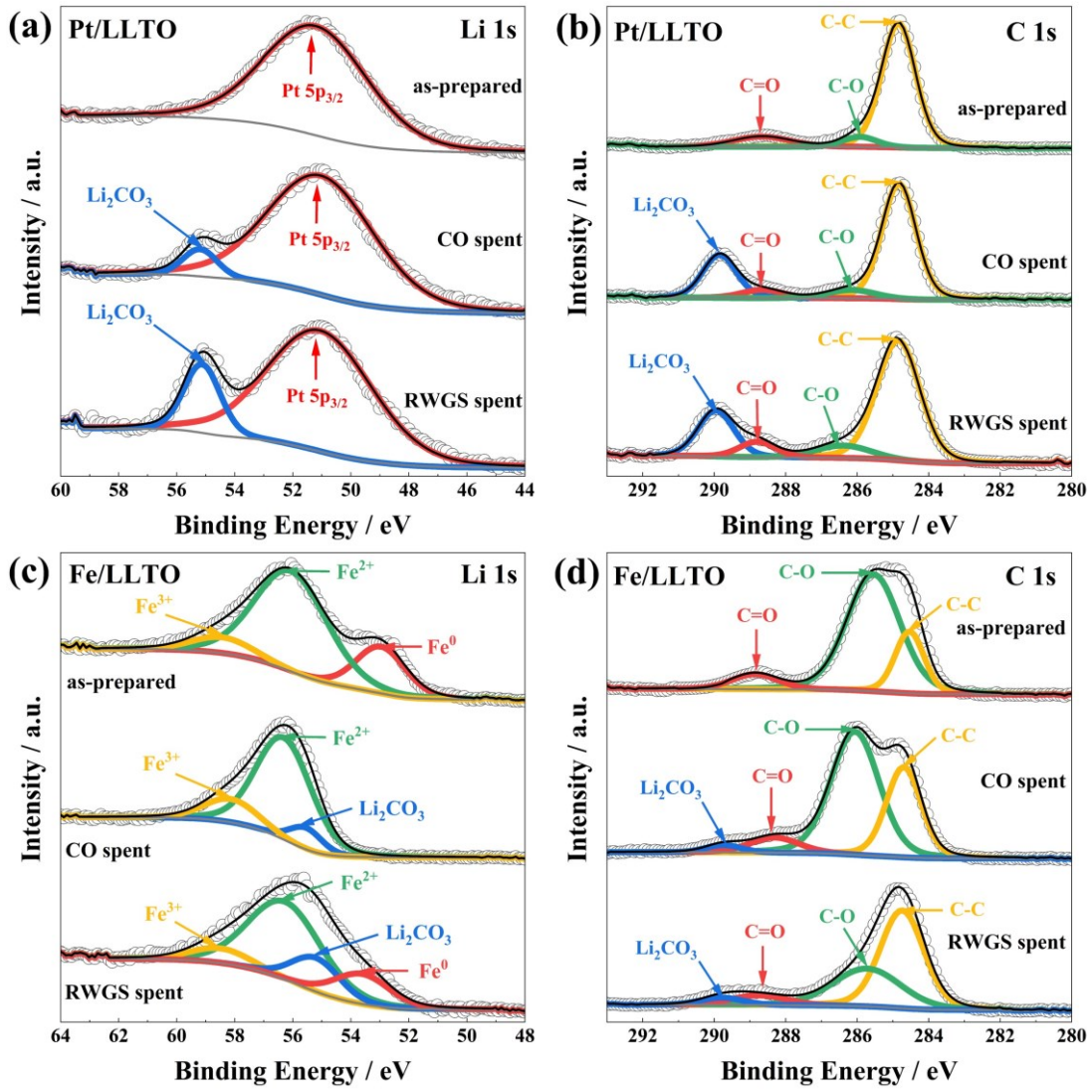

Figure 6-2. High-resolution XPS spectra of as-prepared, CO spent, and RWGS spent Pt-50/LLTO catalysts for (a) Li 1s & Pt 5p and (b) C 1s, as well as Fe/LLTO catalysts for (c) Li 1s & Fe 3p and (d) C 1s.

6.3.2 Open-circuit activity

Figure 6-3a presents the open-circuit activities of RWGS under stoichiometric conditions over Fe/LLTO, Fe/YSZ, Pt/LLTO, and LLTO on its own. Both FeO_x and Pt demonstrated 100% selectivity for CO production across the investigated temperature window. The activity of Fe/LLTO was found to be threefold higher than that of Fe/YSZ, as reported previously[16]. Given that the intrinsic activity of the LLTO alone was substantially limited in comparison to the other systems, the FeO_x was the active phase and was in an inherently promoted state due to the synergistic interactions between FeO_x and LLTO. This interaction was achieved by FeO_x, which was known to take up and release oxygen, thereby leading to the synergistic effect[19].

The catalytic performance of Fe/LLTO under different reaction conditions is compared in **Figure D-7a** and shows that an H_2-rich environment favors the RWGS reaction. Kinetic studies on Arrhenius plots also reveal the lowest activation energy in reducing conditions, which are shown in **Figures D-7 & 8 and Table D-2**. Although the catalytic activity of Pt-50/LLTO was much lower than that of Fe/LLTO, it was still comparable to Fe/YSZ, suggesting a lack of synergistic interactions between Pt and LLTO in this instance. The activity of Pt-100 was even lower, likely due to its dense surface[20].

Figure 6-3b shows the CO oxidation activities of Fe/LLTO and Pt/LLTO. Among the catalysts tested, Pt-50 displayed superior catalytic performance, activating at 150°C and achieving 100% conversion at 250°C, which was consistent with findings reported in the literature[6]. Increasing the Pt thickness to 100 nm led to a decrease in activity for Pt-100 due to the dense surface, with activation occurring at 220°C. Fe/LLTO demonstrated intermediate activity, starting at 200°C and achieving full conversion at 300°C, also in agreement with prior studies[21].

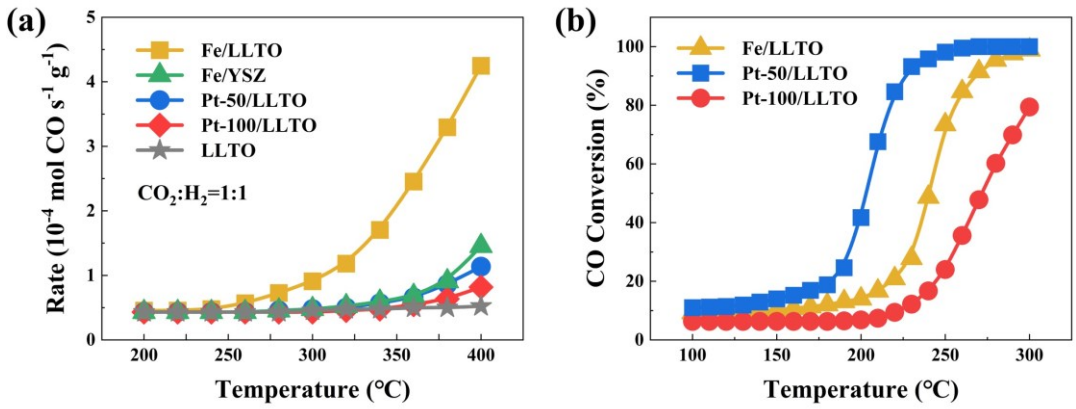

Figure 6-3. Open-circuit (a) RWGS activities and (b) CO conversions of Fe/LLTO and Pt/LLTO.

6.3.3 EPOC for CO oxidation

Figure 6-4 summarizes the EPOC effects for CO oxidation over FeO_x, Pt-100, and Pt-50 catalysts on LLTO. The corresponding applied voltages are summarized in **Figure D-9**. The results demonstrated that EPOC could be executed at temperatures as low as 150°C with FeO_x and 200°C with Pt-50, attributed to the use of LLTO as the solid electrolyte. From **Figure 6-4a**, a rapid decrease in reaction rate was observed upon applying a positive polarization of +3 V over the FeO_x catalyst, with ρ=0.87 and Λ=17.5. However, the rate remained at the suppressed state even after interrupting the polarization, indicative of a permanent EPOC effect. Only when a negative polarization of -0.5 V was applied, the rate would return to its initial state, with ρ=1.13 and Λ=7.5.

Figure 6-4b shows that increasing the applied positive potential leads to more significant decreases in reaction rates. For instance, applying +1 V resulted in a 4% decrease, while +3 V and +5 V led to decreases of 13% and 16%, respectively. Additionally, extending the duration of negative polarization modified the magnitude of rate enhancement. Taking the suppressed rate after a polarization of +3 V for 20 min as an example, **Figure 6-4c** shows that a negative polarization of -0.5 V for 10 minutes is insufficient to fully recover the rate, whereas 15-20 minutes of polarization achieves complete recovery. However, extending the period to 30 min further

promoted the rate, and once the prolonged negative polarization was stopped, the enhanced rate slightly decreased and stabilized shortly afterwards.

Under positive polarization, Li^+ was removed away from the catalyst to LLTO, which happened at the catalyst-electrolyte-gas interface and aligned with analogous EPOC studies involving alkali metal ionic species like Na^+ and K^+[22,23]. Given that Li^+ was proven beneficial for CO oxidation[24], its removal cleaned the interface and resulted in the rate decrease. However, since the Fe catalyst existed mainly in its highly oxidized state (FeO_x) in this environment, the transport of electrons facilitated an interaction between the Li^+ and O^{2-} in FeO_x at the tpb, as represented by Eq. (6-3):

$$FeO_x + Li^+ + e^- \leftrightarrow Li_2O + Fe \quad (6\text{-}3)$$

This process, known as lithiation of transition metal oxide, was reversible and involved the interaction of Li^+ with MO_x (where M = Fe, Ni, Cu, Co, etc.), converting them into M and Li_2O[25]. However, because the resulting Fe was immediately oxidized back to FeO_x by O_2 from the gas phase, the balance was disrupted and the lithiation process continued to move forward as long as the electrons were still passing. At the same time, the Li_2O interacted with the high amounts of produced CO_2 and formed Li_2CO_3 phase. After interrupting the polarization, the continuous removal of Li^+ was ceased and the lithiation process was also stopped due to the absence of electrons. But because of the Li_2CO_3 formation, which functioned as an inert layer and prevented the migrated Li^+ from moving back to FeO_x catalyst, the reaction rate remained suppressed. Moreover, increasing the applied voltage removed more Li^+ and strengthened the lithiation process due to the influx of more electrons, resulting in more significant and permanent suppression.

Under negative polarization, the supply of Li^+ to the FeO_x catalyst from the LLTO was hindered by the existence of undesirable Li_2CO_3. However, due to the flow of electrons in the reverse direction, Li_2CO_3 could be electrochemically removed, as depicted in Eq. (6-4):

$$Li_2CO_3 - e^- \rightarrow Li^+ + CO_2 + O_2^* \quad (6\text{-}4)$$

This process is referred to as the electrochemical oxidation of Li_2CO_3, a reaction commonly observed in Li-O_2/air batteries[26]. In this case, Li_2CO_3 was decomposed into Li^+, CO_2, and O_2 (O_2 originated from the reactive 'nascent oxygen', O_2^*)[27], which was also reported to occur on the surface of $Li_{6.4}La_3Zr_{1.4}Ta_{0.6}O_{12}$ (LLZTO) solid electrolyte[28], a material similar to LLTO used in this study. Consequently, this process not only removed the inert Li_2CO_3 layer but also facilitated the release of Li^+ to the FeO_x catalyst, thereby restoring the reaction rate to its initial state. However, applying negative polarization for 10 min was insufficient to completely decompose the Li_2CO_3, resulting in only partial recovery of the reaction rate. On the contrary, a duration of 30 min proved to be excessive, leading to the depletion of Li^+ within the LLTO and their subsequent supply to FeO_x surface, which in turn caused a permanent further enhancement in the reaction rate.

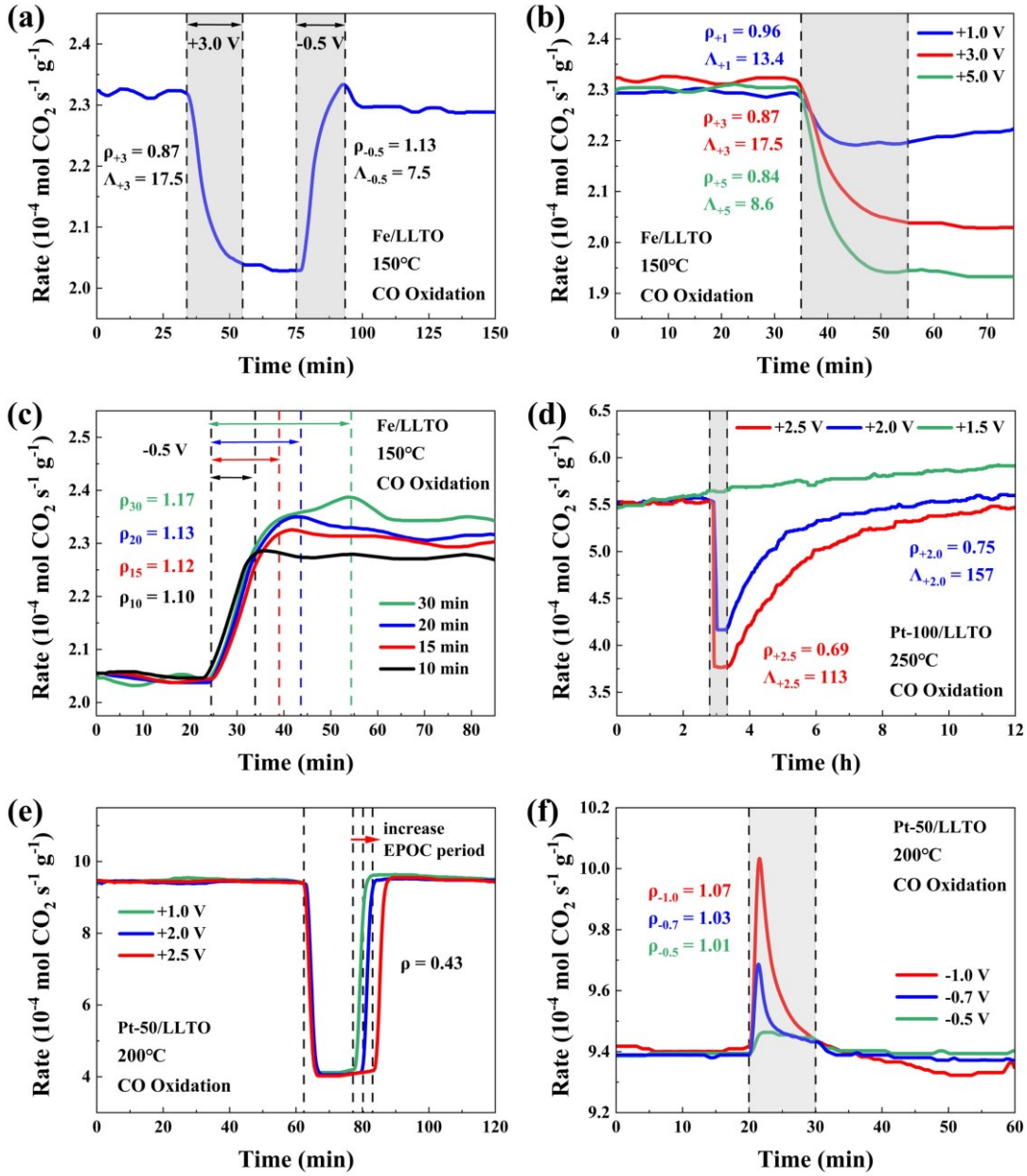

Figure 6-4. CO oxidation rate on FeOx under (a) +3 V and -0.5 V, (b) various positive voltages, and (c) different polarization time at -0.5 V. CO oxidation rate on (d) Pt-100 with positive polarization, and on Pt-50 with (e) positive and (f) negative polarization.

For sputtered Pt on LLTO, although both Pt-100 and Pt-50 showed responses to the applied polarization, the distinct behaviors demonstrated the influence of the Pt film thickness. According to **Figure 6-4d**, EPOC effects were observed for Pt-100 only under positive polarization, leading to a decrease in the reaction rate. The transient rate under negative polarization over Pt-100, shown in **Figure D-10**,

exhibited no rate changes. Furthermore, an application of at least +2 V was required to introduce the EPOC effect, with no responses observed below this voltage. Similarly, increasing the applied voltage resulted in stronger EPOC, with a 25% decrease in reaction rate at +2 V and a 31% suppression at +2.5 V. Interestingly, unlike FeO_x, the suppressed rate started to increase immediately after stopping the polarization and returned to its initial state slowly, taking up to 8 hours.

Pt-50 displayed a similar trend to Pt-100, with the reaction rate decreasing under positive polarization and returning to the initial state after interruption, as shown in **Figure 6-4e**. However, the rate suppression for Pt-50 occurred at a lower voltage of +1 V and the rate recovery took only 5 minutes. The suppression remained stable at ρ=0.43, even when the applied voltage was increased and the polarization period was prolonged. Furthermore, the reaction rate exhibited a sharp and instantaneous increase upon negative polarization, as shown in **Figure 6-4f**. The peak reaction rate diminished gradually during polarization, returning to its initial state, and increasing the applied negative voltage resulted in a higher peak.

Similarly, Li^+ was removed away from Pt catalyst under positive polarization, resulting in a rate decrease. However, given that Pt was commonly used as a non-reactive electrode because of its chemical and thermal stability[8], the Li^+ could only migrate through and be stored by Pt[29], rather than interacting with it as in the case of FeO_x. Therefore, once the polarization was interrupted, Li^+ could freely transport back and the reaction rate recovered as a result. Moreover, due to the thickness of Pt-100 reaching 100 nm, the backspillover of Li^+ required a long time to fully complete. Increasing the applied voltage enabled more Li^+ removal and strengthened EPOC effect.

In comparison, Pt-50, with a thickness of 50 nm, allowed a much easier backspillover and thereby shortened the rate recovery time. Also, since polarization of +1 V for 15 min already cleaned the Pt film completely, further increasing voltage or prolonging polarization time did not have a significant influence. Under negative polarization, although Li^+ was supplied to Pt, Pt-100 was too thick and Li^+ failed to

reach Pt film surface even by depleting the LLTO, resulting in no rate enhancement. For Pt-50, however, Li^+ could easily spillover to Pt film surface and resulted in the rate promotion, which was proportional to the applied negative polarization. The migrated Li^+ on Pt surface would interact with O_2 from the gas phase in the presence of electrons and form lithium oxides[30], which were finally transferred into Li_2CO_3 and led to the rate decrease due to the consumption of Li^+.

6.3.4 EPOC for RWGS

Figure 6-5a-c illustrate the EPOC effects for RWGS over Fe/LLTO under diverse reaction conditions. The corresponding applied polarization was summarized in **Figure D-11**, showing a constant current at -500 μA. Under stoichiometric and oxidizing conditions (**Figure 6-5a and b**), EPOC effects manifested exclusively under negative polarization. In this case, Li^+ was conducted from LLTO towards the Fe catalyst, as discussed before. The catalytic rate during polarization was suppressed by 13% with ρ=0.87 and Λ=3.22 under stoichiometric conditions, while decreased by 27% with ρ=0.73 and Λ=8.98 in CO_2-rich conditions, implying that the migrated Li^+ poisoned the FeO_x catalyst, rendering the new phase less active than bare FeO_x. A prior investigation on EPOC involving iron catalyst elucidated that the RWGS activities of FeO_x followed the sequence of Fe_3O_4 > FeO > Fe^0, while fully oxidized Fe_2O_3 and Fe_3C were found to inhibit the reaction[16].

In RWGS, iron catalyst mainly existed in highly active phases of Fe_3O_4, a slightly higher oxidation state under oxidizing conditions, and FeO, a lower oxidation state under stoichiometric conditions. Consequently, Fe_3O_4, characterized by the highest activity, was more significantly influenced by migrated Li^+. Conversely, under reducing conditions (**Figure 6-5c**), the reaction rate experienced a 21% promotion under the same negative polarization with ρ=1.21 and Λ=8.47. In this scenario, iron catalyst was maintained in the form of metallic Fe due to excess H_2. This more reduced state of Fe had worse RWGS catalytic performance and was activated by Li^+ during polarization.

The beneficial influence of Li^+ on Fe and its negative impacts on Fe_3O_4/FeO

underscored the significance of the Li-O interaction as a potential factor contributing to the deactivation. Specifically, the migrated Li^+ underwent the same process as mentioned in Eq. (6-3), leading to the formation of Li_2O and consequent partial reduction of FeO_x. As a result, the reaction rate decreased over the less oxidized state of iron catalyst (i.e., Fe^0). The particular interaction observed between FeO_x and Li^+ during the polarization and subsequent generation of Fe^0 aligned with results reported elsewhere[31]. Unlike in CO oxidation, the reduced Fe^0 could not be oxidized back by the gas environment because no oxygen existed in RWGS.

Furthermore, upon discontinuing polarization, catalytic rates gradually increased due to the cessation of Li^+ and electron transportation. Li_2O was no longer formed in this case, and Fe^0 began to be oxidized by Li_2O following the reverse process in Eq. (6-3). However, it failed to fully revert to the initial open-circuit rates, likely attributed to the formation of Fe_3C as well as the depletion of Li_2O. Under the reaction conditions, a portion of Li_2O reacted with CO_2 to form Li_2CO_3, which was inert and ineffective in oxidizing Fe. This depletion implied that the lithiation process was not completely reversible. Similarly, studies have revealed that unlike lithiation, the delithiation of FeO_x followed an antisymmetric reaction pattern[31], wherein the FeO phase formed[32] rather than reverting to the original FeO_x phase[33]. The resulting FeO exhibited improved activity compared to Fe^0 but was still inferior to Fe_3O_4. As a result, the reaction rate increased but could not return to its previous level.

In reducing conditions, however, iron catalyst was already in a reduced state. Consequently, the lithiation process encountered limitations due to the absence of O^{2-}. Therefore, when Li^+ were introduced under polarization, the reaction rate did not diminish. Instead, the migrated Li^+ engaged in a reaction with CO_2, leading to the formation of lithium oxalate, which underwent decomposition into Li_2CO_3 and CO when subjected to elevated temperatures[34], a finding that aligned with previous studies on Li-CO_2 batteries[35]. This mechanism facilitated an increased release of CO, thereby contributing to the observed enhancement in the reaction rate. This phenomenon was represented by Eq. (6-5):

$$Li^+ + CO_2 + e^- \rightarrow Li_2C_2O_4 \rightarrow Li_2CO_3 + CO \quad (6\text{-}5)$$

In contrast to CO oxidation, the absence of O_2 in RWGS dictated that the interaction between Li^+ and CO_2 followed Eq. (6-5) rather than the reverse process of Eq. (6-4). When polarization is interrupted, the continuous Li^+ supply from LLTO and electron transport were also stopped. Hence, the absence of $Li_2C_2O_4$ formation and its subsequent decomposition into Li_2CO_3, along with the cessation of CO release, contributed to the restoration of the reaction rate. The transient responses of RWGS rates to positive polarization at different temperatures under various conditions are shown in **Figure D-12-14** and demonstrate no EPOC phenomenon because Li^+ is removed away from iron catalyst in this situation and contributes no interactions. More discussions on the influence of applied currents and temperatures can be found in Appendix D and **Figure D-15**.

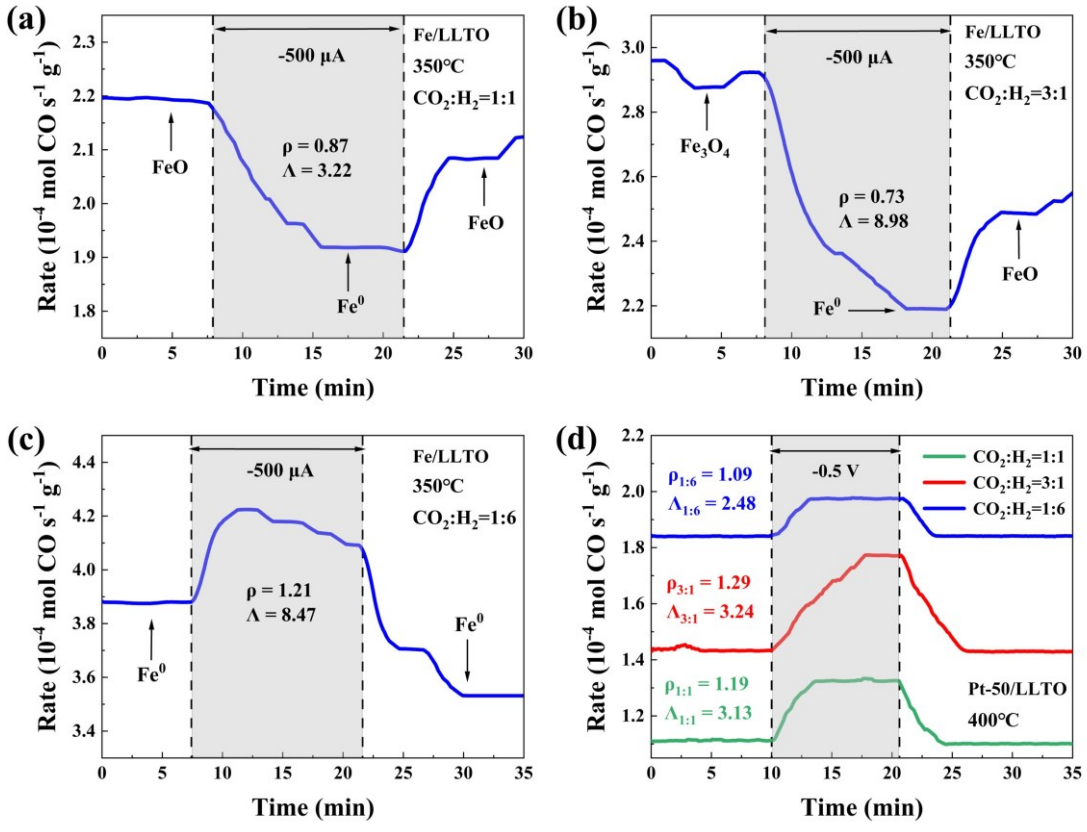

Figure 6-5. Transient responses of RWGS rate to negative polarization at 350°C under (a) stoichiometric, (b) oxidizing and (c) reducing conditions. (d) Transient responses of RWGS rate to different negative polarization on Pt-50 at 400°C.

For the Pt/LLTO, EPOC effects were observed exclusively for Pt-50 and not for Pt-100, which was attributed to the inferior Li^+ migration in Pt-100. As depicted in **Figure 6-5d**, reaction rates were promoted under negative polarization across all conditions (the corresponding applied voltage is shown in **Figure D-16**). Upon interrupting the polarization, the rates decreased and reverted to their initial value. In this scenario, since the supplied Li^+ could not interact with Pt and there was no O_2 in the environment, they instead directly reacted with CO_2 from the gas phase, following Eq. (6-5) under polarization. Consequently, CO was released due to the decomposition of $Li_2C_2O_4$. An increased CO_2 concentration under oxidizing conditions favored this process, while the limited availability of CO_2 under reducing conditions restricted this process. When the polarization ceased, the formation of $Li_2C_2O_4$ and the release of CO were also stopped.

6.3.5 Cyclic voltammetry

The CVs of Fe/LLTO and Pt/LLTO during CO oxidation and RWGS are shown in **Figure 6-6**, reflecting their electrochemical properties. Each CV consisted of five cycles with a scan rate of 20 mV/s. For CO oxidation over Fe/LLTO, shown in **Figure 6-6a**, the 1st cycle exhibited pronounced anodic peaks at +0.2 V, indicative of electrochemical reactions occurring at the Fe-LLTO-gas tpb. This was associated with the interaction between Li^+ and FeO_x catalyst. As previously discussed, the Li_2O reacted with CO_2 to form a Li_2CO_3 solid electrolyte interface (SEI)[36], which was stable and difficult to revert back. The sharp decrease in cathodic cycle starting at +0.1 V suggested the electrochemical decomposition of Li_2CO_3. However, the decomposition was not complete due to the rapid voltage sweep in the CVs. As a result, the anodic peak from the 2nd cycle onward started to decrease and disappeared from the 3rd cycle, confirming the progressive formation of a stable SEI[37]. This SEI served as a protective barrier and prevented further consumption of Li^+[38].

In comparison, according to CVs over Pt-50 as displayed in **Figure 6-6b**, the absence of an anodic peak in all cycles indicated a lack of electrochemical interaction between Li^+ and Pt film. This observation was consistent with EPOC results.

Nonetheless, the current at +1 V exhibited an increase and stabilization over successive cycles, which was attributed to the depletion of Li^+ within the LLTO and their subsequent spillover to the Pt surface.

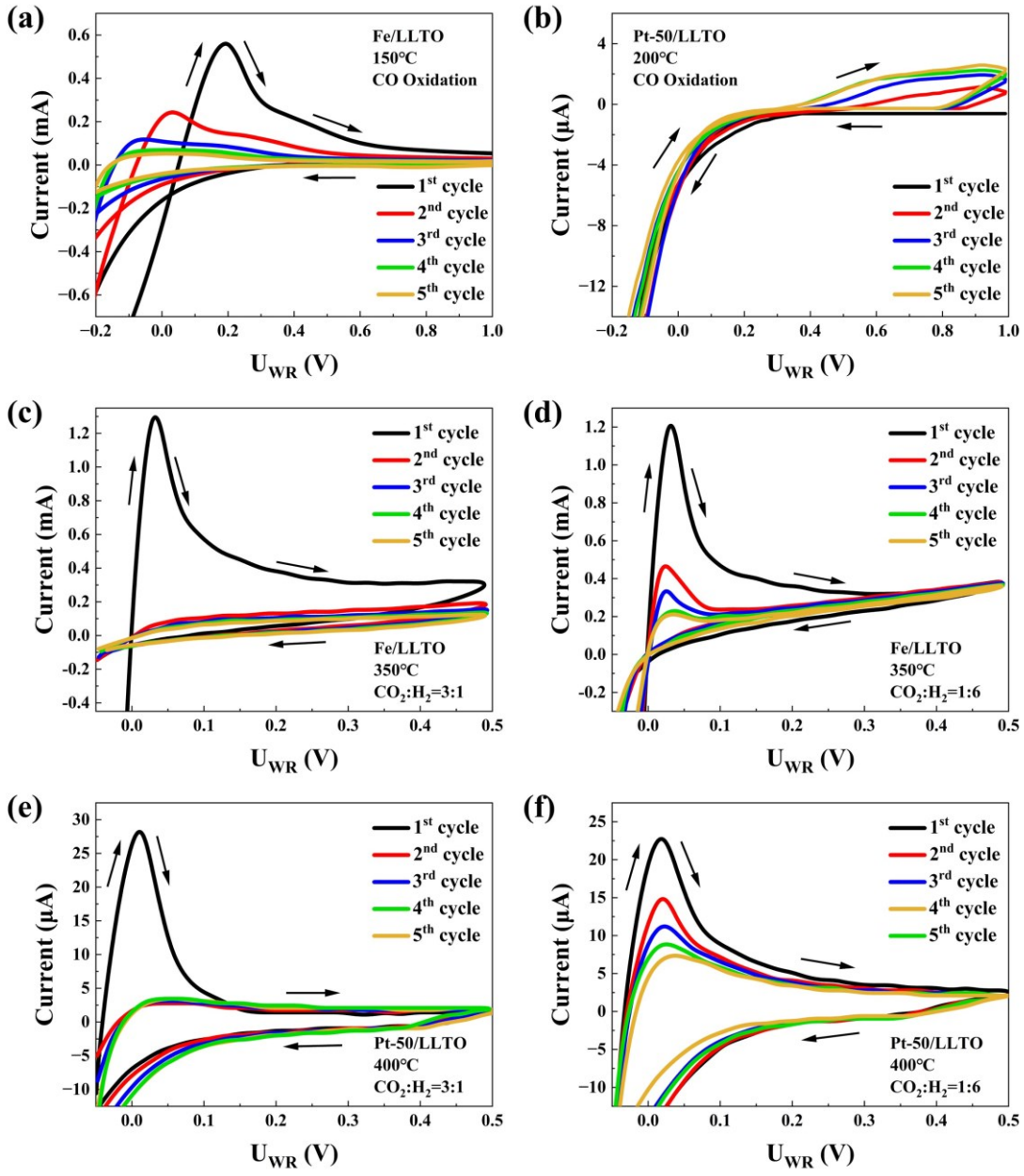

Figure 6-6. CVs of CO oxidation on (a) Fe/LLTO at 150°C and (b) Pt-50/LLTO at 200°C. CVs of RWGS on Fe/LLTO at 350°C under (c) oxidizing and (d) reducing conditions, and on Pt-50/LLTO at 400°C under (e) oxidizing and (f) reducing conditions.

The CVs of Fe/LLTO in RWGS under oxidizing and reducing conditions are shown in **Figures 6-6c and d**, respectively. The CVs under stoichiometric conditions can be found in **Figure D-17**. Similar to **Figure 6-6a**, the pronounced anodic current peaks in the 1st cycles at +0.05 V under stoichiometric and oxidizing conditions indicated the process described by Eq. (6-3). Moreover, the formation of Li_2CO_3 was responsible for the disappearance of the peak from the second cycle in the CO_2-rich environment. In contrast to CO oxidation, where Li_2CO_3 was decomposed completely due to the existence of O_2, the electrochemical process in RWGS was not reversible. This was also demonstrated by the permanent EPOC effects as shown in **Figure 6-5**. As a result, the current peaks decreased significantly after the 1st cycle.

Under reducing conditions, the sharp anodic peak was initially present because of the interaction between Li^+ and CO_2, as described by Eq. (6-5). This peak persisted in subsequent cycles but with a gradually decreasing current value, indicating the formation of a weak SEI attributed to the lower concentration of CO_2. However, with increasing cycle numbers, the gradual accumulation of Li_2CO_3 led to a decrease in the current peaks. **Figures 6-6e and f** exhibit the CVs of Pt-50/LLTO in RWGS under oxidizing and reducing conditions, respectively. The CVs under stoichiometric conditions are also provided in **Figure D-17**. Similar to the case with Fe in its metallic state shown in **Figure 6-6d**, the anodic peak in the 1st cycles also represented the process described by Eq. (6-5), considering the stability of Pt metal. Under stoichiometric and oxidizing conditions, the current peak disappeared soon, indicating a strong SEI due to the abundance of CO_2 gas. In contrast, under reducing conditions, the peak still existed but diminished stepwise, suggesting a weak SEI in this case.

6.4 Conclusion

The EPOC phenomenon was observed over FeOx nanowires and Pt film for both CO oxidation and RWGS reaction. Physicochemical characterizations including STEM, XRD, and XPS confirmed the presence of Li_2CO_3 in the spent sample, which was absent in the as-prepared one, illustrating the Li^+ migration during polarization. For CO oxidation, reaction rates over iron oxide (FeO_x) experienced a permanent

decrease under positive polarization but could revert to their initial state under negative polarization. This was linked to the formation of Li_2CO_3, which consumed and stored Li^+ in this inert form, maintaining a persistently reduced reaction state. Applying reverse polarization led to the electrochemical breakdown of Li_2CO_3 back into Li^+, which restored the reaction rates. Both Pt-50 and Pt-100 displayed similar decreases in reaction rates under positive polarization, but they showed immediate increases upon the cessation of polarization. The removal of Li^+ from the Pt catalyst cleared the surface, leading to the observed rate decrease. This process was easily reversible, as there were no interactions between Li^+ and Pt, which remained in its metallic state. However, thicker Pt films resulted in slower rate recovery due to limited backspillover of Li^+.

For RWGS, the reaction rate was promoted by applying negative polarization in reducing conditions, whereas it was suppressed in stoichiometric and oxidizing conditions. During negative polarization, Li^+ interacted with FeO_x, which was in a higher oxidized state in CO_2-rich environments. This resulted in its reduction to Fe^0, which was less active than FeO_x and contributed to the observed rate suppression. Conversely, the migrated Li^+ reacted with CO_2 to form $Li_2C_2O_4$ in reducing conditions, instead of interacting with the iron catalyst due to its reduced state in H_2-rich atmospheres. Unlike CO oxidation, the absence of O_2 in RWGS resulted in forming $Li_2C_2O_4$ rather than Li_2CO_3 directly. The decomposition of $Li_2C_2O_4$ into Li_2CO_3 and CO at elevated temperatures contributed to the rate promotion. Pt-50 showed reaction rate increase under all conditions and experienced a similar process, where the rate enhancement was due to the CO release from $Li_2C_2O_4$ decomposition.

Therefore, the interaction between metal/metal oxide and migrated Li^+ was considered as the key factor in exhibiting the EPOC effects. When catalysts were in oxidized states, the metal oxide lithiation would happen and resulted in formation of Li_2CO_3. On the contrary, when catalysts were in metallic state, Li^+ would interact with CO_2 directly and led to the formation of $Li_2C_2O_4$ and its subsequent decomposition into CO. Moreover, CV results indicated the formation of Li_2CO_3 SEI and revealed

that the EPOC effect was reversible if Li_2CO_3 was not formed or able to be electrochemically decomposed in an O_2-rich environment. However, it would show a permanent EPOC effect if Li_2CO_3 was formed and could not be completely removed.

References

[1] P. Vernoux, C.G. Vayenas, Recent Advances in Electrochemical Promotion of Catalysis (Modern Aspects of Electrochemistry, 61), Springer, 2023. https://doi.org/10.1007/978-3-031-13893-5.

[2] J. Lu, Y. Li, Perovskite-type Li-ion solid electrolytes: a review, J. Mater. Sci. Mater. Electron. 32 (2021) 9736–9754. https://doi.org/10.1007/s10854-021-05699-8.

[3] S. Yan, C.H. Yim, V. Pankov, M. Bauer, E. Baranova, A. Weck, A. Merati, Y. Abu-Lebdeh, Perovskite solid-state electrolytes for Lithium metal batteries, Batteries. 7 (2021). https://doi.org/10.3390/batteries7040075.

[4] C. Uhlmann, P. Braun, J. Illig, A. Weber, E. Ivers-Tiffée, Interface and grain boundary resistance of a lithium lanthanum titanate (Li3xLa2/3-xTiO3, LLTO) solid electrolyte, J. Power Sources. 307 (2016) 578–586. https://doi.org/10.1016/j.jpowsour.2016.01.002.

[5] C. Bohnke, H. Duroy, J.L. Fourquet, pH sensors with lithium lanthanum titanate sensitive material: Applications in food industry, Sensors Actuators, B Chem. 89 (2003) 240–247. https://doi.org/10.1016/S0925-4005(02)00473-2.

[6] M.S. Chen, Y. Cai, Z. Yan, K.K. Gath, S. Axnanda, D.W. Goodman, Highly active surfaces for CO oxidation on Rh, Pd, and Pt, Surf. Sci. 601 (2007) 5326–5331. https://doi.org/10.1016/j.susc.2007.08.019.

[7] D.U. Nielsen, X.M. Hu, K. Daasbjerg, T. Skrydstrup, Chemically and electrochemically catalysed conversion of CO2 to CO with follow-up utilization to value-added chemicals, Nat. Catal. 1 (2018) 244–254. https://doi.org/10.1038/s41929-018-0051-3.

[8] J. Binns, M. Marqués, P. Dalladay-Simpson, R. Turnbull, M. Frost, E. Gregoryanz, R.T. Howie, Reactivity of lithium and platinum at elevated densities, Phys. Rev. B. 99 (2019) 1–5. https://doi.org/10.1103/PhysRevB.99.220101.

[9] C. Panaritis, J. Zgheib, S.A.H. Ebrahim, M. Couillard, E.A. Baranova, Electrochemical in-situ activation of Fe-oxide nanowires for the reverse water gas shift reaction, Appl. Catal. B Environ. 269 (2020) 118826. https://doi.org/10.1016/j.apcatb.2020.118826.

[10] S. Yan, H. Al-Salih, C.H. Yim, A. Merati, E.A. Baranova, A. Weck, Y. Abu-Lebdeh, Engineered interfaces between perovskite La2/3xLi3xTiO3 electrolyte and Li metal for solid-state batteries, Front. Chem. 10 (2022) 1–12. https://doi.org/10.3389/fchem.2022.966274.

[11] M. Fee, S. Ntais, A. Weck, E.A. Baranova, Electrochemical behavior of silver

thin films interfaced with yttria-stabilized zirconia, J. Solid State Electrochem. 18 (2014) 2267–2277. https://doi.org/10.1007/s10008-014-2477-0.
[12] Y. Yang, Y. Liu, K. Pu, X. Chen, H. Tian, M. Gao, M. Zhu, H. Pan, Highly Stable Cycling of Amorphous Li2CO3-Coated α-Fe2O3 Nanocrystallines Prepared via a New Mechanochemical Strategy for Li-Ion Batteries, Adv. Funct. Mater. 27 (2017) 1–10. https://doi.org/10.1002/adfm.201605011.
[13] K.N. Wood, G. Teeter, XPS on Li-Battery-Related Compounds: Analysis of Inorganic SEI Phases and a Methodology for Charge Correction, ACS Appl. Energy Mater. 1 (2018) 4493–4504. https://doi.org/10.1021/acsaem.8b00406.
[14] E. Kazyak, M. Shin, W.S. Lepage, T.H. Cho, N.P. Dasgupta, Molecular layer deposition of Li-ion conducting "Lithicone" solid electrolytes, Chem. Commun. 56 (2020) 15537–15540. https://doi.org/10.1039/d0cc06077a.
[15] A. Villamayor, D. Galyamin, L. V. Barrio, E.G. Berasategui, S. Rojas, Highly active ultralow loading Pt electrodes for hydrogen evolution reaction developed by magnetron sputtering, Int. J. Hydrogen Energy. 64 (2024) 50–57. https://doi.org/10.1016/j.ijhydene.2024.03.226.
[16] C. Panaritis, J. Zgheib, S.A.H. Ebrahim, M. Couillard, E.A. Baranova, Electrochemical in-situ activation of Fe-oxide nanowires for the reverse water gas shift reaction, Appl. Catal. B Environ. 269 (2020) 118826. https://doi.org/10.1016/j.apcatb.2020.118826.
[17] Y. Momose, K. Tsuruya, T. Sakurai, K. Nakayama, Photoelectron emission and XPS studies of real iron surfaces subjected to scratching in air, water, and organic liquids, Surf. Interface Anal. 48 (2016) 202–211. https://doi.org/10.1002/sia.5942.
[18] Z. Wang, R. Lin, Y. Huo, H. Li, L. Wang, Formation, Detection, and Function of Oxygen Vacancy in Metal Oxides for Solar Energy Conversion, Adv. Funct. Mater. 32 (2022) 1–15. https://doi.org/10.1002/adfm.202109503.
[19] S. Lee, S. Kim, T. Kim, C. Lin, W.J. Lee, S.J. Kim, R.J. Gorte, W.C. Jung, The effects of iron oxide overlayers on Pt for CO oxidation, Catal. Commun. 172 (2022) 106549. https://doi.org/10.1016/j.catcom.2022.106549.
[20] O.K. Alekseeva, A.I. Mikhalev, E.K. Lutikova, V.I. Porembsky, M.Y. Presnyakov, V.N. Fateev, B.L. Shapir, S.A. Grigoriev, Structural and electrocatalytic properties of platinum and platinum-carbon layers obtained by magnetron-ion sputtering, Catalysts. 8 (2018) 1–14. https://doi.org/10.3390/catal8120665.
[21] S. Dey, S. Sun, N.S. Mehta, Carbon monoxide catalytic oxidation over various iron-based nanoparticles at ambient conditions: A Review, Carbon Capture Sci. Technol. 1 (2021) 100013. https://doi.org/10.1016/j.ccst.2021.100013.
[22] I. V. Yentekakis, G. Moggridge, C.G. Vayenas, R.M. Lambert, In Situ controlled promotion of catalyst surfaces via NEMCA: The effect of Na on the Pt-catalyzed CO oxidation, J. Catal. 146 (1994) 292–305. https://doi.org/10.1016/0021-9517(94)90033-7.
[23] A. de Lucas-Consuegra, F. Dorado, J.L. Valverde, R. Karoum, P. Vernoux, Electrochemical activation of Pt catalyst by potassium for low temperature CO

deep oxidation, Catal. Commun. 9 (2008) 17–20. https://doi.org/10.1016/j.catcom.2007.04.038.

[24] C. Stoffelsma, P. Rodriguez, G. Garcia, N. Garcia-Araez, D. Strmcnik, N.M. Marković, M.T.M. Koper, Promotion of the oxidation of carbon monoxide at stepped platinum single-crystal electrodes in alkaline media by lithium and beryllium cations, J. Am. Chem. Soc. 132 (2010) 16127–16133. https://doi.org/10.1021/ja106389k.

[25] Z. Yao, S. Kim, M. Aykol, Q. Li, J. Wu, J. He, C. Wolverton, Revealing the Conversion Mechanism of Transition Metal Oxide Electrodes during Lithiation from First-Principles, Chem. Mater. 29 (2017) 9011–9022. https://doi.org/10.1021/acs.chemmater.7b02058.

[26] A.T.S. Freiberg, J. Sicklinger, S. Solchenbach, H.A. Gasteiger, Li2CO3 decomposition in Li-ion batteries induced by the electrochemical oxidation of the electrolyte and of electrolyte impurities, Electrochim. Acta. 346 (2020) 136271. https://doi.org/10.1016/j.electacta.2020.136271.

[27] N. Mahne, S.E. Renfrew, B.D. McCloskey, S.A. Freunberger, Electrochemical Oxidation of Lithium Carbonate Generates Singlet Oxygen, Angew. Chemie - Int. Ed. 57 (2018) 5529–5533. https://doi.org/10.1002/anie.201802277.

[28] F. Jiang, L. Ma, J. Sun, L. Guo, Z. Peng, Z. Cui, Y. Li, X. Guo, T. Zhang, Deciphering the Enigma of Li2CO3Oxidation Using a Solid-State Li-Air Battery Configuration, ACS Appl. Mater. Interfaces. 13 (2021) 14321–14326. https://doi.org/10.1021/acsami.1c01770.

[29] Y. Kim, W. Choi, O.H. Kim, H. Park, S. Yun, R. Thangavel, Y.H. Cho, W.S. Yoon, Dual lithium storage of Pt electrode: alloying and reversible surface layer, J. Mater. Chem. A. 9 (2021) 18377–18384. https://doi.org/10.1039/d1ta04379j.

[30] W.J. Kwak, N. Rosy, D. Sharon, C. Xia, H. Kim, L.R. Johnson, P.G. Bruce, L.F. Nazar, Y.K. Sun, A.A. Frimer, M. Noked, S.A. Freunberger, D. Aurbach, Lithium-Oxygen Batteries and Related Systems: Potential, Status, and Future, Chem. Rev. 120 (2020) 6626–6683. https://doi.org/10.1021/acs.chemrev.9b00609.

[31] J.H. Kwon, K.N. Chaudhari, E. Coy, J.H. Seo, S.J. Ahn, Y.H. Lee, S. Lee, Y.C. Cho, O. Choi, K.S. Lee, D.I. Son, Y. Kim, Reversible Conversion Reactions of Mesoporous Iron Oxide with High Initial Coulombic Efficiency for Lithium-Ion Batteries, ACS Sustain. Chem. Eng. 9 (2021) 16627–16636. https://doi.org/10.1021/acssuschemeng.1c05335.

[32] X. Ma, M. Zhang, C. Liang, Y. Li, J. Wu, R. Che, Inheritance of Crystallographic Orientation during Lithiation/Delithiation Processes of Single-Crystal α-Fe2O3 Nanocubes in Lithium-Ion Batteries, ACS Appl. Mater. Interfaces. 7 (2015) 24191–24196. https://doi.org/10.1021/acsami.5b07547.

[33] Y. Pan, L. Yin, M. Li, Submicron-sized α-Fe 2 O 3 single crystals as anodes for high-performance lithium-ion batteries, Ceram. Int. 45 (2019) 12072–12079. https://doi.org/10.1016/j.ceramint.2019.03.104.

[34] Z.H. Kafafi, R.H. Hauge, W.E. Billups, J.L. Margrave, Carbon Dioxide

Activation by Lithium Metal. 1. Infrared Spectra of Li+CO2-, Li+C2O4- and Li22+ CO22- in Inert-Gas Matrices, J. Am. Chem. Soc. 105 (1983) 3886–3893. https://doi.org/10.1021/ja00350a025.

[35] S. Zhang, L. Sun, Q. Fan, F. Zhang, Z. Wang, J. Zou, S. Zhao, J. Mao, Z. Guo, Challenges and prospects of lithium–CO2 batteries, Nano Res. Energy. 1 (2022) 1–8. https://doi.org/10.26599/NRE.2022.9120001.

[36] S.K. Heiskanen, J. Kim, B.L. Lucht, Generation and Evolution of the Solid Electrolyte Interphase of Lithium-Ion Batteries, Joule. 3 (2019) 2322–2333. https://doi.org/10.1016/j.joule.2019.08.018.

[37] Y. Kobayashi, J. Abe, K. Kawase, K. Takahashi, B.D. Vogt, S. Shiratori, Enhanced stability of smoothly electrodeposited amorphous Fe2O3@electrospun carbon nanofibers as self-standing anodes for lithium ion batteries, New J. Chem. 42 (2018) 1867–1878. https://doi.org/10.1039/c7nj03970k.

[38] F. Qiu, S. Ren, X. Mu, Y. Liu, X. Zhang, P. He, H. Zhou, Towards a stable Li–CO2 battery: The effects of CO2 to the Li metal anode, Energy Storage Mater. 26 (2020) 443–447. https://doi.org/10.1016/j.ensm.2019.11.017.

Appendix D: Supplementary Information for Chapter 6

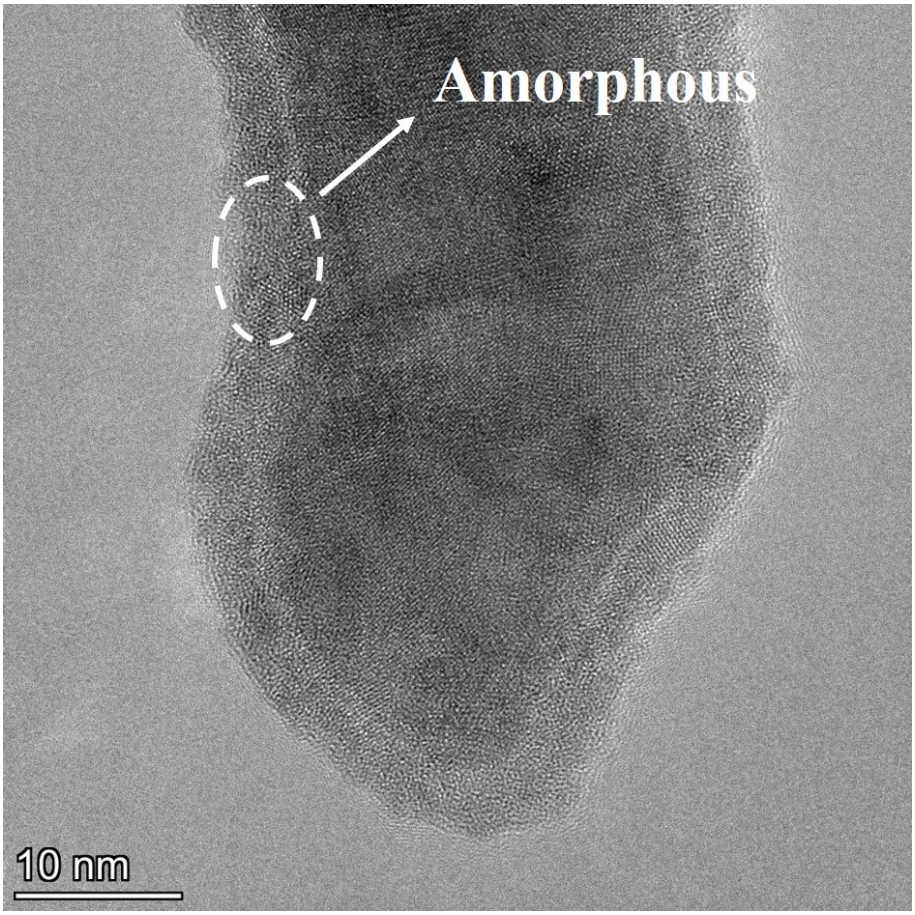

Figure D-1. HRTEM image of RWGS spent Fe/LLTO catalyst showing the amorphous Li_2CO_3 layer on Fe surface.

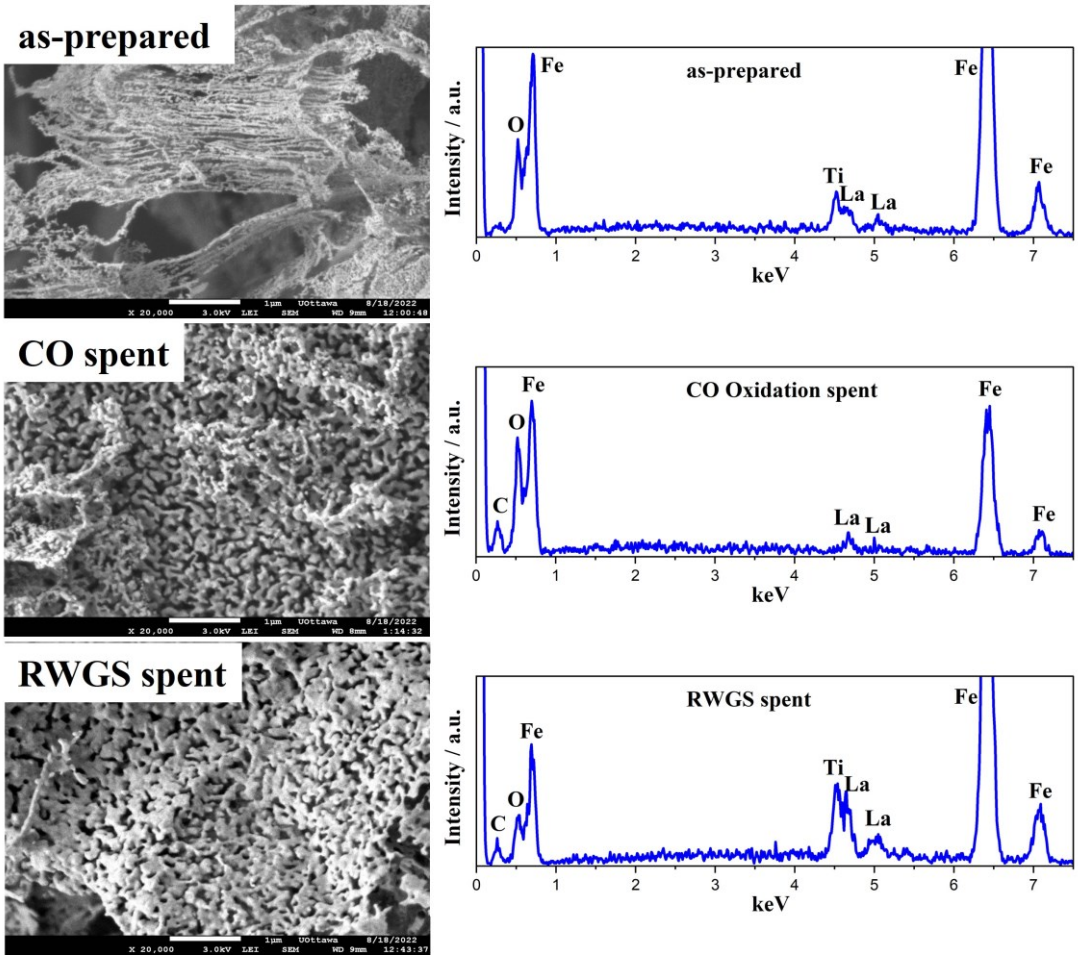

Figure D-2. SEM images and EDS spectrums of as-prepared, CO spent, and RWGS spent Fe/LLTO catalysts.

Table D-1. Detailed XPS species information of as-prepared, CO spent, and RWGS spent Pt/LLTO and Fe/LLTO catalysts.

Pt/LLTO		Position (eV)			FWHM (eV)			%Area		
		as-prepared	CO spent	RWGS spent	as-prepared	CO spent	RWGS spent	as-prepared	CO spent	RWGS spent
Pt 4f	Pt $4f_{7/2}$	70.4	70.3	70.3	0.84	0.83	0.83	-	-	-
	Pt $4f_{5/2}$	73.7	73.6	73.6	0.93	0.87	0.87	-	-	-
Pt 5p	Pt $5p_{3/2}$	51.2	51.1	51.1	4.2	4.26	4.31	100	83.52	93.14
Li 1s	Li_2CO_3	-	55.1	55.2	-	1.47	1.39	0	16.48	6.86
C 1s	C-C	284.8	284.8	284.8	1.11	1.12	1.42	81.91	64.22	68.8
	C-O	285.9	286	286.4	1.13	1.55	1.81	6.73	6.45	7.36
	C=O	288.6	288.6	288.8	1.89	1.37	1.2	11.36	5.62	6.12
	Li_2CO_3	-	289.9	290	-	1.11	1.18	0	23.7	17.73
O 1s	C-O, C=O	531.6	531.7	531.8	1.86	1.6	1.62	100	100	100
Fe/LLTO		Position (eV)			FWHM (eV)			%Area		
		as-prepared	CO spent	RWGS spent	as-prepared	CO spent	RWGS spent	as-prepared	CO spent	RWGS spent
Fe 2p	Fe	707.7	-	707.2	1.7	-	1.62	10.99	0	4.49
	Fe^{2+}	711.2	710.5	710.7	2.77	2.23	3.43	75.97	66.52	85.44
	Fe^{3+}	713.5	712.4	713	2.25	2.6	2.22	13.04	33.48	10.07
Fe 3p	Fe	53.5	-	53.6	1.82	-	2.27	22.04	0	17.12
	Fe^{2+}	56.3	55.8	56.2	2.65	2.1	2.9	68.86	74.19	57.32
	Fe^{3+}	58.4	57.5	58.4	2.2	2	2.43	9.09	16.33	8.97
Li 1s	Li_2CO_3	-	55.1	55.2	-	1.27	1.96	0	9.48	16.59
C 1s	C-C	284.8	284.8	284.8	1	1.2	1.44	20.28	31.34	55.6
	C-O	285.6	286.3	285.7	1.75	1.65	2.23	70.4	58.69	33.45
	C=O	288.8	288.6	288.7	1.53	1.7	1.81	9.31	7.4	8.35
	Li_2CO_3	-	290	289.9	-	1.2	1.4	0	2.58	4
O 1s	O_L	529.8	529.8	529.8	1.57	1.3	1.27	10.55	36.91	17.27
	O_V	530.7	530.7	530.8	1.1	0.74	2.07	34.91	2.14	22.28
	C-O, C=O	532	531.9	532	2.37	1.89	2.52	54.55	60.96	60.45

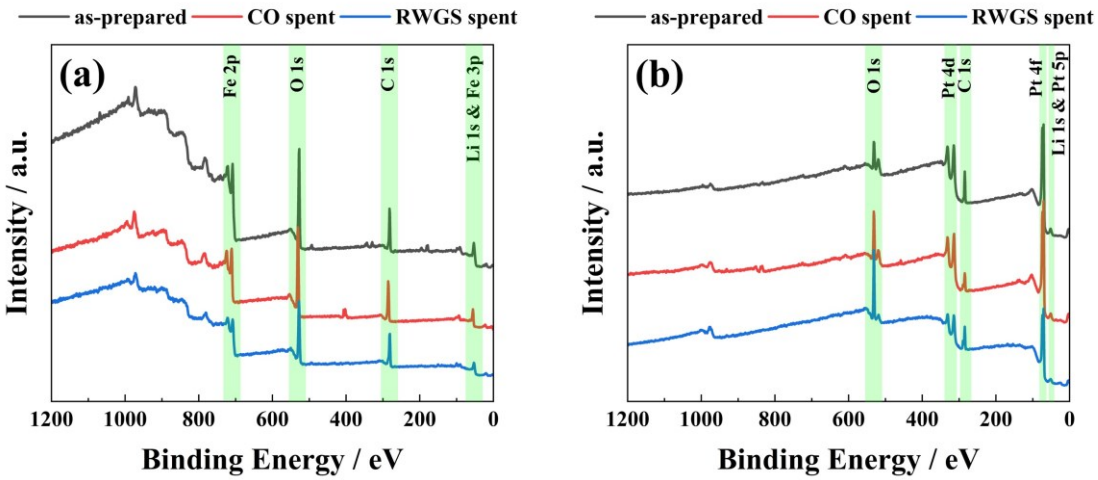

Figure D-3. Wide scan XPS spectra for (a) Fe/LLTO and (b) Pt-50/LLTO.

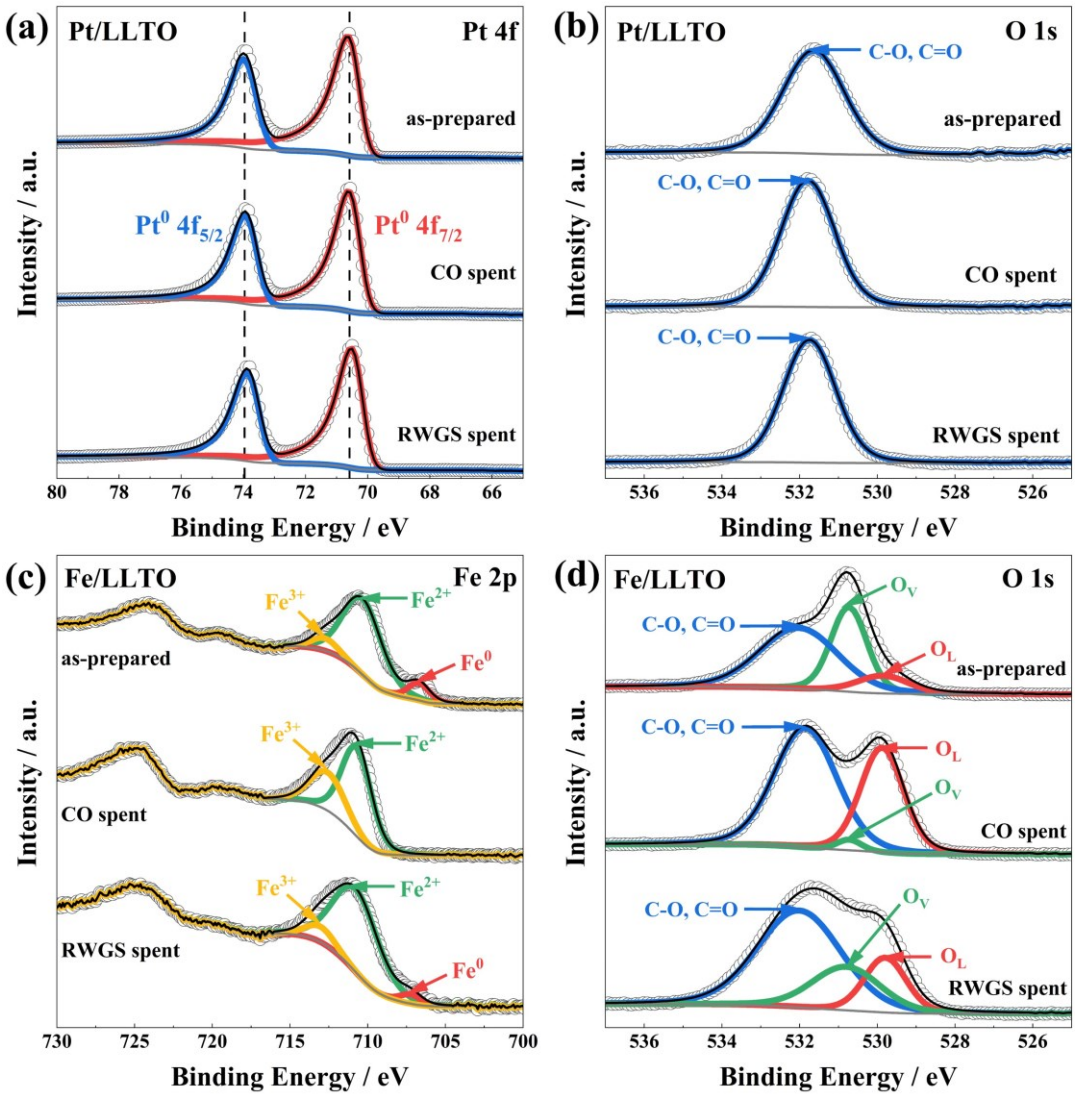

Figure D-4. High-resolution XPS spectra of as-prepared, CO spent, and RWGS spent Pt-50/LLTO catalysts for (a) Pt 4f and (b) O 1s, as well as Fe/LLTO catalysts for (c) Fe 2p and (d) O 1s.

Figure D-5a-c show the XRD patterns of as-prepared and spent samples. The as-prepared iron catalyst predominantly exhibited a reduced state, as evidenced by the presence of three distinct peaks corresponding to metallic Fe (Fe^0) (PDF #87-0722). This observation indicated that the catalyst underwent full reduction during the pre-treatment. However, subsequent electrocatalytic experiments induced notable alterations in the crystalline structure. The XRD patterns obtained for the spent sample revealed the coexistence of multiple phases, including Fe^0 (PDF #87-0722), Fe_3O_4 (PDF #77-1545), Fe_3C (PDF #72-1110), and LLTO (PDF #87-0935). These findings provided insight into the partial oxidation of the iron catalyst under reaction conditions, where CO_2 was identified as a contributing factor. Additionally, the presence of carbon deposition was observed, leading to the formation of Fe_3C. This phenomenon aligned with previous literature reports, supporting the propensity of iron catalysts to undergo such transformations. Furthermore, the detection of the LLTO phase was attributed to its inclusion when removing the catalysts from the LLTO disk surface. The XRD for bare LLTO solid electrolyte is shown in **Figure D-6**.

In addition to the predominant peaks observed in the spent sample, lithium carbonate (Li_2CO_3) phase was also discerned, as presented in **Figure D-5d**. Given the relatively low intensity of the characteristic Li_2CO_3 peaks due to its limited amount in the spent sample, and the overlapping nature of these peaks with those of other phases, a specific scanning window ranging from 19 to 33 °2θ was selected for detailed presentation. The peaks located at 21.3, 23.4, 29.4, 30.5 and 31.8 °2θ identified Li_2CO_3 (PDF #72-1216), which were absent in the as-prepared sample. The presence of Li_2CO_3 phase signified the migration of Li^+ to the iron catalyst during polarization, followed by its interaction with CO_2 to form Li_2CO_3.

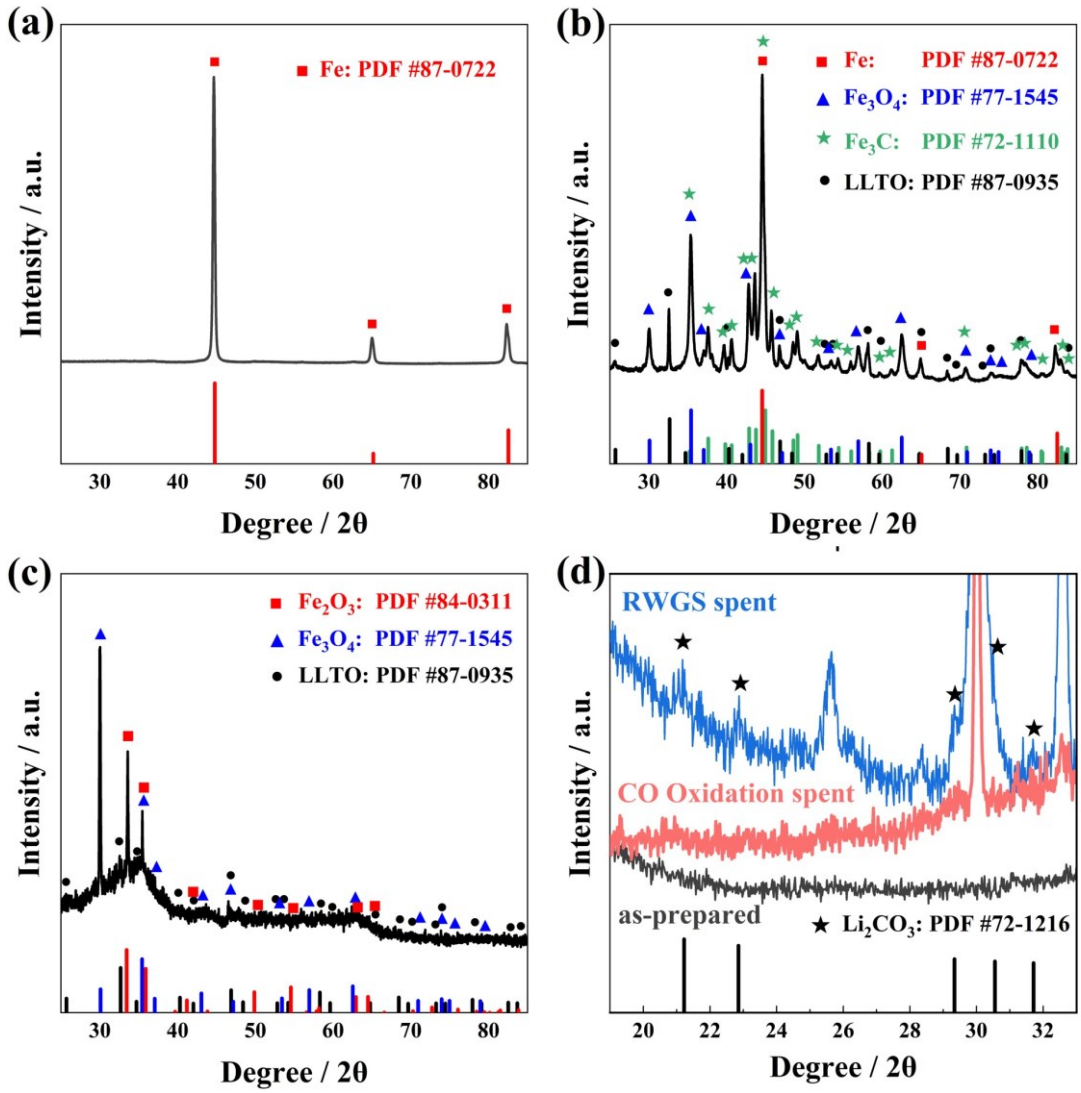

Figure D-5. XRD patterns of as-prepared and spent catalyst (a) in a full range (25 to 85 °2θ) and (b) in a narrow range (19 to 33 °2θ).

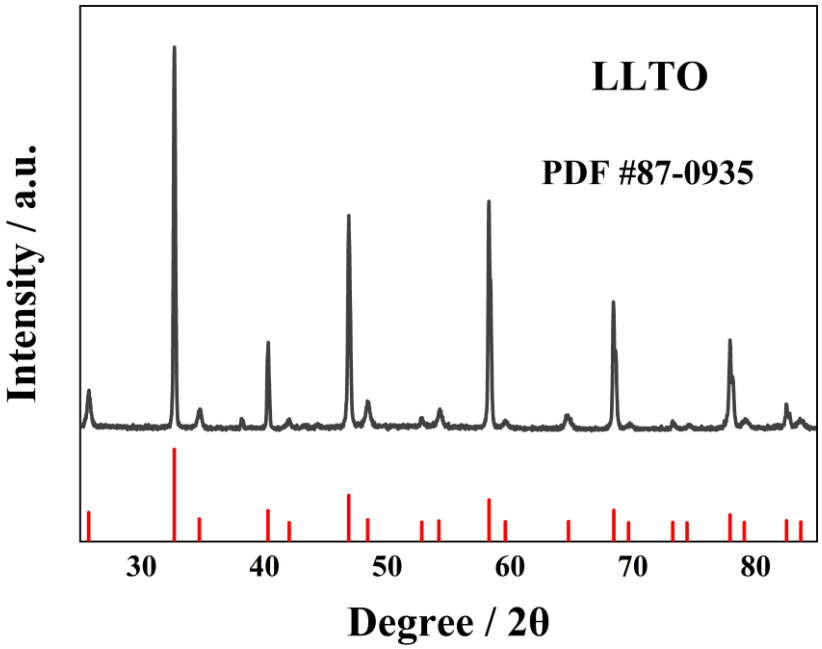

Figure D-6. XRD pattern of bare LLTO solid electrolyte.

Linear sweep voltammetry (LSV), conducted at a scan rate of 1 mV s^{-1}, is employed to generate Tafel plots, expressed as the natural logarithm of current density ($\ln j$) versus the potential difference between WE and RE (U_{WR}). These plots help to infer the exchange current density (j_0), a fundamental parameter in electrochemical kinetics, which is discerned from the intercept of the linear segment. Subsequently, the derived values are utilized to construct Arrhenius plots, wherein $\ln(j_0)$ is plotted against *1000/T*. This analytical method involves estimating the activation energies (E_a) by assessing the slopes derived from Eq. (D-1):

$$E_a = -R \cdot slope \quad \text{(D-1)}$$

The Arrhenius plots under stoichiometric, oxidizing and reducing conditions are presented in **Figure D-7b**. The LSV curves and corresponding Tafel plots used to determine the j_0 are summarized in **Figure D-8**. The detailed parameters of Tafel plots and Arrhenius plots are summarized in **Table D-2**. The findings indicated that the E_a exhibited a minimum value of 15 kJ mol^{-1} under reducing conditions, rose to 33.13 kJ mol^{-1} in oxidizing conditions and reached its maximum at 64.43 kJ mol^{-1} under stoichiometric conditions. This correlation suggested that the RWGS reaction was

preferentially catalyzed in a H_2-rich environment where the activation energy barrier was reduced, thereby promoting the reaction process, as evidenced by the open-circuit activities. These results demonstrated the potential of LLTO as a promising solid electrolyte for Fe nanowires deposition in EPOC applications.

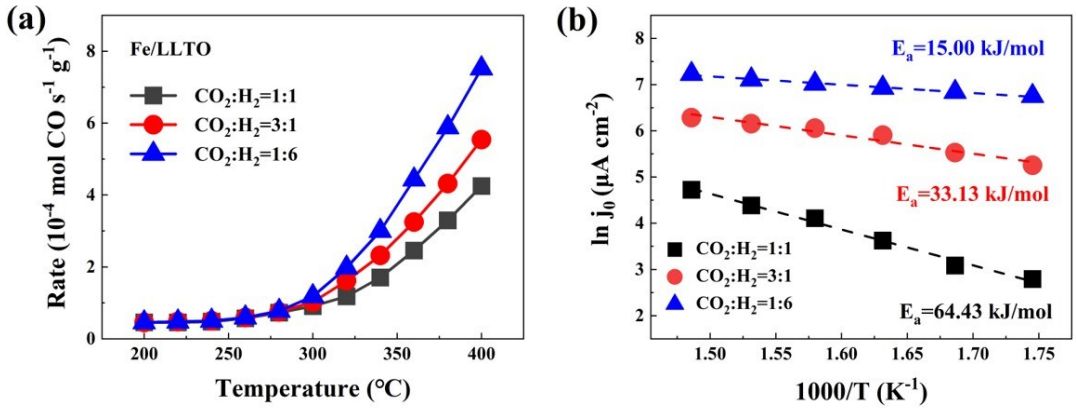

Figure D-7. Open-circuit activities over Fe/LLTO under different reaction conditions (a) and corresponding Arrhenius plots (b).

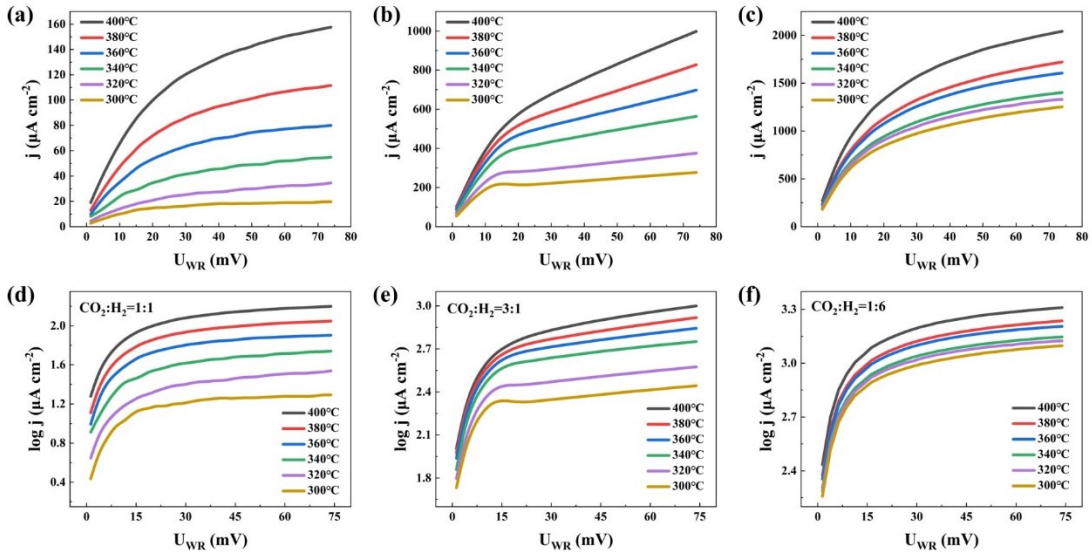

Figure D-8. LSV curves of Fe/LLTO in (a) stoichiometric, (b) oxidizing, and (c) reducing conditions. Tafel plots of Fe/LLTO in (d) stoichiometric, (e) oxidizing, and (f) reducing conditions.

Table D-2. Summary of Tafel intercepts for j_0 evaluation and Arrhenius slopes for E_a determination under different reaction conditions.

	CO_2:H_2=1:1		CO_2:H_2=3:1		CO_2:H_2=1:6	
Temperature (°C)	Tafel intercept	j_0 (μA)	Tafel intercept	j_0 (μA)	Tafel intercept	j_0 (μA)
400	2.0516	112.616	2.7283	534.9338	3.1396	1379.113
380	1.905	80.35261	2.6722	470.1106	3.0874	1222.925
360	1.7838	60.7855	2.6303	426.8743	3.048	1116.863
340	1.5746	37.54914	2.5654	367.6207	3.0087	1020.234
320	1.3392	21.83735	2.4013	251.9417	2.9705	934.3294
300	1.2128	16.323	2.2819	191.3815	2.9322	855.4606
Arrhenius Slope	-7.7494		-3.9845		-1.8044	
E_a (kJ/mol)	64.4285116		33.127133		15.0017816	

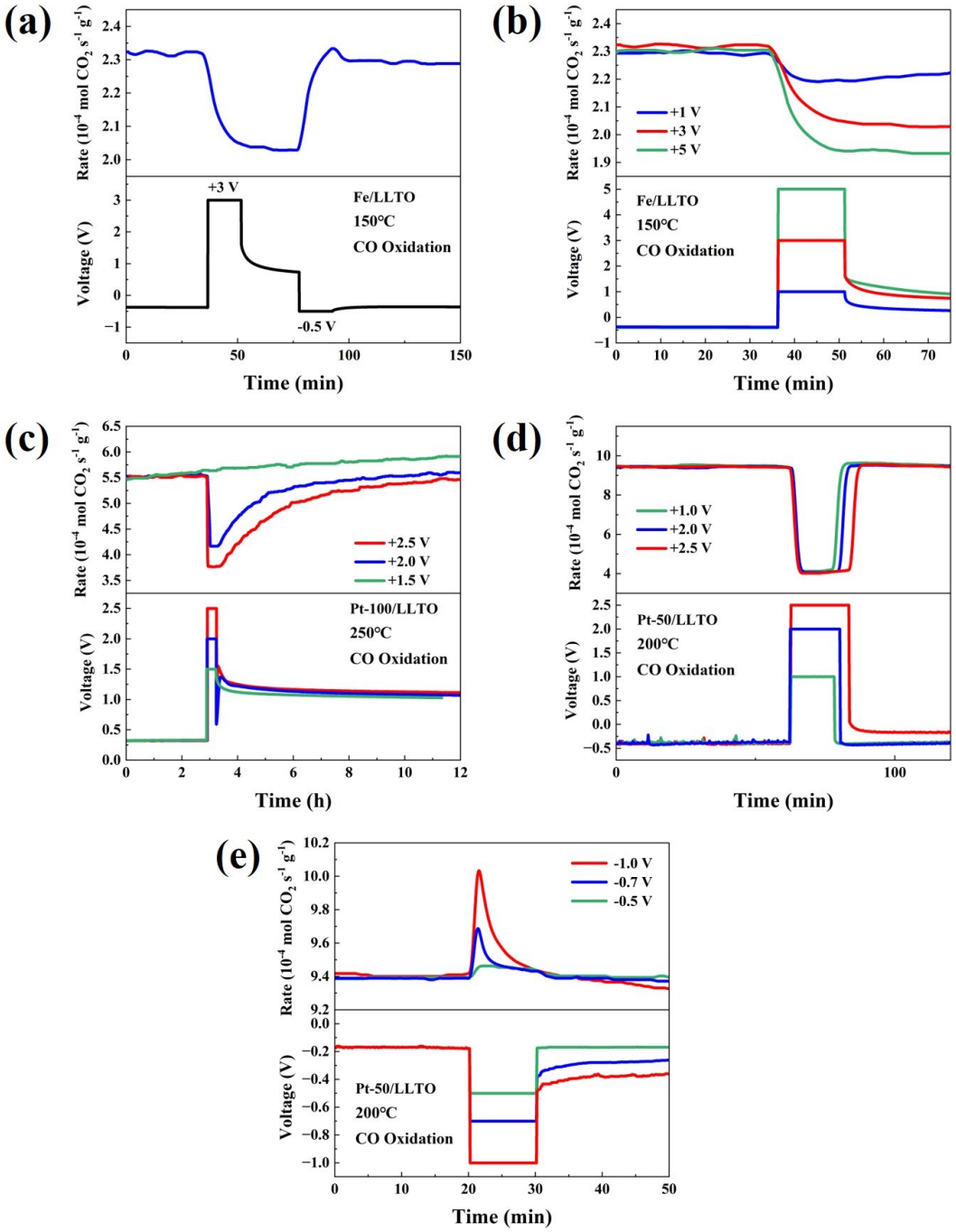

Figure D-9. Transient CO oxidation rates over (a) and (b) Fe/LLTO, (c) Pt-100/LLTO, (d) and (e) Pt-50/LLTO, and corresponding applied voltages.

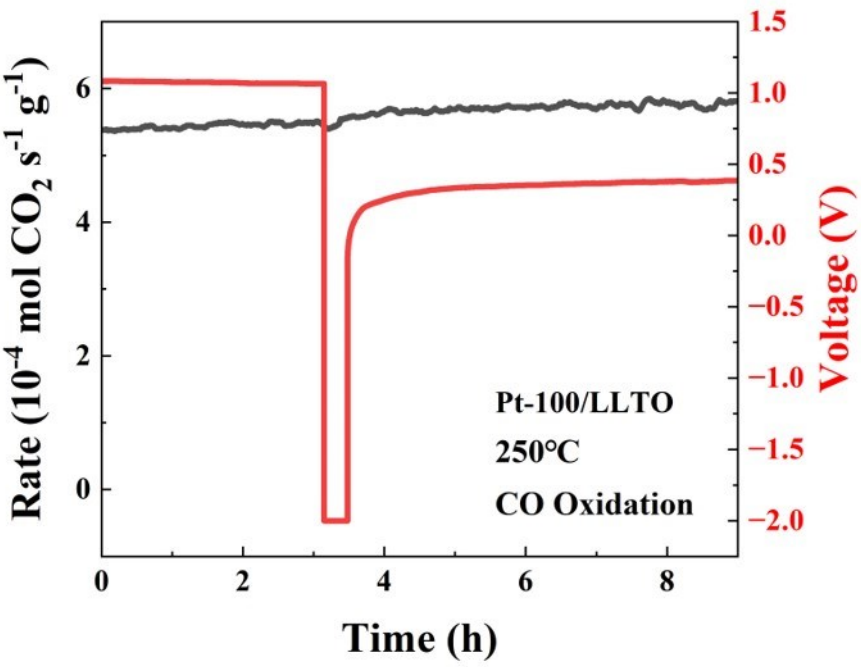

Figure D-10. Transient CO oxidation rate over Pt-100/LLTO at 250°C under negative polarization.

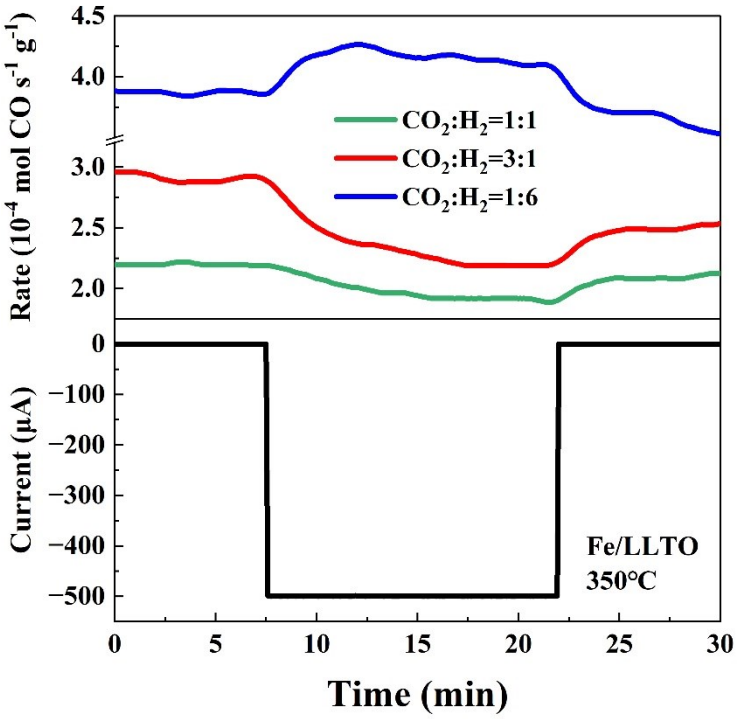

Figure D-11. Transient RWGS rates over Fe/LLTO at 350°C and corresponding applied current of -500 μA under different reaction conditions.

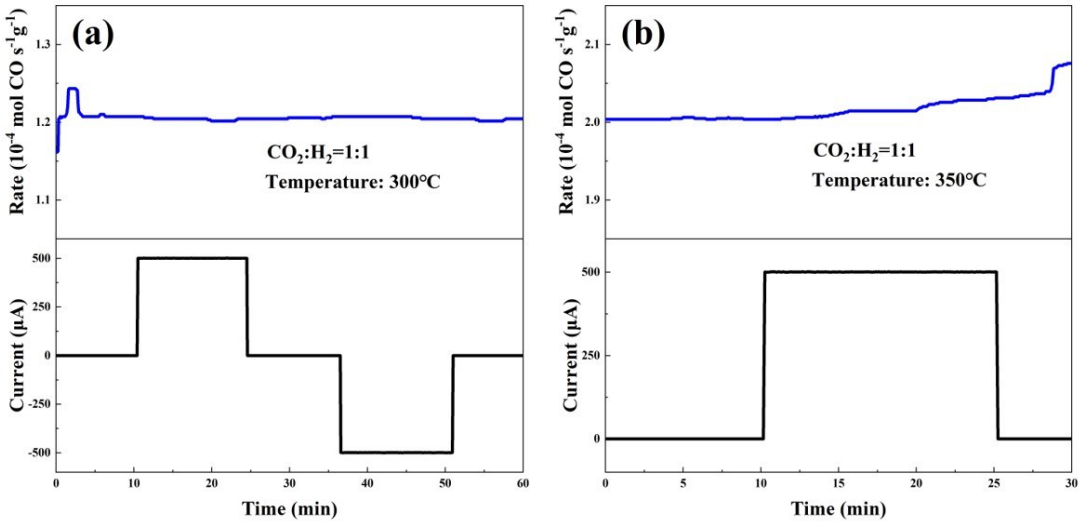

Figure D-12. Transient RWGS rates over Fe/LLTO and corresponding applied currents in stoichiometric conditions (a) under positive and negative polarization at 300℃, and (b) under positive polarization at 350℃.

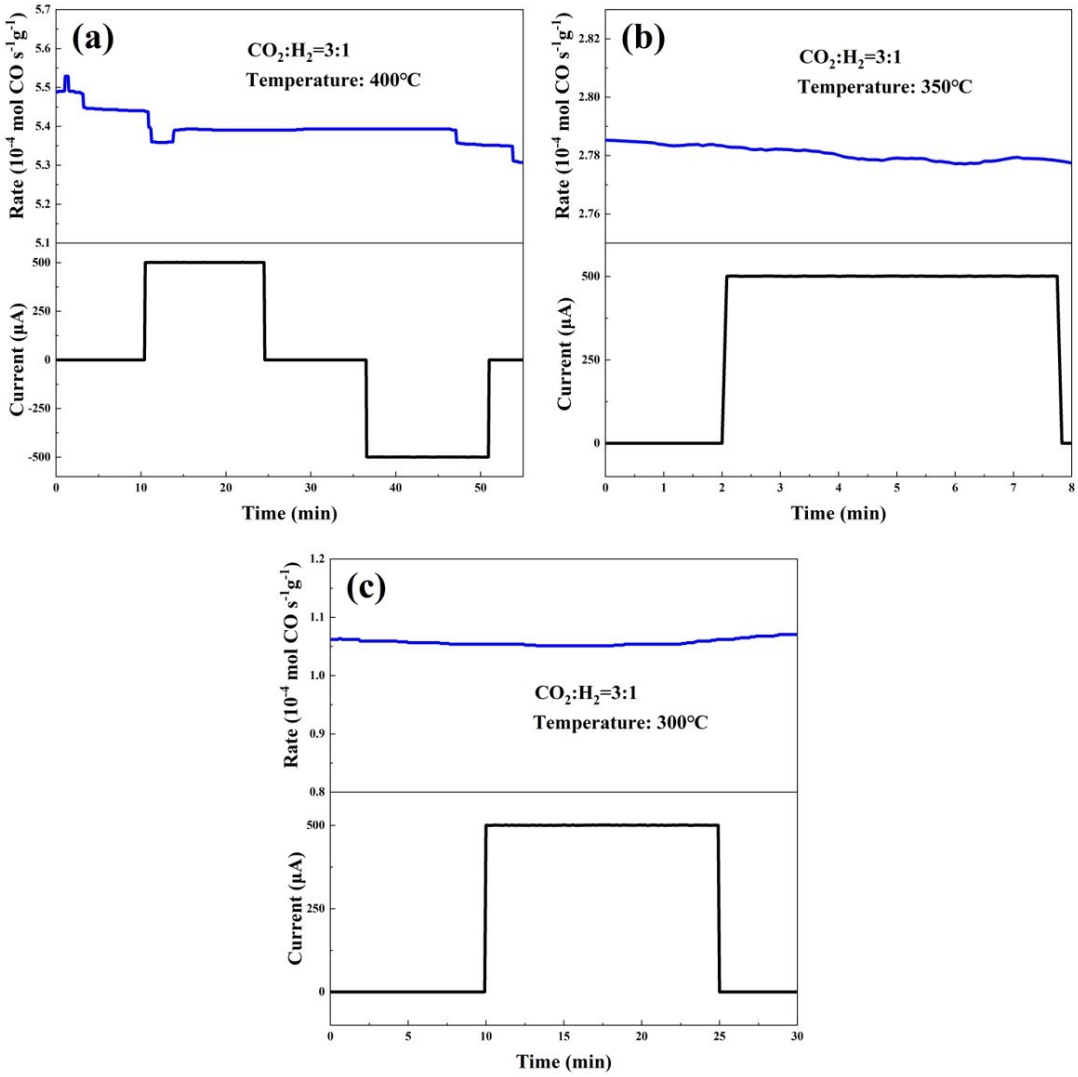

Figure D-13. Transient RWGS rates over Fe/LLTO and corresponding applied currents in oxidizing conditions (a) under positive and negative polarization at 400℃, and under positive polarization at (b) 350℃ and (c) 300℃.

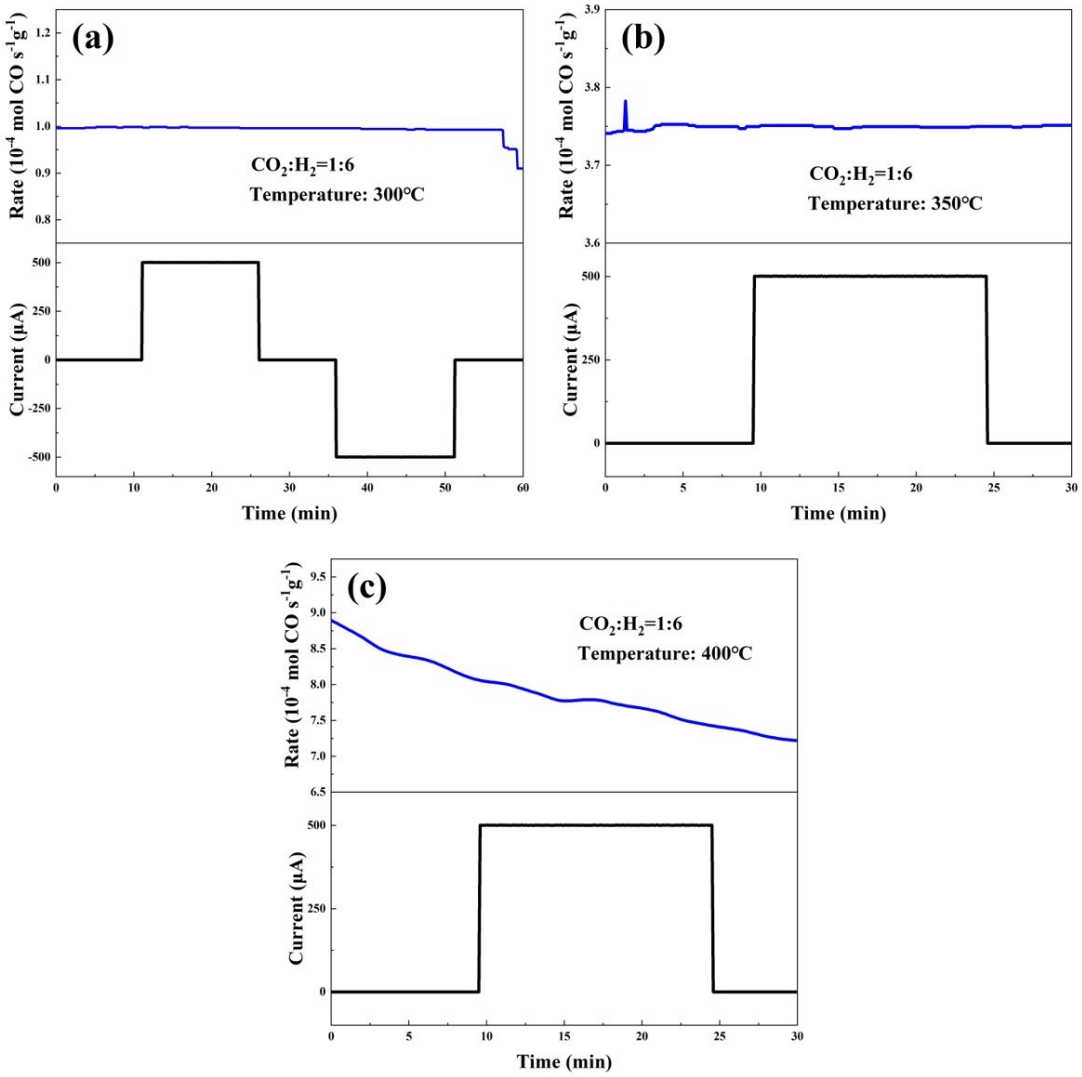

Figure D-14. Transient RWGS rates over Fe/LLTO and corresponding applied currents in reducing conditions (a) under positive and negative polarization at 300°C, and under positive polarization at (b) 350°C and (c) 400°C.

Figures D-15a and b depict the EPOC effects at 350°C in reducing conditions with -400 μA and -300 μA currents, respectively. It was found that the reaction rate increased by 11% (ρ=1.11, Λ=5.69) at -400 μA, and by only 6% (ρ=1.06, Λ=4.04) at -300 μA. Compared to similar conditions at -500 μA according to **Figure 6-6c**, the CO production rate increment was notably lower, attributed to a decreased amount of Li^+ migration under a smaller polarization. In EPOC, N_G (mol) was used to quantify the extent of uptake of reactive promoting species, namely Li^+ (in moles) in this study, during polarization and was calculated using Eq. (D-2):

$$N_G = \frac{I\tau}{2F} \quad \text{(D-2)}$$

where I denoted the applied current, τ referred to the time needed for the catalytic rate to achieve 63% of its suppressed or promoted steady-state value and F represented Faradaic constant. The N_G under reducing conditions were determined to be 1.4×10^{-7}, 1.1×10^{-7}, and 8.5×10^{-8} moles of Li^+ at currents of -500, -400, and -300 μA, respectively. Quantitatively, it showed that the N_G increased with the applied currents, indicating that more Li^+ was involved in the electrocatalytic processes at Fe-LLTO-gas interface by being supplied to the iron catalyst from the LLTO under polarization. Notably, at a current of -500 μA, the N_G was estimated to be 5.1×10^{-7} moles under oxidizing conditions, decreasing to 4.3×10^{-7} moles under stoichiometric conditions. This observation suggested a greater consumption of Li^+ in a CO_2-rich environment, facilitated by a more abundant amount of O^{2-} supply due to the higher oxidation state of FeO_x. Conversely, the N_G was significantly lower under reducing conditions because the iron catalyst was mainly in its reduced state and thereby Li^+ only interacted with limited amount of CO_2 in this case.

The influence of temperature on the EPOC effects was also evident. As shown in **Figure D-15c**, EPOC manifested under oxidizing conditions at 300°C. Similar to **Figure 6-6b**, the reaction rate experienced a 15% reduction under negative polarization at -500 μA (with ρ=0.85 and Λ=1.51). At 300°C, FeO_x predominantly existed in the form of Fe_3O_4. Consequently, it was more susceptible to reduction in the presence of Li^+ supply. At 400°C, despite not reducing to Fe^0, FeO_x underwent further

reduction with a diminished availability of O^{2-}. This led to a constrained transient response of the reaction rate to the applied current, not exhibiting the EPOC phenomenon (**Figure D-13a**). From **Figure D-15d**, EPOC was observed at 400°C (with ρ=1.04 and Λ=3.4) but not at 300°C in reducing conditions, where Fe^0 was the main phase and facilitated the interaction of Li^+ with CO_2 to form $Li_2C_2O_4$. However, the temperature at 300°C was inadequate for the decomposition of $Li_2C_2O_4$ into Li_2CO_3 and CO, which occurred only at higher temperatures. As a result, no EPOC phenomenon was observed herein (**Figure D-14a**). Moreover, RWGS was known to be more favorable in H_2-rich environments at high temperatures. Therefore, at 400°C, CO_2 was more readily converted into CO thermodynamically rather than interacting with migrated Li^+, leading to a limited EPOC effect.

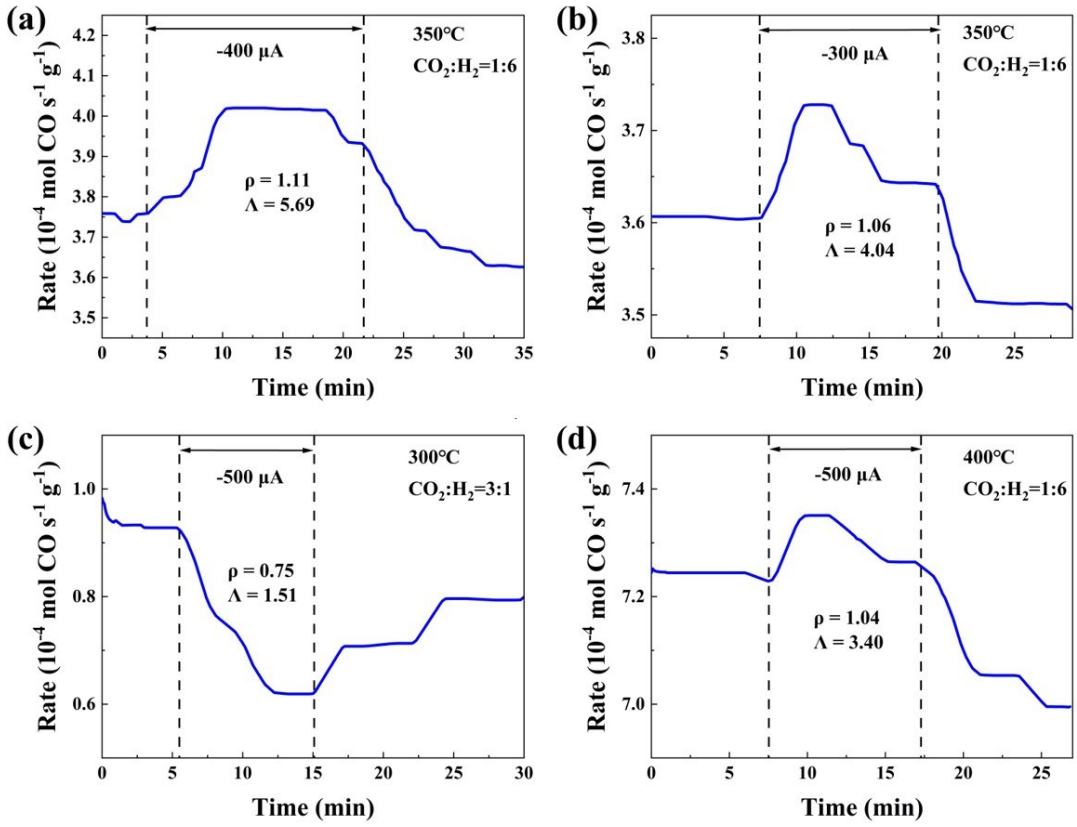

Figure D-15. Transient RWGS rates over Fe/LLTO under different conditions.

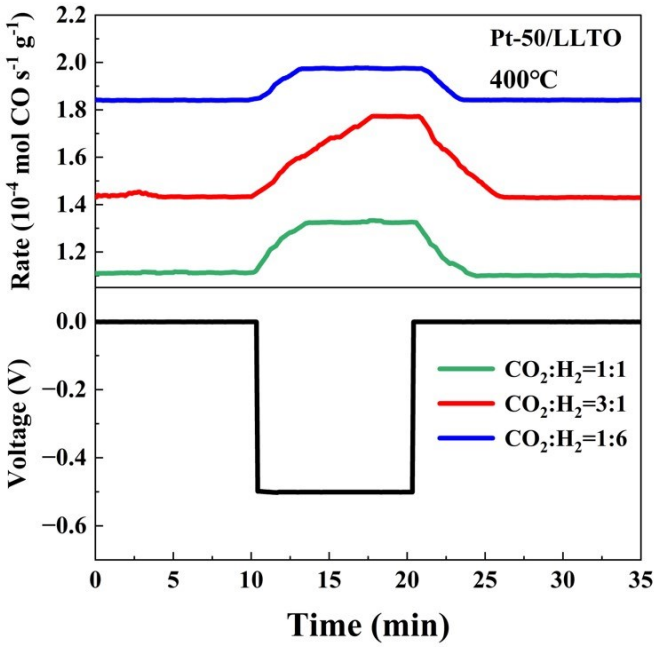

Figure D-16. Transient RWGS rates over Pt-50/LLTO at 400°C and corresponding applied voltage of -0.5 V under different reaction conditions.

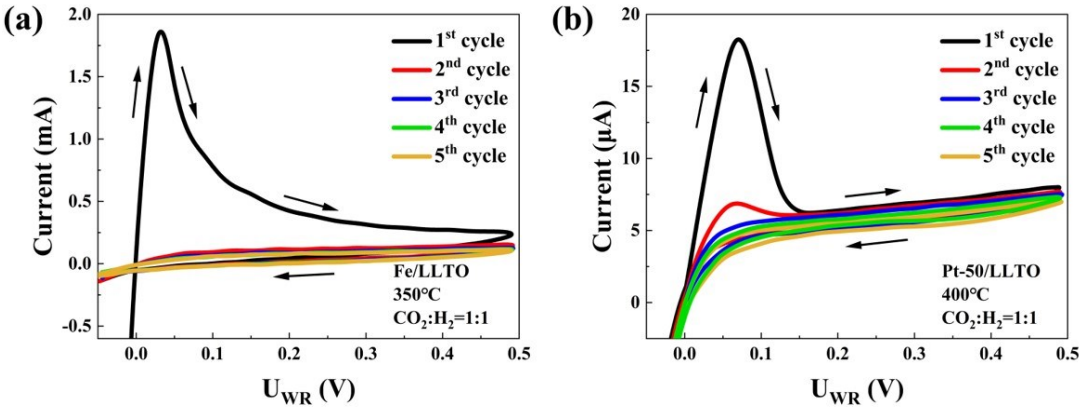

Figure D-17. The 1st to 5th cycles of CV over (a) Fe/LLTO and (b) Pt-50/LLTO in RWGS under stoichiometric conditions.

Chapter 7: Conclusions and Recommendations

7.1 Conclusions

The development of CO_2 conversion technologies in recent years has shown a promising direction and is crucial for addressing the urgent need for sustainable solutions in the face of the environmental crisis caused by climate change. Despite significant progress, the continuous growth in energy demand, which still largely depends on fossil fuels and natural gas, highlights ongoing challenges. This is especially true as the demand for alternatives to fossil fuels increases and the shift to renewable energy sources remains slow. In response to these issues, it is critical to prioritize research and development in CO_2 conversion technologies to help create a sustainable future and protect the planet for future generations. Building on the idea of sustainability, this thesis aims to develop and evaluate novel catalytic systems paired with the EPOC phenomena to recycle CO_2 more efficiently and economically. Focusing on the RWGS reaction, the employment of non-noble metal catalysts deposited on solid electrolytes and the application of electrochemical polarization allows for in-situ control of the catalytic activity. Each chapter encompasses those approaches with the following conclusions:

- In Chapter 3, Cu NPs (13 nm) were synthesized for the first time through the polyol synthesis method and deposited on YSZ solid electrolyte. Upon the application of positive polarization, the RWGS catalytic rate was increased with $\rho = 1.19$ and $\Lambda = 6.52$. Based on XPS characterizations and CV tests, the oxidation of Cu^0 to Cu^{1+} by direct supply of O^{2-} from YSZ was considered the reason for the observed rate enhancement. The reaction conditions, including CO_2:H_2 ratios and temperatures, also showed significant impacts on the oxidation states and surface morphology of Cu NPs. This work provided a new non-noble metal catalyst in EPOC for RWGS reaction, which was active and economical, and showed stable EPOC effects.

- In Chapter 4, Cu NPs were supported on commercial Co_3O_4 particles (with Cu loadings of 1, 4, and 8 wt.%) to form Cu/Co_3O_4 catalysts. Through electrochemical tests, it was proposed that Co_3O_4 functioned as an O^{2-} reservoir, either providing or receiving O^{2-} to or from Cu NPs, thereby influencing EPOC behaviors. The presence of Cu NPs enhanced the electrocatalytic property of Co_3O_4, while Co_3O_4 helped to reduce the sintering of Cu NPs, particularly when the Cu loading was below 4wt.%. This investigation provided new insights into the electrochemical interactions between oxide supports and Cu NPs, opening avenues for further studies on the EPOC effects of supported Cu catalysts.

- In Chapter 5, Cu NPs were supported on synthesized ZnO, chosen for its simple, stable structure, and affordability. The ZnO not only enhanced the catalytic performance of Cu through MSI but also effectively protected Cu from sintering and oxidation. This protection was noted even with a high copper loading of 60wt.% and at elevated temperatures of 400°C, making it an ideal support for Cu NPs. Under positive polarization, partial oxidation of Cu^0 to Cu^{1+} indicated O^{2-} migration from ZnO to Cu. A new DFT model was developed to theoretically illustrate this process and to explain the energy input requirement to initiate the O^{2-} migration, which could be driven by applied currents. Additionally, this work established a link between the ECSA and the magnitudes of EPOC effects, suggesting future directions in the selection of metal oxide supports.

- In Chapter 6, LLTO was utilized as a solid electrolyte for the first time, paired with non-noble metal oxide FeO_x and noble metal Pt as comparative catalysts. The study revealed a notable superior activity of Fe/LLTO over Fe/YSZ, demonstrating an MSI effect. When constant voltages were applied, Li^+ was found to migrate toward the metal catalyst and interact with FeO_x, resulting in a transformation of the active phase of the Fe catalyst during the RWGS reaction. This interaction was absent in Pt, which remained in its metallic state

throughout the process. Expanding the application scope of LLTO, CO oxidation was also performed, with Fe/LLTO demonstrating EPOC effects at 150°C for the first time. This innovative use of Li^+ as a promoter enabled the EPOC phenomenon at low temperatures, leveraging the high ionic conductivity of LLTO, thereby making EPOC more viable for industrial applications.

7.2 Recommendations

In scientific exploration, each discovery sparks new ideas and possibilities. This thesis begins by highlighting the advantages of using Cu-based catalysts for the RWGS reaction, employing MSI and EPOC phenomena. It ends by innovatively proposing the integration of the LLTO solid electrolyte into the EPOC framework. However, further research is needed to fully understand the materials and mechanisms. Recommendations for future EPOC developments are provided for both academic and industrial communities:

- With the assistance of LLTO which is highly conductive at low temperatures, further research can focus on using operando characterizations, including polarization modulation infrared reflection absorption spectroscopy (PM-IRRAS), in-situ XRD, and in-situ Raman spectroscopy, to investigate the ionic species migration mechanisms and their influences on the intermediates and gas adsorption on metal catalyst surface.
- DFT studies on the Li^+ migration within the LLTO structure during EPOC and its influence on metal/metal oxide catalysts, as well as gas adsorption/desorption of reactant gases, are necessary and should be linked to the operando characterizations.
- Given that LLTO is applicable in EPOC studies, which means Li^+ is a promoter, using it in more reactions, like CO_2 methanation, Fischer–Tropsch process, ethylene oxidation, and ammonium synthesis, is essential to broaden

its application and understand the functions of this material in energy conversions.

- Knowing that the ECSA is correlated with the EPOC effect, where the oxygen vacancy plays an important role, more experiments on this using reducible oxides like CeO_2 and TiO_2 and irreducible oxides like Al_2O_3 and SiO_2 as supports for Cu NPs should be done. Typically, the ECSAs and O^{2-} diffusion coefficients of these Cu-based catalysts should be determined from CVs and compared to give a more general result.

- Modify the experimental set-up, making it suitable for EPOC at high pressures (10-20 bars) for methanol synthesis using Cu/ZnO catalysts. The feeding gases should contain CO_2, CO, H_2, and Ar. The negative influence of produced H_2O should also be studied, which might be removed in-situ by using zeolite as support or removed ex-situ by installing a condensing system.

- EPOC for RWGS reaction has been widely studied using metal catalysts, including Pt, Pd, Ru, Rh, Co, Ni, Fe, and Cu, as well as supported-metal catalysts like Ru/Co_3O_4, Ru/YSZ, Pd/ZnO, Ni/Al_2O_3, Fe/Co_3O_4, and Cu/Co_3O_4, which are deposited on various solid electrolytes like YSZ, BZY, β''-Al_2O_3, and LLTO. Therefore, a comprehensive analysis of the catalyst selection, reaction conditions, electrochemical behaviors, and EPOC effects can be done with the assistance of machine learning to give insights into the 'hidden rules' and to direct futural developments of novel materials and systems in the EPOC field. Typically, the machine learning models with the best-performance algorithms for classification and regression should be proposed and validated by new data points collected from systems using new catalysts.

7.3 Scholarly Contributions

List of Publications:

J. Wang, M. Couillard, and E.A. Baranova. Electrochemical Promotion of Copper Nanoparticles for the Reverse Water Gas Shift Reaction. Catalysis Science & Technology. 2022, 12(January), 1562-1573. (PhD Work)

J. Wang, M. Couillard, and E.A. Baranova. Insight into Electrochemical Promotion of Cu/Co_3O_4 Catalysts for the Reverse Water Gas Shift Reaction. ChemCatChem. 2023, 15(9), 1-12. (PhD Work)

J. Wang, M. G. Sandoval, M. Couillard, E. A. González, P. V. Jasen, A. Juan, A. Weck, and E. A. Baranova. Experimental and DFT Study of Electrochemical Promotion of Cu/ZnO Catalysts for the Reverse Water Gas Shift Reaction. ACS Sustainable Chemistry & Engineering. 2024, 12(29), 11044-11055. (PhD Work)

In progress:

J. Wang, S. Yan, K. E. Salem, C. Panaritis, M. S. E. Houache, Y. Abu-lebdeh, D. Higgins, and E.A. Baranova. Electrochemical Promotion of Catalysis by Lithium-Ion. Submitted to ACS Catalysis. (PhD Work)

Conferences and Presentations:

J. Wang and E.A. Baranova (2021). Electrochemical Promotion of Copper Oxides for the Reverse Water Gas Shift Reaction. IUPAC | CCCE 2021 Conference, August, Online. Oral presentation. (PhD Work)

J. Wang and E.A. Baranova (2022). Electrochemical Promotion of Cu/ZnO catalysts for the Reverse Water Gas Shift Reaction. Canadian Chemical Engineering Conference, October, Vancouver, Canada. Oral presentation. (PhD Work)

J. Wang and E.A. Baranova (2023). Electrochemical Promotion of Cu/ZnO catalysts for the Reverse Water Gas Shift Reaction. ECS Meeting, April, Kingston, Canada. Poster presentation. (PhD Work)

J. Wang, S. Yan, and E.A. Baranova (2023). In Situ Electrochemical Modification of Reverse Water Gas Shift Reaction Over FeO_x Supported on a Lithium Ion Conductor. Canadian Chemical Engineering Conference, November, Calgary, Canada. Oral

presentation. (PhD Work)

J. Wang, S. Yan, and E.A. Baranova (2024). Pioneering the Use of LLTO in Electrochemical Promotion of Catalysis. Canadian Symposium on Catalysis, May, Sherbrooke, Canada. Oral presentation. (PhD Work)